

---

# **AGN-ICM interaction in nearby cool core clusters: energetics and transport processes**

Aurora Simionescu

---



München 2009



---

# **AGN-ICM interaction in nearby cool core clusters: energetics and transport processes**

**Aurora Simionescu**

---

Dissertation  
an der Fakultät für Physik  
der Ludwig–Maximilians–Universität  
München

vorgelegt von  
Aurora Simionescu  
aus Brăila, Rumänien

München, den 16. März 2009

Erstgutachter: Prof. Dr. Hans Böhringer  
Zweitgutachter: Prof. Dr. Ortwin Gerhard  
Tag der mündlichen Prüfung: 4. Juni 2009

# Contents

<b>Zusammenfassung</b>	<b>xv</b>
<b>Summary</b>	<b>xvii</b>
<b>1 Introduction</b>	<b>1</b>
1.1 Clusters of galaxies . . . . .	1
1.2 The cooling flow problem . . . . .	2
1.3 AGN feedback . . . . .	3
1.4 Chemical enrichment . . . . .	4
1.4.1 Type Ia supernovae . . . . .	5
1.4.2 Core-collapse supernovae . . . . .	6
1.4.3 Distribution of metals in cooling cores . . . . .	6
1.5 The XMM-Newton observatory . . . . .	7
1.5.1 EPIC . . . . .	8
1.5.2 RGS . . . . .	9
1.6 Structure of this thesis . . . . .	10
<b>2 The gaseous atmosphere of M87 seen with XMM-Newton</b>	<b>11</b>
2.1 Introduction . . . . .	11
2.2 Observations and data reduction . . . . .	13
2.2.1 Broad-band fitting . . . . .	14
2.2.2 Spectral analysis . . . . .	15
2.2.3 Pressure and entropy maps . . . . .	17
2.3 Substructure in the M87 gas halo . . . . .	19
2.3.1 Temperature and entropy . . . . .	19
2.3.2 Pressure . . . . .	20
2.4 Discussion . . . . .	22
2.4.1 Absence of a classical cooling-flow on smaller scale . . . . .	22
2.4.2 Motion of the galaxy to the NW . . . . .	24
2.4.3 Possible core oscillations . . . . .	27
2.4.4 Large-scale correlation of the radio emission and entropy map . . . . .	27
2.4.5 Ellipticity of the underlying dark matter potential . . . . .	29
2.4.6 Heating of the ICM by weak shocks . . . . .	29

2.5	Summary and conclusions . . . . .	30
<b>3</b>	<b>Metal-rich multi-phase gas in M87</b>	<b>33</b>
3.1	Introduction . . . . .	33
3.2	Observations and data analysis . . . . .	35
3.3	Spectral models . . . . .	36
3.4	Temperature structure of the M87 halo . . . . .	36
3.4.1	Two-temperature models . . . . .	36
3.4.2	The differential emission measure model . . . . .	39
3.4.3	Discussion of the temperature structure and physical feasibility of the different models . . . . .	42
3.4.4	Discussion of the implications of multi-temperature structure for thermal conduction . . . . .	42
3.5	The spatial distribution of metals . . . . .	45
3.5.1	Abundance maps . . . . .	45
3.5.2	Metal abundance patterns of different elements in and outside the multi-temperature regions . . . . .	45
3.6	The properties of the cool gas . . . . .	47
3.6.1	The correlation between the amount of uplifted cool gas and metallicity . . . . .	47
3.6.2	The metallicity of the cool gas . . . . .	50
3.6.3	The mass of the cool gas . . . . .	53
3.6.4	Discussion of the origin and uplift of the cool gas . . . . .	55
3.7	Constraints on possible non-thermal emission . . . . .	61
3.8	Conclusions . . . . .	64
<b>4</b>	<b>Chemical enrichment in the cluster of galaxies Hydra A</b>	<b>67</b>
4.1	Introduction . . . . .	68
4.2	Observation and data analysis . . . . .	69
4.2.1	EPIC analysis . . . . .	69
4.2.2	RGS analysis . . . . .	70
4.2.3	Spectral modeling . . . . .	70
4.3	Results . . . . .	72
4.3.1	Global spectra . . . . .	72
4.3.2	Radial profiles . . . . .	74
4.3.3	2D spectral properties . . . . .	76
4.3.4	High resolution spectra . . . . .	78
4.4	Discussion . . . . .	79
4.4.1	Spectral effects of the multi-temperature structure . . . . .	79
4.4.2	Radial distribution of the chemical elements and comparison with other clusters . . . . .	85
4.4.3	ICM abundance patterns and supernova yield models . . . . .	88
4.4.4	The origin of the metal abundance peaks in Hydra A . . . . .	89
4.4.5	Gas uplift by the AGN and metal transport into the ICM . . . . .	93

---

4.5	Conclusions . . . . .	96
<b>5</b>	<b>The large-scale shock in the cluster of galaxies Hydra A</b>	<b>99</b>
5.1	Introduction . . . . .	100
5.2	Observation and data analysis . . . . .	101
5.3	Spectral modeling . . . . .	101
5.4	The shock geometry . . . . .	102
5.5	1D shock model and Mach number estimates . . . . .	103
5.6	The temperature jump associated with the shock . . . . .	106
5.7	Relative motions in the cluster and the shape of the shock front . . . . .	110
5.7.1	Model cluster . . . . .	111
5.7.2	Model jet . . . . .	111
5.7.3	Generation of bulk motion . . . . .	113
5.7.4	Code . . . . .	113
5.7.5	Simulation results . . . . .	114
5.8	Discussion . . . . .	115
5.8.1	Comparison to observation . . . . .	115
5.8.2	Effects of AGN activity on the temperature structure in the cluster core . . . . .	116
5.8.3	Alternative scenarios . . . . .	117
5.9	Summary and Outlook . . . . .	118
<b>6</b>	<b>Conclusions</b>	<b>121</b>
6.1	Mechanisms and energetics of AGN-ICM interaction . . . . .	121
6.2	Sources of chemical enrichment and the transport of metals in the ICM . . . . .	122
	<b>Acknowledgements</b>	<b>133</b>
	<b>Curriculum Vitae</b>	<b>137</b>



# List of Figures

2.1	M87 surface brightness map . . . . .	13
2.2	Temperature map of M87 obtained from spectral analysis. . . . .	17
2.3	Metal abundance map of M87 (single temperature spectral model). . . . .	18
2.4	Pressure and entropy radial profiles and corresponding smooth model . . . . .	19
2.5	Entropy deviations from a smooth radially symmetric model. . . . .	20
2.6	Pressure deviations from a smooth radially symmetric model. . . . .	21
2.7	Pressure deviations from an elliptical model (ratio). . . . .	22
2.8	Data and best-fit <i>vmcflow</i> model with fixed low-temperature cutoff for the small-scale low-temperature feature NW of the core. . . . .	23
2.9	Data and best-fit two-temperature <i>mekal</i> model for the small-scale low-temperature feature NW of the core. . . . .	23
2.10	Entropy (left) and pressure (right) deviations from a smooth radially symmetric model overlaid with radio contours (90 cm). . . . .	24
2.11	Temperature and abundance NW/SE asymmetry. . . . .	25
2.12	Entropy and temperature radial profiles in 90 degree wedges NW and SE of the core of M87. . . . .	28
2.13	Projected temperature and relative pressure jumps around the 3' shock, corresponding to Mach numbers of 1.05 and 1.04 respectively. . . . .	30
3.1	Temperature map of the cool component as determined from the two-temperature <i>mekal</i> fit. . . . .	37
3.2	Temperature map of the hot component as determined from the two-temperature <i>mekal</i> fit. . . . .	37
3.3	Differences in determination of the temperature of the cool component with the <i>apec</i> and the <i>mekal</i> models. . . . .	38
3.4	Map of the fraction of the emission measure of the cool component to the total emission measure for the two-temperature <i>mekal</i> fit. . . . .	39
3.5	Fraction of the emission measure of the gas below 1.5 keV to the total emission measure from the <i>wdem</i> fit. . . . .	40
3.6	Map of the inverse slope $\alpha$ from the <i>wdem</i> fit. Higher values in the map reflect regions where the emission measure distribution is flatter. . . . .	41
3.7	Map of the lower temperature cutoff from the <i>wdem</i> fit. . . . .	41
3.8	Results of fitting various simulated <i>wdem</i> spectra with a two-temperature model. . . . .	43

3.9	Factor by which the Spitzer heat conduction must be suppressed in order to maintain the cool gas in the multi-temperature structure. . . . .	44
3.10	Fe map of M87 determined from the <i>wdem</i> model. . . . .	46
3.11	Comparison of Fe abundance determination using two different multi-temperature models. . . . .	47
3.12	Oxygen and silicon vs. iron abundances in and outside the arm regions. . . . .	48
3.13	Averaged Fe abundance in 2%-wide bins of the fraction of the cool component and linear fit for each arm. . . . .	49
3.14	Map of Fe deviations from a smooth radial profile. . . . .	50
3.15	Results of fitting a simulated combination of two <i>wdem</i> spectra with a high Fe abundance of the cool gas with a <i>wdem</i> model with coupled abundances. . . . .	52
3.16	Map of the mass of gas below 1.5 keV. . . . .	56
3.17	Regions for spectral extraction used to test the presence of a power-law component. . . . .	62
4.1	The EPIC spectrum of the central 3' and fit residuals with respect to the best-fit Gaussian emission measure distribution model. . . . .	73
4.2	Projected radial profiles of temperature, Fe, Si, S and O abundances in Hydra A. . . . .	74
4.3	Radial profiles for O obtained by fitting spectra from the MOS and pn detectors independently. . . . .	75
4.4	Temperature and metallicity maps of Hydra A. . . . .	77
4.5	Combined RGS 1 <sup>st</sup> and 2 <sup>nd</sup> order spectrum of Hydra A. . . . .	78
4.6	Residuals from best-fit soft-band spectral model when extrapolated to the hard band. . . . .	82
4.7	The distribution of emission measure vs. temperature in the central 3'. . . . .	82
4.8	$N_H$ profile determined fitting a single-temperature model to the full and soft energy bands. . . . .	84
4.9	Radial distribution of Fe and O in Hydra A compared to other clusters in the literature. . . . .	86
4.10	Radial distribution of O/Fe, Si/Fe and S/Fe in Hydra A compared to other clusters. . . . .	87
4.11	Observed Fe/Si against Fe/O ratios and expectations based on different supernova yield models. . . . .	90
4.12	Different geometries assumed for the volume of the cool gas in Hydra A. . . . .	94
5.1	Pressure map of Hydra A divided by a radially symmetric, smooth model. . . . .	102
5.2	Chandra surface brightness map of Hydra A divided by a 2D elliptical beta model. . . . .	102
5.3	Surface brightness profiles (from EPIC/pn) and fitted shock models (best-fit and bracketing). . . . .	104
5.4	Temperature profile of Hydra A and analytic fits. . . . .	107
5.5	Temperature profiles in 4 different sectors. . . . .	108
5.6	Expected emission-measure weighted projected temperature profile across the shock relative to the undisturbed temperature for various 1D models. . . . .	109
5.7	Simulated shock front and bubbles at 160 Myr. . . . .	112

---

5.8	Evolution of pressure profiles along the grid's $x$ - and $y$ -axis through the center of the cluster. . . . .	114
5.9	Temperature slices taken at 160 Myr after the jet was launched for two alternative simulations. . . . .	116
5.10	Observed and simulated distribution of emission measure vs. temperature. . . . .	117



# List of Tables

3.1	Comparison of best-fit metal abundance ratios in and outside the multi-temperature regions ( <i>wdem</i> fit). . . . .	49
3.2	Estimates of the average iron abundance of the cool component. . . . .	53
3.3	Total mass of the cool gas in M87. . . . .	55
3.4	Enrichment times needed to produce the metals seen in the cool gas (in Myr). . .	60
3.5	Upper limits on the non-thermal pressure. . . . .	63
3.6	Lower limits on the magnetic field strength. . . . .	64
4.1	Fit results for the EPIC data using a <i>gdem</i> model. . . . .	72
4.2	Radial profiles obtained by fitting the EPIC data with a <i>gdem</i> model. . . . .	74
4.3	RGS fit results using a 3' wide extraction region centered on the cluster core. . .	79
4.4	Uplifted gas mass, Fe mass, and corresponding uplift energy in Hydra A. . . . .	96
5.1	Best-fit parameters for the shocked surface brightness model in the four sectors. .	105
5.2	Best-fit post- and pre-shock temperatures, relative temperature jumps $\delta T$ , and corresponding Mach numbers. . . . .	110
5.3	ICM parameters for the 3D simulation. . . . .	111
5.4	Jet parameters for the 3D simulation. . . . .	113
6.1	Comparison of energies associated with various AGN-ICM interaction mechanisms in M87 and Hydra A. . . . .	122



# Zusammenfassung

Diese Arbeit stellt eine detaillierte Analyse der Eigenschaften des heißen, röntgenhellen Gases in Galaxienhaufen (intra-cluster medium, ICM) vor. Galaxienhaufen sind riesige astrophysikalische Laboratorien, die uns die Untersuchung der Strukturentstehung und Metallanreicherung im Universum ermöglichen. Sie sind die einzigen Objekte, die groß genug sind, um in ihrer Zusammensetzung aus dunkler und baryonischer Materie als repräsentativ für das ganze Universum zu gelten. Der größte Anteil der Baryonen (um 80%) liegt in Form des diffusen ICM vor, das während der Strukturentstehung durch Stoßwellen auf Temperaturen von  $10^7 - 10^8$  K geheizt wird und deswegen hauptsächlich im Röntgenbereich strahlt. Dieses Plasma durchdringt den ganzen Haufen und folgt dem von dunkler Materie beherrschten Gravitationspotenzial. Die tiefen Potenzialtöpfe von Galaxienhaufen bewahren alle Metalle auf, die von Supernovae während der gesamten Lebensdauer des Haufens in den angehörigen Galaxien produziert werden. Deswegen liefern die Metallhäufigkeiten im ICM Information über die durchschnittliche chemische Entwicklung des Universums selbst.

Moderne Beobachtungen legen nahe, dass die energetische Wechselwirkung zwischen dem Aktiven Galaktischen Kern (active galactic nucleus, AGN) in der hellsten Haufengalaxie (brightest cluster galaxy, BCG) und dem ICM benötigt wird, um das Gas im Zentrum mancher Haufen zu heizen. Die hier im Röntgenbereich abgestrahlte Energie ist so groß, dass, wenn sie allein von der thermischen Energie des Haufengases aufgebracht werden müsste, das Gas sich stark abkühlen würde. Die daraus erwartete hohe Sternentstehungsrate wird in der zentralen Haufengalaxie nicht beobachtet (das sogenannte "cooling-flow" Problem). Darüber hinaus sollten die vom AGN verursachten Gasbewegungen und Turbulenz wichtig sein, um die Metalle ins ICM zu transportieren und dort zu verteilen.

Ich untersuche die mit der AGN-ICM Wechselwirkung verbundenen Merkmale in zwei hellen und relativ nahe gelegenen Objekten. Die Galaxie M 87, im Zentrum des nächsten Haufens, Virgo, ist für den Anfang das beste Zielobjekt für solch detaillierte Studien. M 87 ist hell genug für exzellente Spektrenstatistik und auch nah genug, um eine gute Auflösung von räumlich kleinen Strukturen zu ermöglichen. Das nächst interessanteste Objekt, abgesehen vom Perseus Haufen, für den ausführliche Studien schon vorhanden sind, ist Hydra A. Dieser Haufen ähnelt einer vergrößerten Version von M87. Hier sind Energie und typische Ausdehnung der AGN-ICM Wechselwirkungsmerkmale ungefähr zehnmal größer, aber die Auflösung, wegen der größeren Entfernung, auch um einen Faktor zehn reduziert.

In diesen zwei Haufen habe ich die ersten zwei von AGN verursachten klassischen Stoßwellen gefunden, für die die gemessenen Temperatur- und Drucksprünge zu übereinstimmenden Machzahlen

führen. Man vermutet, dass Stoßwellen eines der Hauptmechanismen sind, durch die der zentrale AGN das ICM heizt und dessen beschleunigte Abkühlung verhindert. Ich lege sowohl einfache 1D als auch 3D hydrodynamische Simulationen vor und vergleiche deren Ergebnisse mit den Beobachtungen, um die Machzahl und Energie des Schocks in Hydra A einzuschätzen. In den 3D Simulationen werden Gasbewegungen miteinbezogen, als mögliche Erklärung für die Asymmetrie und Versetzung der Stoßwellenfront vom Haufenzentrum. In M 87 finde ich auch eine "Kaltfront", eine Diskontinuität in den Temperatur- und Flächenhelligkeitsprofilen, die ebenfalls auf Gasbewegungen hindeutet.

Kühle, metallreiche Filamente, die oft aus einer Mischung mehrerer Temperaturphasen bestehen und räumlich mit den vom AGN erzeugten Radioblasen zusammenfallen, deuten darüberhinaus die wichtige Rolle des AGNs für den Transport der in der BCG produzierten Metalle ins ICM an. In M 87, wo die exzellente Photonen-Statistik eine detaillierte Modellierung der Temperaturstruktur auf räumlich kleinen Skalen ermöglicht, finde ich eine Korrelation zwischen dem Anteil kühlen Gases und der durchschnittlichen Metallizität, und berechne damit die Metallizität des kühlen Gases. Dieses Gas wird von aufsteigenden Radioblasen in größere Entfernungen vom Haufenzentrum mitgerissen, kühlt sich aufgrund des niedrigeren Umgebungsdrucks adiabatisch ab, und wird deswegen kühler im Vergleich zum umliegenden ICM. Das Gas ist reicher an Metallen, da es durch Supernovae und Sternwinde in der zentralen Galaxie angereichert wurde. Ich schätze die mit dem Auftrieb verbundene Gasmasse, Eisenmasse und Energie in beiden Haufen ab und stelle fest, dass der AGN einen wesentlichen Anteil der Eisenmasse im Zentrum des Haufens nach außen befördern kann. Ich vergleiche die dafür benötigte Energie mit der Schockenergie und der Energie, die mit der Erzeugung der AGN-verursachten leuchtschwächeren Regionen in den Röntgenbildern verknüpft ist. Diese Röntgen-"Löcher" sind mit Radiostrahlung gefüllt und werden dadurch produziert, dass der AGN relativistische Teilchen ins ICM einbläst, die das Haufengas verdrängen. Die dafür benötigte Energie wird danach in Wärme umgewandelt, deswegen deuten auch diese Merkmale auf einen wichtigen Mechanismus hin, der die beschleunigte Abkühlung des zentralen ICMs verhindert. In M 87 sind die Energien für diese drei verschiedene AGN-bezogenen Prozessen ähnlich. In Hydra A ist die Anhebungsenergie mit der Energie der jüngsten Radioblasenbildung vergleichbar, aber um zwei Größenordnungen kleiner als die mit einem früheren, kräftigeren AGN-Ausbruch assoziierte Schockenergie. Desweiteren untersuche ich die Zeitskalen, in der Supernovae und Sternwinde die beobachteten Mengen und Anteile verschiedener Metalle erzeugen können, und vergleiche die gemessenen relativen Metallhäufigkeiten mit Modellen der Elementproduktion von verschiedenen Supernovatypen.

# Summary

This work focuses on detailed spatial and spectral analysis of the properties of the intra-cluster medium (ICM) in clusters of galaxies, giant laboratories which allow us to probe the formation and chemical enrichment history of the Universe. These are the only objects large enough to contain a fair sample of all types of baryonic and dark matter in the Universe. The largest amount of baryons (about 80%) resides in a diffuse ICM which is shock-heated during mergers associated with hierarchical large-scale structure formation to temperatures of  $10^7 - 10^8$  K and consequently emits mostly in the X-ray domain. This plasma permeates the entire cluster, tracing the gravitational potential dominated by the dark matter. The deep potential wells of clusters of galaxies retain all the metals produced by supernovae in the member galaxies throughout the cluster's life, therefore metal abundances in the ICM constitute a fossil record of the average chemical enrichment history of the Universe.

Energetic interaction between the active galactic nucleus (AGN) in the brightest cluster galaxy (BCG) and the ICM is needed to heat the gas at some cluster centers where the surface brightness profile is very peaked. The energy radiated away here is so large that, if it came from thermal energy alone, the hot X-ray gas would have to cool and form copious amounts of stars, in disagreement with observations (the so-called “cooling flow” problem). Turbulence and gas motions induced by the AGN are moreover believed to be a main ingredient for transporting and distributing the metals within the ICM.

I investigate features associated with AGN-ICM interaction in two bright and relatively nearby systems. M87, at the center of Virgo, the nearest galaxy cluster, is a natural choice as a first target for such detailed studies. Since it is so close, M87 is both bright enough to ensure excellent spectral statistics and enables us to resolve much smaller spatial scales than possible for any other object. The next most interesting case, apart from the Perseus cluster which had already been looked at in detail, is Hydra A. This cluster can be considered a scaled-up version of M87, where the power and scales involved in the AGN-ICM interaction are about an order of magnitude larger.

In these two clusters, we find and map the first two known classical AGN-driven shocks with spectroscopically confirmed temperature and pressure jumps corresponding to consistent Mach numbers. These shocks are thought to be one main mechanism through which the AGN heats the ICM to prevent catastrophic cooling. I present both simplified 1D and 3D hydrodynamic simulations of the large-scale shock in Hydra A and compare the results with observations in order to estimate the Mach number and energy of the shock. The 3D simulations include a bulk flow of the ICM as a possible explanation for the asymmetry of the observed shock front shape

and its offset with respect with the cluster center. In M87, I show a cold front that suggests the presence of bulk motions in the form of sloshing in the ICM.

Cool, metal-rich filaments, which can often be resolved into multi-temperature components and are spatially coincident with AGN-inflated radio lobes, suggest moreover the crucial role of the AGN in uplifting the chemical elements produced by the central galaxy and transporting them into the ICM in both clusters. In M87, where the statistics allow detailed modeling of the temperature structure on small spatial scales, I find a correlation between the amount of cool gas and the metal abundance (averaged over all temperature phases), based on which I deduce the metallicity of the cool gas. This gas is cooler compared to the surrounding ICM most probably because of adiabatic expansion, as it was dragged by the rising radio lobes towards larger radii where the ambient pressure is smaller; it is more metal-abundant because it was enriched by supernovae and stellar mass loss at the center of the galaxy. I estimate the gas mass, Fe mass and energy associated with the uplift for both clusters. I find that the AGN can uplift a sizable amount of Fe compared to the mass of Fe currently present in the cluster center. I compare the energies related with gas uplift with those needed to create the AGN-driven shocks and AGN-inflated bubbles and show that, for M87, the energies required to produce these three substructures are similar. In Hydra A, the energy needed to uplift the gas is similar to that associated with the most recently inflated bubbles, but orders of magnitude smaller than the energy of the large-scale shock created during a much more powerful past outburst. I moreover discuss the timescales in which supernovae and stellar winds can produce the observed amount of metals and metal abundance ratios, and compare the observed metal abundance ratios with models of heavy element production by different supernova types.

# Chapter 1

## Introduction

### 1.1 Clusters of galaxies

Galaxies are not distributed uniformly in the Universe. One can find both agglomerations of thousands of large galaxies within a radius of a few megaparsecs (Mpc) and large volumes almost completely devoid of galaxies. The regions with a very high density of galaxies are usually connected by filaments of intermediate density which delimitate the voids. When we “zoom out” to the point that galaxies start to look like very small polka dots, the Universe looks like a mind-bogglingly big three dimensional spider-web. The “knots” of this cosmic web, the regions with a large over-density of galaxies, are known as clusters of galaxies.

The first detailed report about such a cluster of galaxies (Perseus) was published more than a century ago (Wolf 1906). Abell (1958) performed a systematic search for agglomerations of galaxies on optical plates and created the Abell cluster catalog still widely used today. But a galaxy cluster consists of more than just an agglomeration of galaxies. This was first suggested by Zwicky (1937), who looked at the velocity dispersion of cluster galaxies and concluded that the cluster must be much more massive than the sum of the masses of its member galaxies, otherwise these could not be gravitationally bound. A part of the missing cluster mass was found in the 1960s, when X-ray emission from a diffuse, very hot gas filling the cluster volume was detected (Byram et al. 1966; Kellogg 1973). For rich clusters, the mass of this gas, also known as the intra-cluster medium (ICM), is around 5 times larger than the stellar mass in the member galaxies (Allen et al. 2002). Assuming hydrostatic equilibrium for the ICM allows us to determine the total cluster mass, revealing that still an overwhelming  $\sim 80-90\%$  of the cluster is in the form of dark matter. Clusters of galaxies are unique cosmological probes because they are the only objects large enough to contain a fair sample of all types of baryonic and dark matter in the Universe. Moreover, the number distribution of clusters against their total mass and redshift is also sensitive to cosmological parameters. The X-ray emission from the ICM traces the cluster structure contiguously, making X-ray imaging and spectra crucial elements in understanding the astrophysics of galaxy clusters and using their excellent potential for the study of cosmology.

The ICM plasma is typically well approximated as optically thin and in collisional ionization equilibrium (CIE), which enables a simple modeling and straightforward interpretation of cluster

X-ray spectra. Several models of the bremsstrahlung and line emission in these conditions are available, the most widely used being *mekal* (Mewe et al. 1985; Kaastra 1992; Liedahl et al. 1995) and *apec* (Smith et al. 2001). By comparing the available data with spectra predicted by these models, one can determine a temperature or parameters pertaining to a distribution of temperatures, as well as the abundances of different chemical elements with which the member galaxies enrich the ICM and whose lines are visible in the observed spectrum.

## 1.2 The cooling flow problem

By emitting X-rays, the intracluster gas loses energy and therefore should cool if no other source of heating is available. The intensity of the emitted bremsstrahlung radiation increases approximately with the second power of the gas density, therefore the strongest cooling occurs in the central parts of clusters, where the density is high. Observations of clusters with the Uhuru satellite first indicated that, for some clusters which show a very peaked density profile, the mean cooling time of the central gas can be smaller than the Hubble time (Lea et al. 1973). These were termed “cool(ing)-core” clusters and a model was developed to describe the effects of significant cooling of the central gas (Fabian & Nulsen 1977; Mathews & Bregman 1978). Later observations with Einstein and EXOSAT set the estimated percentage of these cooling core clusters to a significant 70-80% (Edge et al. 1992) of the galaxy cluster population. It is still a matter of debate whether or not this percentage is strongly dependent on the redshift (Vikhlinin et al. 2007; Santos et al. 2008).

The cooling flow model, based on early observations mainly with the Uhuru and Einstein observatories, states that upon cooling (which takes place within the so-called cooling radius where the cooling time is equal to or less than the Hubble time) the gas condenses to cold blobs which sink or “flow” through the remaining hotter atmosphere to the very center of the cluster which is often associated with a central dominant (cD) brightest cluster galaxy (BCG). The cooling radius is small compared to the extent of the entire cluster, such that the gas loss through cooling is negligible compared to the total amount of gas in the ICM; however, the cooling radius can be as large as some hundreds of kiloparsecs, allowing the cooling region to be resolved by X-ray satellites. It was inferred that, through the cooling flow, the BCG is still growing at the present time.

According to the cooling flow model, the mass deposition rate - that is, the mass of cool gas which sinks to the core per unit time - can be calculated from the relation

$$L_{cool} = \frac{5}{2} \frac{\dot{M}}{\mu m} kT \quad (1.1)$$

where  $L_{cool}$  is the luminosity associated with the cooling region, usually of the order of 10% of the total luminosity, and  $T$  is the temperature of the gas at the cooling radius. In deriving this formula, it was assumed that the energy lost by radiation comes only from the heat content of the gas in the cooling region plus the  $pdV$  work done on this gas while it condenses. Typical mass deposition rates calculated from this formula are in the range of hundreds and up to thousands of solar masses per year (Fabian 1994).

Evidence for gas cooling out of the X-ray band was indeed observed at a variety of wavelengths. For example, BCGs show anomalous emission of diffuse blue light associated with star formation (McNamara & O'Connell 1989). Clusters with shorter radiative gas cooling times harbor more infrared-luminous BCGs (Egami et al. 2006a) and clusters with small central gas entropies are generally brighter in  $H\alpha$  (Cavagnolo et al. 2008), which also indicates recent star formation. CO and  $H_2$ -emission from large amounts of very cool gas has been observed in BCGs as well (Salomé et al. 2008; Egami et al. 2006b). Nevertheless, with few exceptions, the strength of these signatures implies mass deposition rates typically one to two orders of magnitude smaller than those calculated from the cooling flow model.

With the launch of XMM-Newton and Chandra in 1999, it was discovered that the X-ray gas was in fact not cooling at the rates implied by Eqn. 1.1. High-resolution spectra of cooling core clusters obtained with the RGS lacked the strong emission lines expected from low-temperature gas. This indicated that, while the mean temperature of the ICM did decrease towards the center of cooling core clusters, there was no significant evidence of gas cooling below a certain threshold, usually one half to one third of the virial temperature (Peterson et al. 2001, 2003). This implied the necessity of a fine-tuned heat source which would provide just enough heat to prevent all but a few percent of the central ICM from cooling out of the X-ray band.

### 1.3 AGN feedback

Several forms of possible heat input have been discussed, among which heat conduction from the ICM outside the cooling radius, reconnection of magnetic field lines and energy output from the active galactic nucleus (AGN) of the central galaxy. The current scientific consensus is pointing toward the latter as the most promising candidate.

One advantage of AGN feedback over other heating sources is that it is relatively straightforward to conceive a toy model explaining how the required fine-tuning can be accomplished: a large amount of cooling gas sinking towards the center causes a high accretion rate onto the supermassive black hole (SMBH), triggering an AGN outburst. This disturbs the accretion rate and sends the AGN into a quiescent stage, during which the entropy excess injected by the outburst is radiated away. When the excess entropy has been lost, the density of the gas at the bottom of the potential well becomes again extremely large and a further outburst of the AGN is stimulated when some of this dense gas accretes onto the SMBH, starting the next cycle of the system.

AGN feedback in fact seems to be a crucial ingredient not only for understanding cooling core clusters but also the evolution of structure in the Universe. Magorrian et al. (1998) for example found a puzzling correlation between the mass of the central black hole and the bulge mass in galaxies, suggesting that their evolutions must be tightly coupled. The mechanism behind this relies most probably on gas being blown out of the galaxy during an AGN outburst, which in turn affects the star formation near the center of the galaxy. This is critical to explain why so much fewer very massive galaxies are observed, compared to predictions from large-scale structure simulations which do not take this effect into account (Croton et al. 2006).

The influence of an AGN on the intracluster medium was considered and modeled early on by Böhringer & Morfill (1988) who looked into the effects of associated cosmic ray production

and by Binney & Tabor (1995) who discussed mechanical energy input via the AGN jet. Apart from the achievable fine-tuning necessary, AGNs are attractive candidates for heat sources also because cooling flow clusters were shown to be statistically more likely to contain radio emission indicating recent black hole activity (Burns 1990). The relativistic radio plasma often coincides with cavities in the X-ray images, suggesting interaction between the AGN and the ICM. There seems to be a correlation between the work needed to inflate the observed X-ray cavities and the energy required to prevent the central gas from cooling (Bîrzan et al. 2004; Rafferty et al. 2006), indicating that a form of feedback does occur. As these cavities or “bubbles” which are less dense than the surrounding medium rise, the gas they displace sinks and thermalizes its gravitational energy. Bîrzan et al. (2004) estimated that each AGN outburst introduces between  $10^{58}$  and  $10^{61}$  ergs into the ICM, sufficient energy to stop the cooling flows provided that an AGN outburst occurs with a period of about  $10^8$  years.

While there is significant observational evidence arguing for the scenario of AGN heating of the ICM, the exact feedback and heat transport mechanisms are still grounds for scientific debate. Weak shocks surrounding the X-ray bubbles have also been observed in some systems, notably M87 and Hydra A which are the focus of this work, and could constitute another important mechanism by which the AGN heats the ICM (see Nulsen et al. 2005; Forman et al. 2007, and also Chapters 2 and 5 of this thesis). Sometimes not just X-ray cavities, but X-ray bright filaments that have probably been uplifted by rising lobes of radio plasma are seen - again, M87 is the most speaking example, and the phenomenon is observed also in Hydra A (Chapters 3 and 4 and references therein). In other systems, AGN outbursts have been claimed to produce sound waves which travel through the ICM, also heating it (the best example to date is the Perseus cluster, the brightest extragalactic X-ray source in the sky, Sanders & Fabian 2007). Due to the complexity of these systems, progress in understanding the physics of cooling-core clusters relies in great part on the results of detailed observations, with the help of which we may hope to unveil episodes of the ICM history.

## 1.4 Chemical enrichment

X-ray spectra of the ICM reveal not only information about its thermal structure but also about the heavier elements with which it is polluted by the member galaxies. Clusters of galaxies are unique in this respect because their deep potential wells retain all the metals produced by their stellar populations within their gravitational potential. The dominant fraction of these metals in fact resides within the hot ICM (Finoguenov et al. 2003), making the study of metal abundances in the X-ray spectra crucial for understanding the chemical evolution of the Universe (by metals in the context of this work, we refer to any element heavier than He).

Modern CCD-type detectors can be used to identify the emission lines of O, Ne, Mg, Si, S, Ar, Ca, Fe, and Ni, although the 2p–1s Ne lines at around 1.02 keV are in the middle of the Fe-L complex (lying between 0.8 to 1.4 keV). A reliable determination of both Fe-L and Ne emission line strengths therefore is only possible with the higher spectral resolution of the RGS. With the exception of very rare cases of bright, cool, nearby objects where also C and N are detected with the RGS (Werner et al. 2006a), X-ray spectra deliver information almost exclusively related

to the abundances of elements heavier than and including oxygen, all of which are primarily produced by supernovae. Their abundances within the ICM thus provide us with the integral yield of all the supernova explosions in the member galaxies during the cluster's history.

Stars which are relatively young form in a metal-rich environment and so trap in their atmospheres some of the metals produced earlier by supernovae. These stars then later release some of these heavy elements by stellar winds. It is important to remember nevertheless that these metals were originally produced by supernovae, so it should be possible to reproduce the observed abundance ratios in the ICM as a linear combination of supernova products from the two important supernova types: core-collapse ( $\text{SN}_{\text{CC}}$ ) and type Ia ( $\text{SNIa}$ ). We explore in more detail in Chapter 4 the constraints that can be put on different supernova yield models using abundances in the ICM.

### 1.4.1 Type Ia supernovae

Formally, a supernova is Type Ia if its early spectrum lacks conspicuous lines of H but contains a prominent Si II absorption feature at about  $6100 \text{ \AA}$  (for the origins of the current classification scheme, see Minkowski 1941; Branch 1986). There is a general agreement that Type Ia SNe are the result of the thermonuclear explosions of carbon and oxygen white dwarfs (CO WDs, Hoyle & Fowler 1960). When a CO WD in a close binary system is destabilized due to accretion from its companion, the temperature of the degenerate material rises to a critical value and ignites, creating a nuclear burning front that propagates through the star. Such explosions would produce mostly  $^{56}\text{Ni}$  and, depending on the conditions, varying amounts of intermediate mass elements (Si, S, Ca), but no H, in agreement with the features present in the optical spectra. Further details about the explosion mechanism are however still a matter of debate, such as whether the companion is another WD (double degenerate scenario) or a main sequence star or red giant (single degenerate case), or whether the destabilization occurs because the WD reaches Chandrasekhar mass or due to a layer of accreted He on top of a sub-Chandrasekhar WD.

Following the ignition of one or many hot spots, the propagation of the burning front can either be driven by heat diffusion at subsonic speeds (deflagration) or by a strong shock at supersonic speeds (detonation). This affects the synthesis of chemical elements, which depends on the density at which the reactions take place and hence on whether the fuel has been able to expand before being reached by the burning front. Burning at high densities usually allows for nuclear statistical equilibrium (NSE) to set in, the main product of which is  $^{56}\text{Ni}$ , while burning at lower densities produces more intermediate mass elements. The prompt detonation of the whole WD would burn too few intermediate mass elements to be consistent with current observations, therefore either the burning front propagates as a deflagration through the whole star (Nomoto et al. 1984) or the flame undergoes a transition to a detonation at some point, in what is known as the delayed detonation scenario (Khokhlov 1991). In this case, the deflagration-to-detonation transition density is one important parameter which changes the relative amounts of different elements produced in the explosion.

### 1.4.2 Core-collapse supernovae

Although originally classified also as Type I for lacking H lines in the spectrum, the explosion mechanism of Type Ib and Ic supernovae is now believed to be similar to that of Type II (idea suggested as early as 1985 by Wheeler & Levreault) and consists in the gravitational collapse of the core of a massive star, usually more massive than roughly 8–10 times the mass of our own Sun. Supernovae of the type Ib, Ic and II are therefore also grouped together under the more general term “core-collapse supernovae”.

In the core of massive stars, not only H and He but also C, Ne, O and Si gradually ignite at the center. The star undergoes repeated stages where fusion in the core stops and the core collapses until the pressure and temperature become sufficient to begin the next stage of fusion. Progressively heavier nuclei are produced, which release progressively less energy when fusing. Because Fe and Ni have the highest binding energy per nucleon of all the elements, their fusion does not release any more energy, therefore a nickel-iron core is formed and grows in the center of the star. When this core has reached Chandrasekhar mass, the degenerate electron pressure can no longer sustain it and it collapses, heating up and producing high-energy gamma rays that photo-disintegrate iron nuclei into helium and free neutrons. As the core’s density increases, it becomes energetically favorable for electrons and protons to merge (via inverse beta decay), producing neutrons and neutrinos. Depending on the progenitor mass, a neutron star or a black hole results, while the neutrinos escape from the core, and some are absorbed by the star’s outer layers, beginning the supernova explosion. The reason why SNe Ib and Ic lack lines of H in their spectrum is that the progenitor stars had lost their outer hydrogen (Ib) or even helium (Ic) envelopes before the explosion, either through very strong winds (Woosley et al. 1993; Swartz et al. 1993) or by mass transfer to a companion star (Woosley et al. 1995).

Core-collapse explosive nucleosynthesis tends to produce relatively large amounts of lighter elements (O, Ne, Mg), some intermediate elements and relatively little Fe-group elements, which are mostly produced by SNIa. The relative abundance patterns of the produced elements are most sensitive to the mass of the progenitor and depend to some extent also on its metallicity (see Nomoto et al. 2006; Kobayashi et al. 2006; Kobayashi & Nomoto 2008, and Chapter 4). For average chemical enrichment patterns, which is what we observe in the abundance ratios of the ICM, it is important to weigh model yields for SN<sub>CC</sub> with different progenitor masses by an appropriate initial mass function (IMF) of the stars that explode as supernovae.

### 1.4.3 Distribution of metals in cooling cores

Apart from the cooling flow problem, cool-core clusters present us with one other puzzle, this time regarding the distribution of metals in their ICM. Early observations showed that, while non-cool core clusters have a relatively flat Fe profile, cool-core clusters show a centrally peaked distribution of the Fe abundance (Allen & Fabian 1998; De Grandi & Molendi 2001). Oxygen however, and the other light elements produced primarily by SN<sub>CC</sub>, showed a much flatter profile (Tamura et al. 2004). This led to the paradigm that the Fe peak is produced by SNIa in the BCGs at the centers of cool core clusters. These cD’s have relatively old populations, where few SN<sub>CC</sub> are expected because these occur within a relatively short time after a star formation event. Most

SNe in BCGs (and indeed in most ellipticals) are thus expected to be Type Ia's, which produce large amounts of Fe but little O, explaining the peaked Fe and flat O distribution.

Some problems with this model include the fact that usually the measured Si profiles, which are typically quite accurate because of the relatively large equivalent widths of the Si lines, are as peaked as the Fe distribution. Si is produced by both SN Ia and SN<sub>CC</sub>, therefore if the scenario described above is correct, the Si peak should be shallower than that for Fe. To solve this discrepancy in M87, Finoguenov et al. (2002) proposed that there are two types of SN Ia with different Si/Fe yields. Those with longer delay times and higher Si yields dominate today the enrichment of elliptical galaxies, while those with shorter delay times and lower Si yields dominate the enrichment in the ICM at larger radii, because the bulk of them exploded in the time of the strongest star formation period at redshifts 2–3. We show in Chapter 4 however that the O abundance profiles in clusters are also peaked, contrary to previous measurements using shallower data sets. This may require a revision of the paradigm describing how the abundance peaks in the ICM of cool-core clusters are created.

If the BCG does produce all the metals seen in the central peak, moreover, one would expect the distribution of the metals to follow the light profile of the central galaxy. That is not the case: the central abundance peak is typically much broader than the light profile of the BCG (David & Nulsen 2008). One of the main culprits in this case is again thought to be the central AGN. Most mechanisms by which the AGN feedback described in the previous section couples to the ICM involve a form of stirring and mixing the hot plasma, either by inflating rising bubbles filled with relativistic electrons or by dragging cool gas in the form of filaments in the wake of buoyant AGN radio lobes. Both analytical models (Rebusco et al. 2006) and simulations (Roediger et al. 2007) have been developed to describe how metals are being distributed in the ICM by turbulence or bubbles induced by the AGN. We show in Chapters 3 and 4 detailed analyses of metal transport by the AGN based on observations of M87 and Hydra A. We constrain for the first time observationally the properties of the gas transported by the AGN: its average metallicity, mass, enrichment history, as well as the energy needed for its uplift.

## 1.5 The XMM-Newton observatory

Most of the results presented in this thesis were obtained from observations with the XMM-Newton X-ray satellite, launched on December 10th, 1999 as the second of ESA's four "cornerstone" missions defined in the Horizon 2000 Program. Its payload consists of three Wolter type 1 X-ray telescopes and a 30 cm optical/UV telescope allowing simultaneous observations in several wavelength regimes. Two of the three X-ray telescopes have at their foci reflecting grating arrays (RGAs) which direct part of the incoming X-ray light to two practically identical reflecting grating spectrometers (RGS) used for high resolution spectroscopy with a resolving power of  $E/\Delta E \sim 200-800$ . The rest of the X-ray photons from these two telescopes is then incident on two EPIC-MOS detectors (European Photon Imaging Camera metal oxide semiconductor) while the X-ray photons from the third telescope are focused onto an EPIC-pn detector. The EPIC MOS and pn detectors are used for X-ray imaging and moderate-resolution spectroscopy with a resolving power of  $E/\Delta E \sim 20-50$ . The optical telescope is connected to the optical monitor

(OM) with imaging and grism spectroscopy capabilities covering the 180 – 600 nm range.

One of the most important characteristics of XMM-Newton is that it has the largest effective area of any focusing X-ray telescope ever built: the total mirror geometric effective area sums up to 4650 cm<sup>2</sup> at 1.5 keV. This implies a very high sensitivity and good photon statistics, a prerequisite for the reliable spatially-detailed spectral analysis presented here. Because of the very eccentric orbit of XMM-Newton, moreover, a target is visible without interruptions to the EPIC detectors for up to as much as 135 ks (more than a day and a half of continuous exposure). The large field of view (30' diameter) of the EPIC detectors ensures a good coverage of extended sources such as nearby clusters of galaxies.

XMM-Newton has an on-axis point-spread function (PSF) with a full width at half maximum of 6'', which varies little over a wide energy range (0.1-4.0 keV) and is only slightly more energy dependent above 4 keV. The off-axis angle, however, can increase the energy dependence of the PSF and affects its shape through aberrations (astigmatism). The energy range (0.1–10. keV) where XMM-Newton offers a good collecting power is appropriate to detect a large part of the diffuse bremsstrahlung emission from a typical ICM plasma. Like the point spread function, the effective area depends on the off-axis angle (the distance to the center of the field of view and the optical axis). This effect is known as vignetting. Response matrices and the associated ancillary response files contain information about energy-dependent telescope effective areas, vignetting, filter transmissions, the quantum efficiency of detectors and the spectral energy redistribution among the energy channels, which are crucial to interpreting the observed data.

### 1.5.1 EPIC

We will focus in this work primarily on results from the EPIC detectors which allow for simultaneous imaging and non-dispersive moderate-resolution spectroscopy. The MOS detectors consist of 7 front-illuminated CCDs, each covering 10.9x10.9' and having a pixel-size of 1.1''. The EPIC pn detector in turn is a single back-illuminated silicon wafer with an integrated array of 12 CCD chips, each covering a sky area of 13.6x4.4' with 4.1''-sized pixels. The advantages of EPIC are the broad bandpass and the possibility to perform spatially resolved spectroscopy. This means that we can detect emission lines from several chemical elements (e.g. O, Si, S, Ar, Ca, Fe, Ni) and, for deep observations of bright clusters, investigate the spatial distribution of the temperature and of the abundances of these elements. We explain below some specific terms needed to understand details of the EPIC data analysis presented in the following chapters of this work.

*Out of Time events:* photons can be recorded not only during the observing mode but also during the readout of the EPIC CCDs, which results in these events being assigned to the wrong detector Y coordinate. These so-called "out-of-time" events (OoT) are particularly important for the pn detector, where they can represent up to 6.3% of the total number of recorded events. The Science Analysis Software (SAS) for the XMM-Newton observatory provides a task used to simulate an OoT event list which can be used to statistically correct for this effect.

*Event pattern and pile-up:* X-ray events can sometimes also be split between CCD pixels. The EPIC detectors record a "pattern" associated with each event, which indicates how many pixels were affected by the same incident photon. Selecting low-pattern events is recommended

for a reliable spectral analysis and can also help to avoid the effects of photon pileup (when more than one photon is incident on the same pixel before readout).

The last factor which is crucial for a correct analysis of the data is the detector background. The EPIC background can be subdivided into three categories: the external "flaring" background, the "quiescent" background, and the internal detector noise.

*Soft proton flares:* The flaring background is due to soft protons (below 100 keV) funneled by the mirrors onto the detectors. Some flares may affect the pn instrument more than the MOS. These flares can be identified by plotting a lightcurve of the observation and looking for times with unusually high count rates. The flared time (when the count rate is often more than a hundred times higher than during quiescence) is then generally removed from the data set before further analysis, since the properties of these soft protons are very variable, poorly understood, and therefore very difficult to eliminate from the observation otherwise. Soft protons are thought of as space weather, the equivalent of cloudy nights for optical astronomy.

The quiescent background is due to high energy particles interacting with the structure surrounding the detectors and with the detectors themselves. The detector noise consists of dark currents of the CCDs and some low-level "flickerings" of a small number of pixels. These background components can be assessed using so-called closed filter observations and generally increase with time, as the CCDs get older. Moreover, there is a "true" cosmic X-ray background (CXB) which consists of several soft thermal components originating from the hot, diffuse gas in our own galaxy and a power-law component due to the unresolved AGN emission across the Universe.

## 1.5.2 RGS

The RGS on the other hand has a high spectral resolution, but operates analogously to slitless spectroscopy in optical astronomy. It thus allows for spatial resolution only in the cross-dispersion direction, which limits its use in the case of extended sources. With RGS, relatively accurate abundances of O, Ne, Mg, and Fe can be measured and, in the case of deep observations of nearby bright clusters and elliptical galaxies, even the spectral lines of C and N are detected. The RGS spectral extraction regions are  $\sim 10'$  long in the dispersion direction and the minimum feasible width in the cross-dispersion direction is determined by the statistics of the observation (however, cannot be smaller than the PSF).

The spectral resolution of the RGS is limited by the broadening of the observed line profiles caused by the spatial extent of the source along the dispersion direction. This makes RGS spectroscopy useful only for cooling core clusters with a strongly peaked surface brightness distribution. In order to account for the line broadening in the spectral modeling, the model is convolved with the surface brightness profile of the source along the dispersion direction. Because the radial profile for a spectral line produced by an ion can be different from the radial surface brightness profile in a broad band, in practice the line profile is multiplied with a scale factor, which is a free parameter in the spectral fit.

## 1.6 Structure of this thesis

This thesis aims to give a detailed picture of the physical mechanisms of AGN-ICM interaction in two nearby bright cooling core clusters. I describe the nature of these mechanisms based on observed substructure, compute the energetics and discuss the implications for metal transport processes in the ICM. The thesis consists of four published papers.

Chapters 2 and 3 present a detailed analysis of the X-ray halo of M87, the nearest cooling flow. In Chapter 2, I analyze the overall distribution of pressure and entropy and discuss the observed substructures, including a weak shock probably induced by a previous AGN outburst and possible gas bulk motions. In Chapter 3, I focus on the spatial coincidence of different temperature phases in regions associated with the radio lobes inflated by the AGN. I determine the distribution of metals and show that the multi-phase regions are relatively more metal rich. I discuss the mechanisms by which the AGN contributes to the metal transport in the ICM, the energetics and time-scales thereof, and the production of chemical elements by the galaxy.

Chapters 4 and 5 are dedicated to a similar study of Hydra A, which can be considered a scaled-up version of M87, where the power and scales involved in the AGN-ICM interaction as well as the distance to the object are about an order of magnitude larger. In Chapter 4, I find indications of metal transport by the central AGN similar to the observations of M87. I also discuss the observed metal abundance ratios in detail, in comparison to expectations from combining several models of type Ia and  $\text{SN}_{\text{CC}}$  yields. I present radial distributions of several elements and test whether metal production by the central galaxy can create the observed abundance profiles. In Chapter 5, I focus on the large-scale weak shock present in Hydra A. I find for the first time a temperature jump associated with the surface brightness jump, confirming that classical shock jump conditions apply. I present hydrodynamic models for this shock to determine its energy, age, and to reproduce the shock shape.

## Chapter 2

# The gaseous atmosphere of M87 seen with XMM-Newton

*A. Simionescu, H. Böhringer, M. Brüggen & A. Finoguenov*

*A&A*, **465** (2007), 749

### **Abstract**

M87 is a key object whose study can reveal the complex phenomena in cooling cores. We use a deep XMM-Newton observation of M87 to produce detailed temperature, pressure and entropy maps in order to analyze the physical processes of cooling cores and of their heating mechanisms. We employed both broad-band fitting and full spectroscopical one-temperature model analysis to derive temperature and surface brightness maps, from which the pseudo-deprojected entropy and pressure were calculated. We discuss possible physical interpretations of small deviations from radial and elliptical symmetry in these maps. The most prominent features observed are the E and SW X-ray arms that coincide with powerful radio lobes, a weak shock at a radius of 3', an overall ellipticity in the pressure map and a NW/SE asymmetry in the entropy map which we associate with the motion of the galaxy towards the NW. For the first time we find evidence that cold, metal-rich gas is being transported out of the center, possibly through bubble-induced mixing. Several edges in the abundance map indicate an oscillation of the galaxy along the NW/SE direction. Furthermore, the radio lobes appear to rise along the short axis of the elliptical pressure distribution, following the steepest potential gradient, and seem to contain a nonthermal pressure component.

## **2.1 Introduction**

As early as 1973, the first detailed X-ray observations with the Uhuru and Copernicus satellites revealed that the X-ray luminosity at the center of some galaxy clusters and elliptical galaxies has a very sharp peak, implying a high enough central gas density that the cooling time falls below the Hubble time (Lea et al. 1973). Consequently, the so-called cooling flow model was

developed which asserted that the gas, in losing energy by means of radiation and in the absence of other heat sources, cools down temperatures so low as to become undetectable in X-rays, and sinks towards the cluster core (e.g. Fabian & Nulsen 1977; Cowie & Binney 1977). The model however failed to explain the ultimate fate of the cooling gas, and the evidence in wavebands other than X-rays showed that much less gas was condensing into a cooler state than the "cooling flow" model predicted (e.g. McNamara & O'Connell 1989).

The latest generation of X-ray satellites, in particular XMM-Newton and Chandra, provided more detailed spectral information showing that indeed much less gas undergoes such a "cooling flow" than the initial model based on the X-ray luminosity peak predicted (Peterson et al. 2001, 2003; Böhringer et al. 2001; Matsushita et al. 2002). This led to the conclusion that a heating source must exist which interacts with the gas in a fine-tuned way, stopping the cooling at just the right level to reproduce the observations (e.g. Böhringer et al. 2002). Active galactic nuclei (AGN) are found in most clusters previously believed to host a "cooling flow" (Burns 1990) and represent the most favoured candidates for providing such heat input. The main challenge remains the understanding of the exact mechanisms by which the heating takes place (e.g. David et al. 2001; Churazov et al. 2001; Fabian et al. 2003; Brüggén et al. 2005; Heinz et al. 2006).

M87, the central dominant galaxy in the nearby Virgo cluster, is an ideal candidate whose study may shed light on the complex phenomena in cooling cores. M87 was recognized early on as having a peaked X-ray surface brightness corresponding, in the absence of heating, to a cooling flow with a mass deposition rate of  $10 M_{\odot}/\text{year}$  (Stewart et al. 1984). However, using the spectral information from XMM-Newton, Böhringer et al. (2001) put an upper limit on the mass deposition rate at least one order of magnitude below this value (see also Matsushita et al. 2002; Molendi 2002). The energy input which may prevent the cooling of the gas could be supplied by the central AGN, powered by the galaxy's central supermassive black hole which has a mass of  $3.2 \times 10^9 M_{\odot}$  (Harms et al. 1994). Based on the observed complex system of radio lobes, believed to be associated with the AGN jet and unseen counterjet, Owen et al. (2000) showed that the mechanical power input from this AGN is more than sufficient to compensate for the energy loss through X-ray radiation.

The radio plasma in M87 clearly interacts with the X-ray gas. The best proof of this is the fact that the two most prominent radio lobes extending to the east and south-west of the M87 center correspond to regions of enhanced X-ray surface brightness, also known as the E and SW X-ray arms. Moreover, these E and SW arms show a more complex multi-phase temperature structure (Molendi 2002) while a previous observation with XMM-Newton showed that the rest of the ICM is locally well approximated as single-phase (Matsushita et al. 2002). This motivated Churazov et al. (2001) to develop a model according to which the bubbles seen in the radio map buoyantly rise through the hot plasma uplifting cooler gas from the central region.

Further features in the X-ray surface brightness map of M87 described by Forman et al. (2005) from Chandra observations include a ring of enhanced emission with a radius of 14 kpc, possibly associated with a weak shock which may be one of the mechanisms contributing to the heating of the ICM, additional arc-like features at 17 and 37 kpc, and excess emission regions NW and SE of the core. Using deeper Chandra data, Forman et al. (2007) confirmed the presence of a weak shock at 14 kpc and determined its Mach number as  $M \sim 1.2$ .

Detailed temperature, entropy and pressure maps are a prerequisite for the physical under-

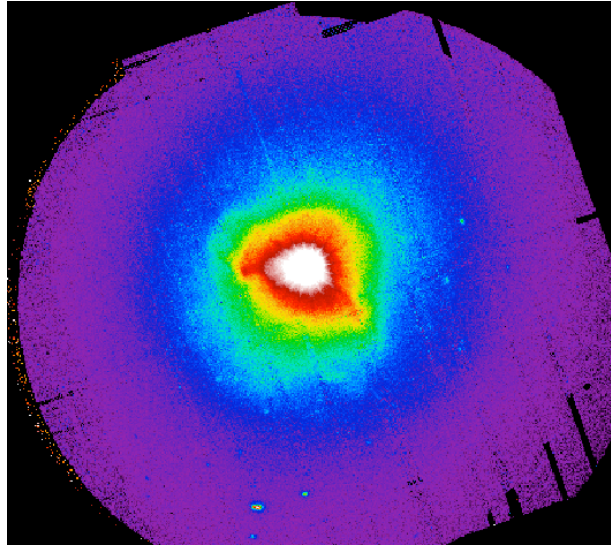


Figure 2.1: M87 surface brightness map from all three EPIC detectors, vignetting corrected and combined, in the 0.5-7.5 keV energy range

standing of the phenomena behind these features. This is the motivation for the second, deeper observation of M87 with XMM-Newton, the results of which are presented in this chapter. In Section 2.2 we present the data set and data analysis methods. The features seen in the resulting temperature, entropy and pressure maps are described in Section 2.3. In Section 2.4 we present more quantitative analyses of these features and possible physical explanations. Our conclusions are summarized in Section 2.5. We adopt a redshift for M87 of  $z=0.00436$  and a luminosity distance of 16 Mpc (Tonry et al. 2001), which yields a scale of 4.65 kpc per arcminute.

## 2.2 Observations and data reduction

M87 was first observed with XMM-Newton in the performance verification (PV) phase on June 19, 2000, for 60 kiloseconds (ksec). A subsequent 109 ksec observation was performed on January 10th, 2005. We will focus in this chapter primarily on the second observation, in which the PN detector was operated in the extended full frame window mode while the full frame mode was employed for the MOS detector. We extracted a lightcurve for each of the three detectors separately and excluded the time periods in the observation when the count rate deviated from the mean by more than  $3\sigma$  in order to remove flaring from soft protons (Pratt & Arnaud 2002). After this cleaning, the net effective exposure is  $\sim 62$  ks,  $\sim 79.3$  ks and  $\sim 80.5$  ks for pn, MOS1 and MOS2, recording in total 13.2, 4.7 and 4.9 million photons respectively. For data reduction we used the 6.5.0 version of the XMM-Newton Science Analysis System (SAS); the standard analysis methods using this software are described in Watson et al. (2001). A vignetting-corrected flux map of the observation for all three detectors combined in the energy band 0.5-7.5 keV is shown in Figure 2.1.

For the background subtraction, owing to the extended nature of our source, which covers the

entire field of view, we used a collection of blank-sky maps from which point sources have been excised (Read & Ponman 2003). We transposed the blank sky-maps to a position in the sky corresponding to the orientation of XMM-Newton during our observation of M87. The backgrounds were scaled according to the corresponding exposure times for each detector, after having removed the time periods affected by proton flares. The scaling factors in this case are calculated as the ratios between the observation exposure times and the background exposure times. An alternative method for calculating background scaling factors was employed by requiring that in the higher energy region (10-12 keV for MOS, 12-14 keV for PN) the emission in the outskirts of the M87 observation should have the same level as the background, since we expect little or no such high-energy emission from the gas halo around M87. The background scaling factors were in this second case calculated as the ratios between the total number of observation to background counts in the higher energy region specified above, in a  $7''$ - $9''$  ring. The values for the scaling factors calculated from the two methods agree to within less than 5%. This justifies confidence in having chosen a correct scaling.

Where a stable minimum signal-to-noise ratio was needed for our analysis, in particular for determining the temperature, we employed an adaptive binning method based on weighted Voronoi tessellations (Diehl & Statler 2006), which is a generalization of the algorithm presented in Cappellari & Copin (2003). The advantage of this algorithm is that it produces smoothly varying binning shapes that are geometrically unbiased and do not introduce artificially-looking structures, as can be the case for e.g. rectangular bins. Binning the dataset from the second XMM-Newton observation alone to  $10^4$  counts per spatial bin in the 0.5-7.5 keV energy range, which should yield temperature values accurate to less than 5% for one-temperature model spectral fits, we obtain bins roughly corresponding in size to the extent of the XMM point-spread function (PSF). Therefore, here we only discuss the results from the second observational dataset, which contains enough counts for the purpose of the current analysis. More detailed spectral models and spectral fitting using data from both observations are presented in Chapter 3.

Out-of-time events were subtracted from the PN data using the standard SAS prescription.

### 2.2.1 Broad-band fitting

In order to obtain a first impression of the temperature and abundance distribution of the hot gas around M87, we restricted the analysis of the surface brightness to four different energy bands selected as follows:

1. Low energy band (0.4-0.9 keV)
2. Fe-L line complex energy band (0.9-1.1 keV)
3. Intermediate energy band (1.1-2.0 keV)
4. High energy band (3.0-7.5 keV)

The principle is to compare the trend of fluxes in each pixel in each of the four bands to fluxes expected in these bands from model-spectra for a range of temperatures  $T=\{0.8, 1.0, 1.5, 1.7,$

2.0, 2.2, 2.5, 2.7, 3.0, 3.3, 3.6, 4.0} keV and metallicities  $z=\{0.1, 0.3, 0.5, 0.7, 1.0, 1.3\}$  solar (using the relative abundance values of Anders & Grevesse 1989). Subsequently, the best-fitting model was determined using a least-chi-square fit. In all models, the absorbing column density  $n_H$  was set to  $0.015 \times 10^{22} \text{cm}^{-2}$  (Lieu et al. 1996), and the redshift to 0.00436.

We merged the two MOS detectors, which have very similar spectral properties, and produced background-corrected flux maps in each of the four selected bands for the PN and combined MOS detectors. Each map was adaptively binned using a binning scheme based on the combined raw counts image from the three detectors in the 0.5-7.5 keV band. We performed one fit with a signal to noise ratio (SNR) of 50 and one with a SNR of 100 which ensured a minimum number of counts of 25...100 per bin in each of the four considered bands and especially the high energy 3.0-7.5 keV band which has the least counts.

This method allowed us to clearly identify the eastern and southwestern arms of M87 as lower temperature features. Furthermore, a lower temperature component could be detected in the direction of the M87 jet (north-west of the core), almost in continuation of each of the arms, spatially connecting them. However, beyond a radius of around 11 arcmin, both the SN 50 and SN 100 temperature maps became very noisy. This was likely due to the fact that our chosen energy bands were tuned to determine rather low temperatures accurately; for a good determination of higher temperatures it would be necessary to sample the higher energy regime (above 3.0 keV) with more bands. The abundance pattern was also rather noisy throughout the produced maps; it seemed to be influenced significantly by the PN gap pattern, and did not show a clear distribution relating to the X-ray arms. This was likely due to the fact that our energy bands are very wide, leading to a washing-out of any emission lines with the exception of the Fe-L complex, which is not sufficient for an accurate abundance determination.

In summary, this method was a very fast, computationally cheap way to gain insight into the spatial distribution of temperatures in the observation. However, the result seemed to be rather sensitive to the choice of the energy bands, and the insufficient sampling of the higher-energy regime caused a noisy fit in the hotter regions of the gas halo. Moreover, it was an insensitive method for obtaining metallicity maps.

### 2.2.2 Spectral analysis

A more reliable method for creating temperature maps is a comprehensive fit to the spectra from each bin using the XSPEC code, taking into consideration a large number of energy channels and allowing the temperature and metallicity to vary continuously until a best fit is found. But, given the large number of spatial bins for this observation, this method can be computationally very demanding.

Point sources were found using the source detection algorithm implemented in SAS and excised from the observation after a visual check to eliminate spurious detections. The central AGN was not considered a point-source contamination and was thus kept in the dataset throughout the analysis. We then adaptively binned the combined counts image in the 0.5-7.5 keV range using the weighed Voronoi tessellations method to a target signal-to-noise ratio of 100 and extracted the spectra of each bin defined in this way. The reason for binning the raw counts map and not the flux map is to obtain larger bins around the gap areas where fewer photons are collected and

to ensure an approximately homogeneous accuracy in the temperature determination across the image. A SNR of 100 should give a temperature accuracy better than 5% (for a one-temperature fit) and a metal abundance accuracy of 10-15%.

For the spectral analysis we chose the method described e.g. by Arnaud et al. (2001) in which the vignetting correction is accounted for by adding a weight column to the event file, allowing the use of a single on-axis ancillary response file (ARF) containing information about the telescope-specific effective area, quantum efficiency attenuation and filter transmission. The redistribution matrix files on the other hand were computed separately for each bin and each detector. Detector gaps were accounted for by dividing the flux in each bin through the corresponding ratio between the average unvignetted exposure time in the bin and the maximum unvignetted exposure time of the detector.

The spectra in each bin were fitted in XSPEC using a *mekal* one-temperature model. The spectra from all the three detectors were grouped together and fitted simultaneously with the same best-fit model in order to have good statistics. We used the 0.5-7.5 keV range to determine the best fit. However, in the rare bins (approximately 10 bins out of a total of about 1500) where one of the EPIC detectors had an effective average exposure time of below 10% of the maximum, the data from that detector was omitted since the number of counts was too low to provide any reliable spectral information. This correction is necessary, as the gaps are not included in the vignetting correction information stored in the weight column.

This method confirms the results obtained from the broad band fitting in that we can clearly identify the same substructure as noted before: the eastern and southwestern arms of M87 as lower temperature features, the lower temperature component NW of the nucleus in the direction of the M87 jet, and the nucleus of M87 distinguished as a high-temperature component. We also observe the positive temperature gradient in the region outside the arms, in agreement with the radial analysis of Matsushita et al. (2002). The outer parts of the gas halo are significantly less noisy than derived from the broad band fitting. However, at smaller radii the values of the temperatures determined with the two methods agree very well. Our temperature map is also in good agreement with the temperature map obtained from the previous XMM-Newton observation of M87, computed following the method of Churazov et al. (1996) and presented in Forman et al. (2005).

The abundance pattern is much better defined with this method compared to the broad-band fitting, however some noise can still be seen. We note that the statistics in each bin were not sufficient to determine individual element abundances, therefore the abundance ratios were assumed to be solar (Anders & Grevesse 1989). Detailed radial profiles of the individual elements (Matsushita et al. 2003) however show that this is not generally the case. Given our signal-to-noise ratios, the obtained abundance values are most likely driven mainly by the iron content whose L-line complex is the most prominent feature in the spectrum. We find that the abundance in the arms is in general lower than in the surrounding medium (Figure 2.3), which is most likely due to the fact that we are using a single-temperature fit in a region which has been shown to have at least two components with different temperatures (Belsole et al. 2001; Matsushita et al. 2002; Molendi 2002). As these authors have already noted, a one-temperature fit severely underestimates the metallicity in this case. Moreover, by creating a map (not shown) of the absorbing hydrogen column density ( $n_{\text{H}}$ ) which was left free in the fit, we find elevated values in the regions

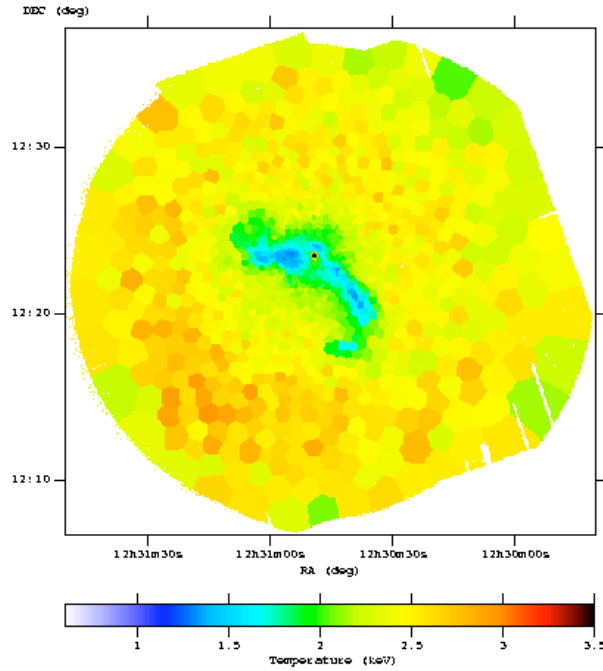


Figure 2.2: Temperature map obtained from spectral analysis, using a binning to SNR of 100.

corresponding to the arms, which may also show that a single-temperature fit is not sufficient to appropriately model the data. We performed a second fit fixing the absorbing hydrogen column density to  $2.0 \times 10^{20} \text{ cm}^{-2}$  which did not significantly change the temperature map. Therefore, any uncertainty in the  $n_{\text{H}}$  seems to have little effect on the temperature results; in the following we will base our discussion on the initial temperature results obtained with an unconstrained  $n_{\text{H}}$  in the fit.

### 2.2.3 Pressure and entropy maps

We used the temperature and spectrum normalization in each bin to determine a quasi-deprojected measure of the pressure and entropy, which we calculated as  $p = n_e kT$  and  $S = kT n_e^{-2/3}$ . The entropy as defined here is somewhat different from the thermodynamic quantity defined as  $S \sim (3/2)k \ln(T \rho^{-2/3})$  but is nevertheless a measure of adiabaticity and has become commonly used in cluster astrophysics.

The electron density  $n_e$  is determined from the spectrum normalization, which is defined and implemented in XSPEC as  $K = 10^{-14} / [4\pi D_A^2 (1+z)^2] \int n_e^2 dV$ , from which follows

$$n_e \propto \sqrt{\frac{K}{V}} D_A (1+z)$$

where  $D_A$  is the angular diameter distance and  $z$  is the redshift. As can be seen from the above formula, we need to also calculate the volume  $V$  along the line of sight corresponding to each

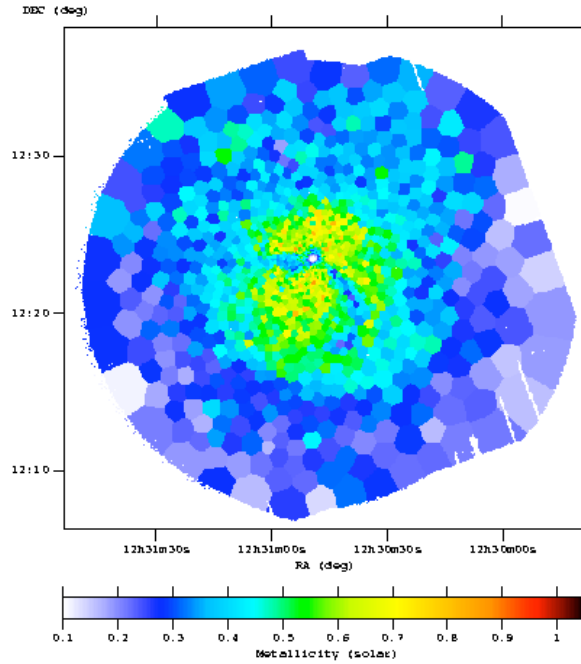


Figure 2.3: Abundance map obtained from spectral analysis, using a binning to SNR of 100.

bin. This was determined as  $V \approx (4/3)D_A^3 \Omega (\theta_{out}^2 - \theta_{in}^2)^{1/2}$ , where  $\Omega$  is the solid angle subtended by the bin and  $\theta_{in}, \theta_{out}$  are the angles corresponding to the smallest and respectively largest distances between any of the bin pixels and the M87 nucleus (Henry et al. 2004). Thus, this method takes into account an approximate estimation of the three-dimensional extent of each bin, but assumes a constant temperature along the line of sight, and can therefore be viewed as a quasi deprojection. Since most of the emission in each bin originates from the densest gas which is found at the smallest effective 3D radii, the maps can be interpreted as measures of the pressure and entropy in a two dimensional slice through the middle of the cluster, perpendicular to the line of sight.

We fitted the radial pressure and entropy profiles using non-parametric, locally weighted, linear regression smoothing. The data points and the corresponding smooth radial model are overplotted in Figure 2.4. The pressure and entropy maps were divided by the resulting radial model in order to reveal small-scale fluctuations (Figures 2.5 and 2.6). We can identify several features pointed out by Forman et al. (2005), such as the 3' (14 kpc) ring of enhanced emission corresponding to an increase in the pressure. This confirms the association of this substructure with a shock, while the NW/SE brightness enhancements seen with Chandra (Forman et al. 2005) appear as low-entropy features. The X-ray arms are clearly low-entropy structures, which also seems to confirm the hypothesis that the gas in these regions was uplifted from more central regions where we expect the smallest entropy in hydrostatic equilibrium conditions. The next section presents a more detailed analysis of these features.

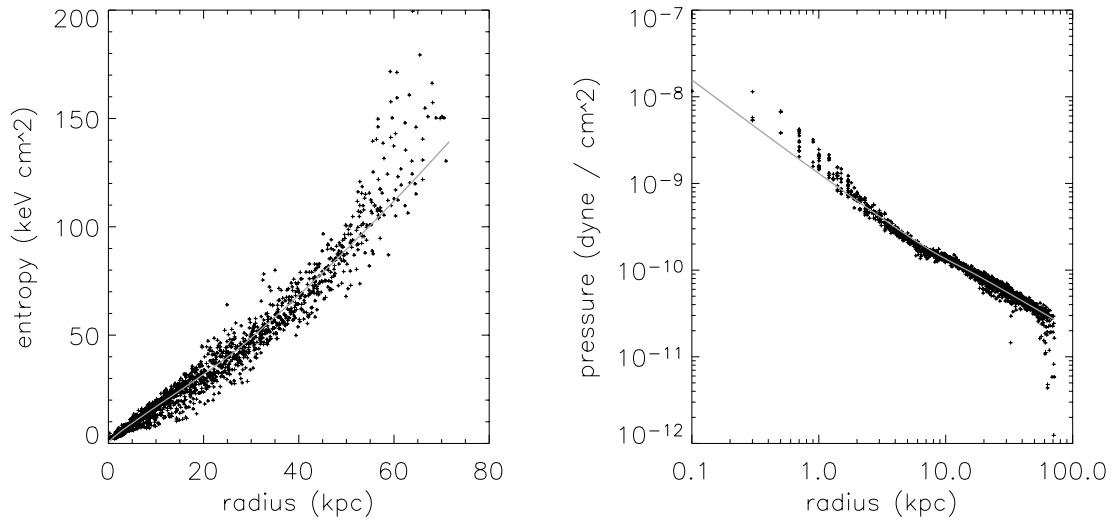


Figure 2.4: Data points and corresponding smooth radial model by which the entropy and pressure maps were divided in order to reveal small deviations from spherical symmetry

## 2.3 Substructure in the M87 gas halo

### 2.3.1 Temperature and entropy

The temperature and entropy maps both show similar substructure details, so that we chose to discuss them in parallel. By far the most striking features in both maps are the E and SW arms characterized by lower temperature and lower entropy with respect to the surroundings. The thermal structure of the arms is described in the next chapter, where a more detailed spectral analysis is employed in order to understand the complex multi-temperature structure that several authors have already found in these regions (Molendi 2002; Matsushita et al. 2002; Belsole et al. 2001). We point out that in the temperature and entropy maps both arms are seen to curve clockwise, thereby connecting to the larger-scale radio halos north and south of the nucleus. This was already known for the SW arm (see for example Forman et al. 2005), but had not previously been observed for the eastern arm.

Apart from the E and SW arms, another low-temperature and low-entropy feature can be identified close to the nucleus towards the NW, almost at the intersection of the lines defining the general directions of the arms. This region corresponds to high X-ray luminosity and low entropy, implying a locally high gas density. Additionally, enhanced  $H\alpha$  emission has been observed here (Sparks et al. 2004), which makes this region an attractive candidate for hosting a classical cooling flow and associated mass deposition. However, detailed spectral analysis of the region, as described in the next section, does not provide evidence for cooling to the lowest X-ray detectable temperatures at the rates predicted in the absence of any heating sources.

Another feature found in both maps is an edge to the SE at a radius of roughly  $6'$ . As one moves outwards across this edge, both the temperature and entropy increase, therefore the

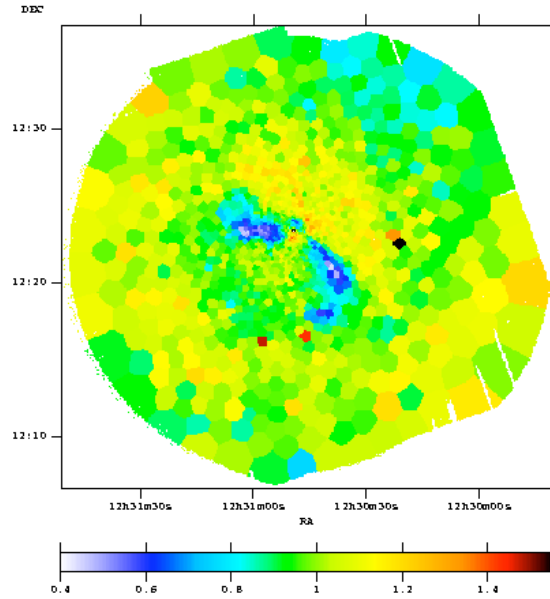


Figure 2.5: Entropy deviations from a smooth radially symmetric model. The E and SW arms, as well as the low-entropy feature close to the NW of the core are seen in dark blue. The entropy edge to the SW is marked by the sharp green to yellow transition. A NW/SE asymmetry is easily seen in the map.

properties at the jump are more consistent with the cold-front interpretation of Markevitch et al. (2001) than with the characteristics of a shock. A more detailed discussion of this is presented in the next section.

Finally, a feature easily seen in the entropy map but which is not readily apparent in the temperature map is a NW/SE asymmetry. Within a radius of  $6'$  the entropy values to the NW are clearly more elevated than in the SE. The edge to the NW where the entropy decreases corresponds spatially very well to the edge of the NW large-scale radio bubble. Possible physical explanations for this are also presented in the next section.

### 2.3.2 Pressure

A map of the pressure deviations from a radially symmetric, smooth model shows three noteworthy features. The first of these is a relative pressure increase towards the NW and SE. Since we subtracted a radially symmetric model, this would suggest an overall ellipticity of the pressure distribution and consequently of the underlying dark matter distribution under the assumption of hydrostatic equilibrium. Secondly, in the direction of the E and SW X-ray arms (coinciding with the prominent radio lobes and orthogonal to the regions of enhanced pressure), we find a pressure decrease. Thirdly, there is a ring of enhanced pressure with a radius of roughly  $3'$ , coinciding with the position of the weak shock proposed by Forman et al. (2005).

We tried to confirm and quantify the ellipticity in the initial pressure map by fitting to it

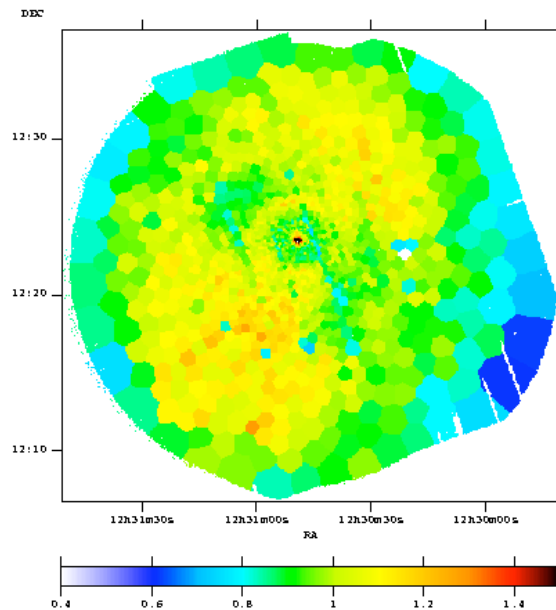


Figure 2.6: Pressure deviations from a smooth radially symmetric model. A relative pressure increase towards the SE and NW suggests an overall ellipticity in the pressure. A pressure decrease is found in the direction of the E and SW arms, which rise perpendicular to the SE/NW ellipticity long axis. A ring of enhanced pressure with a radius of roughly  $3'$  is also seen.

elliptical isocontours with the "ellipse" task in IRAF. The position angle and ellipticity were independently fitted for each pressure contour and the model need not be smooth in intensity as a function of the semi-major axis. We masked the regions corresponding to the radio lobes from the fit, since here it is likely that the pressure deviates from an elliptical model. Dividing the initial pressure map by the fitted model obtained with IRAF, we are able to identify deviations from an elliptical rather than a radially symmetric model (Figure 2.7). We find that, with respect to the elliptical model, all substructure seen previously no longer appear, with the exception of the lower pressure in regions that coincide with the radio lobes. Here the decrease in observed pressure with respect to the elliptical model is on average 5-10%. Assuming an overall pressure balance, this decrease suggests that in the radio lobes there should be an additional contribution to the pressure. This pressure source may be provided by relativistic electrons injected by the AGN. The ring at  $3'$  is no longer visible since we did not require the pressure intensity in the model to be smooth with increasing semi-major axis, while the higher pressures NW and SE of the nucleus which appeared as deviations from a radially symmetric model can be entirely explained by an elliptical pressure distribution.

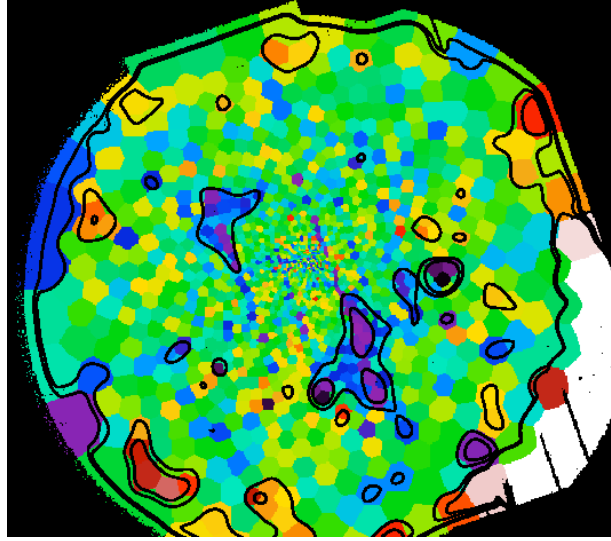


Figure 2.7: Pressure deviations from an elliptical model (ratio). Contour levels are drawn at 0.9, 0.95, 1.05 and 1.1. Two regions roughly corresponding to the end of the E arm and to the SW arm are seen to have lower than average values, indicating the possible presence of nonthermal pressure support.

## 2.4 Discussion

### 2.4.1 Absence of a classical cooling-flow on smaller scale

While a large-scale cooling flow has been ruled out, cooling and condensation could still happen locally, since it is not easy to exactly balance heating and cooling everywhere throughout the cooling core region. A prime candidate target to look for such a local cooling flow region is the small low-entropy feature NW of the nucleus where also diffuse optical emission lines are observed.

We extracted a spectrum from this region and fitted it in XSPEC with a *vmcflow* model fixing the low temperature cutoff at the minimum level available in the model (81 eV) in order to probe the existence of a classical cooling flow spectrum. We find a very poor fit, especially around the Fe-L complex where the data lie below the spectral model between 0.6-1 keV (Figure 2.8). A *vmekal+vmcflow* model with a fixed low-temperature cutoff at 81 eV provides a good fit for an ambient temperature (*vmekal*) of  $1.508 \pm 0.027$  keV and a mass deposition rate of  $3.18 \pm 0.16 \times 10^{-2} M_{\odot}/\text{year}$ . According to a classical cooling flow analysis done by Böhringer (1999), the mass deposition rate in this region in the absence of a heating source should be 0.1-0.2  $M_{\odot}/\text{year}$ , which is a factor of about 5 higher than what we find from spectral fitting. A two-temperature *vmekal* model with  $T1 = 1.016 \pm 0.022$  and  $T2 = 1.855 \pm 0.030$  also describes the data very well. Therefore, although the density in this smaller-scale region is very high and although the region is associated with  $H\alpha$  emission, we find that it does not exhibit spectral evidence of a classical cooling flow and sufficient mass deposition rate.

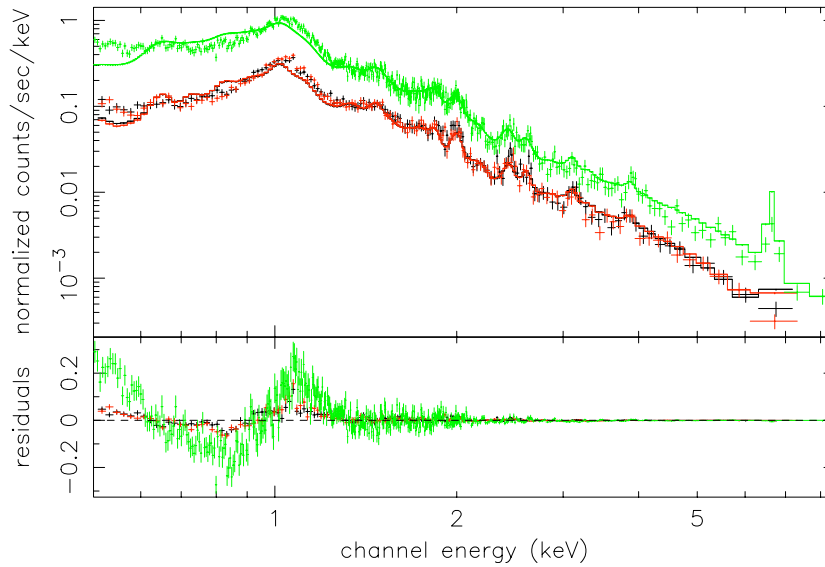


Figure 2.8: Data and best-fit *vmcflow* model with fixed low-temperature cutoff for the small-scale low-temperature feature NW of the core. The disagreement of the model with the data is easily visible, indicating the absence of a classical cooling flow.

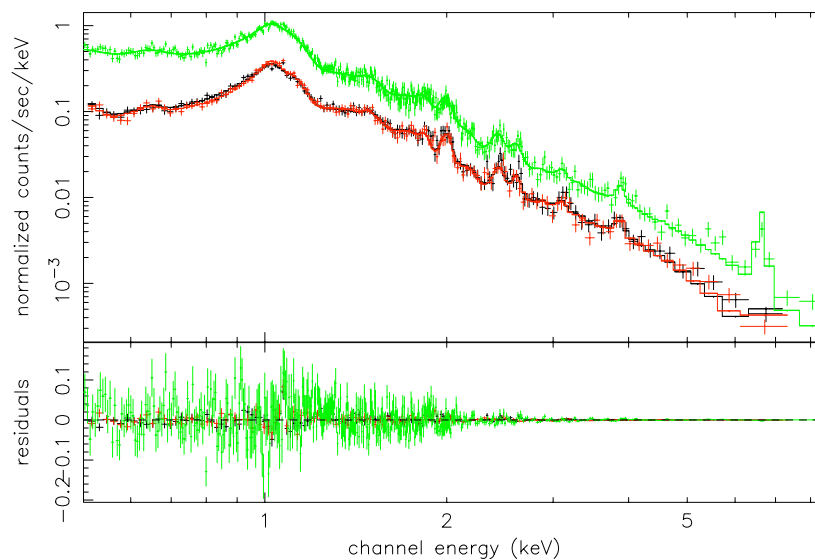


Figure 2.9: Data and best-fit two-temperature *vmekal* model for the small-scale low-temperature feature NW of the core. This model is clearly in better agreement with the data than the classical cooling flow model.

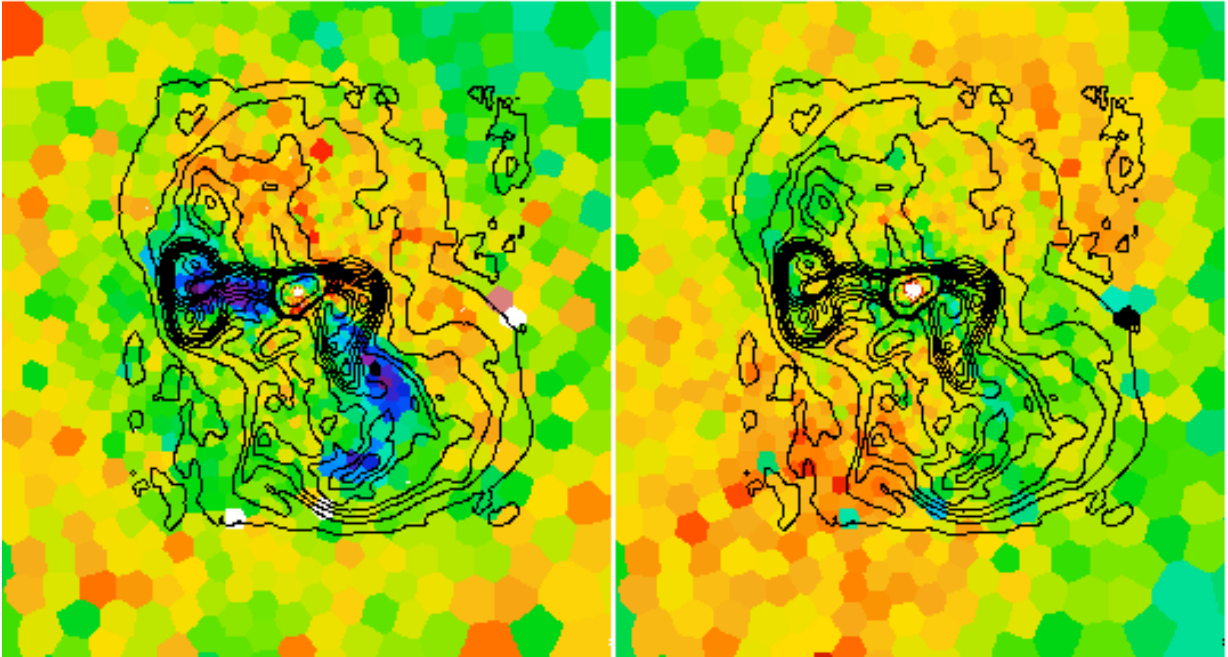


Figure 2.10: Entropy (left) and pressure (right) deviations from a smooth radially symmetric model overlaid with radio contours (90 cm). Radio map kindly provided by F. Owen. The E and SW radiolobes coincide well with the regions of low entropy in the X-ray arms. Also, the edge of the large radiolobe to the north roughly coincides with a NW edge in the entropy map.

### 2.4.2 Motion of the galaxy to the NW

To investigate the NW/SE asymmetry seen in the entropy map, we extracted spectra from concentric ring sectors towards the NW (-25 to 135 degrees counterclockwise of West) and SE (200 to 280 degrees counterclockwise of West). The angles are chosen such that the E and SW arms are excluded. The spectra were fitted with a one-temperature *vmekal* model, since we expect from the results of Matsushita et al. (2002) and Molendi (2002) that the gas outside the arm regions is single-phase locally. The results plotted in Figure 2.11 show that the radial temperature profile towards the SE lies below the profile towards the NW, while the radial abundance profile reveals higher values in the SE than in the NW. The simplest phenomenon that explains such a NW/SE temperature and abundance asymmetry is a motion of M87 to the NW through the hot gas halo, or alternatively, a large-scale bulk motion of the hot gas halo towards the SE while the galaxy itself remains in place. In either case, there are two possible mechanisms related to the motion which would generate the observed asymmetry.

The first possibility is that colder, highly-abundant gas near the center is ram-pressure stripped during the motion. In the case of a large-scale bulk motion of the gas halo, the stripped gas is then carried towards the SE along with the bulk flow, while if the galaxy is moving towards the NW it is left behind in a wake. However, the pressure map is symmetrical and shows no increase to the NW as one would expect if ram-pressure were important.

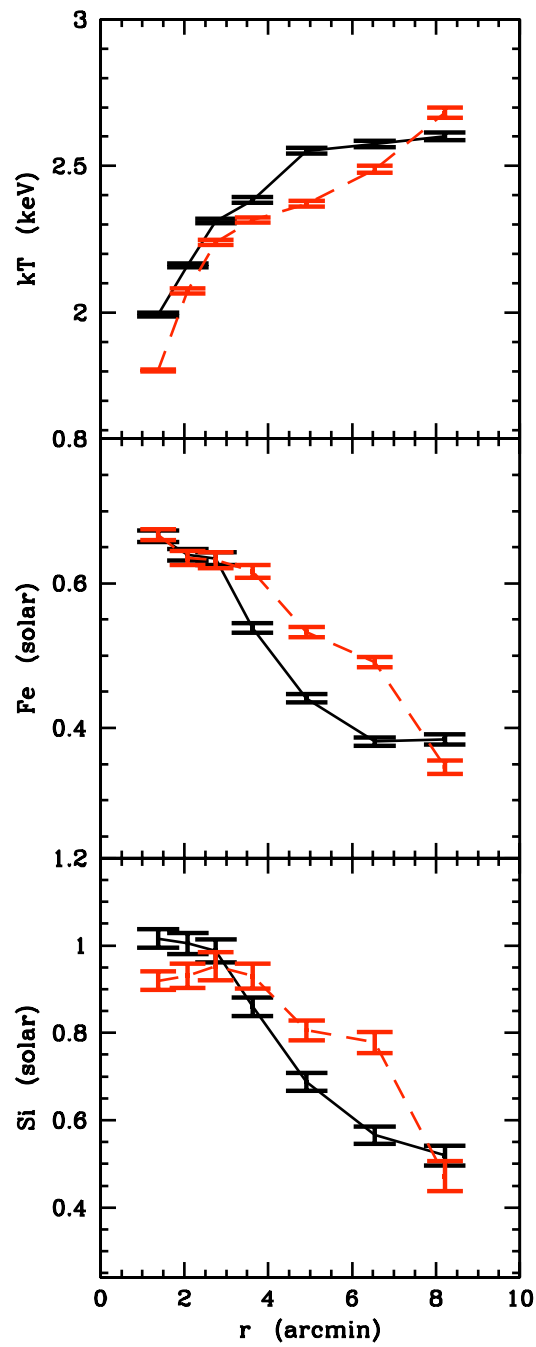


Figure 2.11: Temperature and abundance NW/SE asymmetry. The solid line represents the profile NW of the core, the dashed red line SE of the core.

The second possibility, which is favoured by our entropy and pressure maps, is that, due to

the relative velocity between the nucleus and the gas halo, bubbles emitted initially to the north-west are advected downstream. This effect is important if the relative bulk velocity is at least as high as, and of the order of, the bubble rising velocity and would imply that a large part of the bubbles emitted by the AGN eventually rise to the SE independently of their initial direction of emission. Much more mixing is therefore induced towards the SE, favoring the transport of metals, which explains the relative iron and silicon abundance increase in this direction (Figure 2.11 (b) and (c)). Recent simulations (Roediger et al. 2007) indeed show that bubble-induced metal transport results in elongated abundance profiles along the direction of propagation of the bubbles. The observed NW/SE temperature asymmetry can be explained using this bubble-advective scenario if we consider that the bubble-induced mixing not only favors the transport of metals in the atmosphere but can also bring colder gas from the center out to larger radii. It has been already noted (e.g. Nulsen et al. 2002) that radio bubbles are often surrounded by rims of cold, dense gas which they uplift during their inflation and rising. Therefore it is probable that a preferential propagation of a series of bubbles to one direction may result in lowering the downstream average temperature.

Further indication that bubbles are advected downstream is provided by Chandra data in Forman et al. (2007); the authors describe a series of four consecutive bubbles to the SSE while no counterpart of such structure is seen in the opposite direction.

Finally, one other observational feature leads us to believe that M87 is moving to the NW. If we consider the analogy of M87 with a typical wide-angle tailed (WAT) radio source, the motion through the intracluster medium may help to explain why the E and SW radio lobes, and the corresponding X-ray arms, do not lie along directions exactly opposite to each other. However, the wide angle between the lobes and especially the radio "ear" seen at the end of the eastern arm suggest that the buoyant velocity is at least comparable to the bulk flow velocity. This agrees qualitatively with our previous statement that the relative bulk velocity should be on the order of the bubble rising velocity.

Let us reconsider the model of ICM heating through radio-jet inflated bubbles. Bîrzan et al. (2004), among others, show that the bubble enthalpy is in most cases enough to halt the cooling flow. However, the picture drawn by Nulsen et al. (2002) for Hydra A and in this chapter also for M87 is much more complex. While the AGN does inject energy into the ICM in the form of bubble enthalpy, bubble formation is likely often associated with the uplift and mixing of cool gas from the center. A well known example for the uplift are the X-ray arms of M87 (Churazov et al. 2001). In this chapter, we present for the first time evidence of this phenomenon also at smaller temperature and density contrasts with respect to the ambient medium within the same galaxy, contrasts which could therefore not have been observed without the high-quality statistics of the dataset. This suggests that cool-gas uplifting by buoyant bubbles may be more widespread than previously thought, and has not been detected so far solely owing to insufficient statistics. Whether the uplifted cool negatively buoyant gas will fall back towards the cluster center thermalizing its potential energy (Nulsen et al. 2002), or whether it is heated by thermal conduction once it reaches larger radii, is a matter for future models; however, it seems that bubbles do generally transport cool gas out of the center.

### 2.4.3 Possible core oscillations

While the abundance and temperature profiles of the X-ray gas relatively close to M87 (within the inner  $\sim 6'$ ) are well explained by a simple relative motion between the gas and the galaxy, a look at the features seen further towards the outskirts reveals a more complex nature of the ongoing physical phenomenon. The model subtracted entropy map reveals an edge at about  $6'$  SE of the core which is suggestive of a cold front, with the pressure across the front staying roughly constant and the temperature and entropy being lower on the more X-ray luminous side. This feature corresponds in the metallicity map (Figure 2.3) to a visible sharp edge in the abundance distribution, emphasizing the presence of a contact discontinuity here. Another relatively sharp edge in the metallicity can also be seen at about  $3'$  NW of the core, although it is not associated with any visible entropy or temperature features. Moreover, also NW of the core, we find a region of lower entropy beyond  $6'$ .

The opposite and staggered placement of these low-entropy regions and abundance edges suggests that the current relative motion of the gas and the galaxy, proposed in the previous section, may be part of a longer process of oscillatory motions along the NW/SE direction. Churazov et al. (2003) observed a similar E/W asymmetry and a set of sharp edges in entropy, temperature and surface brightness in the Perseus cluster and performed simulations which suggest that minor mergers may trigger oscillations of the cluster gas, thus generating multiple sharp edges on opposite sides of the central galaxy along the direction of the merger. Similar opposite and staggered features generated by oscillations of the intracluster gas are seen also in numerical simulations by Tittley & Henriksen (2005) and Ascasibar & Markevitch (2006).

Further evidence of a possible oscillatory motion of the gas in the M87 halo comes from an analysis of the pressure map. Fitting an elliptical model to the raw pressure map as described in Section 2.4.5 and allowing the centers of the elliptical isobars to vary, we find that these centers systematically shift towards the SE for higher values of the semimajor axis. Thus the galaxy potential located at smaller scales is not exactly centered with the large-scale halo potential, which would lead to the oscillation suggested here. In a more detailed future analysis, this can be used to reveal information about the amplitude, energy, and time-scale of these oscillations, which may help in understanding how this phenomenon contributes over time to the heating vs. cooling balance, and how it competes with other proposed methods for energy input into the ICM.

### 2.4.4 Large-scale correlation of the radio emission and entropy map

One of the striking large-scale features in Figure 2.10 is the spatial coincidence of the northern outermost radio contour-edge and a decrease in the entropy by 10-15%, which cannot be explained either by a directed motion of M87 to the NW, or by the possible core oscillations. Owen et al. (2000) note that the radio contour-edge represents a sharp decrease in radio intensity over a range of wavelengths, therefore indicating interaction between the radio-loud plasma and the hot gas halo.

To illustrate the entropy variation across the radio edge, we averaged the entropy in circular annuli sectors with an opening angle of 90 degrees in the NW and SE quadrant respectively.

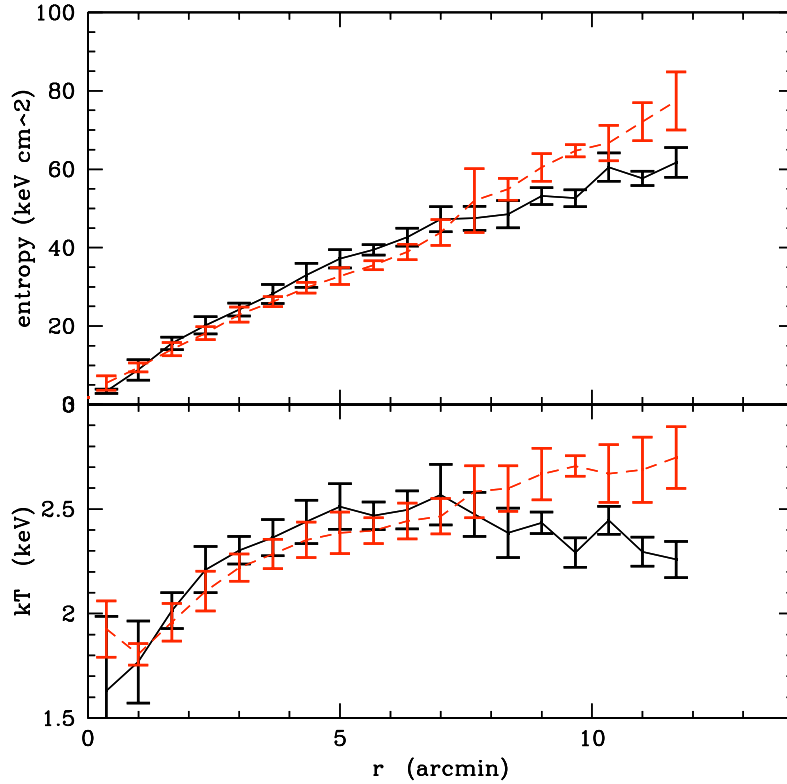


Figure 2.12: Entropy and temperature radial profiles, calculated as an average of the values in the bins whose center falls inside circular annuli sectors with an opening angle of 90 degrees NW and SE of the core. The errorbars represent the corresponding standard deviation in each annulus sector.

We compare the radial profiles of the entropy in these two quadrants in Figure 2.12, which also shows radial trends of the temperature in the corresponding regions. Up to a radius of roughly 6'–7' the entropy in the NW quadrant is higher than in the SE quadrant. Beyond this radius, which corresponds roughly to the radio edge, the entropy and temperature NW of the core show a much shallower increase with radius than in the SE, the temperature displaying even a small negative gradient.

The spatial coincidence between the north radio edge and the point where the entropy and temperature gradients NW of the core decrease suggests a link between the injection of radio-loud plasma into the ICM and the processes leading to entropy generation and gas heating. Such a link is at the basis of the feedback models in which mechanical input, usually by a radio source, offsets the cooling flow, heating the gas at the cluster center and flattening the central entropy profiles. The exact details of the entropy-generation mechanism remain unclear.

### 2.4.5 Ellipticity of the underlying dark matter potential

As mentioned above, we fitted the raw pressure map with an elliptical model in IRAF in order to quantify the eccentricity and position angle-dependency with semi-major axis. The results of the obtained fit show larger variations in the central part but outside 3' a rather constant position angle and ellipticity are reached. The position angle values outside 3' range between 140 and 150 degrees, measured counterclockwise of north. These values are somewhat smaller than, but comparable to, results from the analysis of an optical image of M87 by Carter & Dixon (1978), who obtained values for the elliptical isophote-fit of  $160 \pm 5$  degrees for the position angle. Our results agree also with the work of Böhringer et al. (1997) on ROSAT PSPC data, giving an ellipticity of the X-ray surface brightness with a position angle of  $158 \pm 10$  degrees. Outside of 3', the ellipticity varies generally between 0.08 and 0.17, higher values of 0.13-0.17 being found in the regions from which the radio lobes had been cut out. This is in agreement with Böhringer et al. (1997), who found an ellipticity of 0.1 to 0.16. The ellipticity in the X-rays thus seems to be significantly smaller than in the optical regime, where it ranges from 0.3-0.5. This can be explained by the fact that anisotropic velocity dispersions of the stars can sustain a higher ellipticity of the galaxy in the optical domain while the isotropic nature of the X-ray emitting gas halo makes it more round. Surprisingly, despite the evidence of core oscillations seen in the entropy map, the position angles of the X-ray isobars and the optical isophotes agree very well, and the optical ellipticity is as expected roughly 3 times higher than the X-ray value (see also Buote & Canizares 1996). Therefore the deviations of the hot gas atmosphere from hydrostatic equilibrium cannot be very large outside the arm regions.

A further look at the position angle values found in the fit reveals the fact that the radio lobes rise in directions orthogonal to the semimajor axis of the elliptical dark matter profile, thereby following the steepest dark-matter potential gradient as one would expect.

### 2.4.6 Heating of the ICM by weak shocks

As seen in Figure 2.6, we are able to spectroscopically confirm the 3' shock seen by Forman et al. (2005, 2007) with Chandra. Weak shocks are becoming widely accepted as candidates for heating mechanisms of the X-ray gas, therefore a detailed understanding of their properties is required. To describe the M87 3' shock more quantitatively, we used the elliptical isobars from the fit described above to define eight spectral extraction regions with semi-major axes between 2 and 4 arcminutes. The temperature and spectrum normalization corresponding to the regions contained between each two consecutive elliptical isobars in the chosen semi-major axis range were determined using a *vmekal* one-temperature spectral fit. The corresponding pressure was then determined for each region as described in Section 2.2.3. The results are plotted in Figure 2.13. In the plot, the pressure was divided by a smooth model to emphasize the jump.

The temperature shows a jump of  $\sim 0.1$  keV, which relative to the overall temperature of  $\sim 2$  keV, represents  $\sim 5\%$ . Using the Rankine-Hugoniot jump conditions assuming  $\gamma = 5/3$ , this amounts to a Mach number of 1.05. The pressure jump amounts to 8-10% with respect to the smooth model, which implies a Mach number of about 1.04, in agreement with the Mach number we derived from the temperature jump. This confirms the supersonic nature of the weak shock at

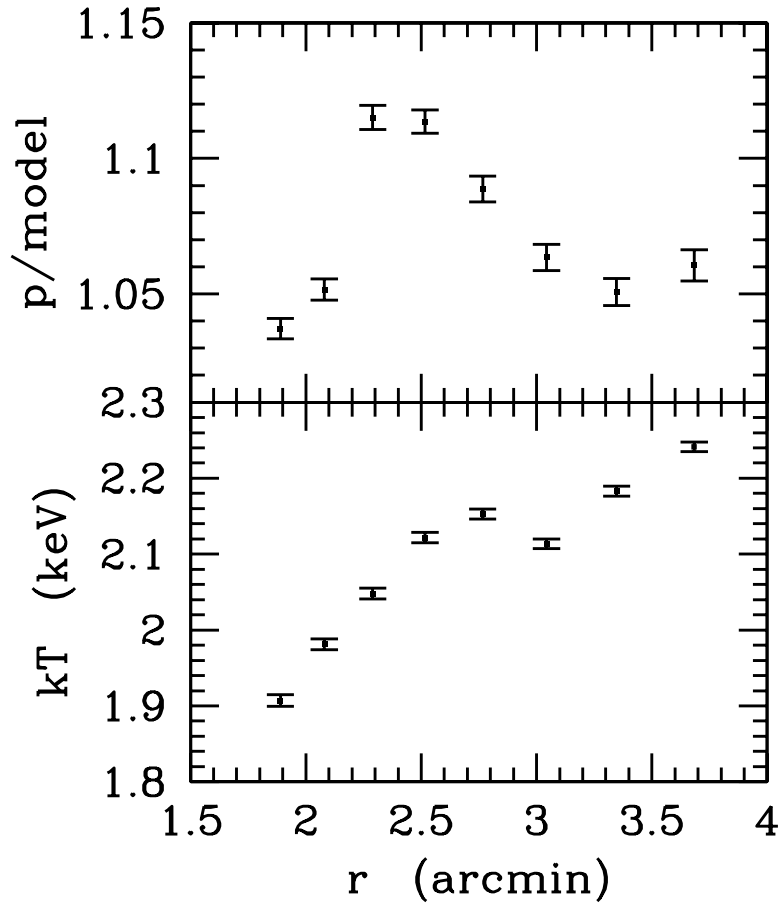


Figure 2.13: Projected temperature and relative pressure jumps around the 3' shock, corresponding to Mach numbers of 1.05 and 1.04 respectively.

3', and seems consistent with the Mach number  $M \approx 1.2$  calculated from deprojection analysis of Chandra data (Forman et al. 2007) considering that the Mach numbers derived from this analysis are lower limits to the real values due to projection effects and the smoothing effect of the XMM PSF.

## 2.5 Summary and conclusions

We present the results from a 109 ksec XMM-Newton observation of the hot gas halo surrounding the giant elliptical galaxy M87. We use two methods, namely broad-band fitting and full spectroscopy, to create spatially resolved temperature maps from the data, and present the advantages and disadvantages of each method. The results of the spectroscopic analysis are used to produce entropy and pressure maps. We describe and discuss the features seen in these maps, the most important of which being the cool E and SW X-ray arms, which coincide with power-

ful radio lobes, a weak shock ring with a radius of 3', an overall ellipticity in the pressure map and a NW/SE asymmetry in the entropy map. For the 3' weak shock we find jumps in both the pressure and temperature corresponding to Mach numbers of 1.04 and 1.05 respectively, which we interpret as lower limits to the real Mach number values. The pressure map shows an overall ellipticity of between 0.08 and 0.17, with position angles in good agreement with the optical data. Under the assumption of hydrostatic equilibrium, the ellipticity in the pressure map implies an elliptical underlying dark matter potential. Furthermore, we find that the X-ray arms and associated radio lobes rise roughly perpendicular to the semimajor axis of the pressure ellipticity following the steepest gradient of the dark matter potential.

The NW/SE entropy asymmetry is indicative of the motion of M87 through the surrounding hot gas, associated with downstream advection of the bubbles injected by the AGN. We conclude that bubble-induced cold gas mixing from the center may appear on a wide variety of scales and should be considered into the cooling-flow energy balance calculations. NW and SE edges in the entropy map moreover suggest that the possible motion of M87 to the NW is part of a longer cycle of core oscillations.

#### **Acknowledgements**

We would like to thank W. Forman, P. Nulsen and E. Churazov for helpful discussion. We acknowledge the support by the DFG grant BR 2026/3 within the Priority Programme "Witnesses of Cosmic History". The XMM-Newton project is an ESA Science Mission with instruments and contributions directly funded by ESA Member States and the USA (NASA). The XMM-Newton project is supported by the Bundesministerium fuer Wirtschaft und Technologie/Deutsches Zentrum fuer Luft- und Raumfahrt (BMWi/DLR, FKZ 50 OX0001), the Max-Planck Society and the Heidenhain-Stiftung, and also by PPARC, CEA, CNES, and ASI. AF acknowledges support from BMBF/DLR under grant 50 OR 0207 and MPG. AS also thanks Steven Diehl and Thomas Statler for making their Weighted Voronoi binning algorithm publicly available.



# Chapter 3

## Metal-rich multi-phase gas in M87

*A. Simionescu, N. Werner, A. Finoguenov, H. Böhringer & M. Brüggen*

*A&A*, **482** (2008), 97

### **Abstract**

We use deep ( $\sim 120$  ks) XMM-Newton data of the M87 halo to analyze its spatially resolved temperature structure and chemical composition. We focus particularly on the regions of enhanced X-ray brightness associated with the inner radio lobes, which are known not to be described very well by single-temperature spectral models. Compared to a simple two-temperature fit, we obtain a better and more physical description of the spectra using a model that involves a continuous range of temperatures in each spatial bin. The range of temperatures of the multiphase gas spans  $\sim 0.6$ – $3.2$  keV. Such a multiphase structure is only possible if thermal conduction is suppressed by magnetic fields. In the multi-temperature regions, we find a correlation between the amount of cool gas (with a temperature below that of the surrounding X-ray plasma) and the metallicity, and conclude that the cool gas is more metal-rich than the ambient halo. In the frame of the assumed thermal model, we estimate the average Fe abundance of the cool gas to  $\sim 2.2$  solar. Our results thus point toward the key role of the active galactic nucleus (AGN) in transporting heavy elements into the intracluster medium by uplifting cool, metal-rich gas from the galaxy. However, the abundance ratios of O/Si/S/Fe in and outside the X-ray arms are similar, indicating that the dominant fraction of metals in the gas halo was uplifted by AGN outbursts relatively recently compared to the age of M87. Our best estimate for the mass of the cool gas is  $5 \times 10^8 M_{\odot}$ , which probably stems from a mixture of ICM, stellar mass loss, and Type Ia supernova products.  $\approx 30$ – $110$  Myr are required to produce the observed metals in the cool gas. Finally, we put upper limits on possible non-thermal X-ray emission from M87 and, combining it with the 90 cm radio maps, we put lower limits of around  $\sim 0.5$ – $1.0 \mu\text{G}$  on the magnetic field strength.

### **3.1 Introduction**

The impact of active galactic nuclei (AGN) is currently the most promising solution for the cooling flow problem in galaxy clusters (e.g. Binney & Tabor 1995; Brüggen & Kaiser 2002;

Böhringer et al. 2002; Bîrzan et al. 2004; Omma et al. 2004; Sijacki et al. 2007 and references therein; for a review, see Peterson & Fabian 2006; McNamara & Nulsen 2007). It is moreover invoked to transport heavy elements into the intracluster medium (ICM) (Brüggen 2002; Omma et al. 2004; Rebusco et al. 2006; Roediger et al. 2007) and to explain the exponential cut-off of the bright end of the galaxy luminosity function (e.g. Croton et al. 2006; Sijacki et al. 2007).

The AGN-ICM interaction is one of the driving motivations for deep observations that allow detailed analysis of the properties and spatial structure of the intracluster gas. While for a complete understanding of the ICM physics a combined analysis of multiwavelength data is usually necessary, most of the information about the ICM is gained from observations in the X-ray domain in which this hot plasma emits most of its radiation. The main targets of such detailed analyses are thus in particular nearby X-ray bright objects, where both good spatial resolution and high spectral statistics can be achieved.

This makes the hot gas halo of M87, which is the second brightest extragalactic X-ray source in the sky located at the center of the nearby Virgo cluster at a distance of only 16 Mpc (Tonry et al. 2001), an ideal target for studying the AGN-ICM interaction in great detail. M87 is known to host an AGN powered by the galaxy’s central supermassive black hole with a mass of  $3.2 \times 10^9 M_{\odot}$  (Harms et al. 1994). The AGN jet and unseen counterjet are believed to drive the complex large-scale system of lobes observed in the radio domain (e.g. Owen et al. 2000), which clearly interact with the X-ray gas. The evidence for this is seen primarily in the spatial correlation between the two “inner” radio lobes extending east (E) and southwest (SW) of the core of M87 and regions of increased X-ray surface brightness, also referred to as the E and SW X-ray arms (Feigelson et al. 1987; Böhringer et al. 1995; Belsole et al. 2001; Young et al. 2002; Forman et al. 2005, 2007).

The impact of the AGN on the X-ray emitting gas in M87 is however not limited to the surface brightness enhancement. Also the spectral properties in the E and SW arms are affected, these regions being the only part of the M87 halo which require more complex multi-temperature spectral modeling while the rest of the gas is well approximated by single-temperature models (Molendi 2002; Matsushita et al. 2002; Belsole et al. 2001). A possible explanation for this is given by Churazov et al. (2001), who suggest that the radio lobes rise buoyantly through the hot plasma, uplifting cooler gas from the central region and mixing it with ambient gas at larger radii. If this model is correct, then M87 offers a unique chance to study the effects of AGN-induced gas mixing and gas transport and the influence of these phenomena on the energy balance in the cooling core and on the metal distribution in the gas halo.

In this chapter we use deep XMM-Newton X-ray observations of the M87 halo to characterize and understand the temperature structure and spatial variation of the multi-temperature gas in the X-ray arms, and to investigate its correlation with the radio plasma. Moreover, we aim to map the distribution of various metals and verify the influence of the AGN and the radio lobes in distributing and transporting these heavy elements from the galaxy center into the M87 hot gas halo.

In Sect. 3.2 we present the data sets and data reduction techniques employed; in Sect. 3.3 we describe the various multi-temperature spectral models used in our analysis; in Sect. 3.4 we discuss the thermal structure and spatial distribution of the multi-temperature phases and comment on possible suppression of the Spitzer heat conduction; in Sect. 3.5 we present the

spatial distribution of the metals in the M87 gas halo and the abundance patterns of different metals relative to Fe in and outside the radiolobe regions; in Sect. 3.6 we estimate and discuss the mass and metallicity of cool gas uplifted by the AGN; finally, in Sect. 3.7 we give an upper limit for non-thermal emission from the radiolobe regions. Our conclusions are summarized in Sect. 3.8. We adopt a redshift for M87 of  $z=0.00436$ , a luminosity distance of 16 Mpc (Tonry et al. 2001), and a scale of 4.65 kpc per arcminute.

## 3.2 Observations and data analysis

M87 was observed with XMM-Newton for 60 kiloseconds (ks) on June 19, 2000 and re-observed for 109 ks on January 10, 2005. After removing the periods affected by soft-proton flares, the net total exposure time is 85 ks for EPIC/pn and 120 ks for each EPIC/MOS detector. This deep exposure of such a near and bright source allows us to analyze the gas halo around M87 in great detail and with excellent statistics.

For the analysis, we used the 7.0.0 version of the XMM-Newton Science Analysis System (SAS) and employed the standard analysis methods as described in e.g. Watson et al. (2001). Point sources were found using the source detection algorithm implemented in SAS and removed from the observation after a visual check to eliminate spurious detections. The spectra from each of the two PN observations were corrected for out-of-time events separately. We note that our observations were affected by gain calibration uncertainties, in some cases the spectra - especially for the PN detector - being blue-shifted by up to  $\sim 1500$  km/s. The MOS detectors were also influenced by this shift, but the effect was a factor of  $\sim 3$  less strong than for the PN. To account for this, we artificially blue-shifted our spectral models.

As background we used a collection of blank-sky maps (Read & Ponman 2003) scaled according to the corresponding exposure times for each detector and each observation. The accuracy of this scaling for the present dataset is discussed in the previous chapter.

We used an adaptive binning method based on weighted Voronoi tessellations (Diehl & Statler 2006), which is a generalization of the algorithm presented in Cappellari & Copin (2003), to bin the combined counts image to a signal-to-noise ratio (SNR) of 200 in the energy range 0.5-2.0 keV, corresponding to 40000 counts per spatial bin. The binning was constrained to follow four different radio contours of the 90 cm radio image at 10, 3, 1 and 0.3 mJy (each region between two successive radio contours was binned separately). The region inside the highest chosen radio contour was not fitted in order to avoid possible contamination by the AGN, whose flux was particularly high in the second observation causing photon pileup in the EPIC detectors (Werner et al. 2006a). The spectra were fitted in the energy range between 0.4-7.0 keV with the various models described in the next section. We fitted the spectra from all six datasets (two observations with three detectors each) simultaneously with the same model parameters except for a factor to account for variations in the relative overall normalization between the detectors. For this, the PN of the new observation was taken as reference.

### 3.3 Spectral models

For the spectral analysis we use the SPEX spectral fitting package (Kaastra et al. 1996). We fit the observed spectra with two models: a simple two-temperature *mekal* model in which the abundances of the two thermal components are coupled to each other, and a differential emission measure (DEM) model with a cut-off power-law distribution of emission measures versus temperature (*wdem*).

The emission measure  $Y = \int n_e n_i dV$  (where  $n_e$  and  $n_i$  are the electron and ion densities,  $V$  is the volume of the emitting region) in the *wdem* model is specified in Eqn. (3.1) following from Kaastra et al. (2004):

$$\frac{dY}{dT} = \begin{cases} AT^{1/\alpha} & T_{\min} < T < T_{\max}, \\ 0 & \text{elsewhere.} \end{cases} \quad (3.1)$$

The emission measure distribution has a cut-off at  $T_{\min} = cT_{\max}$ . For  $\alpha \rightarrow \infty$  we obtain a flat emission measure distribution.

The fraction of the emission measure of the gas lying below a chosen temperature  $T_{\max\text{cool}}$  to the total emission measure is given by:

$$\frac{Y_{\max\text{cool}}}{Y} = \frac{\int_{T_{\min}}^{T_{\max\text{cool}}} \frac{dY}{dT} dT}{\int_{T_{\min}}^{T_{\max}} \frac{dY}{dT} dT}. \quad (3.2)$$

By integrating this equation we obtain a direct relation for  $Y_{\max\text{cool}}/Y$  as a function of  $\alpha$  and  $c$ :

$$\frac{Y_{\max\text{cool}}}{Y} = \frac{(T_{\max\text{cool}}/T_{\max})^{1/\alpha+1} - c^{1/\alpha+1}}{1 - c^{1/\alpha+1}}. \quad (3.3)$$

The *wdem* model appears to be a good empirical approximation for the spectrum in cooling cores of clusters of galaxies (e.g. Kaastra et al. 2004; Werner et al. 2006b; de Plaa et al. 2006).

In the spatial bins where either the normalization of the cool component for the two-temperature fit or the lower cutoff for the *wdem* model were less than  $2\sigma$  significant, we fixed the temperature of the cool component to 1 keV and the lower cutoff to  $0.3T_{\max}$ , respectively. Unless otherwise stated we assume a hydrogen column density of  $2.0 \times 10^{20} \text{cm}^{-2}$  (Lieu et al. 1996).

Throughout the chapter we give the measured abundances relative to the proto-solar values given by Lodders (2003). The recent solar abundance determinations by Lodders (2003) give significantly lower abundances of oxygen, neon and iron than those measured by Anders & Grevesse (1989).

## 3.4 Temperature structure of the M87 halo

### 3.4.1 Two-temperature models

Two-temperature models are the simplest next step beyond the single-temperature model approximation. Based on the first XMM-Newton observation of M87, Belsole et al. (2001); Molendi

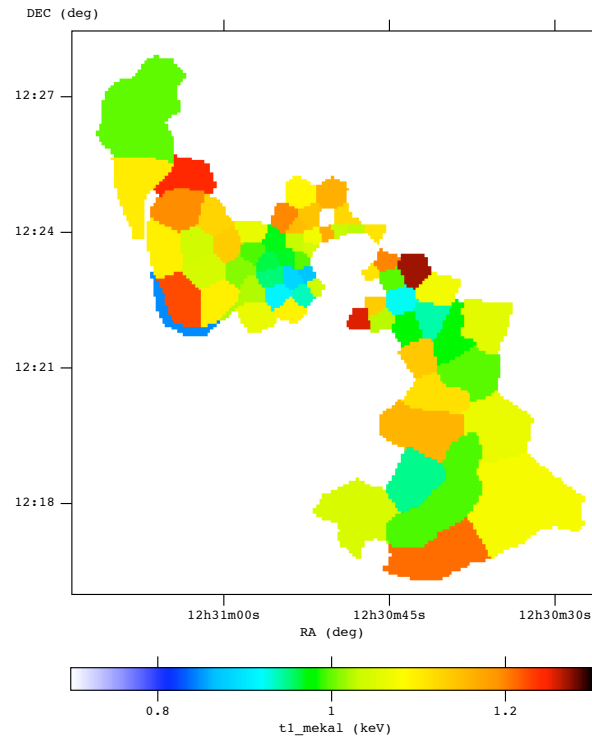


Figure 3.1: Temperature of the cool component as determined from the two-temperature *mekal* fit. Only the bins where the normalization of the cool component was more than  $3\sigma$  significant are shown.

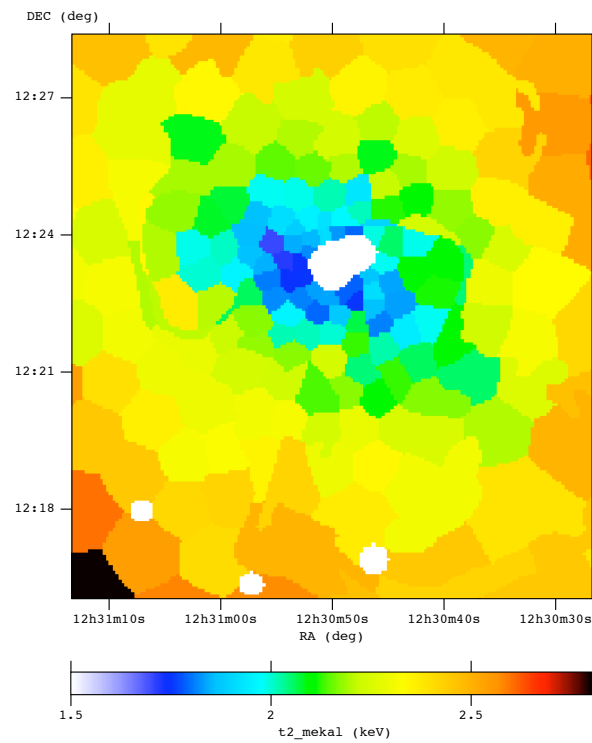


Figure 3.2: Temperature of the hot component as determined from the two-temperature *mekal* fit. The map exhibits a fairly regular radial gradient.

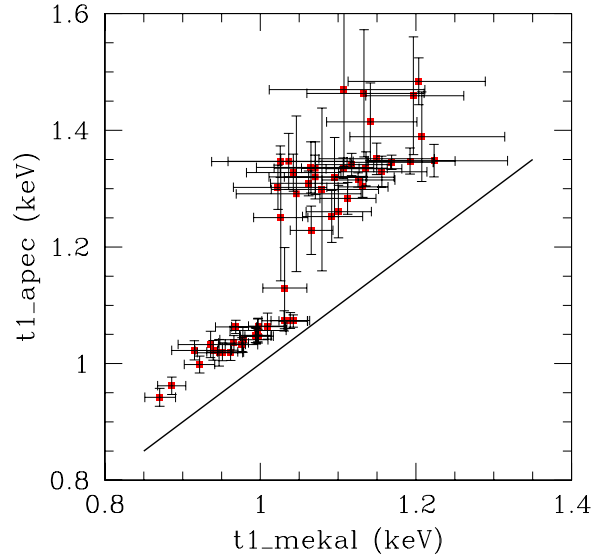


Figure 3.3: Differences in determination of the temperature of the cool component with the *apec* (fitted in XSPEC) and the *mekal* (fitted in SPEX) models. Errorbars are at the  $1\sigma$  level. The equality line  $T_{1,mekal} = T_{1,apec}$  is overplotted.

(2002); Matsushita et al. (2002) have already shown that the X-ray bright E and SW arms associated with the inner radio lobes are significantly better described by two-temperature models with a cool temperature component at around 1 keV and a hotter component at around 2–2.5 keV. With the new data we are able to analyze in much greater spatial detail the properties of the cool component.

We find, in agreement with previous work (Molendi 2002; Matsushita et al. 2002), that the temperature of the cool component remains quite stable between 1 and 1.2 keV and shows little or no trends with radius or with surface brightness (Fig. 3.1). For example, the correlation coefficient between the temperature of the cool component and radius in the E arm is only 0.198. The temperature of the hot phase meanwhile exhibits a fairly regular radial gradient (Fig. 3.2).

For comparison we also performed a similar two-temperature model fit using the *apec* model in XSPEC. The differences in determining the temperature of the cool component can be seen in Fig 3.3. In general, we find very similar trends from both models, however the *apec* model seems to give overall higher values than the *mekal* model. This effect is more pronounced for values of  $T_{cool,apec} > 1.2$  keV than for  $T_{cool,apec} < 1.2$  keV. We note that the *mekal* model implemented in SPEX includes a more recent list of transitions than the *mekal* implemented in XSPEC (J. Kaastra, private communication) and that *apec* is not implemented in SPEX, thus a direct comparison of the two models is not possible.

While the temperature of the cool phase does not seem to vary strongly in the fits, the normalization of the cool gas shows spatial variations correlated with the inner radio lobes. In Fig.

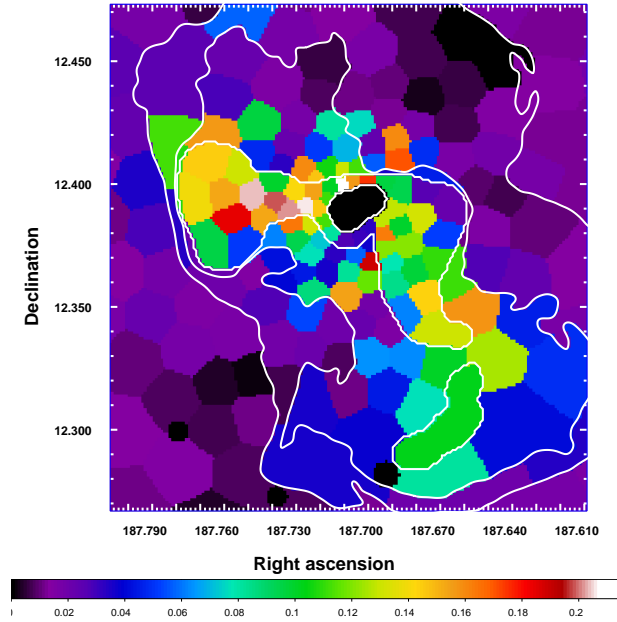


Figure 3.4: Map of the fraction of the emission measure of the cool component to the total emission measure (hot + cool component) for the two-temperature *mekal* fit. 90 cm radio contours are overplotted in white.

3.4 we plot the fraction of the emission measure of the cool phase to the total thermal emission,  $Y_{\text{cool}}/(Y_{\text{hot}} + Y_{\text{cool}})$ , overlaid with the 90 cm radio contours (Owen et al. 2000). As already noted by e.g. Belsole et al. (2001), the spatial correlation is more pronounced in the E arm, while in the SW arm it seems that the radio plasma is twisting around the uplifted arm.

### 3.4.2 The differential emission measure model

We also fitted a model with a continuous temperature distribution where the emission measure is a power-law function of the temperature, as described in Sect. 3.3. As the model by Churazov et al. (2001) also indicates, a multiphase structure with a continuous distribution of the emission measure as a function of temperature is more realistic because, during the rise of the radio lobes, gas at several radii gets entrained and mixed (see also Brüggén & Kaiser 2002). The power-law shape of the emission measure as a function of temperature is the simplest model that entails a continuous temperature distribution.

Our main direct result from the *wdem* fit is shown in Fig. 3.6, where we plot the map of the inverse slope  $\alpha$  of the power-law emission measure distribution. Higher values in the map indicate regions where the emission measure distribution is flatter, hence where one expects proportionally more cool gas to have been mixed together with the ambient gas. To quantify this more exactly, we calculate from the fit results the fraction of the emission measure of the cool gas to the total emission measure according to Eqn. 3.3. We chose  $T_{\text{maxcool}}$  as 1.5 keV, which is roughly the smallest deprojected value of the ambient gas computed by Matsushita et al. (2002). Fig. 3.5 shows the spatial distribution of the cool gas fraction, revealing very similar spatial

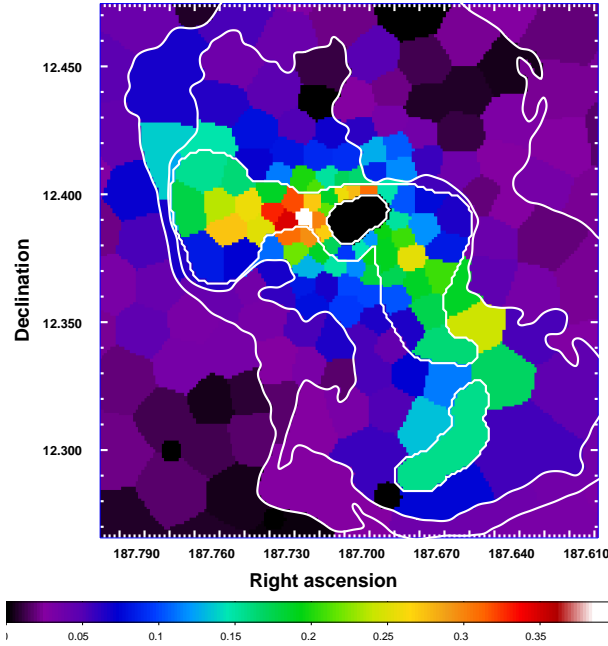


Figure 3.5: Fraction of the emission measure of the gas below 1.5 keV to the total emission measure from the *wdem* fit. 90 cm radio contours are overplotted in white.

trends as in Fig. 3.4 where the fraction of cool gas in the 2T model was plotted. Thus, the relative contribution of the cool gas to the total emission is similar in both models.

However, the temperature structure of the cool gas can be very different, since the same relative contribution can be achieved with a shallower slope (large  $\alpha$ ) and larger low-temperature cutoff or with a steeper slope but a smaller  $cT_{\max}$ . In Fig. 3.7, we plot the map of the lower temperature cutoff  $cT_{\max}$  in the regions where we find a more than  $3\sigma$  significant fraction of cool gas (in the other regions the gas is not significantly non-isothermal, thus it is irrelevant to speak of a lower temperature cutoff). We find lower cutoff temperatures which go down to as little as 0.6 keV, thus the *wdem* model allows for the presence of gas much below the best-fit value of the cool temperature in the 2T fit.

From the fit we find that, based on the chi-square ( $\chi^2$ ) values, we cannot significantly differentiate between the *wdem* and the two-temperature model. The *wdem* model that we fitted had the same number of free parameters (upper temperature cutoff, lower temperature cutoff, power-law slope, normalization and element abundances) as the two-temperature fit (two temperatures, two normalizations and element abundances) and the difference between the  $\chi^2$  values is between -20 and 10 points for a typical number of degrees of freedom per bin of 1050–1100.

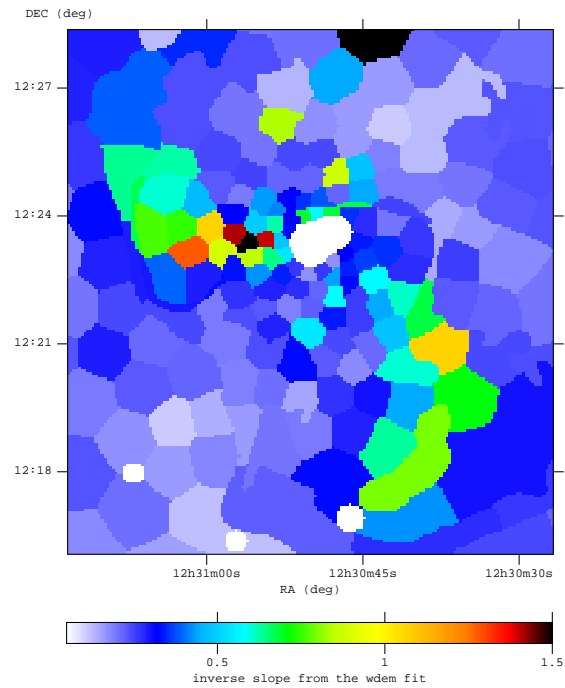


Figure 3.6: Map of the inverse slope  $\alpha$  from the *wdem* fit. Higher values in the map reflect regions where the emission measure distribution is flatter.

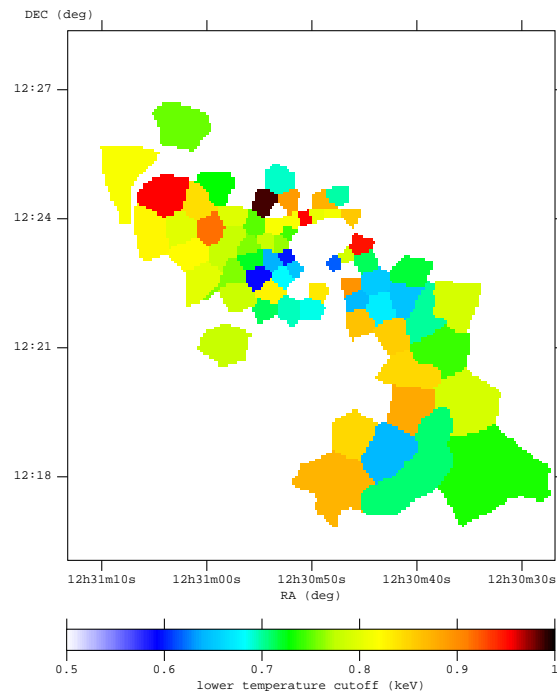


Figure 3.7: Map of the lower temperature cutoff from the *wdem* fit. Emission from gas at as little as 0.6 keV is detected. Only the bins are shown where the fraction of gas below 1.5 keV was more than  $3\sigma$  significant.

### 3.4.3 Discussion of the temperature structure and physical feasibility of the different models

Although based on the improvement of the  $\chi^2$  values we cannot determine which model provides a better description of the data, there are several arguments in favor of the continuous temperature distribution.

Firstly, during the rise of the radio lobes, gas at several radii should get entrained, mixed, and the uplifted gas should expand and cool adiabatically as it moves into regions of lower pressure. Alternatively, the uplifted gas could be heated up by e.g. heat conduction from the surrounding hot phase or by energy dissipation from turbulent motions. In any case, it is very unlikely that the heating and cooling should exactly balance each other to yield the spatially constant temperature of the cool component that we observe in the two-temperature fits (both *mekal* and *apec*). More probably, the constancy of the cool temperature could be an artifact of approximating a more complex temperature structure with a two-temperature model. In order to test this, we simulated a series of *wdem* spectra with different slopes, different high-temperature cutoffs, and a lower temperature cutoff of  $0.25 \times T_{\max}$ , which is a typical value we find in our fits, and fitted these simulated spectra with a two-temperature *mekal* model. We find indeed, as plotted in Fig. 3.8, that the best fit temperature of the cool component in the 2T fit is constant at around 1 keV for a wide range of slopes and high-temperature cutoffs. Thus the fact that the cool temperature in the 2T fit is so constant is very likely an indication that the 2T fit is only an approximation of a more complex continuous temperature distribution. We note that very similar results are also found for lower temperature cutoffs of between  $\sim 0.2\text{--}0.5 \times T_{\max}$ .

Secondly, Werner et al. (2006a) detect Fe xvii lines in the RGS spectra of M87, lines which are emitted between 0.14 and 0.85 keV (Arnaud & Raymond 1992). The presence of these lines is inconsistent with the results of the two-temperature fits (both *mekal* and *apec*) and can only be accounted for with a multi-temperature model which predicts emission from gas with temperatures of as low as 0.6 keV. Moreover, the RGS results show the presence of gas at  $\sim 0.7$  keV out to  $3.5'$  in the SW arm, which also speaks in favor of the *wdem* model.

Our data thus points towards the conclusion that a continuous differential emission measure model for the gas in the X-ray arms is likely to be a more physical and more realistic description than a two-temperature plasma approximation. In most of the following sections we will thus primarily focus on the results of the *wdem* fit.

### 3.4.4 Discussion of the implications of multi-temperature structure for thermal conduction

A gas parcel with volume  $V$  and number density  $n$ , in thermal contact over an area  $A$  with an ambient gas with a temperature which is different by  $\Delta T$ , will reach thermal equilibrium with this ambient gas through heat conduction on a time scale that can be estimated as (adapted from Böhringer & Fabian 1989):

$$\tau_{hc} \approx \frac{\Delta H}{qA} \approx \frac{\frac{5}{2}nk_B\Delta T}{f\kappa_0 T^{5/2}\nabla T} \frac{V}{A} \quad (3.4)$$

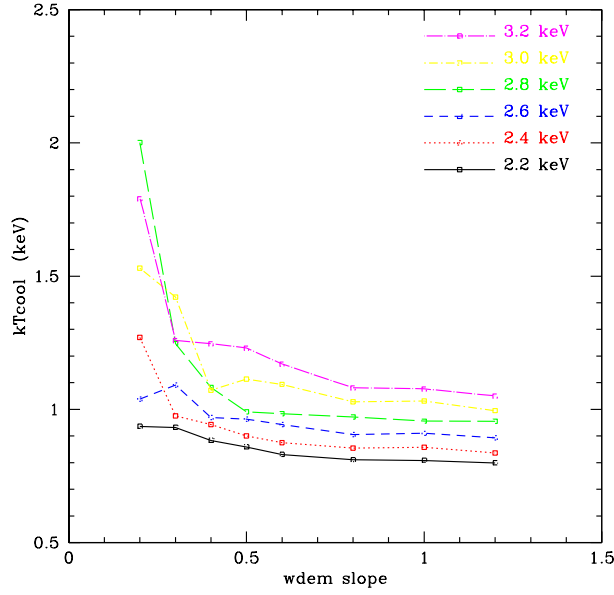


Figure 3.8: Results of fitting various simulated *wdem* spectra with a two-temperature model. The best fit cool temperature in the 2T model remains constant at around 1 keV for a wide range of input parameters in the simulated spectra. The different curves are for different values of the upper temperature cutoff,  $T_{\max}$ .

where  $\Delta H$  is the enthalpy which must be transferred to the gas parcel so that it reaches thermal equilibrium with the ambient gas,  $q$  is the heat flux according to Spitzer (1962),  $\kappa_0$  is the Spitzer heat conduction coefficient,  $\kappa_0 \sim 6 \times 10^{-7} \text{erg cm}^{-1} \text{s}^{-1} \text{K}^{-7/2}$ , and  $f$  is a coefficient allowing for the reduction in the heat conduction due to the effects of the magnetic field. For the case of a continuous multi-temperature distribution as the one described by the *wdem* model, the calculation of the heat conduction flux and hence the heating time scale is generally more complex. We can however make simplifying assumptions which will lead to upper limits on the allowed heat conduction such that the cool gas detected survives for over  $\sim 10^7$  years, which is the estimated age of the inner radio-lobes (e.g. Forman et al. 2007). The temperature gradient, and thereby also the heat flux, is smallest if we assume that the gas is stratified in each spatial bin such that gas at the coolest temperatures is furthest away from gas at the hottest temperatures. Moreover,  $V/A$  is largest assuming a spherical geometry. Combining these two assumptions and the quoted age of the radio lobes we arrive at an upper limit for the allowed  $f$ .

We aim to rewrite Eqn. 3.4, which holds for two gas phases in thermal contact, for the case of the multi-temperature distribution described by the *wdem* model. For this we will calculate how much enthalpy  $\Delta H$  must be transferred to the gas contained in the *wdem* model below a chosen  $T_*$  in order to heat this gas up to  $T_*$ . This is given by:

$$\Delta H = \frac{5}{2} \int_{cT_{\max}}^{T_*} (n_e + n_i) k_B (T_* - T) dV. \quad (3.5)$$

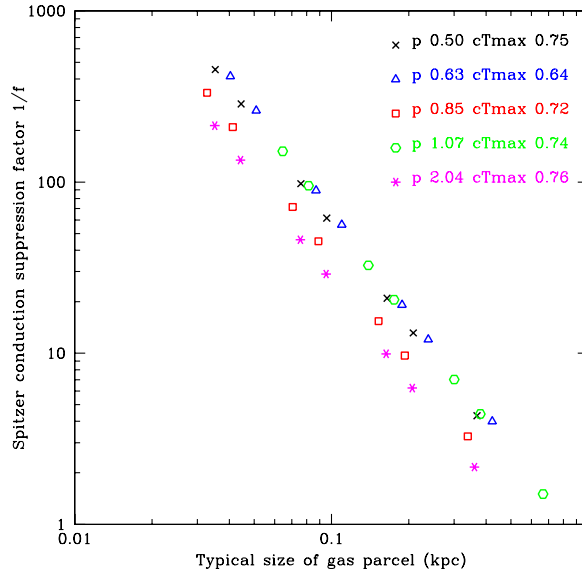


Figure 3.9: Factor by which the Spitzer heat conduction must be suppressed (this corresponds to  $1/f$  in Eqn. 3.4) in order to maintain the cool gas in the multi-temperature structure over at least  $10^7$  years, as a function of the size corresponding to the volume of the cool gas,  $V(< T_*)$ . The *wdem* inverse slope denoted here by  $p$  and lower temperature cutoff  $cT_{\max}$  (in keV) of the 5 different bins used for the calculation are indicated in the legend.

Note that according to the continuous distribution of the *wdem* model,  $T_*$  can be arbitrarily close to  $cT_{\max}$ , although it is probably not physically feasible for the separation to be infinitesimal. Given that  $dY = (dY/dT)dT = n_e n_i dV$  and assuming pressure equilibrium in the form  $(n_e + n_i)T = \text{const}$ , it follows that

$$dV \propto T^{2+1/\alpha} dT. \quad (3.6)$$

The proportionality constants can be calculated assuming a total volume for each bin (see Sect. 3.6.3). The volume  $V$  in Eqn. 3.4 can then be calculated integrating  $dV$  from  $cT_{\max}$  to  $T_*$ . Assuming the gas below  $T_*$  to be inside a sphere, one can then calculate the area  $A$  corresponding to this  $V$ . Finally,  $\nabla T = dT/dr = dT/dV \cdot dV/dr$  can be evaluated at  $T_*$  using the assumption of spherical geometry and Eqn. 3.6. This allows the calculation of  $\tau_{hc}$ , and the requirement that  $\tau_{hc}(T) < 10^7$  years for various  $T_*$  can help us place upper limits on  $f$ . However, we cannot account for possible mechanisms that would change the temperature cutoffs or the slope of the emission measure distribution since the time it was produced. Such mechanisms include mixing and the fact that gas at very low or very high temperatures, which could have been present at the beginning, has already been heated/cooled and is no longer detected.

We plot in Fig. 3.9 the conductivity suppression factor  $1/f$  needed to maintain the cool gas in the multi-temperature structure over at least  $10^7$  years against the radius  $r \sim (3V/4\pi)^{1/3}$  corresponding to  $V(< T_*)$ . For the calculation we used  $T_* - cT_{\max}$  in the range from  $5 \times 10^2 - 5 \times 10^5$  K. We calculated the values plotted in the figure using results from 5 different bins in the E

and SW arms spanning values of  $\alpha$  between 0.5 and 2. All our bins had similar low-temperature cutoffs of  $cT_{\max} \sim 0.64\text{--}0.76$  keV. We find that, for typical blob sizes of 0.1 kpc, similar to the widths of the cool filaments seen in the Chandra image (the filaments do not appear in images produced in energy bands above 2 keV, Forman et al. 2007), a suppression factor on the order of  $\sim 30\text{--}100$  is required.

## 3.5 The spatial distribution of metals

### 3.5.1 Abundance maps

The spectra in each spatial bin provide enough statistics not only to test the multi-temperature structure of the gas but also to determine the abundances of several heavy elements and to analyze their spatial distribution and the influence of different multi-temperature models on the abundance determination. In the spectral fits we left the abundances of O, Mg, Si, S, Ar, Ca, Fe and Ni free. The Ne abundance was fixed to the Mg abundance, since the Ne line falls within the Fe-L line complex and thus the Ne abundance cannot be accurately determined with the spectral resolution of the EPIC detectors.

Because of the good statistics around the Fe-L line complex, the Fe abundance is usually determined with the lowest statistical errors. We present a map of the Fe abundance determined from the *wdem* model in Fig. 3.10. As expected from previous work (e.g. Matsushita et al. 2003), a radial gradient is apparent. Beyond this radial trend however, deviations associated with the inner radio lobes can be seen as clear evidence of the influence of the AGN on the spatial distribution and transport of metals. The best region to illustrate this is the eastern lobe, which from the ‘‘mushroom-cloud’’ shape in the radio image appears as a more undisturbed system than the SW lobe. Here, one clearly sees a stem-shaped enhancement in the Fe abundance which coincides very well with the rising plasma bubble. The SW lobe also presents a higher metallicity with respect to the average radial profile, but this enhancement seems a bit less concentrated than in the E lobe and is more difficult to see from the map in Fig. 3.10. A more detailed quantitative analysis will be presented in Sect. 3.6.1.

Since the Fe-L complex is very sensitive to the temperature of the gas, one might question if and how the determined Fe abundance systematically depends on the model involved. To answer this, we plot in Fig. 3.11 the Fe abundance determined from the 2T and the *wdem* models. Reassuringly, the correlation between the two sets of fit values is very tight, which allows us to be confident in the measured abundance trends.

### 3.5.2 Metal abundance patterns of different elements in and outside the multi-temperature regions

The spatial distributions of other elements, especially S and Si which have the next best determined abundances, are very similar to that of Fe. Thus, we chose not to include 2D maps for these elements but rather to plot their abundance trends relative to Fe. We find that, while the overall abundance in the arms is higher, the Fe, Si, S and O abundances correlate well both inside

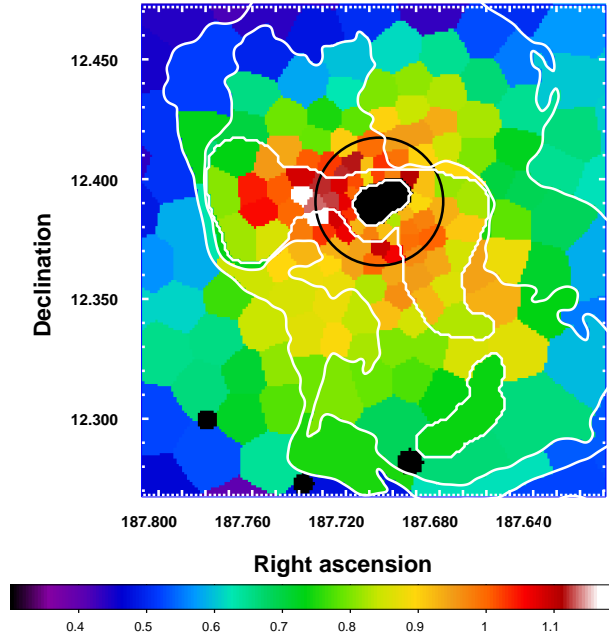


Figure 3.10: Fe map determined from the *wdem* model. Beyond the expected radial gradient, one clearly sees the enhancement in Fe abundance in the arms, especially within the E radio lobe. The half-light radius of M87 is marked with a black circle, the 90 cm radio contours are over-plotted in white.

and outside the radio lobe regions. The scatter in the O/Fe relation is larger than for Si/Fe and the O/Fe slope is much shallower, but we do see a small increase in the O abundance for higher Fe values. Therefore the cool gas must be enriched also with oxygen, for example through stellar mass loss in the galaxy. Fig. 3.12 shows a plot of the Si and O abundances against Fe, both for the bins where the cool gas fraction was significant (marked with special symbols) and for the rest of the bins in the fit. Since the Si and S abundances are very similar, we do not add the S/Fe data points to the plot for legibility. Both for Si/Fe and O/Fe we see that the trend in the multi-temperature regions coincides well with the trend outside the influence of gas-uplift by the radio lobes (note that Gastaldello & Molendi 2002, also find a constant ratio of O/Fe with radius in the inner 9' of M87). To quantify this, we fitted a line to the O vs. Fe, Si vs. Fe and S vs. Fe data points in and outside the arm regions. The best fit slopes are given in Table 3.1. These slopes are expected to become different at low values of the Fe abundance, where the contribution by SNeIa goes to zero and the O/Fe and Si/Fe ratios are determined by the pre-enrichment patterns of SNeII (for detailed discussion of this see, e.g., Matsushita et al. 2003). With the bins included in our plot in Fig. 3.12 however, we do not seem to reach down to low enough Fe abundances to see this effect significantly.

As seen in Table 3.1, there are indications that Fe is slightly more abundant in the multi-temperature regions (O/Fe, Si/Fe and S/Fe are all smaller than in the single-temperature regions), which would imply a more important relative contribution from SNeIa, but none of these differences is more than  $2\sigma$  significant. Because of this and since the O vs. Fe and Si vs. Fe data points

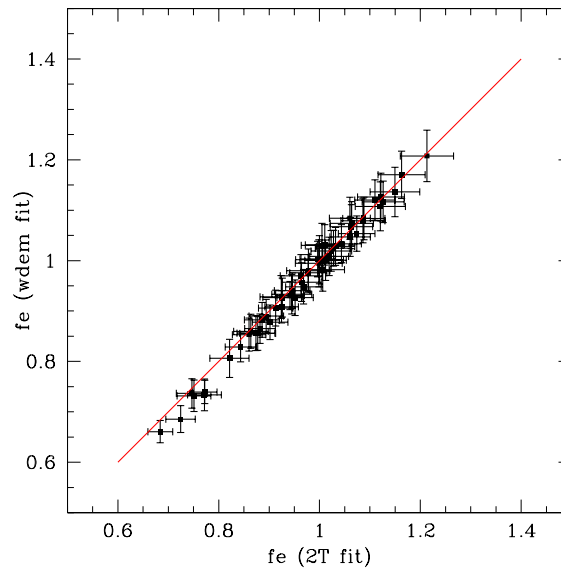


Figure 3.11: Fe abundance determination with two different multi-temperature models. The red line represents the function  $\text{Fe}(wdem) = \text{Fe}(2T)$ . It is easily seen that the abundance determinations from the two models agree very well, with a very low scatter. For clarity, only the points are plotted where the emission measure of the cool component in the 2T fit and the fraction of cool gas in the *wdem* fit were more than  $3\sigma$  significant. We note, however, that the correlation is equally strong also for all the other points in the maps.

in the multi-temperature regions overlap well with the trend outside the influence of gas-uplift by the radio lobes, we conclude that the AGN, at least at this advanced stage of the evolution of the galaxy, enriches the gas halo without altering the relative abundance patterns.

## 3.6 The properties of the cool gas

### 3.6.1 The correlation between the amount of uplifted cool gas and metallicity

Several authors have discussed the AGN/ICM interaction as a driver for metal-transport from the central galaxy into the ICM (for examples of recent work, see e.g. Rebusco et al. 2006; Roediger et al. 2007). Comparing Fig. 3.10 to 3.4 or 3.5, a possible mechanism by which the AGN influences the distribution of the metals in the gas halo is readily apparent: if the cool gas from the center of the galaxy is richer in metals, then the uplift of this gas by the radio bubbles will also enable the transport of the metals towards the outskirts of the cluster. Indeed, it seems that regions of enhanced metallicity in the lobes correspond well to regions where the fraction of the cool component is large.

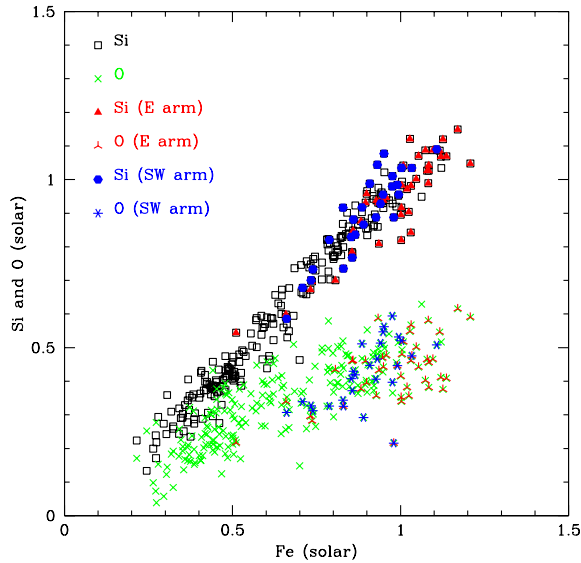


Figure 3.12: Oxygen and silicon vs. iron abundances in and outside the arm regions (*wdem* fit). Both the Si vs. Fe and O vs. Fe in the arms (marked with special symbols, see graph legend) follow the same trends, respectively, as the Si vs. Fe and O vs. Fe data points for bins outside the arms. Thus, the same abundance patterns are seen in all environments.

To illustrate this correlation, we plot in Fig. 3.13 the Fe abundance as a function of the fraction of the cool component in the *wdem* model for the regions where this fraction was more than  $3\sigma$  significant, for the E and SW arm separately. In the plot, the Fe abundance was binned in 2%-intervals of the cool gas fraction. We calculated the linear correlation coefficient for each arm without binning, taking into account the error bars on both axes (Akritas & Bershady 1996), and obtained a value of 0.66 for the E arm and 0.42 for the SW arm. Combining the data points for both arms we obtain a correlation coefficient of 0.48. This confirms a moderate linear dependence of the measured Fe abundance on the fraction of the cool component overall. Furthermore, binning the Fe abundance in 2%-intervals of the fraction of the cool component and recalculating the linear correlation coefficients, we obtain a value of 0.86 for each of the two arms, indicating a very clear correlation. The linear fits were performed taking into account the errors on both axes. Extrapolating the best-fit line equations to 100% cool-component yields an average iron abundance of  $1.88 \pm 0.18$  and  $1.93 \pm 0.12$  solar for the SW and E arm respectively (quoted errors are at the  $1\sigma$  level).

We adapted this procedure also for the results of the two-temperature fits and obtain comparable results for the mean iron abundance of the cool gas:  $2.13 \pm 0.54$  for the SW arm and  $2.38 \pm 0.29$  for the E arm. However, the correlation is not as strong as in the case of the *wdem* model. The correlation coefficients after binning the data in 2%-wide bins of the cool gas fraction are only 0.63 for the E arm and 0.34 for the SW arm. The fact that the Fe abundance correlates

Table 3.1: Comparison of best-fit metal abundance ratios in and outside the multi-temperature regions (*wdem* fit).

	inside multi-temperature region	outside multi-temperature region
O/Fe	$0.44 \pm 0.07$	$0.49 \pm 0.03$
Si/Fe	$1.02 \pm 0.06$	$1.10 \pm 0.02$
S/Fe	$1.05 \pm 0.09$	$1.18 \pm 0.03$

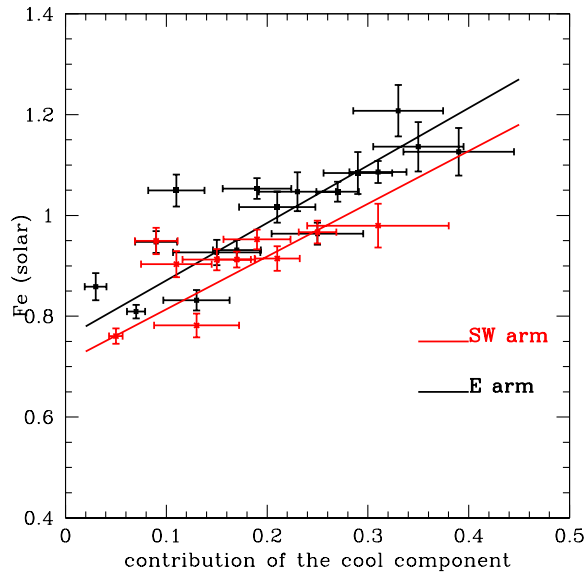


Figure 3.13: Averaged Fe abundance in 2%-wide bins of the fraction of the cool component and linear fit for each arm. The linear correlation coefficients are 0.86 for each of the two arms, indicating a very clear correlation.

much better with the fraction of cool gas determined from the *wdem* model than with the fraction determined from the 2T model may be an additional indication that a continuous temperature distribution is a better description of the temperature structure in the regions associated with the radio lobes.

To check to which extent the correlation presented in Fig. 3.13 may be due to similar radial trends of the cool gas fraction and Fe abundance, we furthermore fitted the radial Fe and  $f_{\text{cool}}$  profiles from the *wdem* results using non-parametric, locally weighted, linear regression smoothing, and divided the Fe and  $f_{\text{cool}}$  maps by the resulting radial models. This should remove any trends due to common radial dependences. We plot in Fig. 3.14 the map of Fe deviations from a smooth radial profile,  $\text{Fe}/\langle \text{Fe} \rangle$ , and over-plot contours of the  $f_{\text{cool}}$  deviations from radial symmetry,  $f_{\text{cool}}/\langle f_{\text{cool}} \rangle$ . The figure shows a tight correlation between regions of relatively higher iron abundance and relatively higher fraction of cool gas with respect to the radial average. The

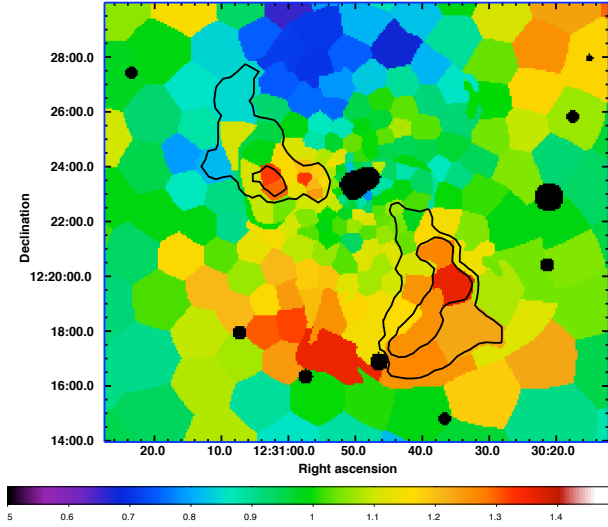


Figure 3.14: Map of Fe deviations from a smooth radial profile,  $Fe / \langle Fe \rangle$ . Contours of the cool gas fraction deviations from radial symmetry are over-plotted. It is clear that the correlation between Fe and  $f_{cool}$  is in most part not due to common radial dependences. The high-abundance feature to the SE corresponds to the cold front presented in Chapter 2.

only exception to this is a high-abundance region to the SE, which does not correspond to a high cool-gas fraction but where Simionescu et al. (2007) have already discovered the presence of a cold front associated with a metallicity jump (Chapter 2). The relatively low-abundance region opposite the SE feature is probably due to the fact that the higher abundances over a relatively large azimuthal range in the cold front pull up the average at that particular radius, so dividing “normal” values at that radius by this average will result in a depression. We calculated the linear correlation coefficients between  $Fe / \langle Fe \rangle$  and  $f_{cool} / \langle f_{cool} \rangle$  and obtain 0.70 for the E and 0.72 for the SW arms (unbinned). The fact that these coefficients are even stronger than for the simple Fe vs  $f_{cool}$  correlation indicates that the underlying radial dependence of the abundance of the hot halo may be responsible for a large part of the scatter in Fig. 3.13. We will investigate this further using spectral simulations in the next section.

### 3.6.2 The metallicity of the cool gas

To explain the correlation between the amount of uplifted cool gas and metallicity presented in the previous section we can begin by assuming that if we fit a multiphase gas for which the Fe abundance is some function of the temperature with a spectral model with a single metallicity, the resulting Fe abundance from the spectral fit can be (neglecting for now e.g. the dependence of the Fe line strength on temperature) approximated by an emission-weighted average:

$$Z'_{Fe} \approx \frac{\int_{cT_{max}}^{T_{max}} Z_{Fe}(T) Y(T) dT}{\int_{cT_{max}}^{T_{max}} Y(T) dT} \approx \langle Z_{Fe_{cool}} \rangle f_{cool} + \langle Z_{Fe_{hot}} \rangle f_{hot} \quad (3.7)$$

$$\approx \langle Z_{Fe_{cool}} \rangle f'_{cool} + \langle Z_{Fe_{hot}} \rangle f'_{hot} \quad (3.8)$$

$$\approx \langle Z_{\text{Fe}_{\text{hot}}} \rangle + (\langle Z_{\text{Fe}_{\text{cool}}} \rangle - \langle Z_{\text{Fe}_{\text{hot}}} \rangle) f'_{\text{cool}} \quad (3.9)$$

where the quantities denoted by the prime are the results of the fitting while the other quantities are the "true" values characterizing the gas, and it holds that  $f'_{\text{cool}} + f'_{\text{hot}} = 1$  since  $f'_{\text{cool}}$  and  $f'_{\text{hot}}$  denote the fitted relative emission measure contributions from the cool and hot gas respectively. The cool gas is, as before, defined as gas with a temperature below 1.5 keV, which is the lowest value found in the deprojected temperature profile outside the X-ray arms (Matsushita et al. 2002).

This means that the measured Fe abundance  $Z'_{\text{Fe}}$  depends in first-approximation linearly on the fraction of the cool, metal-rich gas  $f'_{\text{cool}}$ , or equivalently on  $Y_{\text{cool}}/Y$ , which is in agreement with what we observe. If this approximation holds, then the Fe abundances obtained by extrapolation to 100% cool component contribution, as calculated above, are the real values of the Fe abundance of the cool component.

To investigate the validity of this simple approximation, we simulated spectra combining a *wdem* component between  $c$   $T_{\text{max}}$  and 1.5 keV with Fe = 2 solar and a second *wdem* component between 1.5 keV and  $T_{\text{max}}$  with Fe = [0.6,0.8,1.0] solar. The two *wdem* components had the same slopes and their relative normalizations were chosen such that  $dY/dT$  at 1.5 keV was continuous. We stepped the upper temperature cutoff  $T_{\text{max}}$  between [2.2,2.6,3.0] keV, the lower temperature cutoff between [0.2,0.25,0.3,0.4] $T_{\text{max}}$  and the slope between 0.2 and 1.2 in intervals of 0.2. This parameter space is equivalent to a range of cool gas contributions from 0 to 60% of the total emission measure. We assumed an O/Fe ratio of 0.4 and Si/Fe and S/Fe ratios of 1.0 solar (see Table 3.1) for both of the simulated model components. The simulated spectrum was then fitted with a single *wdem* model with a single abundance.

The results are presented in Fig. 3.15. Most important to note is that from the simulation we do recover, up until quite high percentage contributions of the cool component, a clearly linear dependence of the determined coupled abundance  $Z'_{\text{Fe}}$  on the cool gas fraction  $f'_{\text{cool}}$ , plotted on the X axis. The largest scatter is due to the different abundances of the hot gas component, while there is practically no scatter due to  $c$  and  $T_{\text{max}}$ . However, the slope of  $Z'_{\text{Fe}}$  vs.  $f'_{\text{cool}}$  is slightly different than the slope of  $Z'_{\text{Fe}}$  vs. the true  $f_{\text{cool}}$  (by a factor of approximately 1.2).

This discrepancy can be understood in the following way: if the cold gas is more metal-rich than the hot gas and if the spectral model forces the abundances of all gas phases to be the same, then the cool gas in the fitted model will have a too low abundance compared to the real value (and in turn the hot gas will have a too high abundance). To obtain the best fitting spectral shape of the Fe-L complex thus, which is equivalent to obtaining the correct contribution of emission in the FeL energy range from the cold gas, the fit will have to raise the normalization of the cool component to compensate for the fact that the fitted abundance of the cool component is forced to be lower than in reality. This is why coupling the abundances of the different phases leads to an overestimation of the normalization of the cool component, which is reflected in our simulations by a decrease of the  $Z'_{\text{Fe}}$  vs.  $f'_{\text{cool}}$  (fitted) slope compared to the  $Z'_{\text{Fe}}$  vs.  $f_{\text{cool}}$  (real) slope. This affects our estimates of the normalization of the cool gas, as a consequence also our estimates of the mass of the cool gas, and leads to underestimating the metallicity of the cool component if we simply extrapolate the best-fit  $Z'_{\text{Fe}}$  vs  $f'_{\text{cool}}$  line equations to  $f'_{\text{cool}} = 1$ . If we correct the slopes found in the previous section for the *wdem* model by the factor described above we find

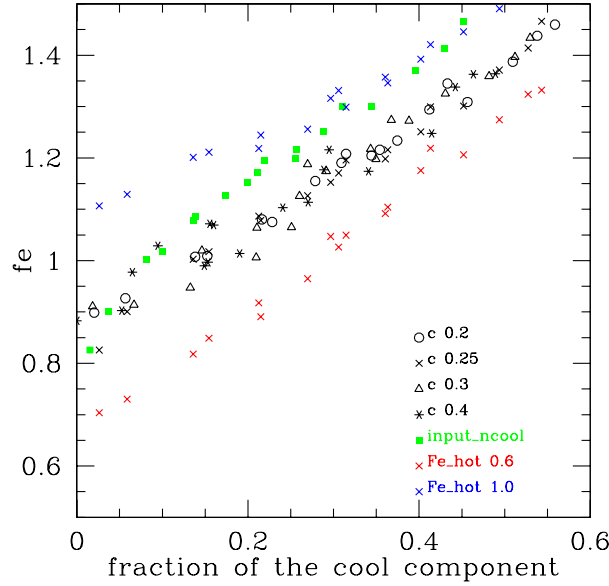


Figure 3.15: Results of fitting a simulated combination of two *wdem* spectra with a high Fe abundance of the cool gas with a *wdem* model with coupled abundances. Blue, black and red crosses plot the fitted (coupled) Fe abundance against the fitted fraction of the cool component for various input *wdem* slopes, various upper temperature cutoffs, an input lower temperature cutoff of  $0.25 T_{\max}$  and a hot component metallicity of 1.0, 0.8 and 0.6 solar, respectively. Black circles, black triangles and black asterisks plot the same for a hot component metallicity of 0.8 solar and lower temperature cutoffs of 0.2, 0.3 and 0.4, respectively. Green squares plot the fitted (coupled) Fe abundance against the original (input) cool gas fraction for an input lower temperature cutoff of  $0.25 T_{\max}$  and a hot component metallicity of 0.8 solar. For an ideal fitting of the cool gas fraction, the black crosses should overlap with the green squares.

Fe abundances for the cool component as summarized in Table 3.2.

We note that similar simulations as described above were performed also for the two-temperature model, recovering again the expected linear dependence of  $Z'_{\text{Fe}}$  on the cool gas fraction  $f'_{\text{cool}}$ , but with a larger scatter due to the assumed metallicities of the hot component. Given the much weaker correlation between  $Z'_{\text{Fe}}$  and  $f'_{\text{cool}}$  in the 2T model and the higher uncertainty in the determination of the observed  $Z'_{\text{Fe}}$  vs.  $f'_{\text{cool}}$  slope, as well as considering our arguments against the two-temperature description of the plasma the X-ray arms, we however choose not to further discuss the 2T results in quantitatively determining  $\langle Z_{\text{Fe,cool}} \rangle$ . The assumed thermal model may have an important influence on the determination of the value for  $\langle Z_{\text{Fe,cool}} \rangle$ . However, more complicated models cannot be fitted to the available data, since any additional free parameters would be unconstrained. In view of the current lack of a clear theoretical prediction regarding the exact thermal structure of the uplifted gas, the *wdem* model is at the moment the simplest and most flexible model which serves as a good first-approximation to a wide range of possible emission measure distribution functions. Hence, we will in the following rely on the *wdem* results for

interpretation.

Table 3.2: Estimates of the average iron abundance of the cool component relative to the proto-solar values of Lodders (2003).

	E arm	SW arm
2T	$2.38 \pm 0.29$	$2.13 \pm 0.54$
wdem uncorrected	$1.93 \pm 0.12$	$1.88 \pm 0.18$
wdem corrected	$2.16 \pm 0.14$	$2.11 \pm 0.22$

Considering the results shown in Table 3.2, we will for the rest of this chapter use an average iron abundance of 2.2 solar. This implies, if we use the abundance ratios presented in Table 3.1, Si and S abundances also around 2.2 solar, and an O abundance of roughly 0.9 solar for the cool gas. Interestingly, the determined Fe abundance for the cool gas is in good agreement with the value of 2.3 solar obtained by Matsushita et al. (2007a) in the Centaurus cluster, where presumably an undisturbed accumulation of metals over a longer time-scale enabled the central metallicity to reach higher values than in the Virgo cluster center. The difference in the central abundances of M87 and Centaurus can be thus explained by AGN-induced transport of heavy elements out of the central region of M87.

### 3.6.3 The mass of the cool gas

The emission measure is defined as

$$Y = \int n_e n_i dV \approx n_e n_i V \approx f_{ei} n_e^2 V \quad (3.10)$$

where  $n_e$  and  $n_i$  are the electron and ion densities,  $f_{ei}$  is the electron to ion number ratio (on the order of 1.2), and  $V$  is the volume of the emitting region. From this, one can estimate the mass of gas according to (where  $\langle m_i \rangle$  is the average ion mass per electron in the cluster gas and  $m_p$  is the proton mass):

$$M \approx \langle m_i \rangle \sqrt{YV/f_{ei}} \approx m_p \sqrt{YV} \quad (3.11)$$

This requires assumptions about the projected geometry. To calculate the mass of cool gas in the arms, we compare two alternatives for determining the depth of each bin along the line of sight (LOS).

#### Assumptions about the projected geometry of the cool component

The first and simplest method is to assume a constant LOS depth for the cool gas component equal to the average width of the radio arms in the plane of the sky. For this, we choose a LOS depth of 200'' (15.5 kpc). The second possibility is to define the center of the gas halo, determine the minimum and maximum radii of each bin with respect to this center and assume

that the longest LOS distance is equal to the longest circle chord that can be drawn between the circle of minimum radius and the circle of maximum radius, in other words that only the gas between the sphere with the minimum radius and the sphere with the maximum radius contribute to the emission (Henry et al. 2004; Mahdavi et al. 2005). This yields, where  $S$  is the area of the region in the plane of the sky,

$$L = 2\sqrt{(R_{\max}^2 - R_{\min}^2)} \text{ and } V = 2SL/3. \quad (3.12)$$

We used both of these geometries combined with the integrated emission measure  $Y_{\text{cool}}$  of the gas below 1.5 keV from the *wdem* fit to calculate different estimates of the mass of the uplifted cool gas. In the calculation we included only the bins where the fraction of gas below 1.5 keV was more than  $3\sigma$  significant. Both methods show similar spatial distributions of the mass of cool gas. The quantitative results for the total mass of the cool gas are summarized in Table 3.3, under the column heading “direct”. For comparison, also the masses of the cool gas determined from the two-temperature model with the two assumed geometries are shown and are in good agreement with the *wdem* results.

### Filling factor

For the two volume estimates considered above we additionally must take into account the fact that the cool component may not fill the entire volume of the bin, but may be concentrated in thin filaments (Forman et al. 2007) which occupy only a fraction (so-called filling factor) of the assumed volume corresponding to each bin. It is very difficult to determine this filling factor from the data, especially since the PSF of XMM-Newton is too large to resolve these filaments.

The easiest method to estimate the filling factor is to assume pressure equilibrium between the different temperature phases present in the spectral models, which for the *wdem* model implies  $\delta V \propto T^{2+1/\alpha}$  (Sect. 3.4.4), yielding

$$\frac{V_c}{V_h} = \frac{\int_{cT_{\max}}^{1.5} T^{2+1/\alpha} dT}{\int_{1.5}^{T_{\max}} T^{2+1/\alpha} dT} \quad (3.13)$$

The results for the new mass estimates using the filling factor corrections according to these calculations are presented in Table 3.3 under the column heading “ff”. We used only the volume estimate given in Eqn. 5.1, since we cannot assume that the hot component also has a constant line of sight distance of only 200". These values are however only lower limits to the true mass of the cool gas because the filaments are most likely supported by extra pressure from the magnetic field. If the magnetic field is higher inside the cool component than in the surrounding hot component, then the magnetic pressure adds to the thermal pressure of the cool gas. This reduces the pressure required to maintain hydrostatic equilibrium with the hot surrounding gas, which allows a lower density of the cool gas and a larger filling factor. Note that we have ignored the effects of magnetic tension which can contain the cool gas and work the other way.

To get a more physical estimate of the filling factors we therefore also reevaluated them including the contribution to the pressure of the cold phase of a uniform magnetic field with a

strength of  $10 \mu\text{G}$ , which is a typical average value in the inner radio lobes obtained by Owen et al. (2000) using the radio data. The results are likewise shown in Table 3.3, under the column heading “ff B10”. We note that the lower limits on the magnetic field strength of  $1 \mu\text{G}$  obtained in this chapter (Sect. 3.7) would result in a magnetic pressure several orders of magnitude below the thermal pressure, therefore we did not include this in our calculations but preferred the higher values obtained by Owen et al. (2000).

### Corrections due to coupling the abundances of different temperature phases in the spectral models

We proved in the Sect. 3.6.2 that the normalization of the cool gas is overestimated by using a model with a single abundance to describe a combination of a metal-rich component and relatively poorer hot ambient plasma. In the case of a *wdem* model, this overestimation amounts to a factor of 1.2 if the average metallicity of the cool component is 2 solar (we redid the simulations for an average metallicity of the cool component of 2.2 solar and find that this factor changes by only 5%). We therefore further correct the mass of the cool gas decreasing it by this factor, as shown in Table 3.2 under the column heading “ffB10 Zcorr”. A map of the mass of cool gas including all the corrections described above is shown in Fig. 3.16.

Table 3.3: Total mass of the cool gas (in  $10^9$  solar masses), including all the different corrections discussed in Sect. 3.6.3.

LOS	model	direct	ff	ff B10	ffB10 Zcorr
const	2T	2.3	-	-	-
Eqn. 5.1	2T	2.4	0.39	0.41	-
const	<i>wdem</i>	2.2	-	-	-
Eqn. 5.1	<i>wdem</i>	2.1	0.54	0.60	0.50

In the following, we will use the estimate of  $5 \times 10^8 M_{\odot}$  for the mass of the cool gas, which includes all the corrections discussed in this section and is determined from the *wdem* model which we believe to describe the data better than the two-temperature model. We note that the cooling time of the cool gas in the multi-temperature regions, computed assuming isobaric cooling and using an average value of the temperature for the multiphase distribution, is longer than the ages of the radio lobes in all bins (between  $2 \times 10^8$  and  $2 \times 10^9$  years). Therefore our mass estimate is not affected by gas which has cooled out of the X-ray domain since the uplift.

### 3.6.4 Discussion of the origin and uplift of the cool gas

We have presented so far in this chapter many arguments in favor of the scenario proposed by Churazov et al. (2001), in which the cold gas in the X-ray arms is a result of gas uplift from the central regions of the galaxy through buoyant radio bubbles. In this section we will try to bring

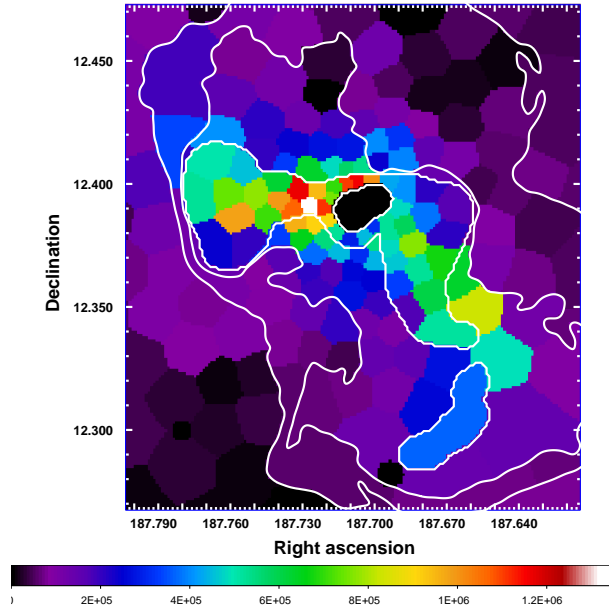


Figure 3.16: Map of the mass of gas below 1.5 keV in the *wdem* model assuming a geometry with a line-of-sight distance for each bin given by Eqn. 5.1. The map has been corrected for the filling factor of the cool gas assuming pressure support for the cool gas from a  $10\mu\text{G}$  magnetic field (Sect. 3.6.3) and for the effects of coupling the abundances of the different phases (Sect. 3.6.3). The units are solar masses per square kiloparsec. Radio contours at 90 cm are overplotted in white.

the observational details together towards a consistent picture of the energetics and chemical composition of the M87 X-ray arms and explain how this relates to the radio activity.

### Energetics

We first use the mass estimates derived in the previous section to compute the gravitational energy needed to uplift the gas:

$$U = \frac{GM_{\text{cool}}M(R)}{R} \quad (3.14)$$

For  $M(R)$  we use the integrated total mass profile of Matsushita et al. (2002). We use the approximation that all the gas with total mass  $M_{\text{cool}}$  is uplifted from  $R=0$  and  $U=0$  to a mean radius

$$R_{\text{mean}} = \frac{\sum M(i)R(i)}{M_{\text{cool}}} \quad (3.15)$$

where  $i$  are all the bins where the cool component was more than  $3\sigma$  significant. We calculated  $R_{\text{mean}}$  in this way for all the different models and volume estimates presented in the previous section and obtain consistent values between 15 and 20 kpc. Assuming a typical mass of the

uplifted gas of  $0.5 \times 10^9 M_\odot$  (see Table 3.3) and  $R_{\text{mean}} = 20$  kpc, we obtain a required gravitational energy of  $4.33 \times 10^{57}$  ergs. If the AGN outburst that created the inner radio lobes occurred  $10^7$  years ago (e.g. Forman et al. 2007), this gravitational energy corresponds to a required power of  $1.37 \times 10^{43}$  erg/s, which is a sizable fraction of the total jet power estimated by Owen et al. (2000) at a few  $\times 10^{44}$  ergs/s. The power needed to uplift the cool gas is much larger than the total radio power cited by Owen et al. (2000) at only  $9.6 \times 10^{41}$  erg/s, consistent with the picture that the bulk of the jet energy is deposited in the gas (in this case, a large part thereof in the form of potential energy), while only a small fraction is leaked to radio emission.

Thus, from energetic considerations, the model of the cool gas being uplifted by the buoyant radio lobes is entirely consistent with the X-ray and radio observations. This provides a clear mechanism for the transport of the cool gas out of the center of the gas halo, together with the metals it has been enriched with.

### Possible sources of cool gas

We have chosen to define the cool gas in the *wdem* model as gas having a temperature below 1.5 keV, the smallest value in the deprojected profile of the hot M87 halo calculated by Matsushita et al. (2002). There are three possible ways to produce gas cooler than 1.5 keV. The most straightforward option is to adiabatically cool gas from the center of the M87 halo by uplifting it into regions of lower pressure at larger radii. Using the pressure profile from Chapter 2 and assuming an adiabatic index of 5/3, gas at 1.5 keV uplifted from a radius of 1 to 10 kpc would cool from 1.5 to 0.6 keV and so could reproduce, in principle, the temperatures that we observe. However, if adiabatic cooling is the only mechanism to reduce the temperature of the gas, we would (neglecting heating processes) expect to see a decreasing trend of  $cT_{\text{max}}$  with radius, which is not the case. More importantly, the average Fe abundance of 2.2 solar for the cool gas, determined in Sect. 3.6.2, is higher than the value observed in the center of M87 ( $\sim 1.6$  solar, Matsushita et al. 2003). Thus, the cool gas could not originate from adiabatically cooled halo gas alone, but must contain a second, metal-rich component.

Another important source of cool gas are the stellar winds. Assuming the stellar mass loss rate proposed by Ciotti et al. (1991),

$$\dot{M}_*(t) \approx -1.5 \times 10^{-11} L_B t_{15}^{-1.3}, \quad (3.16)$$

where  $L_B$  is the blue band luminosity in units of  $L_{B\odot}$  and  $t_{15}$  is the age of the stellar population in units of 15 Gyrs. We take the age of the stellar population to be 10 Gyrs and  $L_B$  to be  $10^{11} L_{B\odot}$ , corresponding to the absolute B magnitude of M87 of -22.14 cited by Peletier et al. (1990). This gives us a stellar mass loss rate of  $2.54 M_\odot/\text{yr}$ . If we further assume that the material lost from stars thermalizes according to the M87 stellar velocity dispersion of 350 km/s (Angione et al. 1980), the temperature of this gas would be 0.64 keV. Interestingly, this is also very close to the lower temperature cutoffs found using the *wdem* spectral model. Beside being a source of cool gas, stellar winds also contribute to the metal-enrichment, as will be discussed in the next section, and are an important candidate for the second, metal-rich component of the uplifted gas.

The third and last possible source of cool gas is the cooling flow. Matsushita et al. (2002) find that within  $4'$  a total mass of  $13.8 M_\odot/\text{yr}$  can cool down to as low as 1.4 keV and 0.63

$M_{\odot}/\text{yr}$  cool down to 0.1 keV. Based on the same metallicity argument as above, the cool gas could not originate from cooling-flow gas alone since this would lead to its metallicity being lower than measured. Using the gas metallicity and temperature, it is not possible to distinguish adiabatically and radiatively cooled ICM as different components of the uplifted gas.

### Metal enrichment of the cool gas

Metals can be either ejected from the stars by the stellar winds or produced by supernovae. We neglect the metal enrichment by type II supernovae, since M87 has an old population where the expected SNeII rate is very low. Rafferty et al. (2006), for example, find an upper limit on the star formation rate (SFR) for M87 of  $0.081 M_{\odot}/\text{yr}$  using far-infrared data. Assuming a Salpeter initial mass function (IMF, Salpeter 1955) for the stars forming between 0.01 and 50 solar masses, the number of stars formed from this cooling gas that would be more massive than 10 solar masses and could become SNeII progenitors is

$$N(> 10M_{\odot}) = 0.081 \cdot \frac{\int_{10}^{50} M^{-2.35} dM}{\int_{0.01}^{50} M^{-2.35} dM} \approx 0.017/\text{century} \quad (3.17)$$

This upper limit on the rate of SNeII is roughly two orders of magnitude below the expected rate of SNeIa in elliptical galaxies (Cappellaro et al. 1999, see calculation below).

This leaves stellar winds and type Ia supernovae (SN Ia) as the main sources of enrichment of the cool gas. Following Böhringer et al. (2004); Rebusco et al. (2006), the rates of iron injection by stellar mass loss is:

$$\dot{M}_{\text{Fe},*} = \gamma_{\text{Fe}} \times \dot{M}_*(t), \text{ with} \quad (3.18)$$

$$\gamma_{\text{Fe}} = Z_{\text{Fe},*} \times \frac{\langle m_{\text{Fe}} \rangle}{\langle m_{i\odot} \rangle} \times \left( \frac{N_{\text{Fe}}}{\sum_i N_i} \right)_{\text{Lodd}}, \quad (3.19)$$

where  $\dot{M}_*(t)$  is the stellar mass loss rate calculated in Eqn. 4.3,  $\gamma_{\text{Fe}}$  is the mean iron mass fraction in the stellar winds of an evolved stellar population,  $Z_{\text{Fe},*}$  is the assumed abundance of the stellar winds in solar units,  $\langle m_{\text{Fe}} \rangle \approx 56$  is the mean weight of an iron isotope with respect to hydrogen,  $\langle m_{i\odot} \rangle$  is the mean weight of an ion with respect to hydrogen in the Sun (in the solar photosphere), and  $(N_{\text{Fe}} / \sum_i N_i)_{\text{Lodd}} \approx 3.16 \times 10^{-5}$  is the relative number abundance of Fe ions to the sum over all ions in the plasma, as determined from Lodders (2003). We assume, as above, a galactic age of 10 Gyr. Kobayashi & Arimoto (1999) derive stellar metallicities in M87 ranging from  $\approx 2$  solar in the center to  $\approx 1$  solar at the galaxy's half-light radius ( $2'$ ) using the  $\text{Mg}_2$  index. We will therefore take  $Z_{\text{Fe},*} \approx 1.6$ . The rate of iron production by SN Ia can be written as:

$$\dot{M}_{\text{Fe,Ia}} = \eta_{\text{Fe}} \times R_{\text{Ia}}, \text{ with} \quad (3.20)$$

$$R_{\text{Ia}} = 0.18 \pm 0.06 (100\text{yr})^{-1} (10^{10} L_{B\odot})^{-1} \quad (3.21)$$

where  $\eta_{\text{Fe}} = 0.79 M_{\odot}$  is the iron yield per SNIa assuming the WDD2 model of Iwamoto et al. (1999) and  $R_{\text{Ia}}$  is the present supernova rate in elliptical galaxies according to Cappellaro et al.

(1999). For M87,  $L_B \approx 10^{11} L_{B\odot}$ , as calculated above, which yields  $R_{Ia} \approx 1.8 \pm 0.6$  SNeIa per century. We assume that the iron production by both SN Ia and stellar winds is constant during the time of enrichment, which as we will show below is much shorter than the Hubble time.

We wish to enrich ICM gas to an average Fe abundance of 2.2 solar. For this, we must assume an initial metallicity  $Z_i$  of the ICM at the center of M87 immediately following the next to last AGN outburst which modified the spatial distribution of metal abundances. After the next to last AGN outburst, stellar mass loss and supernovae enriched this central gas until it reached 2.2 solar and was uplifted by the last AGN outburst, the effect of which we observe today. Ideally we should take the central metallicity immediately after the last outburst and assume it is representative also for the metallicity after the next to last outburst. We however do not know this value. A sensible lower estimate is to assume  $Z_i$  as the average metallicity of the entire hot halo within the region of the arms. This can be calculated as the best-fit y-intercept for the linear fit of the Fe abundance in the multi-temperature regions vs. the fraction of cool gas (Fig. 3.13) and is approximately 0.7 solar. Alternatively, as an upper limit to  $Z_i$ , we can assume the current value at the center of M87 determined by Matsushita et al. (2003) to be 1.6 solar. This is likely to be an upper limit because, since the time of the last outburst, the central region has been enriched with metals beyond the metallicity that it had immediately after the outburst. With these two values for  $Z_i$ , we can bracket the enrichment time needed to reproduce the observed Fe abundance of the cool gas.

Using a mass production rate of stellar winds of  $2.5 M_\odot/\text{yr}$  (Eqn. 4.3) and neglecting the mass of supernova remnants (assuming an average supernova mass of  $10 M_\odot$  and rate  $R_{SN Ia}$  of 1.8 per century, we obtain only  $0.18 M_\odot/\text{yr}$  which is much less than for the stellar winds), we can write for the Fe enrichment of the uplifted material:

$$2.2 \times 5 \cdot 10^8 M_\odot \times f_{\text{Fe},\odot} = Z_i \times M_i \times f_{\text{Fe},\odot} + (\dot{M}_{\text{Fe,Ia}} + \dot{M}_{\text{Fe},*}) \times \tau \quad (3.22)$$

$$M_i + 2.5 M_\odot/\text{yr} \times \tau = 5 \cdot 10^8 M_\odot \quad (3.23)$$

where  $f_{\text{Fe},\odot} = \langle m_{\text{Fe}}/m_{i\odot} \rangle \times (N_{\text{Fe}}/\sum_i N_i)_{\text{Lodd}}$  is the mass fraction of Fe in the Sun,  $\tau$  is the time over which the enrichment takes place,  $M_i$  is the initial mass of cluster gas to which stellar mass loss is added over time  $\tau$ . We solve the system of equations above for  $\tau$  and  $M_i$  making use also of Eqns. 3.18 and 3.20. Assuming  $Z_i=1.6$  solar we obtain  $\tau=30$  Myr, while for  $Z_i=0.7$  solar we need 60 Myr to enrich the ICM before uplift. For  $Z_i=1.6$  solar, the mass originating from stellar mass loss represents 15% of the total uplifted mass, while for  $Z_i=0.7$  solar it amounts to 30%.

We can now try to reproduce the abundances of other elements such as O, Si and S in the cool gas. Using the Fe/O, Fe/Si, Fe/S ratios in Table 3.1, the O, Si and S abundances of the cool gas should be approximately 0.9, 2.2 and 2.2, respectively. For an initial Fe abundance of  $Z_i = 0.7$  solar and assuming the same ratios, we obtain 0.3, 0.7 and 0.7 solar for O, Si and S, respectively. The central values of Matsushita et al. (2003) are consistent with 0.6, 1.6, and 1.6, respectively.

Assuming solar abundance ratios for the stellar winds, we can use the equivalent of Eqn. 3.18 and 3.19 to determine also  $\dot{M}_{\text{O},*}$ . Using  $Z_{\text{O},i}=0.6$  and ignoring contributions by SN Ia to the

oxygen budget, the time needed to enrich the cluster gas to 0.9 solar oxygen abundance is 60 Myr. Correspondingly for  $Z_{O,i}=0.3$ , we obtain 92 Myr. A similar procedure can be applied for Si and S, including contributions by SN Ia according to the WDD2 model of 0.21  $M_{\odot}$  and 0.12  $M_{\odot}$  per supernova, respectively. For Si we obtain, respectively, 63 and 108 Myr for  $Z_{Si,i}=1.6$  and 0.7, while for S we obtain 56 and 98 Myr for the same  $Z_{S,i}$ .

We also computed the required enrichment times using the WDD1 model of Iwamoto et al. (1999) which has a higher Si/Fe ratio and was found by Finoguenov et al. (2002) to provide a better fit to the abundance patterns in the center of the M87 gas halo. These results, together with the results from the WDD2 model, are summarized in Table 3.4. Oxygen enrichment times for the two models are the same since we neglect contributions by SN Ia to the oxygen budget. The WDD1 model requires more similar enrichment times to produce the different metals, in agreement with the results of Finoguenov et al. (2002). The obtained enrichment times differ from each other by up to a factor of  $\approx 2.1$  for the WDD2 and  $\approx 1.7$  for the WDD1 models. A possible source of this discrepancy is that our assumption of solar abundance ratios for the stellar winds is not accurate. If, for the older population of M87, the Si/Fe composition of stellar winds would be higher than solar, we would obtain more consistent enrichment times to produce all three metals. Note also that the enrichment times are in slightly better agreement for  $Z_i = 0.7$  solar than for  $Z_i = 1.6$  solar, suggesting that the former choice may be the more appropriate and reliable one.

Table 3.4: Enrichment times needed to produce the metals seen in the cool gas (in Myr) and, in brackets, the fraction of the stellar mass loss contribution to the total mass of uplifted gas.

	$Z_{Fe/Si/S,i} = 1.6$ $Z_{O,i} = 0.6$		$Z_{Fe/Si/S,i} = 0.7$ $Z_{O,i} = 0.3$	
	WDD2	WDD1	WDD2	WDD1
Fe	30 (0.15)	35 (0.18)	60 (0.30)	69 (0.35)
Si	63 (0.32)	49 (0.25)	108 (0.54)	90 (0.45)
S	56 (0.28)	42 (0.21)	98 (0.49)	79 (0.40)
O	60 (0.30)	60 (0.30)	92 (0.46)	92 (0.46)

At the end of Sect. 3.5.2, we show that the relative abundances of O/Si/ S/Fe are very similar in and outside the multi-temperature regions. This indicates firstly that the metals outside the multi- temperature region, which were (according to our model) uplifted from the galaxy by previous AGN outbursts, must have been transported after the last major epoch of star formation, when contributions of SNIi to the chemical budget of the galactic gas became negligible. Secondly, the SN Ia enrichment must have remained approximately constant in time relative to the enrichment by stellar winds.

We note that Owen et al. (2000) estimate the age of the outer radio halo between 96 and 150 Myr/ $P_{44}$ , where  $P_{44}$  is the total jet power in  $10^{44}$  erg/s. If the total jet power is around  $1-3 \times 10^{44}$  erg/s, we would obtain consistent values with the enrichment times of  $\sim 30-110$  Myr obtained above. Thus, it is possible that both the outer and the inner radio halos generated similar

outbursts  $\sim 3\text{--}11 \times 10^7$  and  $\sim 10^7$  years ago respectively, transporting metal-rich gas outwards, while between the two outbursts the metals could accumulate in the center of the gas halo. Less violent outbursts which do not have such large impact in the distribution of metals in the gas halo could have occurred between these two events, as is suggested by the multiple shocks found in the Chandra data by Forman et al. (2007).

Note that if some of the uplifted metal-rich gas fell back to where it originated between outbursts, the time interval between two such outbursts could be shorter since one would not have to wait for all the extra metals observed in the cool gas to be produced from stellar winds and supernovae.

### 3.7 Constraints on possible non-thermal emission

In Chapter 2, we suggested the presence of non-thermal pressure support by relativistic electrons in the X-ray arms of M87. We performed a more detailed analysis to check for spectral signatures of inverse Compton (IC) scattering of the microwave background photons on the relativistic electrons in the M87 gas halo. For this, we chose 7 annuli between 1 and 9 arcminutes and divided each of these into 4 sectors containing the E arm, the SW arm, and the NW and SE regions between the arms. The sectors containing the arms were fitted with a two-temperature *vmekal* model and a power-law while the NW and SE regions were fitted with a single-temperature *vmekal* model plus a power-law. Our extraction regions can be seen in Fig. 3.17.

We find that the fit cannot constrain the power-law index in any of the extraction regions, therefore we fixed it to 1.7, which is consistent with the number distribution of relativistic electrons in our Galaxy. With a fixed power-law index, we find that the normalization of the power-law component is more than  $3\sigma$  significant everywhere except in the 7th ring of the SW arm sector. The flux of the power-law component in all regions is a factor of more than 10 above the cosmic X-ray background (CXB) found by De Luca & Molendi (2004) in the 2-10 keV band and a factor of more than 5 above the same CXB model in the 7-10 keV band. However, we cannot rule out the possibility that the power-law component is significant simply because it compensates for calibration or spectral model inaccuracies, therefore we cannot confirm it as a detection of IC emission from the M87 halo, but interpret our results rather as an upper limit of the IC flux that is consistent with the data.

For the upper limit on the non-thermal pressure, we use (Lieu et al. 1999)

$$p = \frac{E}{3V} \quad \text{where} \quad (3.24)$$

$$E = 8 \times 10^{61} L_{42} \times \frac{3 - \mu}{2 - \mu} \times \frac{\gamma_{\max}^{2-\mu} - \gamma_{\min}^{2-\mu}}{\gamma_{\max}^{3-\mu} - \gamma_{\min}^{3-\mu}} \quad \text{and} \quad (3.25)$$

$$V = \frac{2\pi}{3} (1 - \cos \theta) (R_{\max}^3 - R_{\min}^3). \quad (3.26)$$

$L_{42}$  is the luminosity of the non-thermal emission between  $\gamma_{\max}$  and  $\gamma_{\min}$  in units of  $10^{42}$  ergs,  $\mu$  is the index of the electron number distribution which is related to the photon index of our power-law model as  $\mu = 2\Gamma - 1 = 2.4$ ,  $\gamma_{\min}$  and  $\gamma_{\max}$  are the minimum and maximum Lorentz factors

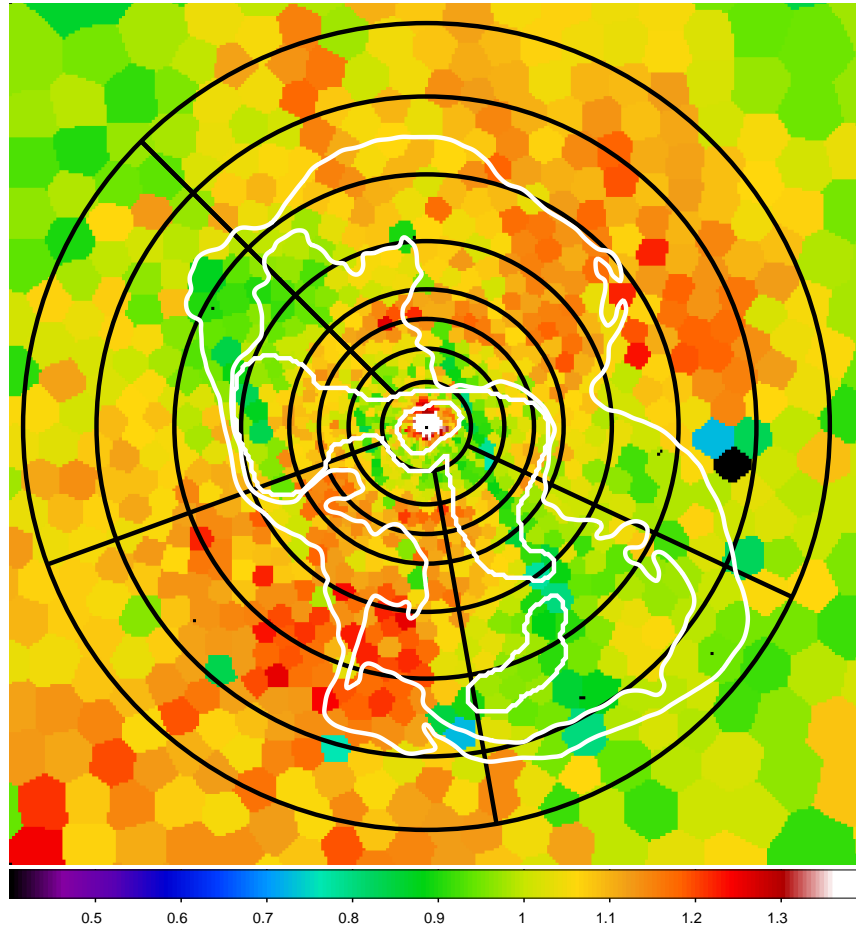


Figure 3.17: Regions for spectral extraction used to test the presence of a power-law component (in black) overlotted on the map of the gas pressure deviations from radial symmetry obtained in Chapter 2. 90cm radio contours are also overlotted in white.

of the electrons contributing to the IC emission,  $V$  is the volume of a spherical shell with half-opening angle  $\theta$  and minimum and maximum radii  $R_{\min}$  and  $R_{\max}$ . We extrapolated our power-law luminosity to include IC scattering by electrons with Lorentz factors between  $\gamma_{\min} = 300$  and  $\gamma_{\max} = 10000$  and find 90% confidence upper limits on the non-thermal pressure as presented in Table 3.5. Note that the pressure calculated in this way is only due to the relativistic electrons, and that relativistic ions may give rise to additional non-thermal pressure up to 30 times higher than that of the electrons. We also computed the thermal pressure as  $p = (1 + 1/f_{ei})n_e kT$  with  $n_e$  given by Eqn. 3.10 in order to present also the relative contribution of the non-thermal pressure to the total (thermal+non-thermal) pressure in Table 3.5.

The upper limits presented in Table 3.5 are consistent with the contribution of the non-thermal pressure of 5-10% suggested in the previous chapter. However, from these upper limits no difference between the arm and off-arm regions can be seen, suggesting that perhaps at least partly the

Table 3.5: 90% confidence level upper limits on the non-thermal pressure (in  $10^{-11}$  dyn/cm<sup>2</sup> and in brackets as percentage of the total pressure).

$r_{\text{mean}}$ (arcmin)	NW	SE	E arm	SW arm
1.38	7.4 (31.5)	27.6 (54.4)	18.2 (40.9)	19.2 (40.5)
2.09	3.2 (19.8)	7.9 (30.1)	6.7 (25.7)	8.5 (32.2)
2.75	1.7 (14.1)	2.8 (16.5)	4.5 (22.6)	2.3 (13.4)
3.63	0.85 (9.4)	1.2 (10.3)	2.1(17.3)	2.1(15.9)
4.92	0.68 (9.9)	0.50 (5.5)	1.1 (12.6)	1.3 (13.6)
6.55	0.22 (4.4)	0.42 (6.1)	0.53 (7.5)	0.84 (11.3)
8.25	0.14 (3.5)	0.22 (4.1)	0.31 (5.7)	0.26 (4.5)

normalization of the power-law is determined by calibration uncertainties. The high contribution of the power-law in the inner regions is probably due to the central AGN, which was very bright during this observation and could influence the spectrum out to larger radii due to the tail of the XMM PSF.

We also used our upper limits on the power-law flux, assuming it is due to IC emission, to determine the lower limits on the magnetic field strength, which can be obtained from the equation (Sarazin 1986)

$$\frac{f_x}{f_r} \left( \frac{\nu_x}{\nu_r} \right)^{\alpha_x} = \frac{2.47 \times 10^{-19} T_r^3 b(\mu)}{B a(\mu)} \times \left( \frac{4960 T_r}{B} \right)^{\alpha_x} \quad (3.27)$$

where  $a(\mu)$  and  $b(\mu)$  are unitless functions of  $\mu$  only, and for our case  $\mu = 2.4$ ,  $a = 0.086$  and  $b = 7.0$ ,  $\alpha_x = (\mu - 1)/2$  is the X-ray spectral index,  $T_r$  is the temperature of the microwave background radiation (2.73 K),  $B$  is the magnetic field strength,  $f_x$  is the X-ray flux density at frequency  $\nu_x$  in ergs/s/cm<sup>2</sup>/Hz and  $f_r$  is the radio flux density at frequency  $\nu_r$ . We used the radio map of Owen et al. (2000) at 90 cm ( $\nu_r=327$  MHz) and chose to calculate the X-ray flux at 6 keV by dividing the 5 - 7 keV power-law flux by the corresponding bandwidth in Hz. Our lower limits on the magnetic field strength  $B$  are summarized in Table 3.6. We could only determine the values for  $B$  in the first 6 rings (5 for the E arm) because the other regions were outside the radio map.

Interestingly, we do find more stringent lower limits on the magnetic field in the X-ray arms, these being the only regions where our data require magnetic fields stronger than 1  $\mu$ G. However, as these values are only lower limits, we cannot draw definitive conclusions based on this fact.

Assuming equipartition, Owen et al. (2000) find B-field strengths on the order of 7 - 10  $\mu$ G, which are consistent with our lower limits. However, in cluster cores, where the particles and magnetic fields have different origins and evolutionary histories, the validity of the equipartition condition is not obvious. To measure a magnetic field of 10  $\mu$ G using X-ray observations would require the ability to determine with significance a power-law flux 50 times lower than our upper limit, which, within the current calibration accuracies of  $\sim 10\%$  is still out of reach. Using the

Table 3.6: 90% confidence level lower limits on the magnetic field strength ( $\mu\text{G}$ ). The sixth ring in the E arm was outside the radio map

$r_{mean}$ (arcmin)	NW	SE	E arm	SW arm
1.375	0.53	0.31	0.51	0.65
2.085	0.62	0.48	0.77	0.94
2.750	0.56	0.64	0.96	1.40
3.625	0.60	0.78	1.26	1.09
4.920	0.47	0.82	0.52	1.16
6.545	0.29	0.52	-	1.20

Faraday rotation of the halo radio source in M87, Dennison (1980) finds a magnetic field in the halo of  $2.5 \mu\text{G}$ . While the magnetic field deduced using the Faraday rotation measure is the average along the line of sight of the product of the magnetic field and the gas density, the lower limit of the magnetic field determined here depends on the volume average of the relativistic electron density and on the square of the magnetic field over the emitting region. The fields determined using these two methods can be quite different, and as shown by Goldshmidt & Rephaeli (1993) the magnetic field determined using the radio and IC X-ray flux densities is in general smaller than the value determined using the Faraday rotation measure.

Sanders et al. (2005) found a non-thermal X-ray emission component in the core of the Perseus cluster extending to a radius of  $\sim 75$  kpc. Assuming this emission to be due to IC scattering of the cosmic microwave background and infrared emission from NGC 1275, they mapped the magnetic field in the core of the cluster. Within the radius of  $\sim 10$  kpc they found a magnetic field between  $0.5\text{--}3 \mu\text{G}$ , while at larger radii their inferred magnetic field decreased to a value of  $\sim 0.1 \mu\text{G}$ . The higher values in the core are mostly consistent with the lower limits found in the core of M87, but the inferred magnetic field at larger radii is significantly smaller than the lower limits we found at similar radii in M87.

For the radio relic in Coma, combining the radio data with XMM-Newton observations, Ferretti & Neumann (2006) found a lower limit on the magnetic field of  $1.05 \mu\text{G}$ , which is consistent with our lower limits found for the radio arms. The deduced magnetic field in Coma based on the detection of tails of hard X-ray emission by BeppoSAX (Fusco-Femiano et al. 2004) is  $\sim 0.2 \mu\text{G}$ . However, the cluster region probed by the large field of view of the BeppoSAX PDS is much larger than the core of Virgo investigated in this work.

### 3.8 Conclusions

We used deep XMM-Newton observations of the M87 halo to characterize the spatially resolved temperature structure and the chemical composition of the multi-temperature gas associated with the inner radio lobes. We found that:

- Compared to a simple two-temperature fit, we obtain a better and more physical description of the spectra using a model which involves a continuous range of temperatures in each spatial bin. The range of temperatures of the multiphase gas spans between  $\sim 0.6\text{--}3.2$  keV. The cooling time of this gas is longer than the age of the lobes, indicating that no significant amounts of gas cooled out from the temperature domain observable in X-rays. If the multiphase gas is distributed in many small spherical blobs with typical blob sizes of 0.1 kpc, similar to the widths of the filaments seen in the Chandra images (Forman et al. 2007), the thermal conduction must be suppressed by a factor of  $\sim 30\text{--}100$ . Such suppression may be provided by the magnetic fields.
- We find a correlation between the amount of gas cooler than 1.5 keV and the metallicity, indicating that the cool gas is more metal-rich than the ambient halo. Extrapolating the linear fit between the cool gas fraction and Fe abundance, we estimate the Fe abundance of the cool gas to  $\sim 2.2$  solar. This suggests the key role of the AGN in transporting heavy elements into the intracluster medium by uplifting cool, metal-rich gas from the galaxy. The abundance ratios of O/Si/S/Fe in and outside the X-ray arms are similar, indicating that the metals outside the multi-temperature region, which were (according to our model) uplifted from the galaxy by previous AGN outbursts, must have been transported after the last major epoch of star formation, when contributions of SNII to the chemical budget of the galactic gas became negligible.
- We estimate the mass of the gas with a temperature below 1.5 keV (the smallest value in the deprojected profile of the hot M87 halo) to be about  $5 \times 10^8 M_{\odot}$ . Its chemical composition indicates that it originates from a mixture of ICM and stellar mass loss enriched with Type Ia supernova products. The amount of mass from stellar winds and SNeIa represents 15–50% of the total mass of uplifted gas. The time required to produce the observed metals in this gas is  $\approx 30\text{--}110$  Myr, suggesting that the uplift of cool gas by AGN radio bubbles is a relatively rare event.
- We put upper limits on possible non-thermal X-ray emission from M87, and combining it with the 90 cm radio maps, we put lower limits of around 0.5–1.0  $\mu\text{G}$  on the magnetic field strength.

### Acknowledgements

We would like to thank E. Churazov and A. Baldi for very helpful discussions. We also thank an anonymous referee for constructive suggestions. We acknowledge the support by the DFG grant BR 2026/3 within the Priority Programme "Witnesses of Cosmic History". NW acknowledges the support by the Marie Curie EARA Early Stage Training visiting fellowship. AF acknowledges support by NASA grants NNX06AE79G, NNG05GM50G and NNG05GH40G, as well as grant 50 OR 0207 from BMBF/DLR. The XMM-Newton project is an ESA Science Mission with instruments and contributions directly funded by ESA Member States and the USA (NASA). The XMM-Newton project is supported by the Bundesministerium für Wirtschaft und Technologie/Deutsches Zentrum für Luft- und Raumfahrt (BMWi/DLR, FKZ 50 OX0001), the Max Planck

Society, and also by PPARC, CEA, CNES, and ASI. The Netherlands Institute for Space Research (SRON) is supported financially by NWO, the Netherlands Organization for Scientific Research.

## Chapter 4

# Chemical enrichment in the cluster of galaxies Hydra A

*A. Simionescu, N. Werner, H. Böhringer, J. S. Kaastra, A. Finoguenov, M. Brüggen & P. E. J. Nulsen*

A&A, **493** (2009), 409

### Abstract

We analyzed global properties, radial profiles, and 2D maps of the metal abundances and temperature in the cool core cluster of galaxies Hydra A using a deep  $\sim 120$  ks XMM-Newton exposure. The best fit among the available spectral models is provided by a Gaussian distribution of the emission measure (*gdem*). We can accurately determine abundances for 7 elements in the cluster core with EPIC (O, Si, S, Ar, Ca, Fe, Ni) and 3 elements (O, Ne, Fe) with RGS. The *gdem* model gives lower Fe abundances than a single-temperature model. Based on this, we explain why simulations show that the best-fit Fe abundance in clusters with intermediate temperatures is overestimated. The abundance profiles for Fe, Si, S, but also O are centrally peaked. Combining the Hydra A results with 5 other clusters for which detailed chemical abundance studies are available, we find a significant decrease in O with radius, while the increase in the O/Fe ratio with radius is small within  $0.1 r_{200}$ , where the O abundances can be accurately determined, with  $d(\text{O}/\text{Fe})/d(\log_{10} r/r_{200}) = 0.25 \pm 0.09$ . We compare the observed abundance ratios with the mixing of various supernova type Ia and core-collapse yield models in different relative amounts. Producing the estimated O, Si, and S peaks in Hydra A requires either the amount of metals ejected by stellar winds to be 3–8 times higher than predicted by available models or the initial enrichment by core-collapse supernovae in the protocluster phase not to be as well mixed on large scales as previously thought. The temperature map shows cooler gas extending in arm-like structures towards the north and south. These structures, and especially the northern one, appear to be richer in metals than the ambient medium and spatially correlated with the large-scale radio lobes. With different sets of assumptions, we estimate the mass of cool gas, which was probably uplifted by buoyant bubbles of relativistic plasma produced by the AGN, to  $1.6 - 6.1 \times 10^9 M_{\odot}$ , and the energy associated with this uplift to  $3.3 - 12.5 \times 10^{58}$  ergs. The best

estimate of the mass of Fe uplifted together with the cool gas is  $1.7 \times 10^7 M_{\odot}$ , 15% of the total mass of Fe in the central 0.5' region.

## 4.1 Introduction

Clusters of galaxies provide a unique environment for elemental abundance measurements and for the study of the chemical enrichment history of the Universe, because their large potential wells retain all the metals produced by the member galaxies. Of particular interest are clusters of galaxies showing a centrally peaked surface brightness distribution and a cool core, whose spectra are often richer in emission lines because of the lower central temperatures. In addition, these “cool-core” clusters have been shown to exhibit a central peak in the abundance distribution of several elements, in particular iron (e.g. De Grandi & Molendi 2001) and other metals produced by type Ia supernovae (SN Ia), which led to the conclusion that the central excess is most probably due to enrichment by SN Ia in the central dominant galaxies (for a review, see Werner et al. 2008, and references therein).

Cooling-core clusters are furthermore in the limelight because of the so-called “cooling-flow problem”: the high surface brightness in the central peak implies a high density and a short cooling time, however the observed rate of cooling of the central gas is often orders of magnitude below what is expected in the absence of any heat sources (for a review, see Peterson & Fabian 2006). As a solution, it has been proposed that active galactic nuclei (AGN) in the central dominant galaxies can provide enough energy to the central gas to balance the cooling, since signs of energetic interaction between the AGN radio plasma and the intra-cluster medium (ICM) have been observed in many systems (for a recent review, see McNamara & Nulsen 2007). Recently, the AGN-ICM interaction has also been shown, by theoretical models (Rebusco et al. 2006), hydrodynamic simulations (Roediger et al. 2007) and observations (Simionescu et al. 2008) to be a main mechanism for transporting the metals produced in the central galaxy into the ICM.

Hydra A was one of the first cooling-core clusters in which a displacement of X-ray gas in the center by radio lobes from the central AGN was found (McNamara et al. 2000) and it is still one of the most dramatic examples of AGN interaction (David et al. 2001; Nulsen et al. 2002, 2005). In a deeper Chandra observation of the cluster, a sharp X-ray surface brightness edge was found at radii between 4.3 – 6' (200 – 300 kpc), interpreted as a shock wave caused by an AGN outburst with an estimated total energy of  $10^{61}$  erg (Nulsen et al. 2005), which is sufficient to balance radiative cooling for at least several  $10^8$  yrs. Further features besides the shock and the inner cavities are a  $\sim 60$  kpc long filament running from the inner cavities outwards, that may be reminiscent of the “X-ray arms” in M87 (e.g. Feigelson et al. 1987; Böhringer et al. 1995; Belsole et al. 2001; Forman et al. 2007), and surface brightness depressions in the outer region inside the shock front, which coincide with the outer radio lobes (Wise et al. 2007). The relatively low temperature ( $T_X \sim 3.1 - 3.7$  keV, David et al. 2001) implies X-ray spectra rich in emission lines providing good spectroscopic diagnostics.

The goal of this chapter is twofold. Firstly, we aim to study the abundances, abundance ratios, and radial trends for different chemical elements. This can reveal clues about the chemical

enrichment history of Hydra A and, by comparison with previous results from deep pointings of other nearby bright clusters, can broaden our overall understanding of the origin and distribution of metals in clusters of galaxies. Secondly, we investigate a two-dimensional metallicity map to determine what influence an AGN outburst as violent as the one in Hydra A can have on the distribution of chemical elements in the ICM.

Throughout the paper, we assume  $H_0 = 70 \text{ km s}^{-1} \text{ Mpc}^{-1}$ ,  $\Omega_\Lambda = 0.73$ , and  $\Omega_M = 0.27$ . At the redshift of Hydra A ( $z = 0.0538$ ),  $1''$  corresponds to 1.05 kpc. Unless otherwise stated, the elemental abundances are given with respect to the proto-Solar values of Lodders (2003), the errors are at the  $1\sigma$  level, and upper limits at the  $2\sigma$  level. The recent solar abundance determinations by Lodders (2003) give significantly lower abundances of oxygen, neon and iron than those measured by Anders & Grevesse (1989). Use of these new determinations affects only the units with respect to which we present the elemental abundances in our paper; the actual measured values can be reconstructed by multiplication of the given values with the solar normalizations. For a compilation of these normalizations for different commonly used abundance determinations, see the review of Werner et al. (2008).

## 4.2 Observation and data analysis

### 4.2.1 EPIC analysis

Hydra A was first observed with XMM-Newton on December 8th, 2000, for 32.6 kiloseconds (ks). A subsequent 123 ks observation was performed on May 11th, 2007. Since the second observation is significantly deeper and large parts of the first observation were affected by soft proton flares, we will focus in this work primarily on the second observation. We extracted a lightcurve for each of the three detectors separately and excluded the time periods in the observation when the count rate deviated from the mean by more than  $3\sigma$  in order to remove flaring from soft protons (Pratt & Arnaud 2002). After this cleaning, the net effective exposure is  $\sim 62$  ks for pn,  $\sim 81$  ks for MOS1, and  $\sim 85$  ks for MOS2. We furthermore excluded CCD 5 of MOS2 from our analysis due to its anomalously high flux in the soft band during the observation (see Snowden et al. 2008). For data reduction we used the 7.1.0 version of the XMM-Newton Science Analysis System (SAS); the standard analysis methods using this software are described in e.g. Watson et al. (2001).

For the background subtraction, we used a combination of blank-sky maps from which point sources have been excised (Read & Ponman 2003; Carter & Read 2007) and closed-filter observations. This is necessary because the instrumental background level of XMM-Newton is variable and increases with time. Both the blank-sky and the closed filter observations were transposed to a position in the sky corresponding to the orientation of XMM-Newton during our observation. We calculated the count rates in the hard energy band (10.–12. keV for MOS, 12.–14. keV for pn) outside of the field of view (OoFoV) for our observation, for the blank-sky maps and for the closed filter observations. These count rates are a good indicator for the level of instrumental background in each data set, since no photons from real X-ray sources should be recorded outside the field of view. For each detector we then added to the corresponding

blank sky background set a fraction of the closed filter data designed to compensate for the difference between the OoFoV hard-band count rate in the observation and in the blank sky data. We note that simply scaling up the blank sky data to match the observed OoFoV hard-band count rate would implicitly also scale up the cosmic X-ray background (CXB) component contained in these blank sky maps, leading to an overestimation of the total background. We compared the blank sky background spectra of Read & Ponman (2003) and Carter & Read (2007) with the current observation in a 10–14′ annulus. We find a good agreement both in the soft (0.35–1 keV) and hard (5–10 keV) bands, while between 1 and 5 keV the spectrum from the observation shows an excess consistent with residual cluster emission with a temperature of around 2 keV. The best agreement with the 10–14′ spectra, both in the soft and hard bands, is provided by the Read & Ponman (2003) background for the MOS detector and the Carter & Read (2007) background for the pn detector. Consequently, we used these respective blank sky fields to estimate our background.

Out-of-time events were subtracted from the PN data using the standard SAS prescription for the extended full frame mode.

#### 4.2.2 RGS analysis

We extract the RGS spectra following the method described by Tamura et al. (2001). We model the background using the standard background model available in SAS (`rgsbkgmodel`, González-Riestra 2004). The cluster spectra are extracted from a region which is 3′ wide in the cross-dispersion direction of the instrument.

The line emission observed with the RGS from extended sources is broadened by the spatial extent of the source along the dispersion direction. In order to account for the line broadening in the spectral modelling, we convolve the line spread function (`lsf`) model with the surface brightness profile of the source along the dispersion direction. We derive the surface brightness profile from the EPIC/MOS1 image in the 0.8–1.4 keV band. Because the radial profile of an ion producing an observed spectral line can be different from the radial surface brightness profile in the broad band, we multiply the line profile with a scale parameter  $s$ , which is left as a free parameter in the spectral fit. The scale parameter  $s$  is the ratio of the observed `lsf` width and the width of the `lsf` model convolved with the surface brightness profile. For a flat radial distribution of the line emitting ions, the scale parameter is  $s = 1$ .

#### 4.2.3 Spectral modeling

We use the SPEX package (Kaastra et al. 1996) to model our spectra with a plasma model in collisional ionization equilibrium (`mekal`). We note that the `mekal` model implemented in SPEX has a more updated line catalog compared to that used by XSPEC; however, SPEX does not support any other plasma models, notably `apec`. Several differential emission measure models which include contribution from gas with a range of different temperatures, rather than a single temperature approximation, are available in SPEX. Throughout the paper we will mainly use a Gaussian distribution of the emission measure (`gdem`) around the best-fit average temperature,

of the form

$$\frac{dY}{dx} = \frac{Y_0}{\sqrt{2\pi}\sigma_T} e^{-(x-x_0)^2/2\sigma_T^2}, \quad (4.1)$$

where  $Y_0$  is the total, integrated emission measure ( $Y_0 = \int n_e n_H dV$ ),  $x \equiv \log T$  and  $x_0 \equiv \log T_0$  with  $T_0$  the average temperature of the plasma. Sect. 4.4.1 gives a detailed explanation why this is the most appropriate available multi-temperature model for the data.

Unless otherwise stated, the Galactic absorption column density was fixed to  $N_H = 4.8 \times 10^{20} \text{ cm}^{-2}$ , the average value from the two available H I surveys: the Leiden/Argentine/Bonn (LAB) Survey of Galactic H I (Kalberla et al. 2005,  $N_H = 4.68 \times 10^{20} \text{ cm}^{-2}$ ) and the H I data by Dickey & Lockman (1990) ( $N_H = 4.90 \times 10^{20} \text{ cm}^{-2}$ ). Point sources identified using the X-ray images are excluded from the spectral analysis. The spectra obtained by MOS1, MOS2 and pn are fitted simultaneously with their relative normalizations left as free parameters. To account for possible gain shifts, the redshift was left as a free parameter in the initial fit and fixed to its best-fit value when estimating the errors.

The global spectrum extracted from a circular extraction region with a radius of  $3'$  (Sect. 4.3.1) is fitted in the 0.35–10 keV band. Because of the low number of counts and the high background above 7 keV, the spectra extracted from all other regions are fitted in the 0.35–7 keV band. The spectra extracted for the analysis of the global properties of the cluster and for the radial profiles are binned to the optimal bin size using the “obin” command of SPEX. This command rebins the data to at least 1/3 of the FWHM of the instrument depending on the count rate at the given energy. The spectra extracted for constructing 2D maps of the spectral properties of the cluster have much lower statistics and are consequently simply binned with a minimum of 30 counts per bin.

We fitted the normalization, temperature and, where the statistics allowed, the abundances of O, Ne, Mg, Si, S, Ar, Ca, Fe, and Ni as free parameters. The abundances of the other elements heavier than He are fixed to 0.5 of the Solar value.

Due to the high photon statistics of this deep observation, our best fit reduced  $\chi^2$ s are sensitive to calibration problems and to the differences between the individual EPIC detectors. To account for this, we include 3% systematic errors over the entire energy band used for fitting the global properties of the cluster and the radial profiles. We usually obtain good ( $< 2\sigma$ ) agreement between the different detectors, the only notable exception is mentioned in Sect. 4.3.2.

In addition, to insure an optimal determination of element abundances, it is crucial to accurately fit the continuum around emission lines. This is not guaranteed by available emission measure model distributions, which are always a simplification of the true thermal structure in any given spectral extraction region. It is necessary therefore, after determining the best average temperature or temperature distribution using the full spectral band, to fix the thermal structure parameters and fit the elemental abundances in narrower bands around the emission lines of the respective elements, allowing the spectrum normalization to vary and thereby correct for small inaccuracies in the best determination of the continuum in those narrow energy bands. We accordingly fitted the Si, S, Ar, and Ca metallicities in the 1.5–5. keV energy band, and the O abundance in the 0.35–1.5 keV band. Unless otherwise stated, we report the best-fit Fe abundance using the full energy band (both Fe-L and Fe-K lines).

Table 4.1: Fit results for the EPIC data using a *gdem* model.  $\sigma_T$  is the width of the Gaussian temperature distribution. All abundances are relative to the proto-Solar units of Lodders (2003).

Extraction region	0–3′	3–8′
$Y$ ( $10^{66} \text{ cm}^{-3}$ )	$24.85 \pm 0.09$	$9.27 \pm 0.05$
$kT$ (keV)	$3.42 \pm 0.01$	$3.65 \pm 0.03$
$\sigma_T$ ( $\log T$ )	$0.251 \pm 0.006$	$0.210 \pm 0.017$
O/Fe	$0.85 \pm 0.09$	–
Si/Fe	$0.65 \pm 0.05$	$0.45 \pm 0.07$
S/Fe	$0.58 \pm 0.05$	$0.30 \pm 0.10$
Ar/Fe	$0.48 \pm 0.14$	–
Ca/Fe	$1.28 \pm 0.16$	$0.47 \pm 0.33$
Fe	$0.445 \pm 0.007$	$0.324 \pm 0.013$
Ni/Fe	$1.35 \pm 0.20$	–
$\chi^2$ / d.o.f.	1449 / 1211	985 / 972

The Ne abundance could not be constrained with the EPIC spectra because the Ne x line lies in the Fe-L complex where the EPIC cameras cannot resolve the individual lines, thus a high Ne abundance can be confused with a higher contribution of cooler multi-temperature gas (a higher  $\sigma_T$ ) and vice versa. Consequently, the Ne abundance was fixed relative to Fe based on the RGS fit (Sect. 4.3.4). The Mg abundances could not be determined with more than  $3\sigma$  significance in any of the regions. Moreover, as reported by de Plaa et al. (2007), the systematic error in the effective area calibration of EPIC around the Mg energy is so large that the Mg abundance determination cannot be trusted. The Ni abundance was not determined in any of the regions for which the chosen spectral fitting band was 0.35–7 keV, which does not include the energy of the Ni lines. The abundances of Si, S and Fe, on the other hand, can be determined with good accuracy in most regions and, where the surface brightness is sufficiently high, we also obtain reliable O, Ar, Ca and Ni abundance determinations.

## 4.3 Results

### 4.3.1 Global spectra

To characterise the global properties of the cluster and to determine accurate abundance values for as many elements as possible, we extract spectra from two large spatial regions: a circular region with a radius of 3′ centered on the cluster core and an annulus with an inner radius of 3′ and outer radius of 8′. This should insure good statistics in both regions, while keeping the number of source counts in the outer annulus well over the background level.

The best-fit width of the *gdem* distribution,  $\sigma_T$ , as well as all other best-fit parameters are shown in Table 4.1. The  $\sigma_T$ 's determined from our fits are significantly larger than zero both

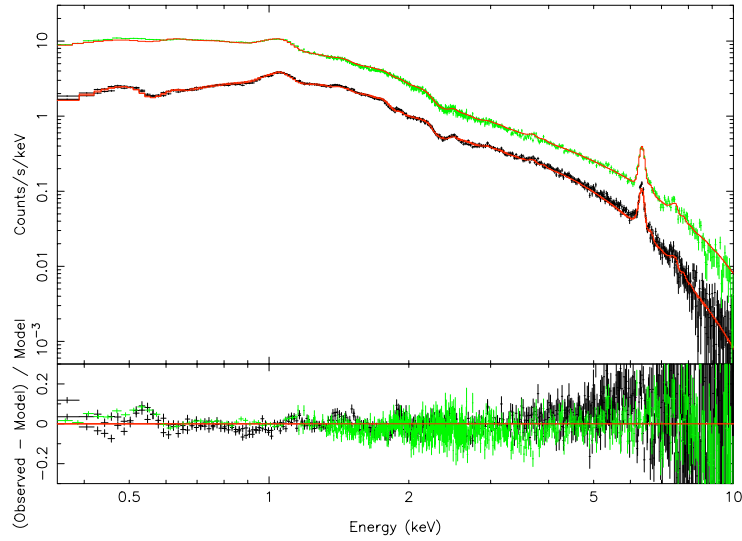


Figure 4.1: The EPIC spectrum of the central 3' and fit residuals with respect to the best-fit Gaussian emission measure distribution model. Data points from pn are shown in green, MOS in black, and the best-fit model in red.

in the inner and outer annuli and the values are similar to those found by de Plaa et al. (2006) in Sérsic 159-03. A spectrum of the central 3' region and the best-fit model are shown in Fig. 4.1. It can be seen that the *gdem* model provides a good fit to both Fe-L and Fe-K lines, which a single temperature model did not achieve. For a more detailed discussion about the effects of the presence of such a multi-temperature structure on the spectral properties, see Sect. 4.4.1.

The deep observation of Hydra A in combination with the large collecting area of XMM-Newton make this one of the best cluster observations for investigating the chemical composition of the intra-cluster medium. The spectrum extracted from the circle with the radius of 3' allows us to determine relatively accurate abundance values for 7 elements including Ar and Ca which have relatively small equivalent widths (see Table 4.1). We note that there is a good agreement between all fit parameters determined using the MOS and pn spectra separately: the largest difference ( $2\sigma$ ) is in determining the Ca abundance. Therefore the effect of calibration uncertainties should be small. The abundances in the cluster core relative to Fe are consistent with the values measured by de Plaa et al. (2007) for a sample of 22 clusters. The absolute abundance values are lower in the outer part of the cluster than in the core. The observed relative abundances with respect to Fe are also lower in the outer part, although the differences are in most cases not significant.

We do not report the O/Fe value in the outskirts, which has a large error and is furthermore uncertain because of the low energy wing of the EPIC response which does not allow us to resolve the O line well and makes its abundance value strongly dependent on calibration uncertainties and on the uncertainties in the modelling of the low energy X-ray foreground, especially in regions of low surface brightness. The equivalent widths of the Ar and Ca are relatively low and the lower statistics in the outer extraction region make the abundance determination for these elements uncertain. Except for Si/Fe and S/Fe these uncertainties make it difficult to draw strong

Table 4.2: Radial profiles obtained by fitting the EPIC data with a *gdem* model. The emission measure  $Y$  was corrected for chip gaps and excluded point sources.

	0–0.5′	0.5–1.0′	1.0–2.0′	2.0–3.0′	3.0–4.0′	4.0–6.0′	6.0–8.0′
$Y$ ( $10^{66} \text{ cm}^{-3}$ )	$5.15 \pm 0.03$	$5.82 \pm 0.03$	$7.25 \pm 0.03$	$5.56 \pm 0.03$	$3.66 \pm 0.02$	$3.74 \pm 0.03$	$1.89 \pm 0.02$
$kT$ (keV)	$3.17 \pm 0.02$	$3.44 \pm 0.02$	$3.41 \pm 0.02$	$3.57 \pm 0.03$	$3.82 \pm 0.04$	$3.60 \pm 0.04$	$3.46 \pm 0.08$
$\sigma_T$ ( $\log T$ )	$0.218 \pm 0.008$	$0.215 \pm 0.011$	$0.246 \pm 0.009$	$0.258 \pm 0.013$	$0.23 \pm 0.02$	$0.23 \pm 0.02$	$0.08 \pm 0.08$
O/Fe	$0.80 \pm 0.09$	$0.77 \pm 0.11$	$0.85 \pm 0.13$	$0.74 \pm 0.16$	$0.59 \pm 0.24$	$< 0.31$	–
Si/Fe	$0.60 \pm 0.06$	$0.67 \pm 0.06$	$0.64 \pm 0.08$	$0.81 \pm 0.13$	$0.52 \pm 0.18$	$0.63 \pm 0.16$	$0.80 \pm 0.33$
S/Fe	$0.65 \pm 0.07$	$0.56 \pm 0.08$	$0.51 \pm 0.10$	$0.74 \pm 0.16$	$0.38 \pm 0.21$	$0.53 \pm 0.22$	$< 0.80$
Ar/Fe	$0.85 \pm 0.18$	$0.54 \pm 0.23$	$0.62 \pm 0.26$	$< 0.57$	$< 0.69$	$< 0.63$	$< 0.65$
Ca/Fe	$1.02 \pm 0.24$	$1.50 \pm 0.27$	$1.82 \pm 0.31$	$1.52 \pm 0.49$	$1.55 \pm 0.70$	$< 0.68$	$< 0.72$
Fe	$0.550 \pm 0.012$	$0.483 \pm 0.013$	$0.392 \pm 0.010$	$0.308 \pm 0.012$	$0.287 \pm 0.016$	$0.323 \pm 0.018$	$0.29 \pm 0.07$
$\chi^2 / \text{d.o.f}$	1388 / 1222	1211 / 1107	1196 / 1067	1025 / 1029	972 / 996	1063 / 1117	1071 / 917

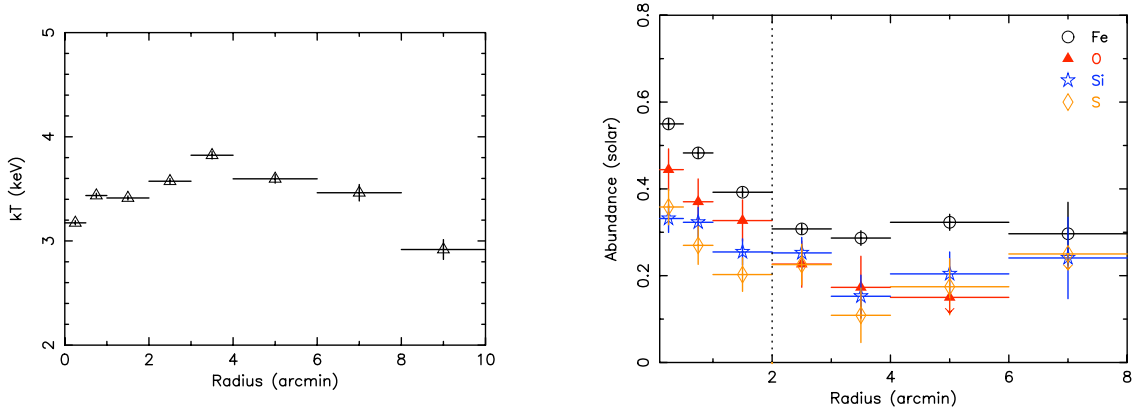


Figure 4.2: *Left panel:* projected radial temperature profile of Hydra A. *Right panel:* radial profiles for four elements with the best determined abundance values. The radius at which the onset of an abundance peak is seen is indicated by a vertical dotted line.  $r_{200}$  (from Reiprich & Böhringer 2002, adapted to  $H_0 = 70 \text{ km s}^{-1} \text{ Mpc}^{-1}$ ) corresponds to  $23.7'$ .

conclusions about the differences in the relative abundances between the inner and outer regions.

### 4.3.2 Radial profiles

We also extracted spectra from 7 circular annuli centered on the cluster core in order to determine average radial temperature and abundance trends. Our results are summarized in Table 4.2.

The upper panel of Fig. 4.2 shows that the radial temperature distribution has a dip in the core of the cluster and is relatively flat from  $1'$  to  $7'$ , with the exception of an elevated value in the  $3\text{--}4'$  bin, which is likely associated with the large-scale shock in Hydra A (Nulsen et al. 2002, 2005). For a study of the thermal structure associated with the shock, see Chapter 5. Beyond  $7'$ , we see the onset of a significant temperature decrease.

The radial distribution of all investigated metal abundances peaks at the core of the cluster

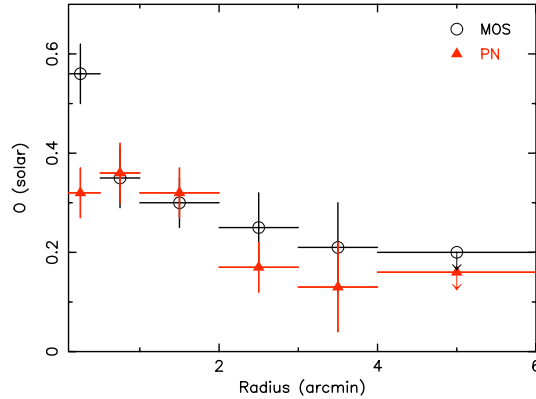


Figure 4.3: Radial profiles for O obtained by fitting spectra from the MOS and pn detectors independently.

(see lower panel of Fig. 4.2). Radial gradients are seen in the distribution of elements which are predominantly produced both by SN Ia (e.g. iron) and by core-collapse supernovae (SN<sub>CC</sub>, e.g. oxygen). Again, the most robustly determined abundances are those for Fe, Si, and S, but in the inner regions (within  $\sim 3'$ ) where the O abundance determination is less sensitive to background subtraction, its value is also quite accurate.

In the last bin, uncertainties in determining the background at low energies become important. Thus, we do not report the O abundance, which is the most affected by such uncertainties, and present in Table 4.2 the Fe abundance determined based on Fe-K only. The best-fit Fe abundance based on Fe-L and Fe-K combined would have been  $0.43 \pm 0.03$  solar (consistent both for MOS and pn), which is unlikely at such a large radius from the cluster center.

To confirm the presence of a peak in the distribution of the O abundance which, as discussed above, is difficult to determine, we also checked the results from the MOS and pn detectors separately. The two obtained O abundance profiles are plotted in Fig. 4.3. We find a discrepancy in the O determination from the two different detectors in the most central bin, but beyond this the agreement is very good and it is clear that in both detectors the O abundances in the inner 3 radial bins (central  $2'$ ) are systematically higher than outside the  $2'$  radius, indicating that the peaked O distribution is indeed real. The discrepancy in the central bin might stem from calibration problems at this particular position of the detector, causing somewhat different values of  $\sigma_T$  (0.19 for MOS and 0.245 for pn) and different abundances. At other detector coordinates, the results agree well.

David et al. (2001) obtain from Chandra data a temperature profile with a dip in the center down to 3.1 keV, increasing up to 3.8–4.0 keV at  $3.4'$ , in very good agreement with what we find in Fig. 4.2. Our Fe profile is also roughly in agreement with that obtained from Chandra data, showing the most pronounced peak in the inner  $\sim 90$ – $150$  kpc ( $1.5$ – $2.5'$ ). However, the XMM-Newton data gives much lower Si abundances, and does not confirm the very high Si/Fe ratio obtained previously by David et al. (2001). While the deprojection used for the Chandra analysis

could account for relatively higher abundances of both Si and Fe compared to our projected radial profiles, it would not explain the discrepancy in the Si to Fe abundance ratios.

### 4.3.3 2D spectral properties

To produce two-dimensional maps of the temperature and abundance distribution in the cluster, we divided our observation into spatial bins with a fixed minimum number of counts employing an adaptive binning method based on weighted Voronoi tessellations (Diehl & Statler 2006), which is a generalization of the algorithm presented in Cappellari & Copin (2003). The advantage of this algorithm is that it produces smoothly varying bin shapes that are geometrically unbiased and do not introduce artificially-looking structures. We created a background-subtracted count map of the observation in the energy range 0.4-7.0 keV, combining all three EPIC detectors, and binned this map to  $50^2$  counts per bin for generating the temperature map and  $150^2$  counts per bin for generating an abundance map, which requires higher statistics. The binning to  $50^2$  counts was constrained to follow the large-scale radio lobes seen at 327 MHz (Lane et al. 2004, see white contours in the upper panel of Fig. 4.4), while the  $150^2$ -count bins were constrained to follow the temperature contours shown in black in the upper panel of Fig. 4.4. We furthermore constrained the bins in the central regions (with a high count rate) not to be smaller than the extent of the XMM point-spread function (PSF). Since the statistics do not allow a reliable determination of any abundance except that for Fe, we fixed the O, Ne, Mg, Si, S, Ar, Ca and Ni abundances in the fit relative to Fe by the ratios representative of the global properties in the inner  $3'$ , as presented in Sect. 4.3.1. Also, in the bins with  $50^2$  counts, the statistics do not allow us to fit the spectra with free  $\sigma_T$ . We therefore fixed it to 0.2, a typical value found in the radial profiles in Sect. 4.3.2. We note that fitting the bins for the temperature map with a single temperature model, both with free and fixed  $N_H$ , shows the same structures. In the bins with  $150^2$  counts used to determine the metallicity map, we can obtain best-fit values for  $\sigma_T$ , however these are very uncertain, resulting in a very noisy  $\sigma_T$  map, and almost always in agreement with 0.2 (only one bin out of 80 is more than  $5\sigma$  away from 0.2 and three bins more than  $2.5\sigma$ ). The obtained metallicity maps with  $\sigma_T$  free and fixed to 0.2 are very similar and show the same features. We therefore choose to present the Fe abundance map obtained using  $\sigma_T = 0.2$  in the lower panel of Fig. 4.4.

The temperature map clearly shows cooler gas extending in arm-like structures towards the north and south. The cool gas structure to the north follows well the northern radio lobe, which rises from the cluster core towards the NE and then either bends towards the NW (however, the bend in the cool gas feature is stronger than that of the radio lobe) or extends out into an umbrella/mushroom-shape at the position where the N radio lobe bends. The cool gas towards the south is also most probably associated with the AGN activity, although the feature in the temperature map is oriented at a slightly more easterly angle than the southern radio lobe. The Fe abundance map also shows features extending towards the north and south, in the same direction as the cool gas features, suggesting that the cool gas is more abundant than the surrounding halo. The cool ‘‘arm’’ to the NE is associated with a bright  $1'$  long filament found by Nulsen et al. (2005) using Chandra data.

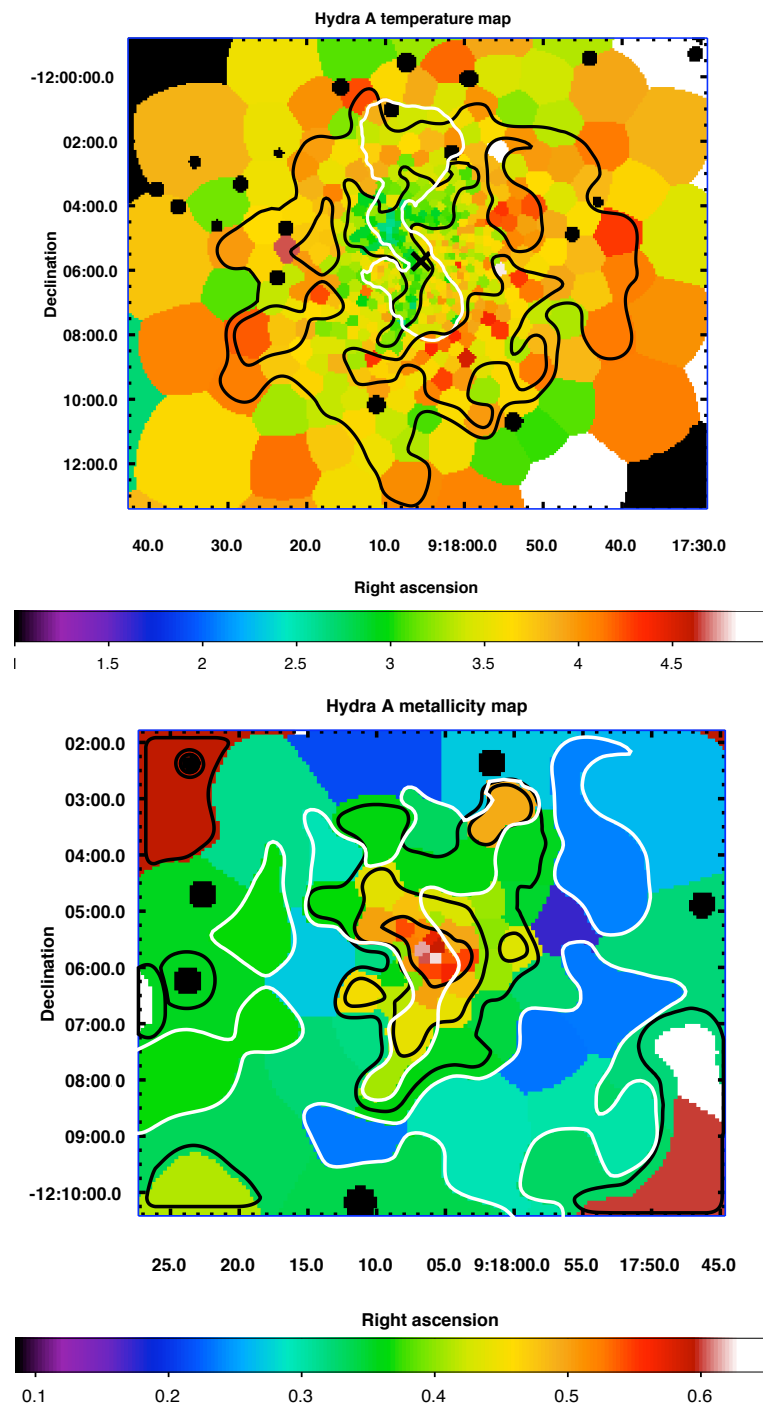


Figure 4.4: *Top panel*: temperature map of the Hydra A cluster, using a minimum of  $50^2$  counts per spatial bin (colorbar units are keV). Temperature contours are over-plotted in black, 327 MHz radio contours from Lane et al. (2004) are over-plotted in white. The cross marks the surface brightness peak associated with the cluster center. *Bottom panel*: Fe abundance map, using a minimum of  $150^2$  counts per spatial bin. Contours are over-plotted in black (colorbar units are solar, Lodders 2003), temperature contours are over-plotted in white. Note that the Fe map is a zoom-in of the region shown in the temperature map.

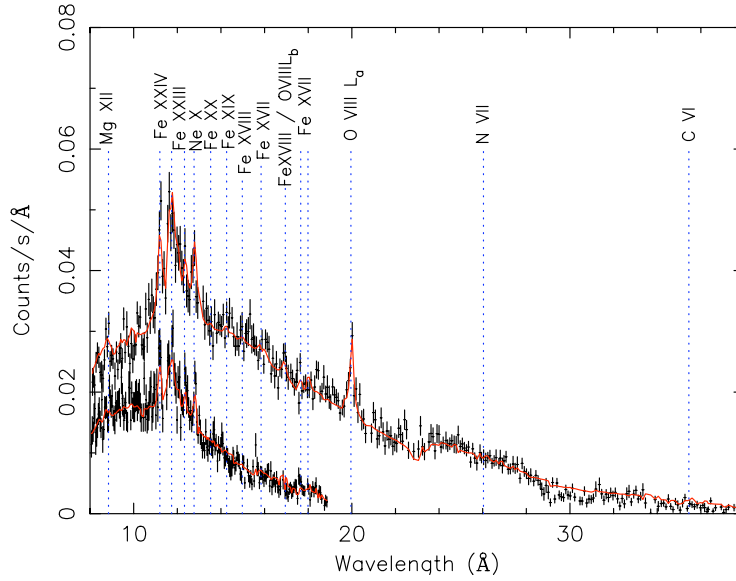


Figure 4.5: Combined RGS 1<sup>st</sup> and 2<sup>nd</sup> order spectrum of Hydra A extracted from a 3' wide strip centered on the core of the cluster. The continuous line represents the fitted model. The Fe xvii–Fe xx lines emitted by cooling gas between the Ne x and O viii lines are not visible in the spectrum.

#### 4.3.4 High resolution spectra

The spectrum from an extraction region which is 3' wide in the cross dispersion direction and effectively  $\sim 10'$  long in the dispersion direction allows us to determine more accurate projected O/Fe and Ne/Fe abundances than possible with EPIC. RGS also allows us to put better constraints on the presence of cooling gas in the cluster core than EPIC by looking at individual lines of the Fe-L complex.

The projected global temperature determined by RGS is  $\sim 1$  keV lower than that determined by EPIC. Similar differences between the mean temperatures determined by EPIC and RGS were found in other clusters (e.g. 2A 0335+096, M 87; Werner et al. 2006b,a). In the case of Hydra A, the reason for this discrepancy could be the fact that the RGS fit is performed in the soft-energy band, which is not sensitive to emission from higher-temperature gas present in the *gdem* model (see Sect. 4.4.1 for a more detailed discussion). To check this, we also performed a fit to the RGS data fixing the temperature to the best-fit EPIC temperature in the central 3' and leaving the  $\sigma_T$  free. We obtain a value for  $\sigma_T$  comparable to the typical results from EPIC. The elemental abundances in this case are considerably higher than for the single-temperature case, and thus in better agreement with the absolute values determined with EPIC. The abundance ratios, on the other hand, are unchanged. The reduced  $\chi^2$  is somewhat worse for the *gdem* fit than for the single temperature fit, which is partly due to the low-temperature wing of the *gdem* approximation not being a perfect description of the temperature structure and partly due to the

Table 4.3: RGS fit results using a  $3'$  wide extraction region centered on the cluster core.

	2T	<i>gdem</i> +1T
$Y_1$ ( $10^{66}$ cm $^{-3}$ )	$21.58 \pm 0.22$	$21.29 \pm 0.25$
$kT_1$ (keV)	$2.37 \pm 0.06$	3.42 (fixed)
$\sigma_{T1}$ (log $T$ )	0.0 (fixed)	$0.19 \pm 0.03$
$Y_2$ ( $10^{66}$ cm $^{-3}$ )	$0.30 \pm 0.06$	$0.26 \pm 0.04$
$kT_2$ (keV)	$0.64 \pm 0.04$	$0.62 \pm 0.04$
O/Fe	$0.74 \pm 0.10$	$0.76 \pm 0.11$
Ne/Fe	$0.73 \pm 0.18$	$0.84 \pm 0.20$
Fe	$0.23 \pm 0.02$	$0.35 \pm 0.03$
Scale $s$	$0.95 \pm 0.14$	$1.01 \pm 0.20$
$\chi^2$ / d.o.f.	1145 / 915	1273 / 915

fact that the RGS/EPIC cross-calibration is not fine-tuned enough and the RGS and EPIC spatial extraction regions are different, such that fixing the temperature to the best-fit EPIC temperature causes a poorer fit.

While in several other cooling cores observed with RGS (M 87, 2A 0335+096, Centaurus; Werner et al. 2006a,b; Sanders et al. 2008), the spectral lines from the intermediate ionization states of Fe (Fe xvii, Fe xviii, Fe xix, Fe xx) are well resolved, we do not observe these lines in Hydra A. However, the spectrum fitted with a single temperature model or with a *gdem* model leaves strong residuals between  $\sim 13$  Å and  $\sim 19$  Å. These residuals can be well fitted, both for the single-temperature and *gdem* models, by adding a cool gas component with  $kT \approx 0.6$  keV and emission measure of  $\approx 1\%$  of the emission measure of the hot gas. The presence of this cool gas is detected with  $5.0$  and  $6.5\sigma$  significance for the single-temperature and *gdem* models, respectively. The fit results shown in Table 4.3 and Fig. 4.5 assume that the abundances of the cooler gas are the same as the abundances of the hot gas.

The best fit O/Fe ratio is consistent with the value determined by EPIC. At the 3 keV temperature of Hydra A, carbon and nitrogen are almost completely ionised and their lines cannot be detected by the RGS.

## 4.4 Discussion

### 4.4.1 Spectral effects of the multi-temperature structure

Throughout this paper, we used a Gaussian distribution of the emission measure around the best-fit average temperature to model our spectra. We will explain in this section why this is necessary, what the implications on the best-fit spectral parameters are, and we will evaluate how accurate the *gdem* approximation is.

Usually, the strongest evidence of the presence of multi-temperature structure is the shape

of the Fe-L complex, which is located at an energy where the effective area of the detectors is high, and whose shape changes drastically with the temperature of the emitting gas, especially for temperatures below  $\sim 2$  keV (e.g. Böhringer et al. 2004). In Hydra A, however, the shape of the Fe-L complex in the EPIC spectrum does not show strong indications of the presence of cooler gas as observed in other cooling core clusters (e.g. Werner et al. 2006b; de Plaa et al. 2006, and Chapter 3). The evidence of a multi-temperature structure in this case lies primarily in the fact that, when fitting spectra with high statistics, it becomes evident that the best-fit temperatures obtained fitting independently the soft (0.35–2 keV) and hard (2–7 keV) energy bands are in disagreement. Moreover, when using the entire energy band, the spectral model cannot simultaneously fit both Fe-L and Fe-K lines adequately. In particular, the Fe-K line in the data shows a shoulder towards higher energies, indicating Fe-K $\beta$  emission which suggests the presence of gas at higher temperatures than the fitted value from the single temperature model.

In Fig. 4.6 we illustrate the difference between the soft and hard-band fits for the central 3' spectrum. The upper panel shows the best-fit single-temperature model in the soft band, which provides a very good fit to the Fe-L complex indicating the lack of a significant amount of cooler gas. The lower panel shows this model extrapolated to the hard band. The clear discrepancy indicates the fact that the best-fit single temperature model from the soft band does not account for the presence of gas at higher temperatures present in the spectrum. For the central 3' spectrum, the best-fit soft-band temperature is  $2.81 \pm 0.05$  keV, while the hard-band temperature is  $3.86 \pm 0.03$  keV, approximately the values spanned by the temperature profile and the 2D maps (Sect. 4.3.2 and 4.3.3). A Gaussian emission measure distribution is one of the simplest models which can account for such a mixing of emission from plasma spanning a wider range of temperatures. Using this model significantly improves the fit ( $\chi^2/\text{d.o.f.}$  1449/1211) with respect to a single temperature model ( $\chi^2/\text{d.o.f.}$  2005/1212).

### Intrinsic multi-temperature structure

The multi-temperature structure can be partly due to the mixing of different regions with slightly different temperatures in the 2D map and partly due to intrinsic multi-temperature structure in each of these regions. To disentangle these two effects, we took the average temperatures and the emission measures in all the Voronoi bins with  $50^2$  counts within a radius of 3' and, assuming the gas in each spatial bin to be single-phase, constructed a total  $dY/dT$  curve, shown in Fig 4.7. We over-plot also the best-fit *gdem* model for the central 3' spectrum. As the figure shows, the shape of the  $dY/dT$  curve due solely to spatial variations in the different bins does also have a Gaussian shape, however it is much narrower than the best-fit value from the *gdem* model (full-width at half maximum of about 1 keV compared to the 4.2 keV corresponding to  $\sigma_T = 0.251$ ). With the statistical errors on  $\sigma_T$  from Table 4.1, the difference is highly significant ( $\approx 35\sigma$ ). Note that hydrodynamic simulations of clusters which have recently undergone energetic events show a similarly wide  $dY/dT$  curve (Rasia et al. 2006) as our best-fit *gdem* model.

Assuming, instead of isothermality, a *gdem* distribution with  $\sigma_T = 0.2$  in each spatial region, we find a significantly better agreement between the total  $dY/dT$  curve constructed from the bins in the temperature map and the best-fit *gdem* model for the central 3' spectrum. Remaining small disagreements could be explained for example by deviations of  $\sigma_T$  from 0.2 in different regions.

However, Fig 4.7 does clearly suggest the need for intrinsic multi-temperature structure in each spatial bin.

According to the best-fit *gdem* model, roughly 9.5% of the total emission measure in the central  $3'$  comes from gas between 0.5–1.5 keV, 10.7% from gas between 1.5–2.0 keV, and 9.2% from gas between 6–8 keV. In part, this intrinsic multi-temperature structure can be due to projection: on one hand, the large-scale shock in Hydra A can produce the hard-tail in the  $dY/dT$  distribution (for more quantitative analysis, see Chapter 5); on the other hand, cool gas in the cluster outskirts can add to the tail at low temperatures. The low density in the outskirts makes it however unlikely that all the cool gas arises from projection alone and suggests the possible presence of denser, unresolved cool gas blobs. To make this statement more quantitative: the observed temperature profile in Hydra A peaks at roughly 3.8 keV (in agreement with the deprojected profile of David et al. 2001 from Chandra data). An average temperature of 2.0 keV thus is a factor 0.53 less than the peak temperature. If we compare for example with the scaled temperature profiles of Vikhlinin et al. (2006), we do not expect the temperature in the outskirts to drop to 0.53 of the peak temperature until around  $r_{500}$ , where little cluster emission is expected. Since we consider projection along a cylinder of  $3'$  radius, the volume does not increase significantly at large radii ( $dV$  converges to  $\pi(3')^2 dr$  for large  $r$  and is larger for smaller  $r$  because of the curvature of the spherical shell with radius  $r$  contained inside the considered cylinder). Thus, unless we have reason to believe in a very small  $dT/dr$  in the outskirts compared to the cluster center, which scaled temperature profiles do not suggest,  $dY/dT = n_e n_H dV/dT \propto n_e^2 dr/dT$  should decrease roughly as the square of the electron density beyond  $\sim 3'$ , where projection effects come into play. According to Vikhlinin et al. (2006), the density drops by a factor of 15 between  $0.23r_{500}$  ( $3'$ ) and  $r_{500}$ , thus the emission measure should decrease by at least a factor of  $\sim 200$ . Clearly, Fig. 4.7 shows that the emission measure around 2 keV is only a factor of a few, as opposed to a factor of a few hundred, below the emission measure from temperatures expected around  $3'$  radius. This shows that projection cannot have an important contribution and that the observed cool gas in the multi-temperature distribution must come from unresolved cool gas blobs in the central parts.

### Comparison with other available multi-temperature models

The *gdem* model provides a significant improvement over a single temperature model, yet the real temperature distribution is probably even more complex, therefore we should test the reliability of the Gaussian approximation.

Unfortunately, other available models except single-temperature and *gdem* are either poorly constrained by the current data set or give unphysical results. A power-law shaped emission measure distribution (*wdem*), which provides a good fit to other cooling-core cluster spectra (e.g. Werner et al. 2006b; de Plaa et al. 2006, Chapter 3), requires a very flat, poorly constrained slope, which is what would be expected if the best approximation of the emission measure is Gaussian and we try to approximate it with a power-law.

A two-temperature fit to the central  $3'$  spectrum requires  $kT_1 = 2.05^{+0.04}_{-0.05}$  keV and  $kT_2 = 5.08^{+0.20}_{-0.13}$  keV with normalizations  $Y_1 = 9.8^{+0.8}_{-0.5}$  and  $Y_2 = 11.7^{+0.4}_{-0.5} \times 10^{66} \text{ cm}^{-3}$ . This fit gives only a small improvement with respect to the *gdem* fit ( $\chi^2/\text{d.o.f.} = 1379/1209$  compared to 1449/1211).

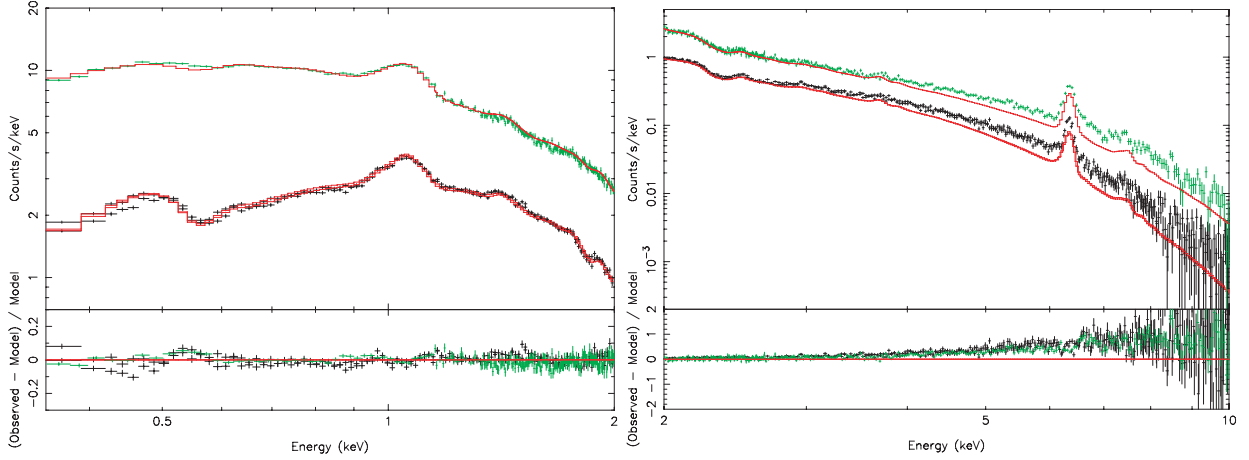


Figure 4.6: *Left panel:* EPIC spectrum from the central 3' region in the soft band and best-fit single temperature model. *Right panel:* EPIC spectrum from the central 3' region in the hard band and the extrapolation of the best-fit single temperature model from the soft band. Data points from pn are shown in green, MOS in black, and the best-fit model in red. The clear residuals show the need for a multi-temperature model.

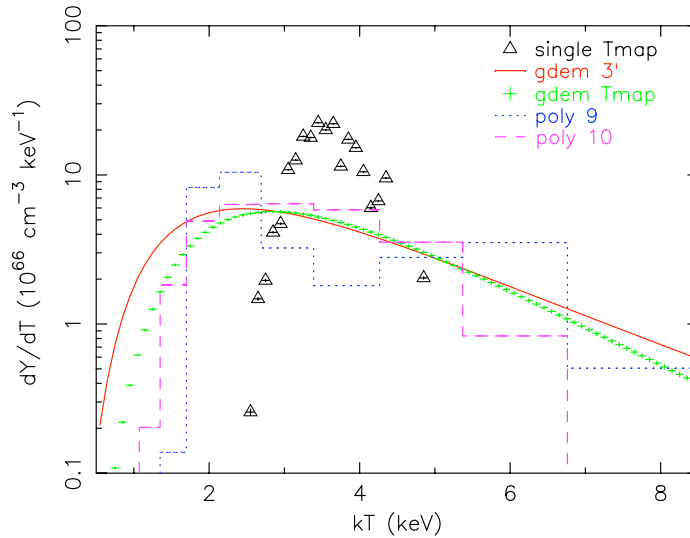


Figure 4.7: Total  $dY/dT$  curve constructed from the bins in the central 3' of the temperature map, showing the multi-temperature structure: in black, assuming single-phase in each bin; in green, assuming intrinsic  $gdem$  emission measure distribution with  $\sigma_T = 0.2$  in each bin. The red curve shows the best-fit  $gdem$  model for the 3' region (Table 4.1). In blue and magenta, different best-fit polynomial  $dem$  models for the 3' spectrum (Sect. 4.4.1).

The best-fit  $kT_1$  and  $kT_2$  are approximately the minimum and maximum temperatures represented in the *gdem* model within  $1\sigma_T$  and the normalizations of the two components are similar, which is again what we would expect if the best approximation of the emission measure is Gaussian and we try to fit it with a two-temperature model (in the two-temperature model, the contribution of any phase between the two best-fit temperatures can always be reproduced by combining these two phases with appropriate normalization ratios). The *gdem* model thus provides an equally good fit and a more physical interpretation of the spectrum than the two temperature model, because it is difficult to imagine a scenario which would generate  $\sim 2$  and  $\sim 5$  keV gas in roughly equal amounts, no gas at intermediate temperatures and, implicitly, no mixing between the two gas phases. If the 5 keV component comes from the projected shocked gas layer, for instance, which would fulfill the requirement for the absence of mixing, it should certainly contain much less gas than the entire cluster center which would constitute the cooler phase.

The last test is to fit a generic differential emission measure model (*dem*) available in SPEX. For a grid of temperatures spaced by  $0.1 \log T$  between a user-defined minimum and maximum value, this model constructs a spectrum corresponding to each grid point, and then can apply several methods to determine how to optimally combine these spectra in order to reproduce the data (for further details, see Kaastra et al. 1996). We chose the polynomial method, which finds the best  $dY/dT$  in the form of a polynomial of a desired degree. Other methods gave either very similar results to the polynomial method or were computationally unstable. The disadvantage of the *dem* model is that it cannot fit any other parameters except those related to the  $dY/dT$  behavior. We thus had to fix the elemental abundances to the best-fit *gdem* values.

We show in Fig. 4.7 the best-fit  $dY/dT$  curves obtained from the *dem* model using 9<sup>th</sup> and 10<sup>th</sup> degree polynomials. It is immediately clear that, also using this method, we find a very broad multi-temperature distribution, similar to that required by the Gaussian model. The 10<sup>th</sup> degree polynomial agrees very well with the *gdem* model between  $\sim 2$ – $5$  keV and falls somewhat faster at lower and higher temperatures. The 9<sup>th</sup> degree polynomial agrees with the *gdem* model at large temperatures but shows a hint of a bimodal  $dY/dT$  distribution with peaks at 2.5 and 6 keV (however, still with significant amounts of emission between 2.5 and 6.0 keV, excluding a simple 2T approximation). While keeping in mind these small differences, we can conclude that the broad best-fit Gaussian emission measure distribution is a good simple approximation to the best-fit results of the polynomial *dem* model.

It is interesting to further note the fact that the  $dY/dT$  curves for both the *gdem* fit to the central 3' spectrum and for the 9<sup>th</sup> and 10<sup>th</sup> degree polynomial *dem* models peak around 2.3–2.5 keV, the best-fit temperature from RGS. This suggests that the discrepancy between the best-fit RGS and EPIC temperatures is partly due to the more limited RGS band, which corresponds to low energies and is therefore insensitive to the presence of the hard tail in the real temperature distribution.

### Confusion with soft excess

Another way to account for temperature differences in the soft- and hard-bands (Fig. 4.6) is to allow the Galactic absorption column density to vary in the spectral fits. A best-fit  $N_H$  lower than the real value, allowing for emission from gas at low energies, in combination with a best-fit

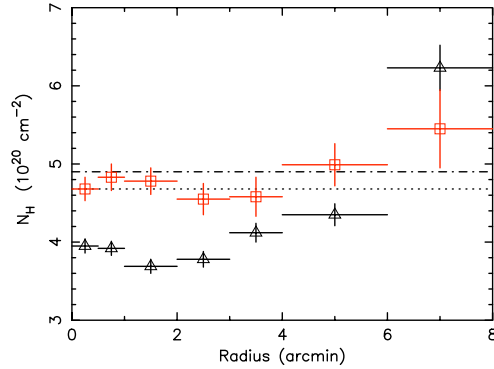


Figure 4.8:  $N_H$  profile determined fitting a single-temperature model to the full (0.35–7 keV, black triangles) and soft (0.35–2 keV, red squares) energy bands. The values determined from H I surveys (Kalberla et al. 2005; Dickey & Lockman 1990). are over-plotted with a horizontal dotted and dash-dotted line, respectively.

temperature slightly higher than the real value, can combine to give a good description of both the soft and hard part of the spectrum. If the multi-temperature structure is such as we describe above, the single-temperature fit with free  $N_H$  will be a significant improvement compared to the single-temperature fit with fixed  $N_H$ .

We show in Fig. 4.8 the  $N_H$  profile determined fitting a single temperature model to the full (0.35–7 keV) energy band. The  $N_H$  has a dip on the cluster center, which can be mistaken for the possible presence of soft excess generated either by non-thermal inverse Compton scattering of cosmic-microwave photons on relativistic electrons in the cluster or by the presence of a soft ( $\sim 0.2$  keV) thermal component (for a review on soft excess, see Durret et al. 2008). However, the  $N_H$  profile determined fitting a single temperature model only to the soft (0.35–2 keV) energy band is flat and in good agreement with the value determined from H I surveys, disproving this scenario.

The Gaussian emission measure distribution model with  $N_H = 4.8 \times 10^{20} \text{ cm}^{-2}$  provides a better fit than a single temperature model with free  $N_H$  ( $\chi^2/\text{d.o.f.}$  1449/1211 compared to 1718/1211 for the central 3' region). Fitting a *gdem* model with free  $N_H$  further improves the fit to  $\chi^2/\text{d.o.f.}=1291/1210$ , with a best-fit  $N_H = 3.92 \pm 0.07 \times 10^{20} \text{ cm}^{-2}$ , still significantly lower than the Galactic value but closer to it than the best-fit  $N_H$  using a single-temperature fit ( $3.69^{+0.06}_{-0.11} \times 10^{20} \text{ cm}^{-2}$ ). Since the best-fit  $N_H$  using only the soft band is in agreement with the Galactic value ( $4.74 \pm 0.07 \times 10^{20} \text{ cm}^{-2}$ ), the lower  $N_H$  in the full band must reflect some residual fitting problems. The most important effect is that the fitting tries to compensate for the residuals around the O-edge (around 0.5 keV, see Fig. 4.1) while constraining the average temperature by the continuum at higher energies; on the other hand, there might be some uncertainties in the calibration of the spectral slope of the EPIC detectors at low/high energies. Alternatively, the low  $N_H$  could be due to the presence of more cool gas in the real multi-temperature distribution than accounted for by

the best-fit *gdem* model, although Sect. 4.4.1 suggests that this is not the case.

### The “inverse” Fe bias

The best-fit Fe abundances from fitting the soft- and hard-bands individually with single-temperature models are both significantly lower than the best-fit Fe abundance determined from a single-temperature fit of the full spectral band (for the central 3' spectrum,  $0.37 \pm 0.02$  solar for the soft band,  $0.41 \pm 0.01$  for the hard band,  $0.499 \pm 0.007$  for the full band). The discrepancy with the best-fit Fe abundance from the Gaussian emission measure distribution model ( $0.445 \pm 0.007$ ) is smaller. This can be explained in the following way. The strength of the Fe-L complex is, for the same Fe abundance, higher for a cooler temperature. Similarly, the strength of the Fe-K complex is higher for a hotter temperature. If the model allows for some contribution to the spectrum of cooler and hotter gas compared to the average, a lower Fe abundance can reproduce the same Fe-L and Fe-K strengths for which a larger Fe-abundance would be needed if only gas at the average temperature is allowed in the model. This is especially important in clusters with intermediate average temperatures (2–4 keV), where both Fe-L and Fe-K emission lines are seen with relatively similar statistics, thus neither of the two lines predominantly drives the fit of the Fe abundance.

This effect is opposite to that described by Buote & Fabian (1998), in which not considering the presence of cooler gas in the multi-temperature structure leads to an underestimation of the real Fe abundance. That effect occurs primarily in cool systems (with an average  $kT$  below about 2 keV) where the Fe abundance is determined largely based on the Fe-L complex, since Fe-K emission at those temperatures is very weak.

In our case, on the other hand, neglecting the contribution of both cooler *and* hotter gas in a Gaussian-like emission measure distribution leads to an overestimation of the Fe metallicity if both Fe-L and Fe-K lines are seen with good statistics in the spectra. We are able thus to explain exactly the bias found by Rasia et al. (2008), who analyzed six simulated galaxy clusters processed through an X-ray Map Simulator (X-MAS), which allowed to create mock MOS1 and MOS2 observations. They showed that the Fe abundances determined from fitting the mock X-ray spectra is systematically overestimated for intermediate (2–3 keV) clusters, while for both hot and cold systems, where either only the Fe-L or only the Fe-K emission lines dominate, the Fe abundance is recovered with good accuracy.

## 4.4.2 Radial distribution of the chemical elements and comparison with other clusters

In recent years, abundance profiles for several elements were determined for clusters which have deep observations with XMM-Newton and Suzaku. In Fig. 4.9, we compare the radial distributions of the O and Fe abundances in Hydra A with those found in other detailed spectroscopical analyses of clusters: 2A 0335+096 (obtained by fitting the “*wdem*” differential emission measure distribution, no O abundances were presented; Werner et al. 2006b), Sérsic 159-03 (using the “*gdem*” model; de Plaa et al. 2006), M87 (using the 2T model within 2' and the MOS data; Matsushita et al. 2003), Centaurus (using the 2T model and MOS data; Matsushita et al. 2007a), For-

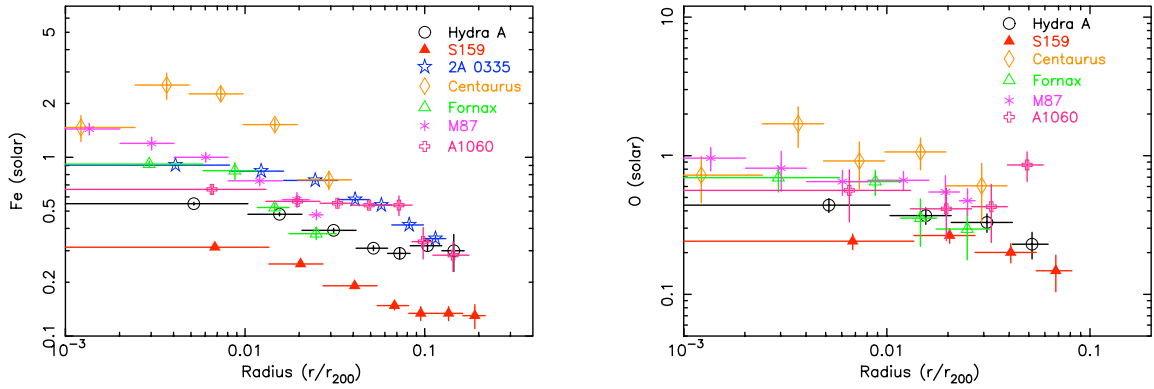


Figure 4.9: *Left panel:* The radial distribution of the Fe abundance. *Right panel:* The radial distribution of the O abundance. The Hydra A data are from this paper, 2A 0335+096 from Werner et al. (2006b), Sérsic 159-03 from de Plaa et al. (2006), M87 from Matsushita et al. (2003), Centaurus from Matsushita et al. (2007a), Fornax from Matsushita et al. (2007b), A 1060 from Sato et al. (2007). The  $r_{200}$  values were taken from Reiprich & Böhringer (2002) and scaled to  $H_0 = 70 \text{ km s}^{-1} \text{ Mpc}^{-1}$ . All the abundances are given with respect to the proto-Solar abundances by Lodders (2003).

nax (using the 2T model within  $4'$ ; Matsushita et al. 2007b), and A 1060 (Sato et al. 2007). The  $r_{200}$  values were taken from Reiprich & Böhringer (2002) and scaled to  $H_0 = 70 \text{ km s}^{-1} \text{ Mpc}^{-1}$ . We excluded all abundance values determined with less than  $3\sigma$  significance. The Fe abundance increases towards the center in all clusters, only Centaurus shows a drop of Fe in the innermost bin (this is also the case for Perseus, not included in our sample, e.g. Sanders et al. 2004). The Fe abundance in the Centaurus cluster is about a factor of 2 higher than in the other clusters, indicating a longer enrichment time scale.

In Fig. 4.10, we compare the radial distributions of the relative metallicities of O, Si, and S with respect to Fe in all the above named data sets. The radial distribution of the relative abundance of Si/Fe is roughly constant within  $0.1r_{200}$  and the ratio is between  $\sim 0.6$  and  $\sim 1.1$  Solar. There seems to be a drop in Si/Fe in several data sets at  $0.05r_{200}$ , but the uncertainties of the Si/Fe ratio are generally large and they do not allow us to make definitive conclusions. The radial distribution of the S/Fe ratio shows a large scatter between the different clusters, and there is no obvious trend with radius.

Interestingly, the observed trend with radius of the O/Fe ratio is much less pronounced than previously described by Tamura et al. (2004), who found a peaked distribution for Fe and a flat radial profile for O, leading to a marked increase in O/Fe with radius (up to O/Fe of 10 solar). Also, the trend of O with radius is clearly not flat, and there are indications of an increase in the O abundance towards the center for most clusters plotted in Fig. 4.9 (exceptions are the last data point in A1060 and a central drop in Centaurus, where Fe also shows a lower value in the center). In fact, taking into account all data points used in the plots and their respective

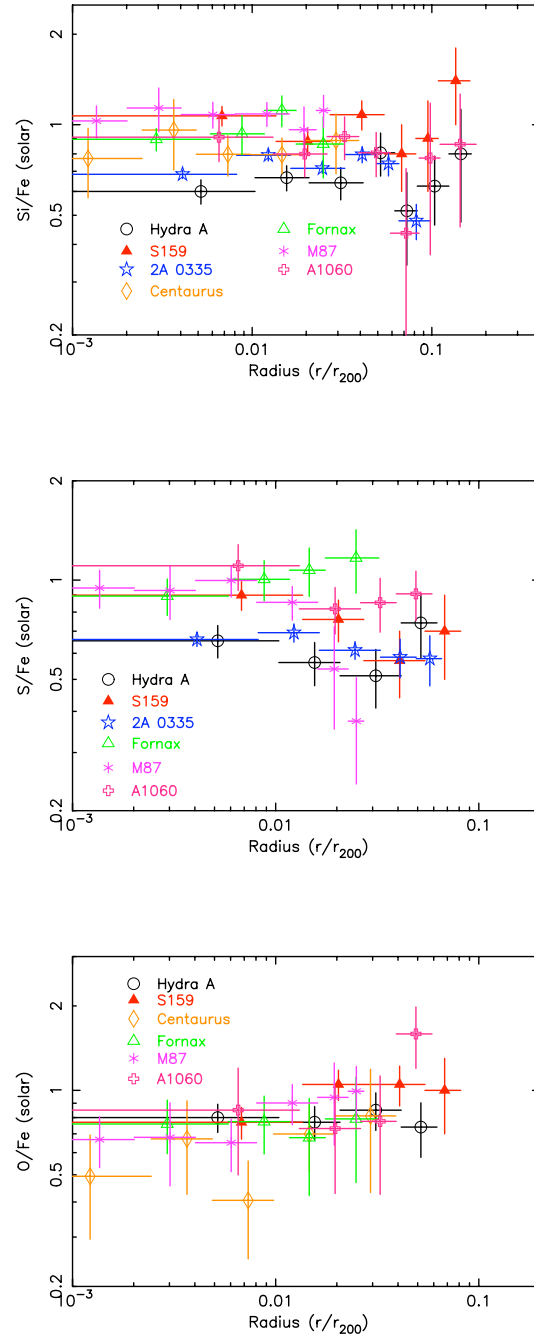


Figure 4.10: *Top panel:* The radial distribution of the Si/Fe ratio. *Middle panel:* The radial distribution of the S/Fe ratio. *Bottom panel:* The radial distribution of the O/Fe ratio.

error bars, we find that the O abundance significantly decreases with increasing radius, with a best-fit  $dO/d(\log_{10}r/r_{200}) = -0.48 \pm 0.07$ , while the increase in the O/Fe ratio with radius is only less than  $3\sigma$  significant,  $d(O/Fe)/d(\log_{10}r/r_{200}) = 0.25 \pm 0.09$ . The Fe abundance does however decrease with radius significantly faster than the O abundance ( $dFe/d(\log_{10}r/r_{200}) = -0.72 \pm 0.04$ ), suggesting that the slight trend in O/Fe is real.

The interpretation of the flat O and peaked Fe profiles was, in previous publications, an early enrichment by  $SN_{CC}$  in the protocluster phase, which led to the  $SN_{CC}$  products being well mixed, and a later continuous enrichment by SN Ia in the cD galaxy which continued to enrich the ICM on time scales much longer than  $SN_{CC}$ , creating a peak in SN Ia products at the cluster center. The flat Si/Fe ratio found in many clusters contradicted this picture. Si is produced by both SN Ia and  $SN_{CC}$  and according to this scenario its radial distribution should be shallower than that of Fe. This prompted Finoguenov et al. (2002) to propose that there are two types of SN Ia with different Si/Fe yields enriching the ICM. The authors proposed that, while the SN Ia with higher Si yields and longer delay times contribute mostly within the elliptical galaxy, the SNe Ia with lower delay times and lower Si yields would dominate the enrichment in the ICM at larger radii.

However, Fig. 4.9 shows that based on deep cluster observations with superior signal to noise ratio, there is evidence that the radial distribution of O is also centrally peaked. The O abundance determination with EPIC type CCDs is intrinsically very uncertain and sensitive to many systematics – some of them already discussed above – like background subtraction, calibration of the oxygen edge,  $N_H$ , temperature determination, insufficient subtraction of the Galactic foreground emission which contains O VIII emission. This is especially important in cluster outskirts with low photon statistics. The results of Tamura et al. (2004) are based on relatively short observations with XMM-Newton and their significances of the O abundance determinations in the outer parts of the individual clusters are typically only around  $1\sigma$ . We can conclude that the more accurate values shown in Figs. 4.9 and 4.10 suggest different O and O/Fe radial trends than previously assumed.

We must therefore revise the picture that O/Fe significantly increases with radius and that the central abundance peak in clusters is created almost entirely by SNe Ia and look for a mechanism that could create not only a peak in Fe and Si but also a peak in O. Sources of chemical enrichment in the ICM are SN Ia,  $SN_{CC}$ , and stellar winds. Slight increases in the relative abundances of O and Mg towards the center have been reported by Böhringer et al. (2005), who associate the presence of these peaks with stellar mass loss in the central galaxy. After a short incursion into what the observed abundance patterns can or cannot convey about supernova yield models, we will test this scenario for the case of Hydra A by evaluating the contributions from each source of chemical enrichment.

#### 4.4.3 ICM abundance patterns and supernova yield models

We plot in Fig. 4.11 the  $[Fe/Si] \equiv \log_{10}(Fe/Si)$  against the  $[Fe/O]$  ratios for all data points available and over-plot the expected trends obtained by mixing an increasing amount of SN Ia products into a gas whose initial composition is according to  $SN_{CC}$  model yields. We use a variety of available SN Ia models (from Iwamoto et al. 1999) and  $SN_{CC}$  models (Tsujiimoto et al. 1995; Nomoto et al. 2006; Kobayashi et al. 2006).

The amount of [Fe/Si] produced by different SN Ia models decreases from WDD3 to W7, WDD2 and WDD1. This is shown by the four curves in the left panel of Fig. 4.11, which all assume the same SN<sub>CC</sub> initial mass function (IMF) weighted average (between 0.07 and 50  $M_{\odot}$ ) yields from Kobayashi et al. (2006) with an initial metallicity of the SN<sub>CC</sub> progenitor of  $Z=0.004$  (0.2 solar). In the right panel of the same figure, we also show the influence on the expected [Fe/Si] vs. [Fe/O] curve if we assume different initial metallicities of the SN<sub>CC</sub> progenitor but the same SN Ia model (in this case we chose to show this comparison for W7, which is most commonly used in galactic chemical evolution models). The two dashed line curves use the yields from Kobayashi et al. (2006) with  $Z=0$  (bottom) and  $Z=0.02$  (top). Using the IMF weighted (10–50  $M_{\odot}$ ) SN<sub>CC</sub> yields of Tsujimoto et al. (1995) and Nomoto et al. (2006) (for IMF-weighted values between 10 and 50  $M_{\odot}$ , see Werner et al. 2008) would shift the model curves toward higher [Fe/Si].

We find a large diversity in the collected data, which do not strongly favor any particular SN Ia model. Because the O/Fe radial trends are weak, as discussed above, there is no clear tendency for data points from larger radii to move along the plotted curves towards lower fractional contributions from SN Ia. Rather, most data points are clustered at around 80% of Fe coming from SN Ia, which translates to a contribution of 30–40% of SN Ia by number.

Two interesting extreme examples are Hydra A, whose very low Si abundance places it at the uppermost limit of [Fe/Si] which can be reached by any combination of SN Ia and SN<sub>CC</sub> models considered, and M87 at the opposite end. The high Si abundance in M87 places it at the lower limit of Fe/Si that can be reproduced by currently available supernova models, and the data points here favor the WDD1 scenario. Most of the observed values for other clusters fall between the WDD1 and WDD2 model curves. An exciting puzzle is that, as Fig. 4.11 shows, a higher initial metallicity of the SN<sub>CC</sub> progenitor tends to shift the expected curve upwards to higher [Fe/Si]. Higher initial  $Z$  results in a higher [Ne/Fe] abundance ratio (Nomoto et al. 2006; Kobayashi et al. 2006). The RGS observations however show exactly the opposite trend: M87 which has the lowest [Fe/Si] has the largest [Ne/Fe] ( $1.40 \pm 0.11$  using a 2T model, Werner et al. 2006a) while Hydra A with the highest [Fe/Si] has the lowest [Ne/Fe] ( $0.73 \pm 0.18$  using a 2T model, this chapter).

Since supernovae are the most important sources of heavy elements, it should be possible to reconstruct the composition of any ICM by an appropriate fraction of SN Ia to SN<sub>CC</sub> contributions. Understanding if the scatter of the data points in the [Fe/Si] vs. [Fe/O] plot has a physical meaning or is simply due to spectral fitting issues remains a challenge for future observational work, while trying to reproduce the diversity of abundance patterns we see can become a further input for supernova modeling.

#### 4.4.4 The origin of the metal abundance peaks in Hydra A

In Sect. 4.3.2, we pointed out that the abundances of Fe, O, Si and S are larger in the core than in the cluster outskirts. We investigate here how these metal peaks can be produced. For this, we

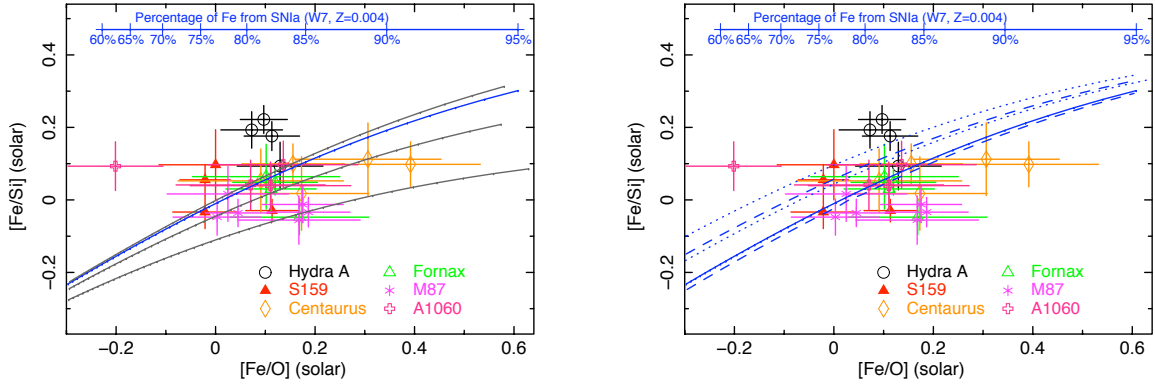


Figure 4.11: The observed  $[\text{Fe}/\text{Si}]$  against  $[\text{Fe}/\text{O}]$  ratios (logarithmic values). *Left*: Expected trends for different SN Ia models (Iwamoto et al. 1999, WDD1-3 in gray increasing upwards and W7 in blue), assuming the SN<sub>CC</sub> yields from Kobayashi et al. (2006) with  $Z=0.004$  for the SN<sub>CC</sub> progenitor. *Right*: The effect on the expected trends when using different available SN<sub>CC</sub> models (SN Ia yields were assumed to follow the W7 model). Dashed lines indicate the effect of using SN<sub>CC</sub> models with different  $Z$ 's from Kobayashi et al. (2006) (0. and 0.02, increasing upwards), dotted lines show trends using other published SN<sub>CC</sub> yields (above, Tsujimoto et al. 1995; below, Nomoto et al. 2006).

must first evaluate the mass of each metal needed to create the respective peak. This is given by:

$$M_{\text{met}} = \sum_j \gamma_{\text{met}} \Delta Z_{\text{met},j} M_{\text{gas},j} \quad (4.2)$$

where  $j$  is an index running over all annuli in the radial profile which are part of the peak,  $\Delta Z_{\text{met},j} = Z_{\text{met},j} - Z_{\text{met},\text{out}}$  is the average metallicity excess between annulus  $j$  and the value in the outskirts at which the profile flattens out,  $M_{\text{gas},j}$  is the gas mass inside annulus  $j$ , and  $\gamma_{\text{met}}$  is the mass fraction of the considered metal in the solar atmosphere, as determined from Lodders (2003).

For each element, we assume as a “base” abundance  $Z_{\text{out}}$  (the abundance value outside the peak, to which the radial profiles flatten out) the value determined in the 3–8' region in Sect. 4.3.1. For O, the value in the outer region is not well constrained, therefore we will use the average of the two data points outside 2' where the O abundance could be determined in Sect. 4.3.2. Our estimated “base-abundances” are thus 0.32 solar for Fe, 0.15 solar for Si, 0.10 solar for S, and 0.20 solar for O. If there is a continuing weak radial trend outside 3' for any of the elements (see Leccardi & Molendi 2008), these 3–8' values are an upper limit to the real abundances outside the peak. Given all the uncertainty sources involved, we show in this section only calculations based on the best-fit abundances without giving formal error bars. The presented results depend on the exact abundance profiles but also, among others, on the exact supernova yield and stellar wind modeling and on the IMF, star formation history and average stellar abundances in

the central galaxy. We present estimates obtained using the best-guess assumptions based on available models for these parameters.

From Fig. 4.2, it can be seen that the abundance peak for all elements is clearly visible inside a radius of  $2'$  (126 kpc), marked by a vertical dotted line in the plot. We thus sum Eqn. 4.2 over the first three bins ( $0-0.5'$ ,  $0.5-1'$ , and  $1-2'$ ) in the radial profile to obtain  $M_{\text{met}}$  for each element.  $M_{\text{gas}}$  can be determined from the spectrum normalization assuming a spherical or spherical shell geometry of the emitting region and using Eqn. 4.5. The corresponding metal masses in the peak are, in units of  $10^8 M_{\odot}$ , 2.7 for Fe, 1.9 for Si, 1.0 for S and 18.5 for O.

We assume that the enrichment of the metal abundance peak by the central galaxy took place over the last  $10^{10}$  years (approximately between redshift  $z = 2$  and the present). This puts lower limits on the rates of metal production required to produce the peak, because mergers between  $z = 2$  and now could have dispersed some of the metals out towards the cluster outskirts. However, many clusters do require enrichment times of  $\sim 10^{10}$  years (Böhringer et al. 2004), which may imply that mergers are not very efficient at disrupting cool cores.

According to Ciotti et al. (1991), the gas mass contributed by stellar winds as a function of time  $t$  can be, in a simplified form which presupposes a Salpeter IMF (Salpeter 1955) and single-age passively evolving stellar population, approximated as:

$$\dot{M}_*(t) \approx 1.5 \times 10^{-11} L_B (t/t_H)^{-1.3}, \quad (4.3)$$

where  $L_B$  is the present-day blue band luminosity in units of  $L_{B\odot}$  and  $t_H$  is the Hubble time. The blue-band luminosity corresponding to the magnitude presented by Peterson (1986) for the central dominant galaxy is  $9.2 \times 10^{10} L_{B\odot}$  within an aperture of  $1.65'$  (108 kpc diameter at the redshift of Hydra A, which likely includes the light emitted out to several times the galaxy's effective radius). Integrating this equation from  $t(z = 2)$  to the present ( $t = t_H$ ), we obtain a gas mass contribution from stellar winds of  $33.6 \times 10^9 M_{\odot}$ . Assuming the average metallicities of the stellar population to be solar, we estimate that the corresponding masses of Fe, Si, S and O ejected with the stellar winds are, respectively, 0.47, 0.28, 0.14, and 2.2 (in units of  $10^8 M_{\odot}$ ). We caution that the assumption of solar abundances for the stellar winds is a very uncertain one. Firstly, the stellar metallicities in the centers of central dominant galaxies can reach super-solar abundances. Secondly, elliptical galaxies have old stellar populations, meaning that their stars formed in the presence of less SN Ia ejecta and the stellar composition should be closer to the  $\text{SN}_{\text{CC}}$  abundance ratios. However, Kobayashi & Arimoto (1999) find an average  $[\text{Mg}/\text{Fe}]$  ratio in elliptical galaxies not very different from solar (1.3 solar in the units of Lodders 2003). Moreover, cDs in cooling core clusters do show anomalous blue light emission and have star-forming regions (see McNamara 1995, for the case of Hydra A). These young stars (which, being young, should have relatively strong stellar winds) must have incorporated much more SNIa products than the old populations of typical ellipticals.

If the rest of the Fe in the peak is produced entirely by SN Ia, then assuming the yield from the WDD3 model of Iwamoto et al. (1999), which best reproduces the unusually high Fe/Si ratio in Hydra A,  $2.6 \times 10^8$  supernovae are required. For the W7 model, in turn,  $3.0 \times 10^8$  supernovae would be needed. On a time-scale of  $10^{10}$  years, this implies an average rate of 2.6–3.0 SN Ia

per century. The current rate of SN Ia in elliptical galaxies is (Cappellaro et al. 1999)

$$R_{Ia} = 0.18 \pm 0.06 (100\text{yr})^{-1} (10^{10}L_{\odot})^{-1}, \quad (4.4)$$

which implies 1.66 SN Ia per century for the blue luminosity of the central galaxy in Hydra A, a factor of 1.6–1.8 too small compared to the required rate. There is however recent evidence that the SN Ia rate in cluster ellipticals is larger than in field ellipticals. Mannucci et al. (2008) find a SN Ia rate in cluster ellipticals of  $0.28_{-0.08}^{+0.11} (100\text{yr})^{-1} (10^{10}L_{\odot})^{-1}$ , in excellent agreement with the rate required in Hydra A. Furthermore, the rate of SN Ia may have been larger in the past. Renzini et al. (1993) propose a time-dependence of  $(t/t_H)^{-k}$  with  $k$  spanning 1.1 up to 2. Integrating this between  $t(z=2)$  and now, the average SN Ia rate over the past  $10^{10}$  years could be 2 to 4.1 times greater than the present one, and could have produced the observed amount of Fe in the peak over the assumed enrichment time.

Using the yields from the WDD3 model,  $2.6 \times 10^8$  supernovae would produce  $0.41 \times 10^8 M_{\odot}$  of Si, 0.25 of S and 0.15 of O. Adding the contributions from SN Ia and stellar winds therefore, we still lack  $16.2 \times 10^8 M_{\odot}$  of O,  $1.2 \times 10^8 M_{\odot}$  of Si, and  $0.6 \times 10^8 M_{\odot}$  of S compared to the estimated total masses of these elements in the central peak. Even with the W7 SN Ia model, which produces the highest amount of O among the models of Iwamoto et al. (1999), still  $15.9 \times 10^8 M_{\odot}$  of O would be unaccounted for solely by adding the contributions of SN Ia and stellar winds.

One possible solution is to consider that the metal input by stellar winds is larger than we previously assumed, either because of super-solar metallicities in the central galaxy or a higher stellar mass loss rate than predicted by models (due, for example, to a more complex star formation history than assumed). Keeping the assumption of solar ratios, if the stellar winds would produce around 8 times more of each metal than assumed above, meaning that a correspondingly lower number of SN Ia would be needed to create the Fe peak, we could reproduce well the observed masses of O, Si and S in the peak both assuming W7 and WDD3 SN Ia yields. Without the assumption of solar ratios but keeping the solar Fe abundance in the stellar winds and the mass loss rate calculated in Eqn. 4.3 does not present a viable alternative, since the Si/Fe and S/Fe in the stellar winds would need to be 5.3–5.4 solar, more than is reproduced by any SN<sub>CC</sub> model. As a combination of the two possibilities, if the stellar winds would produce only 3 times more Fe than assumed above but would have Si/Fe and S/Fe of 2 solar and O/Fe of 2.8 solar, we could also reproduce the observations well.

An alternative for creating the additional O, Si and S is to consider a contribution from SN<sub>CC</sub> to the metal peak. Assuming an unchanged stellar mass loss rate and average stellar wind metallicity and using the initial mass function weighted average SN<sub>CC</sub> yields from Kobayashi et al. (2006), approximately  $8 \times 10^8$  core-collapse supernovae would be needed, in addition to the contribution of SN Ia and stellar winds, to reproduce the observed O peak. For Si and S, only 6 and  $3 \times 10^8$  SN<sub>CC</sub> are needed, respectively. This would mean either that there was a significant contribution by SN<sub>CC</sub> in the central galaxy over the last  $10^{10}$  years (note that almost twice as many SN<sub>CC</sub> than SN Ia are required!), or if the initial enrichment by SN<sub>CC</sub> in the protocluster phase was not as well mixed on large scales as previously thought, and some peak in the distribution of SN<sub>CC</sub> products existed prior to further enrichment with predominantly SN Ia elements. Both cases provide alternatives to the approach of Finoguenov et al. (2002) for explaining why

the radial distribution of Si is not shallower than that of Fe, as would be expected if only SN Ia contributed to the central abundance peak.

Additionally, according to recent simulations (Domainko et al. 2006), ram-pressure stripping of cluster galaxies also leads to a stronger enrichment of the cluster centers compared to the outskirts, and could lead to comparable Fe, Si, S and O peaks. The typical spatial scale of this enrichment however ( $\sim 1$  Mpc) is considerably larger than the extent of the peak in Hydra A ( $\sim 130$  kpc).

#### 4.4.5 Gas uplift by the AGN and metal transport into the ICM

As we point out already in Section 4.3.3, there is a remarkable correlation between the 327 MHz large-scale radio lobes, cool arm-like extensions in the temperature map, and metal-rich filaments in the Fe abundance map. This suggests that buoyant radio bubbles produced by the AGN uplift cool, metal-rich gas from the central parts of the X-ray halo, thereby contributing to the transport and distribution of heavy elements produced in the central galaxy into the ICM (Churazov et al. 2001, Chapter 3).

The metallicity map shows a clear elongation along the N–S direction, with filaments coinciding very well with low-temperature features in the central parts of the temperature map (Fig. 4.4). Similar elongations in the metallicity map are seen in simulations of AGN-induced metal-transport in galaxy clusters (Roediger et al. 2007). Towards the North, the cool, metal-rich gas overlaps well with the rising stem of the northern radio-lobe. Towards the South, the low-temperature feature is oriented at a slightly more easterly angle than the southern radio lobe, and is associated with a weaker increase in metallicity than in the N. The southern radio lobe is bent and clearly more disturbed than the northern lobe, and the same process which leads to the deformation of the radio plasma could also account for the displacement between the radio emission and the cool filament.

In the previous chapter, we used the fact that the gas uplifted by the AGN in M87 is multi-phase to infer the metallicity, mass, origin and chemical enrichment history of this gas. Unfortunately, in Hydra A, the EPIC spectra of the cool arm-like features in the temperature map do not require additional temperature components. This can be explained if the amount of cool gas which has a temperature around and below  $\approx 1$  keV, where the shape of the Fe-L complex becomes clearly different and can indicate multi-phase structure, is very low. Based on the Fe-L shape, one of the very few spectral indications for multi-temperature accessible with EPIC, gas above  $\approx 2$  keV is difficult to distinguish from gas in hotter phases. Indeed, as shown in Section 4.3.4 where we do detect a small amount of cool gas below 1 keV, the spectrum normalization of this gas is only 1.2–1.4% of the total emission of the hot halo, which is impossible to uniquely identify using the EPIC cameras.

Based on the RGS result, we can try to infer some further properties of the cool gas. The RGS extraction region we used was  $3'$  wide in the cross dispersion direction and effectively  $\sim 10'$  long in the dispersion direction. If we assume that the cool gas is concentrated in the cluster center, thus within a  $3'$ -diameter circular region which is the 2D-projection of a sphere with a radius of  $1.5'$  (94.5 kpc), then the mass of the cool gas corresponding to its emission measure of

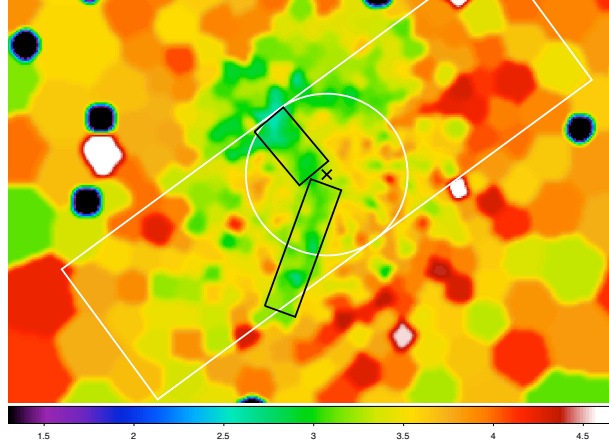


Figure 4.12: Zoom-in on the temperature map in Fig 4.4 smoothed with a  $16''$  Gaussian filter. A circle with radius of  $1.5'$  and the  $3$  by  $10'$  RGS extraction region are overlaid in white. The cluster center is marked with a black cross and the black rectangles mark, in projection, the cylinders by which we approximate the volume of the cool “arms”. Colorbar units are keV.

$2.6 \times 10^{65} \text{ cm}^{-3}$  would be  $1.8 \times 10^{11} M_{\odot}$ . The mass is determined using:

$$Y = \int n_e n_H dV \approx n_e n_H V \approx 1.2 n_H^2 V$$

$$M = \sum_i m_i n_i V \approx (m_H n_H + m_{\text{He}} n_{\text{He}}) V \approx 1.4 m_H n_H V \quad (4.5)$$

where  $n_e$ ,  $n_H$  and  $n_{\text{He}}$  are the electron, proton and helium number densities, respectively,  $m_H$  is the proton mass,  $m_{\text{He}} = 4m_H$ , and  $V$  is the volume of the emitting region. Approximately,  $n_e \approx 1.2n_H$ , and assuming a solar He/H fraction,  $n_{\text{He}}/n_H \approx 9.5\%$ . We neglect the mass contribution of ions heavier than He which are scarce compared to H and He.

If we assume on the other hand that the cool gas comes only from the cool “arms” seen in the maps and not from the entire  $1.5'$ -radius sphere, we can approximate the volume of this gas by a sum of cylinders for the Northern and Southern “arms”, depicted in Fig. 4.12. Both cylinders are bound to lay inside the  $3$  by  $10'$  RGS extraction region. The N cylinder has a radius of  $0.35'$  and a length of  $1.3'$ , the S cylinder has a radius of  $0.3'$  and is  $2.5'$  long. This yields a volume of  $8.9 \times 10^{69} \text{ cm}^3$ , and a mass of  $5.1 \times 10^{10} M_{\odot}$ . This is only a rough estimate because it assumes the cold gas to be distributed uniformly in the considered cylindrical regions.

We furthermore need to take into consideration the possibility that the cool gas may not fill the entire assumed volume of the “arms”, but may be concentrated in thin filaments which occupy only a fraction (so-called filling factor) of this volume. Since these filaments are unresolved, the only way to estimate this filling factor is to assume pressure equilibrium between the cool and hot phases, in the form  $n_c k T_c = n_h k T_h$  which, using  $n_{c,h} \propto \sqrt{Y_{c,h}/V_{c,h}}$ , implies

$$\frac{V_c}{V_h} = \frac{Y_c}{Y_h} \left( \frac{T_c}{T_h} \right)^2 \quad (4.6)$$

where c and h are subscripts denoting the properties of the cool and hot gas determined by RGS, respectively. From Eqn. 4.6, we obtain  $V_c/V_h = 1.0 \times 10^{-3} \approx V_c/V_{\text{tot}}$ , which leads to a mass of cool gas of  $1.6 \times 10^9 M_\odot$ . This is a factor of  $\sim 3$  larger than the mass of uplifted cool gas calculated in M87 (Chapter 3).

If we assume that the average displacement of the mass of cool gas determined above is on the order of  $1'$ , which is about 63 kpc, and use the integrated mass profile presented by David et al. (2001), we can estimate the gravitational energy needed to uplift this gas at  $3.3 \times 10^{58}$  ergs, which is 8 times greater than the energy needed for gas uplift in M87 but nevertheless very small compared to other processes related to AGN-ICM interaction in Hydra A, which require approximately  $10^{61}$  ergs (large-scale shock, Nulsen et al. 2005; Simionescu et al. 2009a, and cavities, Wise et al. 2007).

Finally, we estimate the amount of Fe which is being transported by the AGN through the uplift of the cool gas. Assuming a gas mass for the cool gas of  $1.6 \times 10^9 M_\odot$  and a metallicity, as determined from RGS, of 0.35 solar, and using  $M_{\text{Fe}} = \gamma_{\text{Fe}} M_{\text{gas}}$ , this gives  $M_{\text{Fe}} = 7.9 \times 10^5 M_\odot$ . However, this is almost certainly too low, since the uplifted cool gas should be more metal-rich than the ambient gas, as the structure in the Fe map suggests, while the abundances of the hot and cool gas were coupled in the RGS fit. Moreover, some of the uplifted metal-rich gas may have higher temperatures, therefore its mass is not included in our estimate of  $1.6 \times 10^9 M_\odot$  of uplifted gas, which is based solely on the RGS best-fit normalization of the 0.62 keV gas. This leads to an underestimation of the mass of uplifted gas and implicitly of the mass of uplifted Fe.

Another way to estimate the mass of transported Fe is to assume a typical metallicity outside the metal-rich regions and apply Eqn. 4.2 summing over all bins which lie inside the rectangles by which we approximated the projected shape of the N and S arms in Fig. 4.12. Assuming the average metallicity outside the metal-rich regions to be 0.445 solar (the average in the inner  $3'$ , Sect. 4.3.1), the mass of uplifted Fe would be  $1.7 \times 10^7 M_\odot$ , while if the metallicity outside the metal-rich regions is 0.32 solar (the “base” abundance for Fe discussed in Sect. 4.4.4), we obtain an upper limit of  $6.9 \times 10^7 M_\odot$  for the mass of Fe transported by the AGN together with the uplifted gas.

In turn, the total mass of Fe in the central  $0.5'$  region is  $11.5 \times 10^7 M_\odot$ , meaning that the AGN transported about 15% and up to 60% of the amount of Fe currently present in the inner part of the Hydra A halo out to larger radii by uplifting central, metal-rich gas. We note that the O/Fe value determined by extracting a spectrum in the N arm ( $0.80 \pm 0.14$ ) is consistent with the average O/Fe ratio in the inner  $3'$  (Table 4.1). This means, in agreement with Chapter 3, that the AGN, at least at this advanced stage of the evolution of the galaxy, transports metals into the ICM without altering the relative abundance patterns.

We already noted that some of the uplifted gas may have temperatures higher than 0.62 keV, therefore its mass is not included in our estimate of  $1.6 \times 10^9 M_\odot$ , which results in underestimating the uplifted gas mass. We showed a method of estimating the uplifted mass of Fe independent of the estimated mass of the 0.62 keV component. If we then assume an average metallicity for the uplifted gas of 2 solar (as in the case of M87, see Chapter 3), we can compute the total mass of uplifted gas to be  $6.1 \times 10^9 M_\odot$ , corresponding to an uplift energy of  $1.25 \times 10^{59}$  ergs. The results for different methods of estimating the gas and Fe mass and the uplift energy are summarized in Table 4.4.

Table 4.4: Uplifted gas mass, Fe mass, and energy, <sup>\*)</sup> with equal metallicities of the 0.62 keV and the hot gas from the RGS fit, <sup>\*\*)</sup> if the average metallicity of the total uplifted gas is 2 solar.

	gas mass ( $M_{\odot}$ )	Fe mass ( $M_{\odot}$ )	energy (ergs)
0.62 keV	$1.6 \times 10^9$	$7.9 \times 10^5$ <sup>*)</sup>	$3.3 \times 10^{58}$
total	$6.1 \times 10^9$ <sup>**)</sup>	$1.7 \times 10^7$	$1.25 \times 10^{59}$

## 4.5 Conclusions

We analyzed a deep  $\sim 120$  ks XMM-Newton exposure of the cooling core cluster of galaxies Hydra A. We extracted spectra from two large regions in the cluster core and in the outskirts to study the global properties of the cluster with the best statistics possible. We also analyzed the RGS spectrum extracted from a 3 by 10' region. We find that

- the shape of the Fe-L complex in the EPIC spectrum does not show strong indications for the presence of cooler gas as observed in other cooling core clusters. However, a multi-temperature model is needed to simultaneously fit both Fe-L and Fe-K lines appropriately. The best available model achieving this is a Gaussian distribution of the emission measure ( $gdem$ ) around the best-fit average temperature.
- the best-fit ( $gdem$ ) model shows a very broad distribution, with a full-width at half-maximum of 4.2 keV. We also fitted polynomial emission measure distributions which confirm the broad shape of  $dY/dT$ . The distribution is significantly broader than expected from the substructures visible in the 2D map in the considered region, suggesting the presence of intrinsic multi-temperature structure in each bin of the temperature map. We suggest that this multiphase structure can be due in part to the projection of shocked gas in front of and behind the cluster center, in part to the projection of cooler gas from the cluster outskirts along the line of sight, and in part to dense, unresolved cool gas blobs in the considered extraction region.
- we can accurately determine abundances for 7 elements in the cluster core with EPIC (O,Si,S,Ar,Ca,Fe,Ni). In the cluster outskirts, only Si, S and Fe abundances are determined with better than  $3\sigma$  significance and the large errors do not enable us to draw conclusions about possible differences in Si/Fe and S/Fe with respect to the cluster center.
- the abundances of 3 elements (O,Ne,Fe), one of which is inaccessible with EPIC, are determined with RGS. The O/Fe ratios from EPIC and RGS are consistent. While no multi-temperature structure beyond the  $gdem$  model can be constrained with EPIC, the RGS fit requires a cool component with a temperature of  $0.62 \pm 0.04$  keV and a normalization of only 1.2% of the hot ambient. This gas is detected with a significance of  $6.5\sigma$ .
- the Gaussian emission measure distribution model gives lower Fe abundances than a single temperature model, which can explain why simulations show that the best-fit Fe abundance

in clusters with intermediate temperatures is over-estimated.

We also determined temperature and abundance profiles from seven annuli and compared our results with radial profiles of other clusters for which deep observations and detailed chemical enrichment studies are available. We show that

- the abundance profiles for Fe, Si, S, but also O are centrally peaked in Hydra A.
- the radial profiles of the O abundance are peaked also in other clusters for which deep data are available. The increase in O/Fe with radius is very small. Combining the Hydra A results with 5 other clusters for which a detailed chemical abundance study has been performed, we find  $dO/d(\log_{10}r/r_{200}) = -0.48 \pm 0.07$ , while the increase in the O/Fe ratio with radius is only less than  $3\sigma$  significant,  $d(O/Fe)/d(\log_{10}r/r_{200}) = 0.25 \pm 0.09$ .
- stellar winds and the chemical enrichment by the number of type Ia supernovae needed to produce the Fe peak in Hydra A do not reproduce the estimated O, Si and S peaks. For this, either the amount of metals produced by stellar winds would have to be 3–8 times higher than predicted by available models or  $3 - 8 \times 10^8$  SN<sub>CC</sub> would be needed in addition to the contribution from stellar mass loss and SN Ia. Possibly, the initial enrichment by SN<sub>CC</sub> in the protocluster phase was not as well mixed on large scales as previously thought, and some peak in the distribution of SN<sub>CC</sub> products existed prior to further enrichment with predominantly SN Ia elements.
- mainly because of the low Si abundance, Hydra A requires either a WDD3 or W7 SN Ia model to reproduce the observed relative abundance patterns. Most other clusters lie between the WDD1 and WDD2 models. A 30–40% contribution by SN Ia compared to SN<sub>CC</sub> (by number) is needed to reproduce the observed relative abundance patterns at all radii (below  $0.1 r_{200}$ ) in all the considered clusters.
- the best-fit Galactic absorption column density,  $N_H$ , when fitting the full energy band, is lower than the value determined from H I data and has a minimum on the cluster center, which may be interpreted as inverse Compton or soft excess emission. The best-fit  $N_H$  in the 0.35–2 keV band however is in agreement with the H I data, dismissing this possibility.

Finally, we produced 2D temperature and metallicity maps of Hydra A. From these we can conclude that

- the temperature map shows cooler gas extending in arm-like structures towards the north and south. The cool gas structures, and especially the northern one, appear to be richer in metals than the ambient medium and spatially correlated with the large-scale radio lobes. The northern “arm” is associated with a bright 1′ long filament seen in the Chandra image.
- based on the geometry of the cool “arms” seen in the temperature map and on the best-fit normalization of the 0.62 keV component in RGS, the estimated mass of cool gas, which was probably uplifted by the AGN to create these structures, is  $1.6 \times 10^9 M_\odot$ . The energy needed for this uplift is  $3.3 \times 10^{58}$  ergs, which is 8 times greater than the energy needed for

gas uplift in M87 but nevertheless very small compared to other processes related to AGN-ICM interaction in Hydra A (large-scale shock and cavities), which require approximately  $10^{61}$  ergs.

- the best estimate of the mass of Fe uplifted together with the cool gas is  $1.7 \times 10^7 M_{\odot}$ , 15% of the total mass of Fe in the central  $0.5'$  region. If the average metallicity of the uplifted gas is 2 solar, as in M87, the total mass of uplifted gas (not only the 0.62 keV component) is  $6.1 \times 10^9 M_{\odot}$  and the uplift energy is  $1.25 \times 10^{59}$  ergs.
- the O/Fe value in the N arm is consistent with the average O/Fe ratio in the inner  $3'$ . The transport of metals by the AGN thus presently does not alter the relative abundance patterns.

#### Acknowledgements

We would like to thank W. R. Forman and J. Vink for helpful discussions. We acknowledge the support by the DFG grant BR 2026/3 within the Priority Programme "Witnesses of Cosmic History" and NASA grant NNX07AQ18G 16610022. AS would like to thank the Harvard-Smithsonian CfA, SRON, and Jacobs University Bremen for their hospitality. AF acknowledges support from BMBF/DLR under grant 50 OR 0207 and MPG. This work is based on observations obtained with XMM-Newton, an ESA science mission with instruments and contributions directly funded by ESA member states and the USA (NASA). The Netherlands Institute for Space Research (SRON) is supported financially by NWO, the Netherlands Organization for Scientific Research.

## Chapter 5

# The large-scale shock in the cluster of galaxies Hydra A

*A. Simionescu, E. Roediger, P. E. J. Nulsen, M. Brüggen, W. R. Forman, H. Böhringer, N. Werner & A. Finoguenov*

A&A, **495** (2009), 721

### **Abstract**

We analyzed a deep XMM-Newton observation of the cluster of galaxies Hydra A, focusing on the large-scale shock discovered in Chandra images as a discontinuity in the surface brightness. The shock front can be seen both in the pressure map and in temperature profiles in several sectors. We compared the results of a spherically symmetric hydrodynamic model to surface brightness profiles and temperature jumps across the shock to determine the shock properties. The Mach numbers determined from the temperature jumps are in good agreement with the Mach numbers derived from EPIC/pn surface brightness profiles and previously from Chandra data and are consistent with  $M \sim 1.3$ . In this simple model, the estimated shock age in the different sectors ranges between 130 and 230 Myr and the outburst energy between  $1.5$  and  $3 \times 10^{61}$  ergs. The shape of the shock seen in the pressure map can be approximated with an ellipse centered  $\sim 70$  kpc towards the NE from the cluster center. This is a good simple approximation to the shock shape seen in the Chandra image, although this shape shows additional small deviations from ellipticity. We aimed to develop a better model that can explain the offset between the shock center and the AGN, as well as give a consistent result on the shock age and energy. To this end, we performed 3D hydrodynamical simulations in which the shock is produced by a symmetrical pair of AGN jets launched in a spherical galaxy cluster. As an explanation of the observed offset between the shock center and the AGN, we consider large-scale bulk flows in the intracluster medium, which were included in the simulation. The simulation successfully reproduces the size, ellipticity, and average Mach number of the observed shock front. The predicted age of the shock is 160 Myr and the total input energy  $3 \times 10^{61}$  erg. Both values are within the range determined by the spherically symmetric model. To match the observed 70 kpc offset of the shock ellipse from the cluster center by large-scale coherent motions, these would need to have a

high velocity of  $670 \text{ km s}^{-1}$ . We discuss the feasibility of this scenario and offer alternative ways to produce the observed offset and to further improve the simulation.

## 5.1 Introduction

Many clusters of galaxies show central surface brightness peaks associated with a decrease in the temperature of the X-ray emitting gas. In the centers of these clusters, the cooling time usually falls below the Hubble time. Thus, it was initially believed that the X-ray gas in the cluster cores radiates its energy away and, in the absence of other heat sources, cools out of the X-ray band. This was known as the cooling-flow scenario (Fabian & Nulsen 1977; Cowie & Binney 1977). Early results of the latest generation of X-ray observatories, however, showed that the central gas in cooling-flow clusters does not cool below about one third of the cluster virial temperature (Peterson et al. 2001, 2003). This requires a fine-tuned heat source which allows the gas to cool down to 1/3 of its initial temperature but not below this (e.g. Böhringer et al. 2002).

Currently, AGN are considered the best candidate as a heating engine for solving the cooling flow problem because they are present in a large fraction of the central galaxies in cool core clusters (71% of such galaxies are radio loud, Burns 1990) and substructures associated with AGN-ICM interaction are frequently observed. The most common among these features are X-ray cavities (also referred to as bubbles) often associated with low-frequency radio emission, which are thought to arise when the AGN injects relativistic plasma into the cluster medium during an outburst. As these bubbles rise buoyantly through the cluster, they deposit their energetic content into the ICM, thus heating it. In general, the most powerful cavities are found in the most X-ray-luminous systems which require the largest heat inputs (Bîrzan et al. 2004; Rafferty et al. 2006). By heating or otherwise disturbing the gas, outbursts can affect the accretion rate, creating a feedback loop that could regulate the energy input and explain the fine-tuning. In some clusters, additional substructure such as X-ray bright filaments (a spectacular example is M87 in the Virgo cluster, e.g. Forman et al. 2007) and shocks associated with AGN outbursts are also seen, providing several other possible mechanisms by which AGN heat the ICM.

The cluster of galaxies Hydra A shows a wealth of substructure associated with AGN-ICM interaction. A pronounced set of X-ray cavities was seen in an early Chandra observation (McNamara et al. 2000; Nulsen et al. 2002), and deeper data revealed the presence of a second, larger set of cavities, a large-scale shock and an X-ray bright filament near the cluster center (Nulsen et al. 2005; Wise et al. 2007). Modeling the surface brightness profiles across the shock, Nulsen et al. (2005) found Mach numbers between  $M \approx 1.2$  in the W and  $M \approx 1.34$  on the NE side and a total energy associated with creating the shock of the order of  $10^{61}$  ergs, in agreement with the energy needed to generate the observed cavity system. This ranks the outburst in Hydra A among the most powerful ones known.

So far, however, a temperature jump associated with the large-scale shock in Hydra A has not been detected. A new exposure with XMM-Newton allows us to find this temperature jump and confirm that classical shock jump conditions apply: both the surface brightness and temperature jumps reflect the same shock Mach number, which is around  $M \sim 1.3$ . We furthermore extend the one-dimensional shock analysis of Nulsen et al. (2005) using 3D hydrodynamic simulations,

in order to improve our understanding of the shock geometry and the morphology of the cavity system.

## 5.2 Observation and data analysis

Hydra A was observed with XMM-Newton on December 8th, 2000, for 32.6 kiloseconds (ks) and on May 11th, 2007, for 123 ks. Since the second observation is significantly deeper and large parts of the first observation were affected by soft proton flares, we will focus primarily on the second observation.

We extracted a lightcurve for each of the three detectors separately and excluded the time periods in the observation when the count rate deviated from the mean by more than  $3\sigma$  in order to remove flaring from soft protons (Pratt & Arnaud 2002). After this cleaning, the net effective exposure is  $\sim 62$  ks for pn,  $\sim 81$  ks for MOS1, and  $\sim 85$  ks for MOS2. We furthermore excluded CCD 5 of MOS2 from our analysis due to its anomalously high flux in the soft band during the observation (see Snowden et al. 2008). For data reduction we used the 7.1.0 version of the XMM-Newton Science Analysis System (SAS); the standard analysis methods using this software are described in e.g. Watson et al. (2001). Out-of-time events were subtracted from the PN data using the standard SAS prescription for the extended full frame mode.

For the background subtraction, we used a combination of blank-sky maps from which point sources have been excised (Read & Ponman 2003; Carter & Read 2007) and closed-filter observations. The exact procedure and a short discussion about the agreement between the blank-sky maps and the local background can be found in Chapter 4.

## 5.3 Spectral modeling

We use the SPEX package (Kaastra et al. 1996) to model our spectra with a plasma model in collisional ionization equilibrium (*mekal*). Unless otherwise stated, the Galactic absorption column density was fixed to  $N_{\text{H}} = 4.8 \times 10^{20} \text{ cm}^{-2}$ , the average value from the two available H I surveys: the Leiden/Argentine/Bonn (LAB) Survey of Galactic H I (Kalberla et al. 2005,  $N_{\text{H}} = 4.68 \times 10^{20} \text{ cm}^{-2}$ ) and the H I data by Dickey & Lockman (1990) ( $N_{\text{H}} = 4.90 \times 10^{20} \text{ cm}^{-2}$ ). Point sources identified using the X-ray images are excluded from the spectral analysis. The spectra obtained by MOS1, MOS2 and pn are fitted simultaneously with their relative normalisations left as free parameters.

The spectra are binned with a minimum of 30 counts per bin and fitted in the 0.35–7 keV band with a Gaussian differential emission measure distribution model (*gdem*), which we showed in Chapter 4 to be the most appropriate for the data. We note that the average temperature is the same for the *gdem* model as for a single temperature fit, but the *gdem* model usually provides a significantly improved fit.

Due to the high photon statistics of this deep observation, our best fit reduced  $\chi^2$ s are sensitive to calibration problems and to the differences between the individual EPIC detectors. To account for this, we include 3% systematic errors over the entire energy band used for fitting.

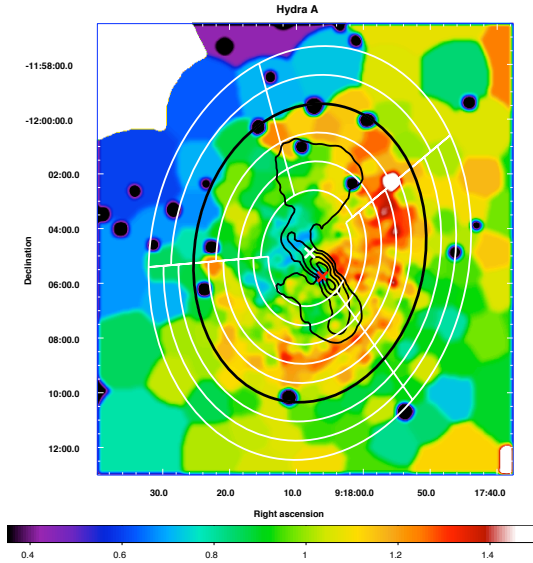


Figure 5.1: Pressure map divided by a radially symmetric, smooth model. 90 cm radio contours (Lane et al. 2004) are shown in black. The shock is clearly seen as a ring of enhanced pressure, whose shape is simplest approximated by the black ellipse. The center of this ellipse (white cross) is shifted towards the NE with respect to the cluster center (red cross).

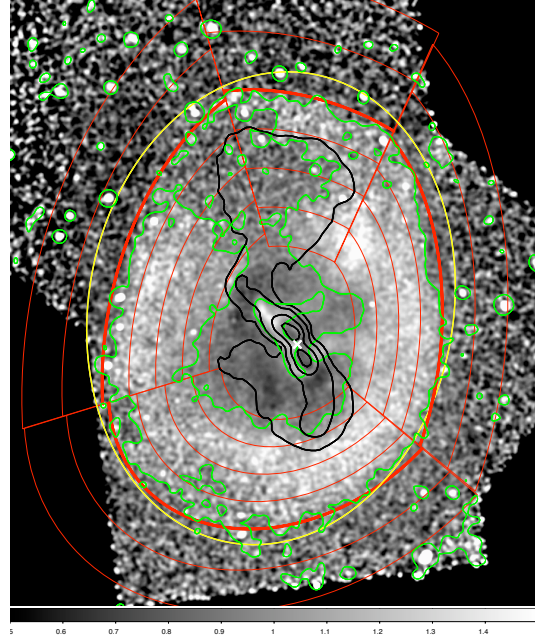


Figure 5.2: Chandra surface brightness map divided by a 2D elliptical beta model. Contours of the surface brightness to beta model ratio are shown in green, 90 cm radio contours (Lane et al. 2004) are shown in black. The yellow ellipse is the best-fit ellipse to the shock front in the pressure map. The thick red elliptical sectors show a further improved approximation to the shock shape. The white cross marks the cluster center.

## 5.4 The shock geometry

Using the fit results for the 2D temperature map of Hydra A presented in Chapter 4, we created a quasi-deprojected pressure map of the cluster, with pressure defined as  $p = n_e kT$ . The electron density  $n_e$  is determined from the spectrum normalization  $Y \propto n_e^2 V$ , with  $V$  being the volume along the line of sight (LOS) corresponding to each spatial bin in the 2D map. Let  $R_{\max}$  and  $R_{\min}$  be the maximum and minimum radii with respect to the cluster center between which a spatial bin is contained. Assuming that only the gas between the sphere with the minimum radius and the sphere with the maximum radius contribute to the emission (Henry et al. 2004; Mahdavi et al. 2005) yields, where  $L$  is the length of the contributing volume along the LOS and  $S$  is the area of the bin in the plane of the sky,

$$L = 2 \sqrt{(R_{\max}^2 - R_{\min}^2)} \text{ and } V = 2SL/3. \quad (5.1)$$

We thus take into account an approximate estimation of the three-dimensional extent of each bin, but assume a constant temperature along the line of sight. Since most of the emission in each bin originates from the densest gas which is found at the smallest effective 3D radii, the map mostly reflects the distribution of the gas pressure in a two dimensional slice through the middle of the cluster, perpendicular to the line of sight. We fitted the radial pressure profile using non-parametric, locally weighted, linear regression smoothing and subsequently divided the pressure map by the resulting radial model in order to reveal small-scale fluctuations. The result is shown in Fig. 5.1.

The shock is clearly seen as an approximately elliptical ring of enhanced pressure, on average 20% higher than the value in the radially smooth model. The simplest approximation to the shock shape seen in the pressure map is an ellipse, indicated in black in Fig. 5.1, with a semi-major axis of 5.5' (360 kpc) oriented 10 degrees clockwise from the N–S direction, and a semi-minor axis of 4.2' (275 kpc). The center of this ellipse (white cross in Fig. 5.1) is shifted by  $\sim 1.1'$  (70 kpc) towards the NE with respect to the cluster center (shown with a red cross in the same figure).

We divided the exposure and background corrected Chandra image obtained by combining the two deepest exposures of Hydra A (totaling 200ks observing time) by the best-fit 2D elliptical beta model (with ellipticity 0.17 and position angle 50.7 degrees counterclockwise from west) in order to highlight the position of the shock front and compare it to the ellipse described above. The resulting map is shown in Fig. 5.2. We find that, although the shock front shape is not exactly elliptical, the ellipse which best matches the shock in the pressure map does provide a good simple approximation, especially taking into consideration that the spatial bins used for the pressure map are up to 0.8' in diameter around the position of the shock. In a more exact approximation, the shock front shape can be described as a set of 4 elliptical sectors, each centered on the cluster center, over-plotted in thick red lines Fig. 5.2.

## 5.5 1D shock model and Mach number estimates

To quantify the shock, we first use a spherically symmetric hydrodynamic model of a point explosion at the center of an initially isothermal, hydrostatic atmosphere (as employed also by e.g. Nulsen et al. 2005). We assume the initial gas density profile to be a power law,  $\rho(r) \propto r^{-\eta}$ , with  $\eta$  adjusted to make the surface brightness profile of the undisturbed gas consistent with the observed surface brightness profile beyond the shock. The gravitational field,  $g \propto 1/r$ , and gas temperature are scaled to make the undisturbed atmosphere hydrostatic.

The XMM-Newton 0.4 – 7. keV response for a range of temperatures was tabulated using XSPEC, with detector response files appropriate for these observations and an absorbed *mekal* model with metal abundances set to 0.3 times solar (the results are insensitive to these parameters, including the preshock temperature). We scale the temperature profile from the model to obtain an unshocked gas temperature of 3.6 keV. The surface brightness profiles are then determined using the tabulated XMM response, the density and temperature model profiles, and assuming spherical symmetry to calculate the effects of projection along the line of sight. We additionally smooth the obtained profile by the XMM-Newton point-spread function (PSF), which we model by a King profile with a core radius of 3.5'' and a slope of 1.36 (Markevitch 2002).

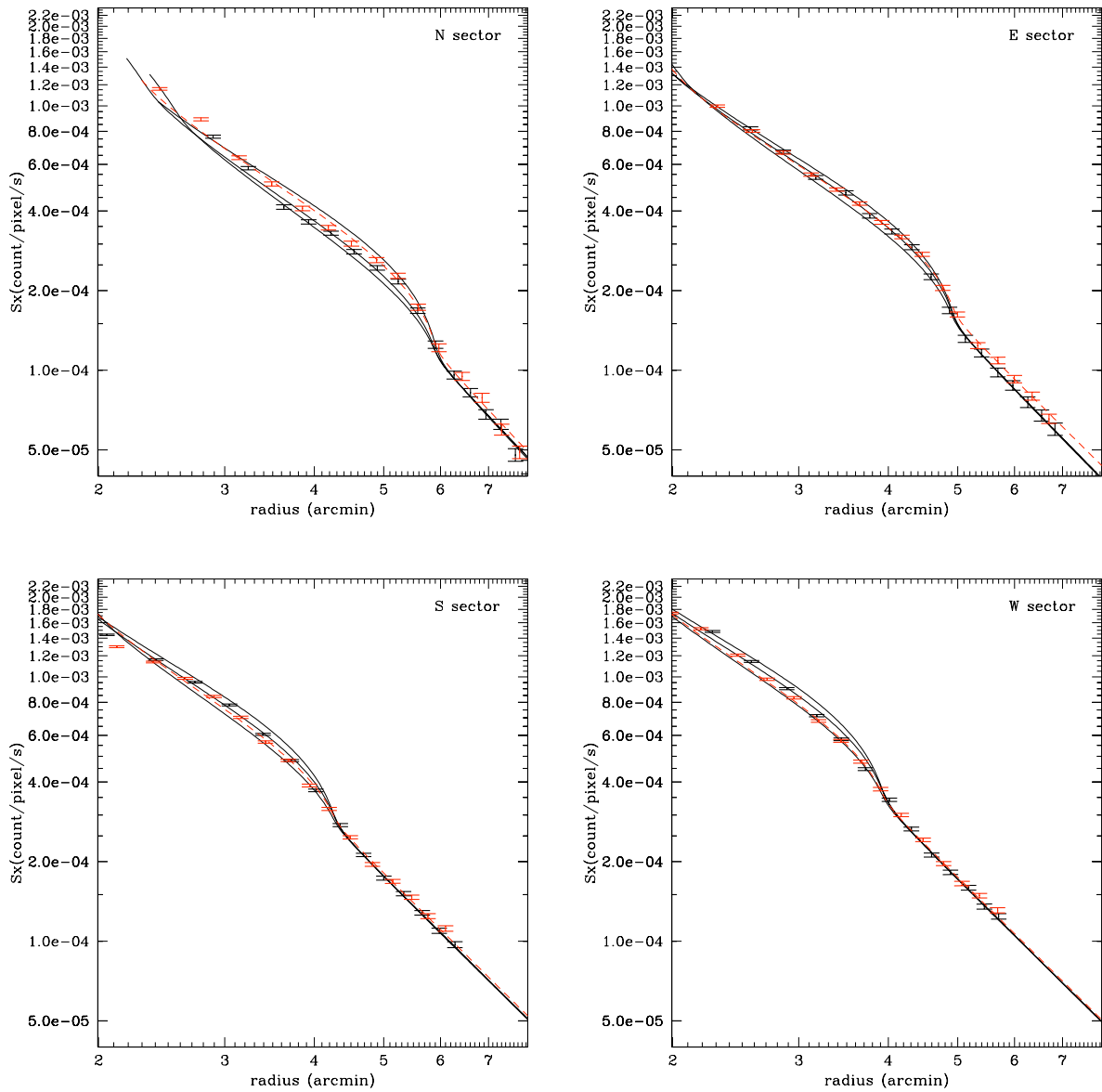


Figure 5.3: Surface brightness profiles (from EPIC/pn) and fitted shock models (best-fit and bracketing). Data points from the pressure-map based annuli are indicated in black. The three lines show model surface brightness profiles for shocks with Mach numbers of 1.41, 1.30, 1.25 to the N; 1.35, 1.30, 1.25 to the E; 1.32, 1.27, 1.22 to the S; 1.35, 1.30, 1.25 to the W (increasing upward). Red points show the results from the Chandra-shape based annuli. For plot legibility, the bracketing models for the Chandra-shape based annuli are not shown. The model surface brightness profiles have Mach numbers of 1.33 to the N; 1.30 to the E; 1.23 to the S; 1.25 to the W.

The shock weakens as the hydrodynamic model evolves and, since the initial conditions are self-similar, the flow can be scaled radially to place the model shock at the location of the observed shock. Surface brightness is finally scaled to match the observed profile in the unshocked region.

In Fig. 5.3, we show background-subtracted, exposure corrected EPIC/pn surface brightness profiles from elliptical annuli in four different sectors towards the N, E, S, and W from the core and the best-fit shock models (whose parameters are presented in Table 5.1). The error estimates are based on the three (one best-fit and two bracketing) models plotted in Fig. 5.3 for each sector, respectively. We compare two different choices for the shape of these annuli: parallel to the ellipse which approximates the shock seen in the pressure map (Fig. 5.1) and parallel to the four elliptical sectors which provide a more exact approximation to the shock seen in the Chandra surface brightness map (Fig. 5.2). A Mach 1.3 shock with an age of 130–230 Myr and an energy of  $1.5\text{--}3\times 10^{61}$  ergs gives a reasonably good fit to the observed shock profile in each of the sectors using both choices of extraction region shape, in agreement with the values derived by Nulsen et al. (2005). Note that a Mach 1.3 model with a radius of approximately  $5'$  (the average radius of the entire shock front) and age of 180 Myr also provides a reasonable fit to the integrated profile obtained by combining all the four sectors, apart from 2-3 data points immediately inside the shock front where, due to the non-spherical geometry, the jump appears smoother compared to the model prediction. The pre-shock electron density needed to calculate the shock energy was determined by fitting the data points outside 200 kpc in the deprojected profile of David et al. (2001) with a power-law and extrapolating.

Table 5.1: Best-fit parameters for the shocked surface brightness model in the four sectors.

Sector	radius (arcmin)	$\eta$	Mach number	Shock energy ( $10^{61}$ ergs)	Shock age (Myr)
Np <sup>a</sup>	6.0	2.9	$1.30 \pm 0.08$	$2.3 \pm 1.0$	$230 \pm 30$
Ep	5.0	2.8	$1.34 \pm 0.06$	$2.6 \pm 0.6$	$170 \pm 16$
Sp	4.3	2.7	$1.30 \pm 0.06$	$2.0 \pm 0.7$	$154 \pm 20$
Wp	4.0	2.7	$1.33 \pm 0.06$	$2.3 \pm 0.7$	$132 \pm 16$
Nc <sup>b</sup>	6.0	2.9	$1.33 \pm 0.08$	$2.7 \pm 1.0$	$215 \pm 30$
Ec	5.0	2.7	$1.30 \pm 0.05$	$2.0 \pm 0.5$	$180 \pm 16$
Sc	4.3	2.7	$1.23 \pm 0.06$	$1.4 \pm 0.6$	$171 \pm 18$
Wc	4.0	2.7	$1.25 \pm 0.06$	$1.6 \pm 0.6$	$151 \pm 18$

<sup>a</sup>Annuli shape based on the pressure map

<sup>b</sup>Annuli shape based on the Chandra image

Based on the best-fit radii in the different sectors, we can also obtain an independent estimate of the offset of the shock center with respect to the cluster center, which can be approximated as

$$\sqrt{\left(\frac{r_N - r_S}{2}\right)^2 + \left(\frac{r_E - r_W}{2}\right)^2} \approx 1', \text{ within 10\% of the value estimated in Sect. 5.4.}$$

There are several caveats in using this simple hydrodynamic model: the initial density profile is only well approximated as a power law locally, the shock front is clearly aspherical, and the

outer radio lobes lie close behind the shock front in the N and S, so that they still have an influence in driving the shock, violating our assumption that the shock front is driven by a point explosion. The different shock ages required for different sectors (Table 5.1) also point out the need for a more complicated scenario. Despite these shortcomings, the models do provide reasonable fits to the surface brightness in the region of the shock front.

## 5.6 The temperature jump associated with the shock

A hint of a temperature jump in Hydra A can already be seen in the radial profiles presented in Chapter 4. The data point in the 3–4' radial bin, behind the W and S shocks (located at 4 and 4.3', Table 5.1), cannot be fit with a smooth function going through the other data points (Fig. 5.4). The radial bins in the previous chapter were chosen independently of the shock in order to determine metallicity profiles; we further show in Fig. 5.4 the temperature profile obtained from elliptical annuli designed to follow the shock ellipse seen in the pressure map. These data points are plotted against the mean radius of the extraction regions. Note that each region contains emission from a larger range of radii than the circular annuli used for the radial profile. The average radius of the shock ellipse (Fig. 5.1) is shown with a vertical dashed line. There is a good agreement with the radial profile and a temperature jump can be clearly seen behind the average radius of the shock ellipse. The temperature jump corresponds to an average Mach number  $M = 1.20 \pm 0.05$  (Table 5.2). The profile extracted from regions parallel to the Chandra-based shock shape is very similar and the temperature jump corresponds to  $M = 1.25^{+0.05}_{-0.10}$ .

The temperature varies little between 2–8', the region we are interested in for determining the shock properties. However, to eliminate any effects due to an underlying temperature profile in the cluster, we used a 3<sup>rd</sup> degree polynomial fit to the radial temperature profile (excluding the point at 3.5') to compare the temperature differences between the pre- and post-shock regions with expected temperature differences from this polynomial approximation of the cluster temperature profile. The polynomial fits the data points in the radial profile well (see Fig. 5.4), but drops very rapidly at large radii (beyond the region of interest for determining the shock properties). For this reason, we adopt a different function for the radial dependence of the temperature for the 3D hydrodynamic simulations in Section 5.7.1. This function, over-plotted in cyan in Fig. 5.4, agrees very well with the polynomial approximation in the region around the shock and shows a slower decrease at large radii, ensuring that the temperature does not become negative in the simulation box.

To describe the shock in more detail and to obtain temperature profiles using spectral extraction regions spanning a smaller range of radii, we also divided the data in four different sectors (N, E, S, and W) again using two sets of annuli for each sector: one parallel to the ellipse in the pressure map (following the white lines in Fig. 5.1) and one parallel to the corresponding elliptical sector approximating the position of the Chandra surface brightness discontinuity (thin red lines in Fig. 5.2). Towards the N and E we use wider annuli compared to the S and W, where the shock is closer to the cluster center providing a higher surface brightness around the shocked region.

The temperature profiles obtained for the two choices of extraction regions are in good agree-

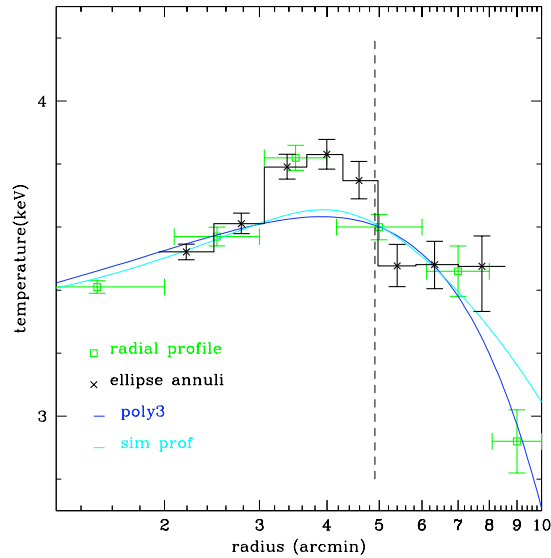


Figure 5.4: Radial temperature profile from Chapter 4. Best-fit third degree polynomial overplotted in blue, temperature profile assumed as initial condition for the simulations in Sect. 5.7.1 in cyan. Temperature profile in elliptical annuli parallel to the shock seen in the pressure map as a function of average radius of the extraction region shown with black crosses. The average radius of the shock ellipse (Fig. 5.1) is shown with a vertical dashed line.

ment for all four sectors (see Fig. 5.5). The clearest indication of the presence of a temperature jump associated with the shock is seen in the W sector. Towards the south, a temperature jump is seen, but slightly further behind the surface brightness jump compared to the west (and the two different choices of extraction regions give different shifts). Towards the E, there is clear indication that the gas behind the shock is hotter than the expected average at that radius, but the temperature drop immediately beyond the shock raises the question of whether the used polynomial approximation is reliable for describing the undisturbed temperature distribution in this sector. Towards the N, there are only very weak ( $< 1\sigma$ ) deviations of the gas temperature in the shocked region from the radial average, and the errors in this sector are the largest given that it is furthest away from the cluster center and its opening angle is the smallest.

We grouped the two annuli with the largest jumps compared to the radial average to obtain a more accurate temperature of the shocked gas,  $kT_{\text{sh}}$ , and the next two annuli at larger radii to obtain the temperature of the unshocked gas,  $kT_{\text{unsh}}$ . For the elliptical shock shape approximation, the grouped annuli are marked in Fig. 5.5. For the Chandra-based regions, we always grouped the two annuli immediately before and after the vertical dashed line indicating the position of the shock from the surface brightness fits. The results are shown in Table 5.2. We find a temperature jump at the position of the shock above that expected from a simple polynomial approximation of the cluster profile with a significance of typically  $2\sigma$  (between 0 and  $2.9\sigma$ ) in individual sectors (statistical only, neglecting the errors in determining the polynomial). The  $1\sigma$

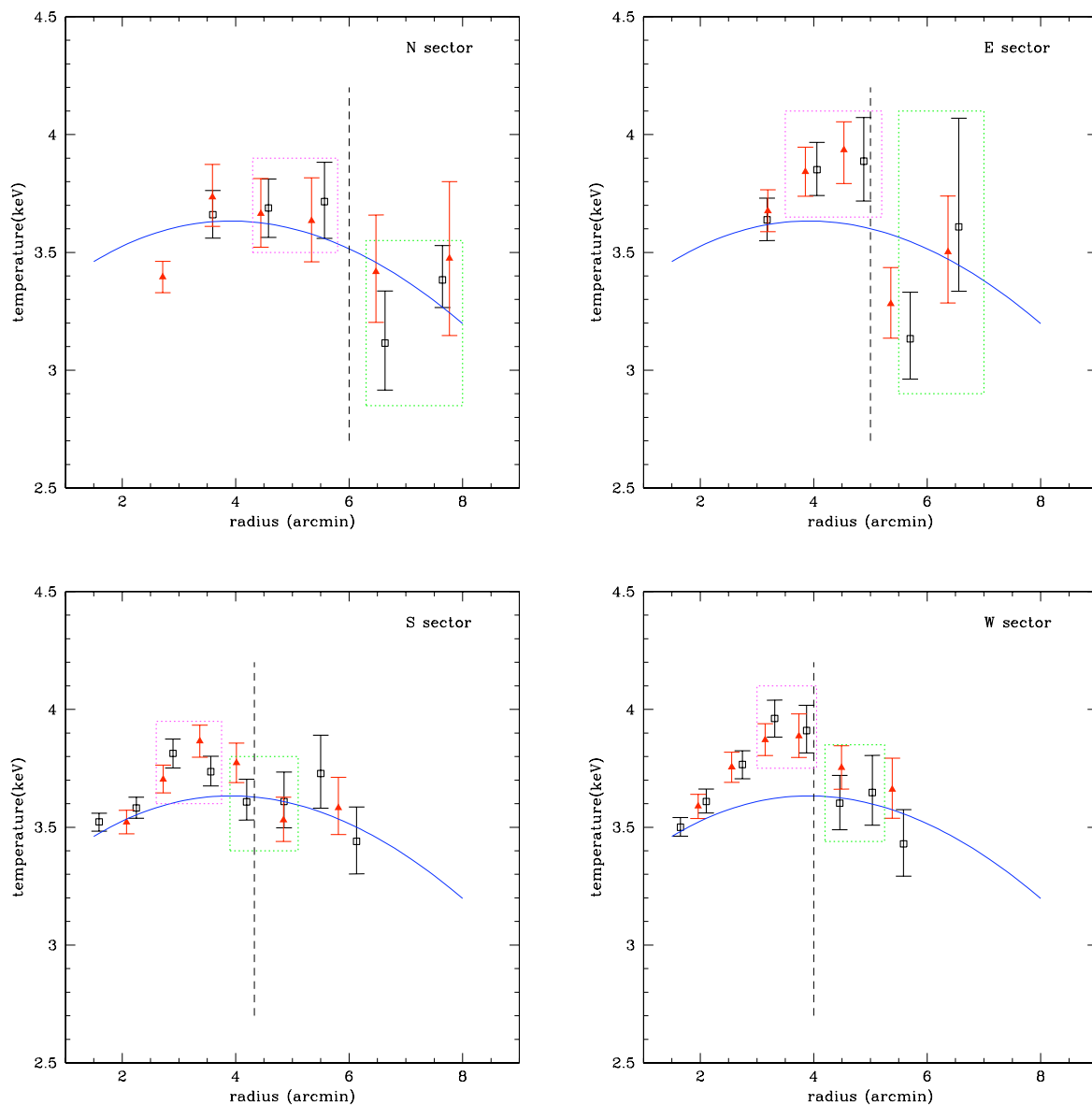


Figure 5.5: Temperature profiles in 4 different sectors. Data points from the pressure-map based annuli are indicated with black squares, red triangles show the results from the Chandra-shape based annuli. The blue line represents a third-degree polynomial fit to the radial temperature profile. The dotted magenta and green rectangles indicate the pressure-map based annuli used to determine the temperature of the shocked gas and unshocked gas, respectively. The vertical dashed line indicates the position of the shock from the surface brightness fits (Table 5.1).

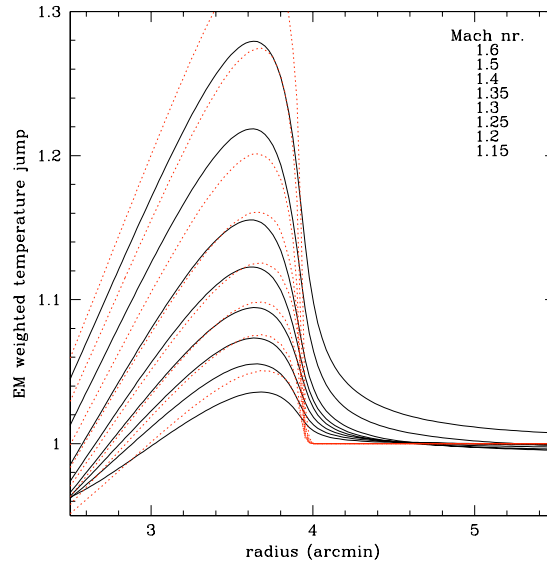


Figure 5.6: Expected emission-measure weighted temperature profile across the shock relative to the undisturbed temperature (the cluster is assumed isothermal) using the 1D model. The red dotted line represents shock models including only projection effects, the black solid line additionally takes into account the smoothing due to the XMM-PSF. This particular plot assumes the power-law index of the density profile to be  $\eta = 2.7$ . Model Mach numbers are from 1.15 to 1.6 (see plot labels, top line represents model with highest Mach number).

error intervals for the temperature jumps obtained using the two different region choices overlap in each of the 4 sectors. Combining the significances in the four sectors, the total significance of the temperature jump associated with the shock is  $4.3\sigma$  for the pressure-based regions and  $4.0\sigma$  for the Chandra-based regions. This is larger than the significance obtained fitting the entire annuli without dividing into sectors. A possible explanation is that for large, asymmetric regions spanning a wide range of radii, the average temperature is not so well represented by evaluating the polynomial fit to the radial temperature profile at the average radius of those regions, which may overestimate the expected temperature differences in the absence of a shock ( $\Delta T_{\text{exp}}$  in Table 5.2) and thus underestimate the temperature jump. This effect is less important if the extraction regions are smaller (e.g. the sectors) and cover a smaller range in radius.

To calculate the Mach number from the observed temperature jumps, we resort again to the 1D shock model. We use the 1D temperature and density model profiles and the assumption of spherical symmetry to determine an emission-measure weighted temperature profile which takes into account the effects of projection along the line of sight. We then apply the correction due to the XMM-PSF. By plotting the temperature profiles obtained in this way for models with several Mach numbers (Fig. 5.6), we can identify which Mach number corresponds to the temperature jump (in percent) which we observe. These are also reported in Table 5.2.

Table 5.2: Best-fit post- and pre-shock temperatures, relative temperature jumps  $\delta T$ , and corresponding Mach numbers.

Sector	$kT_{\text{sh}}$	$kT_{\text{unsh}}$	$\Delta T = kT_{\text{sh}} - kT_{\text{unsh}}$	$\Delta T_{\text{exp}}^a$	$\delta T^b$	Mach
All p <sup>c</sup>	$3.80^{+0.03}_{-0.03}$	$3.56^{+0.05}_{-0.05}$	$0.24 \pm 0.06$	0.10	$3.9 \pm 1.7\%$	$1.20^{+0.05}_{-0.05}$
Np	$3.73^{+0.09}_{-0.10}$	$3.22^{+0.18}_{-0.17}$	$0.51 \pm 0.20$	0.24	$7.5 \pm 5.6\%$	$1.35^{+0.10}_{-0.20}$
Ep	$3.86^{+0.10}_{-0.09}$	$3.33^{+0.17}_{-0.15}$	$0.53 \pm 0.19$	0.12	$11.3 \pm 5.2\%$	$1.40^{+0.05}_{-0.15}$
Sp	$3.79^{+0.04}_{-0.05}$	$3.62^{+0.07}_{-0.07}$	$0.17 \pm 0.08$	0.00	$4.7 \pm 2.2\%$	$1.25^{+0.05}_{-0.10}$
Wp	$3.95^{+0.07}_{-0.06}$	$3.63^{+0.10}_{-0.09}$	$0.32 \pm 0.11$	0.02	$8.3 \pm 3.0\%$	$1.30^{+0.10}_{-0.05}$
All c <sup>d</sup>	$3.85^{+0.03}_{-0.03}$	$3.60^{+0.05}_{-0.05}$	$0.25 \pm 0.06$	0.09	$4.5 \pm 1.7\%$	$1.25^{+0.05}_{-0.10}$
Nc	$3.71^{+0.11}_{-0.11}$	$3.44^{+0.18}_{-0.17}$	$0.51 \pm 0.20$	0.25	$< 6.4\% (1\sigma)$	$< 1.35$
Ec	$3.87^{+0.08}_{-0.07}$	$3.35^{+0.12}_{-0.12}$	$0.53 \pm 0.19$	0.11	$11.3 \pm 3.9\%$	$1.40^{+0.10}_{-0.10}$
Sc	$3.84^{+0.05}_{-0.05}$	$3.57^{+0.08}_{-0.07}$	$0.17 \pm 0.08$	0.06	$5.8 \pm 2.5\%$	$1.25^{+0.10}_{-0.05}$
Wc	$3.90^{+0.06}_{-0.06}$	$3.73^{+0.08}_{-0.08}$	$0.32 \pm 0.11$	0.03	$3.9 \pm 2.6\%$	$1.20^{+0.10}_{-0.10}$

<sup>a</sup>“exp” always refers to the expected value based on the radial dependence of the cluster temperature

<sup>b</sup> $(\Delta T - \Delta T_{\text{exp}}) / kT_{\text{sh,exp}}$

<sup>c</sup>Annuli shape based on the pressure map

<sup>d</sup>Annuli shape based on the Chandra image

## 5.7 Relative motions in the cluster and the shape of the shock front

In Sect. 5.4, we showed that the shock front is elliptical and that its center is offset from the cluster center by  $\sim 70$  kpc. However, in Sect. 5.5, we conclude that the Mach number is roughly the same for all the four different sectors, although the distance between the shock front and the cluster center differs. This is puzzling because, if the shock originates at the cluster center - which currently coincides roughly with the position of the AGN - then the shock front must have been moving faster on average towards the N, where it is now further away from the center, than towards the S or W. If the shock was moving as much as 1.5 times faster on average in one direction than in another (the ratio of the shock radii in the N and W, Table 5.1), one would expect to see some differences also in the current distribution of Mach numbers along the shock front: scaling up the Mach number in the W by a factor 1.5 means the expected Mach number in the N should be around 1.8, which is excluded by the data. The discrepancy between the model shock ages in different sectors also hints at the same problem, namely that the observed shape and properties of the shock cannot be simply explained by a point explosion.

Not only the shock front but also the radio lobes show a N–S asymmetry. While the shock radius to the N is 1.5 times bigger than to the S, the N radio lobe also extends much further out than the S lobe, which rises and then seems to bend back towards the cluster center. This led us to investigate whether relative motions between the AGN and the ICM could explain both the disturbance of the southern radio lobe and the elliptical, offset shape of the shock front.

To this end, we performed 3D hydrodynamical simulations of a symmetrical pair of back-to-

Table 5.3: ICM parameters for the 3D simulation.

	component 1	component 2
$R_{\text{ICM}}$ (kpc)	27.7	235.6
$\rho_{\text{ICM}0}$ ( $\text{g cm}^{-3}$ )	$8 \cdot 10^{-26}$	$3.33 \cdot 10^{-27}$
$\beta$	0.686	0.907
$m_1$ (K/kpc)		25,000
$n_1$ (K)		$3.6 \times 10^7$
$m_2$ (K/kpc)		-21,000
$r_{\text{break}}$ (kpc)		250
$a_{\text{break}}$ (kpc)		100

back jets that originate from the cluster center. These jets interact with the surrounding ICM in which we triggered large-scale motions.

### 5.7.1 Model cluster

We assume the gas density and temperature distribution in the cluster to be spherically symmetric. The initial radial density profile for the ICM is modelled by a double  $\beta$ -profile (Wise et al. 2007; David et al. 2001). The parameters are given in Table 5.3. As a temperature profile,  $T(r)$ , we use

$$\begin{aligned}
 T(r) &= T_1(r)C(r) + T_2(r)[1 - C(r)], \text{ where} & (5.2) \\
 T_1(r) &= m_1 \cdot r + n_1 \\
 T_2(r) &= m_2 \cdot r + n_2 \\
 n_2 &= (m_1 - m_2)r_{\text{break}} + n_1 \Leftrightarrow T_1(r_{\text{break}}) = T_2(r_{\text{break}}) \\
 C(r) &= 1 - \frac{1}{\pi} \left( \arctan \frac{r - r_{\text{break}}}{a_{\text{break}}} + \frac{\pi}{2} \right), & (5.3)
 \end{aligned}$$

which connects two linear functions smoothly. The parameters (see Table 5.3) are chosen to fit the data from the previous chapter. The temperature is declining both inwards and outwards from a cluster-centric radius of 250 kpc. For the initial cluster we assume hydrostatic equilibrium, so that the given ICM density and temperature profiles determine the pressure distribution, and thus the gravitational potential in the cluster.

### 5.7.2 Model jet

The jet pair is modelled by defining two jet “nozzles” composed of all grid cells immediately below and above the  $x$ - $z$ -plane, whose distance to the  $y$ -axis falls below the jet nozzle radius,  $r_{\text{jet}}$ . For the grid cells immediately above the  $x$ - $z$ -plane, the fluxes towards the  $+y$ -direction are set to a strong outflow with density  $\rho_{\text{jet}}$ , pressure  $p_{\text{jet}}$  and velocity  $v_{\text{jet}}$ . The grid cells immediately

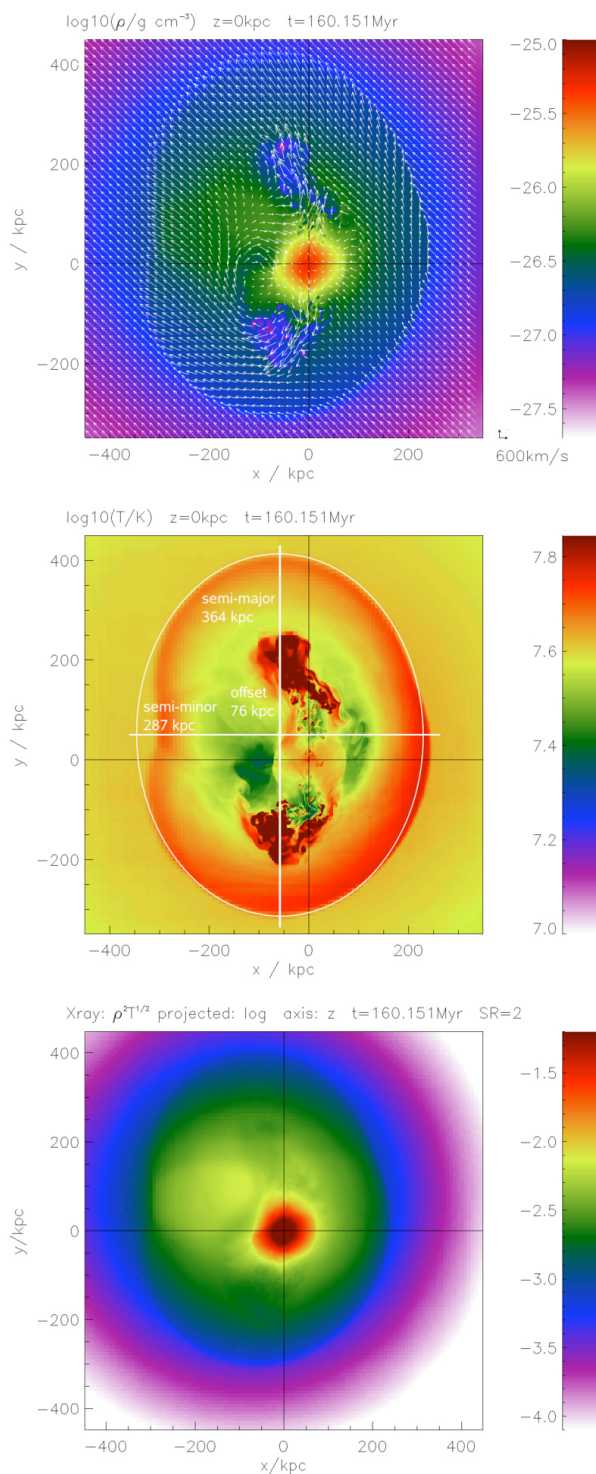


Figure 5.7: Shock front and bubbles at 160 Myr. *Top:* slice through the computational domain, showing density (colour-coded) and velocity field (arrows). *Middle:* temperature (colour-coded), with fitted shock ellipse (white line) and labelled axes and offset. *Bottom:* Projected X-ray emission from simulated cluster.

Table 5.4: Jet parameters for the 3D simulation.

radius $r_{\text{jet}}$	6 kpc
power $P_{\text{jet}}$	$4.75 \times 10^{46}$ erg/s
lifetime $\tau_{\text{jet}}$	10 Myr
total energy input	$3 \times 10^{61}$ erg
velocity $v_{\text{jet}}$	$20\,000$ km s $^{-1}$
Mach number $M_{\text{jet}}$	5.9

below the  $x$ - $z$ -plane are treated accordingly to produce the flow in the  $-y$ -direction. We use the parameters listed in Table 5.4. The chosen Mach number brings the jet gas close to pressure equilibrium with the ICM in the cluster center, so that during the active phase the jet is mainly momentum driven.

### 5.7.3 Generation of bulk motion

The ICM in galaxy clusters is known to be in motion, the velocity field being both inherited from cluster formation and more recently achieved by current gas accretion flows. Heinz et al. (2006) showed that these motions can have an important impact on the buoyant rise of radio bubbles. Although such flows are not necessarily coherent over scales of several 100 kpc, in Hydra A the offset of the shock ellipse and morphology of the radio lobes suggest a large-scale predominantly coherent flow. As a most simple model for such a scenario, we initialize a smooth velocity field in the ICM of our model cluster, namely a potential flow around a sphere of a 100 kpc radius, centered on the cluster center. This choice has the advantage that the ICM in the cluster center is only mildly affected by the bulk motion, but the shock front and the bubbles spend enough time in the flow region to be affected. Furthermore, the direction and amplitude of the bulk flow are clearly defined by requiring that when the shock reaches the observed size and age, its center is offset from the cluster center by the observed distance of 70 kpc towards the NE (Sect. 5.4). We use a flow velocity of  $670$  km s $^{-1}$  towards  $(-1, 1, 0)$  based on the simple analytical argument that exposing the shock to a bulk flow of  $670$  km s $^{-1}$  for about 100 Myr (the approximate estimated age minus the time it takes for the shock to reach the flow region), it would be carried along with the flow by  $670$  km s $^{-1} \times 100$  Myr  $\approx 70$  kpc. This assumes that the bulk flow is in the plane of the sky; if the actual gas motions make an angle  $\theta$  with respect to this plane, one would need a higher velocity of  $670/\cos\theta$  km s $^{-1}$ .

### 5.7.4 Code

We use the Eulerian adaptive-mesh refinement code FLASH (version 2.5) with radiative cooling (Sutherland & Dopita 1993) and static gravity. The cluster potential is defined by the parameters described in Sect. 5.7.1. The jet module is similar to the one in Brügggen et al. (2007).

The total grid size is  $(-1$  Mpc,  $1$  Mpc) $^3$ . The adaptive mesh refinement allows us to use a resolution of 0.5 kpc in the cluster center, which ensures that the jet nozzle is resolved sufficiently. In order to limit computational requirements, we restrict the refinement with increasing distance

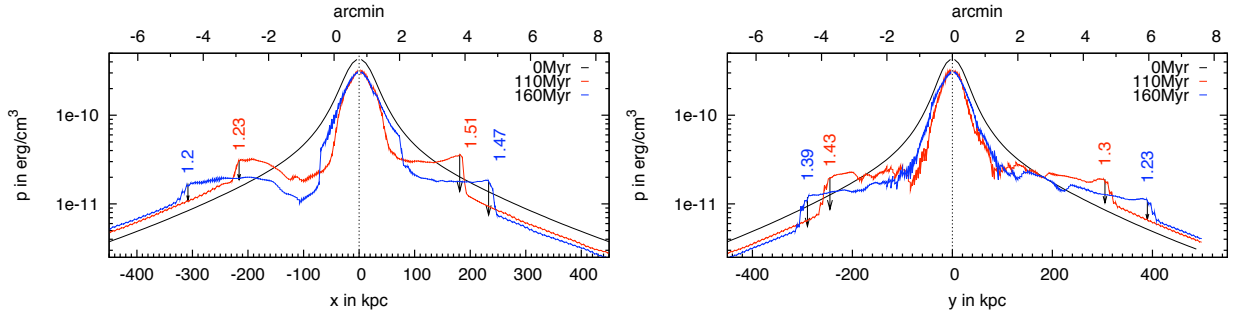


Figure 5.8: Evolution of pressure profiles along the grid’s  $x$ - and  $y$ -axis through the center of the cluster. The shock is marked by the black arrows, numbers of corresponding colour indicate the Mach numbers of the shock as derived from the pressure jump.

to the cluster center. The best resolution allowed outside 16, 100, and 200 kpc is 1, 4, and 8 kpc, respectively. We note that the lowest achieved resolution is of the order of the XMM-PSF.

### 5.7.5 Simulation results

The evolution of the jet-induced structures proceeds in two stages: the active jet phase and the subsequent passive phase (compare also Reynolds et al. 2001). During the active phase, the jets evacuate two channels along the  $y$ -axis. During this interval, the jet-induced structure still resides inside the inner 100 kpc and thus does not feel the bulk flow. When the jets are switched off, the evolution proceeds passively. At that moment, the jet cocoons are still overpressured and continue to expand and drive a shock into the surrounding ICM. The expanding cocoons form two bubbles which rise buoyantly. While doing so, in their wakes, they drag up cooler gas from the cluster center. Eventually, the shock detaches from the bubbles, while the shock is still expanding and the bubbles are still rising. At 160 Myr, the shock has reached the size observed in Hydra A.

About 50 Myr after the jet was started, the shock enters the region of the bulk flow, which causes different shock propagation speeds with respect to the cluster center for different directions. Thus, after 160 Myr, the shock ellipse is offset approximately towards  $(-1, 1, 0)$  from the cluster center by 70 kpc, as shown in Fig. 5.7. This figure shows a density and a temperature slice through the grid at 160 Myr as well as the corresponding simulated X-ray map obtained by integrating  $\rho^2 \sqrt{T}$  along the  $z$  direction.

In Fig. 5.8, we show pressure profiles along the grid’s  $x$ - and  $y$ -axes. The discontinuities due to the shock can be clearly seen. From the ratio of the pre- and post-shock values we calculated a Mach number for each profile, resulting in an average Mach number of 1.3 at 160 Myr. The Mach numbers in different directions range between about 1.2 and 1.5.

## 5.8 Discussion

The simulation successfully provides one possible explanation for the problem posed at the beginning of the previous section, namely why the Mach number is roughly the same in different sectors although the distance between the shock front and the cluster center differs. The simulated shock has Mach numbers and radii which agree with the observations in all sectors, and requires a consistent shock age in all directions, which a simple point explosion did not.

### 5.8.1 Comparison to observation

The simulation successfully reproduces:

- the size and shape (ellipticity) of the observed shock. The ellipse we fitted to the simulated shock (see Fig. 5.7) has a semi-major axis of  $\approx 365$  kpc and a semi-minor axis of  $\approx 290$  kpc.
- the observed overall shock Mach number of around  $M \sim 1.3$ .
- the observed offset of the shock ellipse, about 70 kpc.
- a total energy input and average shock age of  $3 \times 10^{61}$  ergs and 160 Myr, respectively. These are within the range of the values derived from the 1D model.

We see, therefore, an encouraging agreement with the observations. Several drawbacks, on the other hand, are listed below:

- a bulk flow in the ICM leads to different Mach numbers at opposite sides of the shock: Where the shock has to move against the ICM flow, its effective velocity with respect to the ICM is larger and thus the shock is stronger (in this simulation, in the  $-y$ - and  $+x$ -direction, respectively S and W). The observational data seems to indicate the opposite, namely a Mach number which is stronger in the E than in the W. However, with the current error bars, the observational results are still consistent with the simulation.
- the strong bulk flow affects the shape of the simulated southern radio lobe but does not bend it nearly as much as the observed lobe.
- In the simulation, the shock is detached from the northern bubble, whereas in Hydra A, the northern bubble still seems to be driving it. This is one of the main difficulties in making a realistic model for the shape of the shock front. In the simulation, the southern bubble is also somewhat further away from the shock than observations suggest.
- The simulation shows an offset temperature dip at approximately  $(0, -100, 0)$  kpc, which is not observed. The temperature contrast however is not very large and may be washed out by projection. For a lower bulk flow velocity, this feature is absent (see Fig. 5.9). At that location, a surface brightness enhancement, also not present in the observation, can be seen in the projected X-ray map.

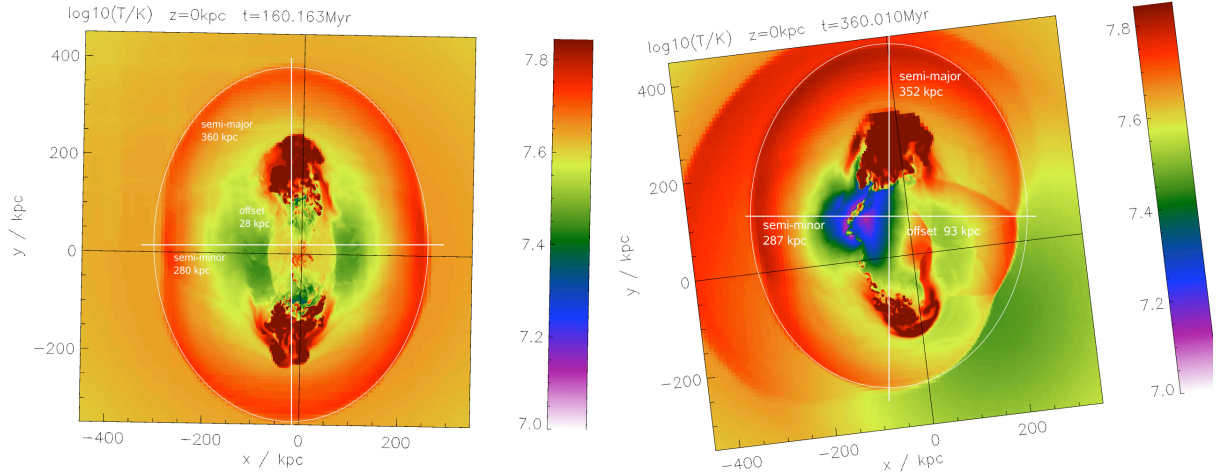


Figure 5.9: Temperature slices taken at 160 Myr after the jet was launched for two alternative simulations. *Left*: the bulk flow velocity was reduced to  $260 \text{ km s}^{-1}$ . *Right*: The ICM bulk flow was generated by ICM sloshing.

### 5.8.2 Effects of AGN activity on the temperature structure in the cluster core

The plasma in many cool cores of galaxy clusters was proved to have an intrinsic multi-temperature structure (e.g. Kaastra et al. 2004). Among many examples, the most remarkable are M87 (Belsole et al. 2001; Molendi 2002, Chapter 3), Perseus (Sanders & Fabian 2007), Centaurus (Matsushita et al. 2007a; Sanders et al. 2008), 2A0335+096 (Werner et al. 2006b). This multi-temperature structure can be due either to a small amount of gas which does cool radiatively down to low temperatures ( $< 1 \text{ keV}$ ) or to AGN-ICM interaction. The latter generates both hotter gas compared to the ambient (through shocks) and cooler gas which adiabatically expands as it is entrained by the rising radio lobes. Both of these processes are also observed in Hydra A (Nulsen et al. 2005; Wise et al. 2007; Simionescu et al. 2009b, and this chapter). The temperature structure in Hydra A in fact is best described by a very broad Gaussian distribution with a full-width at half maximum of around  $4.2 \text{ keV}$  (see previous chapter). We aim to determine from this simulation what is the effect of the AGN-ICM interaction on the multi-temperature structure and compare this to the multi-temperature structure observed in Hydra A. To this end, we considered a cylinder with  $3'$  radius going through the center of the simulation box along the  $z$  axis and constructed a histogram of the emission measure as a function of temperature at the initial and final stages of the simulation. Initially, only different temperatures as a function of radius (inside the central  $3'$  or projected along the cylinder) contribute to the multi-temperature structure, which has a very narrow distribution. At the end of the simulation, the AGN activity has broadened the multi-temperature distribution significantly both towards higher and lower temperatures. However, we still do not achieve the best-fit width obtained for the temperature distribution in the central  $3'$  spectrum extracted from the observation (Fig. 5.10). This suggests either that the initial distribution of temperatures should be much broader than we assumed be-

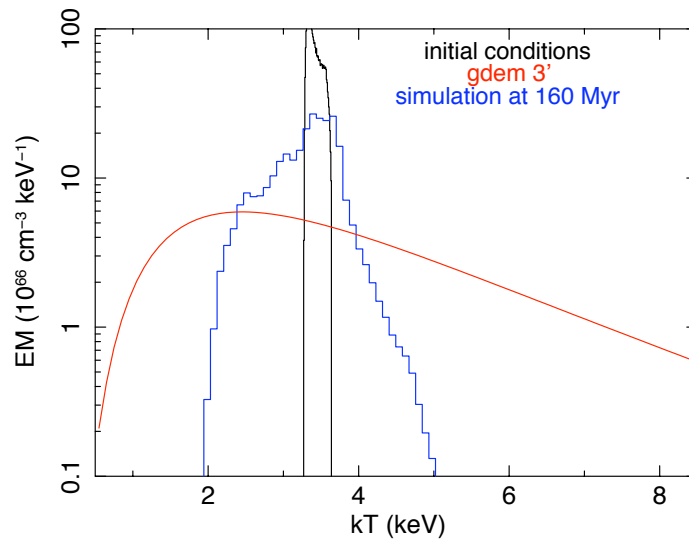


Figure 5.10: Emission measure vs. temperature in a cylinder of 3' radius whose axis goes through the cluster center. In black, the initial conditions for the simulation are shown. In blue, the multi-temperature structure at the end-stage of the simulation, i.e. after 160 Myr, is plotted. The AGN activity significantly broadens the distribution compared to the initial conditions, but the best-fit Gaussian emission measure distribution model for the integrated spectrum in the central 3' region, shown in red, has an even larger full-width at half maximum.

cause of a more complex cluster formation history or that the history of the AGN outburst itself is more complex. A series of several outbursts following each other could for example contribute to a further broadening of the temperature distribution. Moreover, the cool core could have been more pronounced than we considered in the initial conditions of the simulation and could have been disrupted by the outburst, which could also contribute to a broadened temperature distribution towards the low temperature side. The shock could furthermore accelerate electrons and generate a non-Maxwellian tail in the electron distribution, which would mimic the presence of additional hot gas.

### 5.8.3 Alternative scenarios

A physical set-up like the one described by the model, may prove very difficult to achieve in reality. The flow velocity required to reproduce the observed offset of the shock ellipse from the cluster center is large (about Mach 0.7) and must operate on a large spatial scale to effectively deflect the shock. It is not necessary in principle for the velocity field to be completely coherent - having a complex velocity field with an average velocity of that magnitude and orientation over this large spatial scale would suffice - but it is unclear whether accretion flows or cluster

formation history can reproduce these conditions, even on average.

Another option is to consider that the AGN and the central galaxy, rather than the rest of the ICM, are moving at  $670 \text{ km s}^{-1}$ . However, peculiar velocities of BCGs are typically around only  $160 \text{ km s}^{-1}$  (Oegerle & Hill 2001). Although extreme examples have been observed, such as A 2255 showing two BCGs separated by as much as  $2600 \text{ km s}^{-1}$  (Burns et al. 1995) due to an ongoing merger, it is unlikely that the cD in Hydra A has such a high average velocity, especially given its current proximity to the cluster center.

An alternative scenario we simulated was that the large-scale velocity field is due to so-called “sloshing” of the ICM following, for example, a minor merger. We mimicked this in a simple manner by offsetting the whole ICM from the gravitational potential by 100 kpc. The ICM falls back into the potential well, leading to a large-scale bulk flow, which is, however non-homogeneous in space and time. Typical velocities are between  $660 \text{ km s}^{-1}$  in the cluster center and  $300 \text{ km s}^{-1}$  at 300 kpc. A temperature slice of this simulation taken at 160 Myr after the jet was launched is shown in Fig. 5.9. The ellipticity, energy and age of the shock remain similar, the offset is slightly larger than observed (93 kpc, which could be easily corrected by adjusting the initial offset or viewing direction) and, in this scenario, we begin to see an angle between the jets due to the fact that, after turning off the jet, its former channels are transported along with the flow. It is possible that the bend in the observed large-scale N radio lobe coincides with the bend in Fig. 5.9 and a more recent outburst in the cluster center along the NE-SW direction completed the radio morphology observed today. However, the sloshing seems to also produce an offset temperature dip which is not observed and the shock Mach number to the W is around 1.7, which is too high compared to the observed value (the Mach numbers in all other directions are consistent with the observed values).

Other possibilities to explain the shock shape in Hydra A include a combination of a smaller flow velocity in the cluster (at a more plausible value of  $260 \text{ km s}^{-1}$ , the offset of the shock ellipse would be 28 kpc and no additional substructure such as offset temperature dips would appear, Fig. 5.9), asymmetrical density/temperature profiles such that shocks may run down different profiles with different speeds, and a more pronounced influence of the bubbles in actively driving the shock front towards the north. The latter could be achieved, for example, if an existing older bubble recommences expansion due to a more recent outburst.

The actual shape of the shock front, which is only roughly an ellipse (Sect. 5.4), and the radio morphology betray the likely necessity to include both a very complex flow pattern and a combination of additional physics and initial conditions before a truly realistic model is obtained. A detailed analysis of the cavity properties by Wise et al. (2007), as well as the multi-temperature structure in Hydra A (Sect. 5.8.2) both suggest a much more complex outburst history. The simulation presented here is successful at reproducing several of the observed features and gives us insights about the next steps to be taken in order to further improve the modeling.

## 5.9 Summary and Outlook

We analyzed a deep XMM-Newton observation of the cluster of galaxies Hydra A and focused on the large-scale shock discovered as a surface brightness discontinuity in Chandra images (Nulsen

et al. 2005). We find

- that the shock front can be seen in the pressure map as a 20% enhancement with respect to the radial average.
- that the shape of the shock seen in the pressure map can be approximated with an ellipse with a semi-major axis of 360 kpc oriented 10 degrees clockwise from the N–S direction, a semi-minor axis of 275 kpc, and centered  $\sim 70$  kpc towards the NE with respect to the cluster center. This is a good simple approximation to the shock shape seen in the Chandra image, which shows however some more complex deviations from ellipticity.
- for the first time, indications of temperature jumps corresponding to the shocked regions. We divided the data in four sectors towards the N, E, S and W and find temperature jumps with typical significances of  $2\sigma$ . Combining the significances in the individual sectors we obtain a total significance of  $4.3\sigma$ .

We then used a spherically symmetric hydrodynamic model of a point explosion at the center of an initially isothermal, hydrostatic atmosphere (Nulsen et al. 2005) to simulate surface brightness profiles and temperature jumps across the shock. These were compared to the observational data to estimate the shock properties, such as Mach number, energy and age. We find

- that the Mach numbers determined from the temperature jumps in the shocked regions are in good agreement with the Mach numbers derived from EPIC/pn surface brightness profiles and previously from Chandra data (Nulsen et al. 2005). This confirms that the large-scale surface brightness discontinuity in Hydra A is due to a classical shock.
- that the shock in all the four sectors has a Mach number consistent with  $\sim 1.3$ , although the distance between the shock front and the cluster center differs. This is contrary to what we would expect from a point explosion.
- estimated shock ages between 130 and 230 Myr. The larger shock age in the sectors where the shock is further from the cluster center suggests again that the shock generation mechanism is more complex.
- estimated shock energies between 1.5 and  $3 \times 10^{61}$  ergs.

To further improve the modeling of the shock in Hydra A, we also employed 3D hydrodynamical simulations in which the shock is produced by a symmetrical pair of jets that originate from the cluster center, mimicking AGN activity. This creates an approximately elliptical shock front. To reproduce the observed 70 kpc offset between the cluster center and the center of the ellipse approximation to the shock front, we included large-scale coherent motions in the simulated ICM. We find

- that the simulation can successfully reproduce the size, ellipticity and average Mach number of the observed shock front.

- that the variation of the Mach number along the simulated shock is small, although the shock is asymmetric. This is in good agreement with the observed properties and could not be explained with a simple point explosion model.
- that the shock age and energy from the 3D simulation are 160 Myr and  $3 \times 10^{61}$  ergs, respectively, within the range of the estimated values based on the 1D shock model.
- that for the case of a potential flow around the central 100 kpc, the flow velocity needed to reproduce the observed offset of the center of the shock ellipse with respect to the cluster center is very large,  $670 \text{ km s}^{-1}$ .
- that the AGN activity significantly broadens the temperature distribution in the cluster core.

However, such a high bulk flow velocity coherent over large regions in the ICM is unlikely, and the simulation does not reproduce the proximity of the observed northern radio lobe to the shock front, which is potentially an important additional factor contributing to the offset of the shock ellipse. The morphology of the radio lobes, especially the bending of the southern lobe, is also difficult to reproduce, suggesting the necessity for more detailed simulations. In an upcoming paper, we plan to further investigate the shock modeling using more complex initial conditions, such as an elliptical cluster potential and the presence of older bubbles through which the shock propagates. We will also vary the jet physics to include intermittent activity. Switching the jet on and off with different frequencies could put more momentum into bubbles, so that the shock becomes detached from them at a later stage. Moreover, the physics of the bubbles is important: we will check the effect of including sub-grid turbulence models which should prevent the shredding of the bubbles (see Scannapieco & Brüggén 2008), making them easier to bend and be affected by bulk flow motions. This should significantly alleviate the problems described above and provide a more realistic model.

#### **Acknowledgements**

We acknowledge the support by the DFG grant BR 2026/3 within the Priority Programme “Witnesses of Cosmic History”, the supercomputing grants NIC 2195, 2256 and 2877 at the John-Neumann Institut at the Forschungszentrum Jülich, and NASA grant NNX07AQ18G 16610022. AS would like to thank the Harvard-Smithsonian CfA and Jacobs University Bremen for their hospitality. AF acknowledges support from BMBF/DLR under grant 50 OR 0207 and MPG. This work is based on observations obtained with XMM-Newton, an ESA science mission with instruments and contributions directly funded by ESA member states and the USA (NASA). The Netherlands Institute for Space Research (SRON) is supported financially by NWO, the Netherlands Organization for Scientific Research. Part of the results presented were produced using the FLASH code, a product of the DOE ASC/Alliances-funded Center for Astrophysical Thermonuclear Flashes at the University of Chicago.

# Chapter 6

## Conclusions

### 6.1 Mechanisms and energetics of AGN-ICM interaction

The interaction between AGN and their environments is currently believed to be the key to understanding galaxy and structure formation in detail. Both the formation of very massive galaxies and the distribution of the hot X-ray emitting ICM at the center of clusters of galaxies seem to be affected by AGN feedback. While the most common signatures of AGN-ICM interaction in clusters of galaxies are typically in the form of X-ray cavities filled with radio plasma injected by the AGN, I focused in this thesis on two other types of substructure features in the X-ray gas generated by the supermassive black holes in the BCGs: bright filaments dragged in the wake of buoyantly rising radio lobes and weak shocks. As the results summarized in Table 6.1 show, these two mechanisms contribute significantly to heating the central ICM.

While keeping in mind that the observed substructure is often a superposition of several AGN outbursts, some during which more energy may be deposited by one particular mechanism than another, it is worthwhile noting that

- the energy in the AGN-induced weak shocks is comparable to and typically slightly higher than the heat provided by all the observed buoyant X-ray cavities combined. The shocks in M87 and Hydra A are to date the only AGN-driven shocks where temperature and density discontinuities consistent with classical Rankine-Hugoniot jump conditions have been confirmed (Chapters 2 and 5).
- the typical energies associated with AGN-ICM interaction differ by as much as 4 orders of magnitude between the two clusters investigated here. This is partly due to the different energy required to quench the cooling (which is directly proportional to the nominal mass deposition rate shown in Table 6.1, the gas mass which should cool in the absence of heating) and partly to how often AGN outbursts occur. The cooling of the central ICM can be offset either by very energetic events separated by longer time intervals (potentially the case of Hydra A) or by less energetic outbursts occurring more frequently.
- the ratio of the energy deposited in weak shocks vs. cavities is similar for the two investigated clusters. The energy needed to uplift the observed X-ray bright filaments on

Table 6.1: Comparison of energies associated with various AGN-ICM interaction mechanisms in M87 and Hydra A.

Interaction mechanism	M87	Hydra A
X-ray cavities (total)	$2.1 - 3.9 \times 10^{57}$ ergs <sup>a</sup>	$0.8 - 1.6 \times 10^{61}$ ergs <sup>b</sup>
Filaments	$4.3 \times 10^{57}$ ergs (Chapter 3)	$1.3 \times 10^{59}$ ergs (Chapter 4)
Weak shock	$8 \times 10^{57}$ ergs <sup>c</sup>	$3 \times 10^{61}$ ergs (Chapter 5)
Nominal mass deposition rate	10 M <sub>⊙</sub> /yr (Stewart et al. 1984)	300 M <sub>⊙</sub> /yr (David et al. 2001)

<sup>a</sup>(Forman et al. 2005, 2007)

<sup>b</sup>(Wise et al. 2007)

<sup>c</sup>(Forman et al. 2005)

the other hand is comparable to the weak shock energy in M87 while being two orders of magnitude less than the weak shock energy in Hydra A. Thus, either the outburst energy in different clusters is not distributed in the same relative amounts between the three different mechanisms discussed here, or the uplifted filaments are a much more fragile feature. The energy of only the most recent, smallest cavities in Hydra A is only  $6.4 \times 10^{59}$  ergs (Wise et al. 2007), comparable to that associated with the filaments. We could thus be seeing only the filaments associated with the latest outburst, while those associated with the previous, more energetic one, which created the larger outer bubbles, have been destroyed and mixed into the ICM and are no longer observed.

The conclusion to be drawn from this section is therefore that AGN do provide enough energy to prevent catastrophic cooling of the central ICM for tens to hundreds of megayears, but there are several mechanisms which all contribute significantly to depositing this energy into the ICM. One fourth possibility debated at the moment, apart from the three mechanisms presented in Table 6.1, are sound waves induced by the AGN which travel through the cluster towards the outskirts also depositing energy into the ICM (e.g. Sanders & Fabian 2007). These sound waves have not been observed in either of the two clusters presented here. To progress in our future understanding of AGN feedback therefore, one main goal will be to investigate more closely which of the different AGN-ICM interaction mechanisms observed so far is responsible for what fraction of the total energy budget, and if and under which conditions these relative contributions vary.

## 6.2 Sources of chemical enrichment and the transport of metals in the ICM

Emission lines in the X-ray spectra of the ICM reveal information about the abundances of elements which are primarily produced by type Ia and core-collapse supernovae. Because the deep gravitational potentials of galaxy clusters retain all the metals produced by the member galaxies, these abundances represent the integral yield of all the supernova explosions during the clusters'

history. The chemical elements whose abundances can be measured from X-ray spectra can be divided into three basic groups: those produced predominantly by SN<sub>CC</sub> (O, Mg, Ne), those produced predominantly by SN Ia (Fe, Ni) and intermediate elements where both supernova types contribute in comparable amounts (Si, S). From the O/Fe abundance ratio for example it is then possible to infer the relative contribution of SN Ia vs. SN<sub>CC</sub> and its spatial variation in the ICM. Once the relative number of SN Ia to SN<sub>CC</sub> for a particular region is estimated, the corresponding Si/Fe ratio is sensitive to different supernova explosion models, which can be thus in principle constrained based on the existing observations of abundances in the ICM. We showed the results of such an analysis in Chapter 4 for several clusters including Hydra A and M87 and concluded that:

- in cool-core clusters, the radial profiles of all elements are centrally peaked, although there is evidence of the Fe abundance increasing faster towards the center than the abundance of O, a predominantly SN<sub>CC</sub> product.
- while SN Ia in the BCG can be responsible for creating the Fe abundance peak associated with the central surface brightness peak, as previously proposed, a non-negligible amount of SN<sub>CC</sub>-products is also present in this central metallicity peak. This implies either a very large contribution by stellar mass loss in the BCG to the metal enrichment (the abundance ratios of metals injected by the stellar winds follows roughly the stars' own composition, which can be more SN<sub>CC</sub>-like depending on when the stars formed) or a remaining metal peak from the protocluster phase, when many SN<sub>CC</sub> exploded, or significant recent episodes of star formation in the BCG (the massive stars formed in such an event exhaust their fuel in a short time and then explode as SN<sub>CC</sub>).
- currently, the distribution of observed points in an O/Fe vs. Si/Fe diagram shows significant scatter around the predictions using combinations of available SNIa and SN<sub>CC</sub> yield models. On average, the WDD2 SN Ia yield model is preferred (de Plaa et al. 2007); however, studying the cause of the existent spread around this best-fit model can reveal further details about the physics and chemistry of SNIa explosions and about the average stellar population producing the SN<sub>CC</sub>. The energy, explosion mechanism, and initial metallicity of the progenitor white dwarf affect SNIa yields, while the initial mass function of the star formation and the typical initial metallicities of the stars that explode as core-collapse supernovae change the average SN<sub>CC</sub> yields per cluster (e.g. Kobayashi et al. 2006; Werner et al. 2008).

The BCG seems to play an important role in producing the metallicity peak at the center of cooling-core clusters. This peak seems absent in non-cooling core clusters which also do not have a dominant central galaxy. However, if the metals in the peak came from stars and supernovae in the BCG, one would expect the distribution of chemical elements to follow the light distribution in the central galaxy. The fact that the distribution of metals is much broader than that of the light in the BCG is thought to be the result of the AGN stirring the central gas. We discussed for the first time (Chapters 3 and 4) concrete observations of metal-rich gas dragged in the wake of buoyantly-rising AGN radio lobes, confirming this scenario. As much as

$1.5 \times 10^6 M_{\odot}/\text{yr}$  of Fe are transported by the AGN outburst in M87 and one order of magnitude more Fe is uplifted by the more energetic outburst in Hydra A. The time required for supernovae together with stellar mass loss to produce the observed metals transported by the AGN in M87 is  $\sim 30 - 110$  Myr. The average metallicity of the uplifted gas is roughly 2 solar. Both in M87 and Hydra A, the abundance ratios in the uplifted gas are similar to those in the ambient gas, therefore the transport of metals by the AGN presently does not seem to alter the relative abundance patterns, but only affects the overall metallicity distribution. In conclusion, we are able to quantify by direct observations several important properties of the metal transport driven by AGN in the two clusters we studied in detail in this work, properties which are likely similar for most other galaxy clusters.

Apart from the AGN, one more mechanism can be responsible for metal transport in the ICM: large-scale bulk motions. From the shape of the shock in Hydra A, we infer the presence of relatively high-velocity flows (Chapter 5); however, no discontinuities in the metal distribution due to these motions is seen. On the other hand, in Chapter 2 we describe a cold front in M87 with a  $\sim 37$  kpc radius SW of the core, across which we do observe a jump in the temperature, surface brightness, and also metallicity profiles. Another, much stronger, similar feature can be seen about 90 kpc north-northwest of M87. Cold fronts are common in cool-core clusters and are thought to arise from a process known as “sloshing”. This takes place when the central, dense gas starts to oscillate in the gravitational potential of the cluster as a result of a disturbance of the central potential by past subcluster infall (Markevitch & Vikhlinin 2007). This oscillation displaces central high-metallicity gas outwards, bringing it in contact with lower-metallicity gas, spreading thus heavy elements towards the cluster outskirts and creating jumps in the abundance profiles.

We recently obtained two deep pointings with the Japanese Suzaku X-ray telescope to observe the 90 kpc cold front in M87, as well as a mosaic of 7 shorter pointings in a full circle around the existing deep exposure of M87 with XMM-Newton. The latter will give us a good overview of the outskirts of M87 both in the direction of the 90 kpc surface brightness jump and away from it, so that we can compare temperature and surface brightness profiles in different sectors. We will be able to determine how the motion of M87 is influencing the surrounding gas distribution as a whole, estimate the velocity and energy associated with the motion, and check if this motion can explain the angle between the E and SW radio lobes and the associated X-ray bright arms. Using the Suzaku observations, we will determine gradients in the absolute metal abundances and abundance ratios across the cold front. For the first time, we will be able to compare in detail the chemical composition and enrichment history of the gas on either side of a cold front discontinuity. Following the efforts presented here to characterize the effect of the central AGN on the distribution of heavy elements in the ICM, we will thus study in detail the metal transport induced also by gas sloshing.

# Bibliography

Abell, G. O. 1958, *ApJS*, 3, 211

Akritas, M. G. & Bershadsky, M. A. 1996, *ApJ*, 470, 706

Allen, S. W. & Fabian, A. C. 1998, *MNRAS*, 297, L63

Allen, S. W., Schmidt, R. W., & Fabian, A. C. 2002, *MNRAS*, 334, L11

Anders, E. & Grevesse, N. 1989, *Geochim. Cosmochim. Acta*, 53, 197

Angione, R. J., Junkkarinen, V., Talbert, F. D., & Brandt, J. C. 1980, *PASP*, 92, 149

Arnaud, M., Neumann, D. M., Aghanim, N., et al. 2001, *A&A*, 365, L80

Arnaud, M. & Raymond, J. 1992, *ApJ*, 398, 394

Ascasibar, Y. & Markevitch, M. 2006, *ApJ*, 650, 102

Belsole, E., Sauvageot, J. L., Böhringer, H., et al. 2001, *A&A*, 365, L188

Binney, J. & Tabor, G. 1995, *MNRAS*, 276, 663

Bîrzan, L., Rafferty, D. A., McNamara, B. R., Wise, M. W., & Nulsen, P. E. J. 2004, *ApJ*, 607, 800

Böhringer, H. 1999, in *Diffuse Thermal and Relativistic Plasma in Galaxy Clusters*, ed. H. Böhringer, L. Feretti, & P. Schuecker, 115–120

Böhringer, H., Belsole, E., Kennea, J., et al. 2001, *A&A*, 365, L181

Böhringer, H. & Fabian, A. C. 1989, *MNRAS*, 237, 1147

Böhringer, H., Matsushita, K., Churazov, E., & Finoguenov, A. 2004, in *The Riddle of Cooling Flows in Galaxies and Clusters of galaxies*, ed. T. Reiprich, J. Kempner, & N. Soker, 189–193

Böhringer, H., Matsushita, K., Churazov, E., Finoguenov, A., & Ikebe, Y. 2004, *A&A*, 416, L21

Böhringer, H., Matsushita, K., Churazov, E., Ikebe, Y., & Chen, Y. 2002, *A&A*, 382, 804

- Böhringer, H., Matsushita, K., Finoguenov, A., Xue, Y., & Churazov, E. 2005, *Advances in Space Research*, 36, 677
- Böhringer, H. & Morfill, G. E. 1988, *ApJ*, 330, 609
- Böhringer, H., Neumann, D. M., Schindler, S., & Huchra, J. P. 1997, *ApJ*, 485, 439
- Böhringer, H., Nulsen, P. E. J., Braun, R., & Fabian, A. C. 1995, *MNRAS*, 274, L67
- Branch, D. 1986, *ApJ*, 300, L51
- Brüggen, M. 2002, *ApJ*, 571, L13
- Brüggen, M., Heinz, S., Roediger, E., Ruszkowski, M., & Simionescu, A. 2007, *MNRAS*, 380, L67
- Brüggen, M. & Kaiser, C. R. 2002, *Nature*, 418, 301
- Brüggen, M., Ruszkowski, M., & Hallman, E. 2005, *ApJ*, 630, 740
- Buote, D. A. & Canizares, C. R. 1996, *ApJ*, 457, 565
- Buote, D. A. & Fabian, A. C. 1998, *MNRAS*, 296, 977
- Burns, J. O. 1990, *AJ*, 99, 14
- Burns, J. O., Roettiger, K., Pinkney, J., et al. 1995, *ApJ*, 446, 583
- Byram, E. T., Chubb, T. A., & Friedman, H. 1966, *Science*, 152, 66
- Cappellari, M. & Copin, Y. 2003, *MNRAS*, 342, 345
- Cappellaro, E., Evans, R., & Turatto, M. 1999, *A&A*, 351, 459
- Carter, D. & Dixon, K. L. 1978, *AJ*, 83, 574
- Carter, J. A. & Read, A. M. 2007, *A&A*, 464, 1155
- Cavagnolo, K. W., Donahue, M., Voit, G. M., & Sun, M. 2008, *ApJ*, 683, L107
- Churazov, E., Brüggen, M., Kaiser, C. R., Böhringer, H., & Forman, W. 2001, *ApJ*, 554, 261
- Churazov, E., Forman, W., Jones, C., & Böhringer, H. 2003, *ApJ*, 590, 225
- Churazov, E., Gilfanov, M., Forman, W., & Jones, C. 1996, *ApJ*, 471, 673
- Ciotti, L., Pellegrini, S., Renzini, A., & D'Ercole, A. 1991, *ApJ*, 376, 380
- Cowie, L. L. & Binney, J. 1977, *ApJ*, 215, 723
- Croton, D. J., Springel, V., White, S. D. M., et al. 2006, *MNRAS*, 365, 11

- David, L. P. & Nulsen, P. E. J. 2008, *ApJ*, 689, 837
- David, L. P., Nulsen, P. E. J., McNamara, B. R., et al. 2001, *ApJ*, 557, 546
- De Grandi, S. & Molendi, S. 2001, *ApJ*, 551, 153
- De Luca, A. & Molendi, S. 2004, *A&A*, 419, 837
- de Plaa, J., Werner, N., Bleeker, J. A. M., et al. 2007, *A&A*, 465, 345
- de Plaa, J., Werner, N., Bykov, A. M., et al. 2006, *A&A*, 452, 397
- Dennison, B. 1980, *ApJ*, 236, 761
- Dickey, J. M. & Lockman, F. J. 1990, *ARA&A*, 28, 215
- Diehl, S. & Statler, T. S. 2006, *MNRAS*, 368, 497
- Domainko, W., Mair, M., Kapferer, W., et al. 2006, *A&A*, 452, 795
- Durret, F., Kaastra, J. S., Nevalainen, J., Ohashi, T., & Werner, N. 2008, *Space Science Reviews*, 134, 51
- Edge, A. C., Stewart, G. C., & Fabian, A. C. 1992, *MNRAS*, 258, 177
- Egami, E., Misselt, K. A., Rieke, G. H., et al. 2006a, *ApJ*, 647, 922
- Egami, E., Rieke, G. H., Fadda, D., & Hines, D. C. 2006b, *ApJ*, 652, L21
- Fabian, A. C. 1994, *ARA&A*, 32, 277
- Fabian, A. C. & Nulsen, P. E. J. 1977, *MNRAS*, 180, 479
- Fabian, A. C., Sanders, J. S., Allen, S. W., et al. 2003, *MNRAS*, 344, L43
- Feigelson, E. D., Wood, P. A. D., Schreier, E. J., Harris, D. E., & Reid, M. J. 1987, *ApJ*, 312, 101
- Feretti, L. & Neumann, D. M. 2006, *A&A*, 450, L21
- Finoguenov, A., Briel, U. G., & Henry, J. P. 2003, *A&A*, 410, 777
- Finoguenov, A., Matsushita, K., Böhringer, H., Ikebe, Y., & Arnaud, M. 2002, *A&A*, 381, 21
- Forman, W., Jones, C., Churazov, E., et al. 2007, *ApJ*, 665, 1057
- Forman, W., Nulsen, P., Heinz, S., et al. 2005, *ApJ*, 635, 894
- Fusco-Femiano, R., Orlandini, M., Brunetti, G., et al. 2004, *ApJ*, 602, L73
- Gastaldello, F. & Molendi, S. 2002, *ApJ*, 572, 160

- Goldshmidt, O. & Rephaeli, Y. 1993, *ApJ*, 411, 518
- González-Riestra, R. 2004, <http://xmm.vilspa.esa.es/docs/documents/CAL-TN-0058-1-0.ps.gz>
- Harms, R. J., Ford, H. C., Tsvetanov, Z. I., et al. 1994, *ApJ*, 435, L35
- Heinz, S., Brüggén, M., Young, A., & Levesque, E. 2006, *MNRAS*, 373, L65
- Henry, J. P., Finoguenov, A., & Briel, U. G. 2004, *ApJ*, 615, 181
- Hoyle, F. & Fowler, W. A. 1960, *ApJ*, 132, 565
- Iwamoto, K., Brachwitz, F., Nomoto, K., et al. 1999, *ApJS*, 125, 439
- Kaastra, J. S. 1992, *An X-ray Spectral Code for Optically Thin Plasmas (Internal SRON-Leiden Report, Updated Version 2.0)*
- Kaastra, J. S., Mewe, R., & Nieuwenhuijzen, H. 1996, in *UV and X-ray Spectroscopy of Astrophysical and Laboratory Plasmas* p.411, K. Yamashita and T. Watanabe. Tokyo : Universal Academy Press
- Kaastra, J. S., Tamura, T., Peterson, J. R., et al. 2004, *A&A*, 413, 415
- Kalberla, P. M. W., Burton, W. B., Hartmann, D., et al. 2005, *A&A*, 440, 775
- Kellogg, E. M. 1973, in *IAU Symposium, Vol. 55, X- and Gamma-Ray Astronomy*, ed. H. Bradt & R. Giacconi, 171–183
- Khokhlov, A. M. 1991, *A&A*, 245, 114
- Kobayashi, C. & Arimoto, N. 1999, *ApJ*, 527, 573
- Kobayashi, C. & Nomoto, K. 2008, [arXiv\[0801.0215\]](https://arxiv.org/abs/0801.0215)
- Kobayashi, C., Umeda, H., Nomoto, K., Tominaga, N., & Ohkubo, T. 2006, *ApJ*, 653, 1145
- Lane, W. M., Clarke, T. E., Taylor, G. B., Perley, R. A., & Kassim, N. E. 2004, *AJ*, 127, 48
- Lea, S. M., Silk, J., Kellogg, E., & Murray, S. 1973, *ApJ*, 184, L105
- Leccardi, A. & Molendi, S. 2008, *A&A*, 487, 461
- Liedahl, D. A., Osterheld, A. L., & Goldstein, W. H. 1995, *ApJ*, 438, L115
- Lieu, R., Ip, W.-H., Axford, W. I., & Bonamente, M. 1999, *ApJ*, 510, L25
- Lieu, R., Mittaz, J. P. D., Bowyer, S., et al. 1996, *ApJ*, 458, L5
- Lodders, K. 2003, *ApJ*, 591, 1220

- Magorrian, J., Tremaine, S., Richstone, D., et al. 1998, *AJ*, 115, 2285
- Mahdavi, A., Finoguenov, A., Böhringer, H., Geller, M. J., & Henry, J. P. 2005, *ApJ*, 622, 187
- Mannucci, F., Maoz, D., Sharon, K., et al. 2008, *MNRAS*, 383, 1121
- Markevitch, M. 2002, arXiv:astro-ph/0205333
- Markevitch, M. & Vikhlinin, A. 2007, *Phys. Rep.*, 443, 1
- Markevitch, M., Vikhlinin, A., & Mazzotta, P. 2001, *ApJ*, 562, L153
- Mathews, W. G. & Bregman, J. N. 1978, *ApJ*, 224, 308
- Matsushita, K., Belsole, E., Finoguenov, A., & Böhringer, H. 2002, *A&A*, 386, 77
- Matsushita, K., Böhringer, H., Takahashi, I., & Ikebe, Y. 2007a, *A&A*, 462, 953
- Matsushita, K., Finoguenov, A., & Böhringer, H. 2003, *A&A*, 401, 443
- Matsushita, K., Fukazawa, Y., Hughes, J. P., et al. 2007b, *PASJ*, 59, 327
- McNamara, B. R. 1995, *ApJ*, 443, 77
- McNamara, B. R. & Nulsen, P. E. J. 2007, *ARA&A*, 45, 117
- McNamara, B. R. & O'Connell, R. W. 1989, *AJ*, 98, 2018
- McNamara, B. R., Wise, M., Nulsen, P. E. J., et al. 2000, *ApJ*, 534, L135
- Mewe, R., Gronenschild, E. H. B. M., & van den Oord, G. H. J. 1985, *A&AS*, 62, 197
- Minkowski, R. 1941, *PASP*, 53, 224
- Molendi, S. 2002, *ApJ*, 580, 815
- Nomoto, K., Thielemann, F.-K., & Yokoi, K. 1984, *ApJ*, 286, 644
- Nomoto, K., Tominaga, N., Umeda, H., Kobayashi, C., & Maeda, K. 2006, *Nuclear Physics A*, 777, 424
- Nulsen, P. E. J., David, L. P., McNamara, B. R., et al. 2002, *ApJ*, 568, 163
- Nulsen, P. E. J., McNamara, B. R., Wise, M. W., & David, L. P. 2005, *ApJ*, 628, 629
- Oegerle, W. R. & Hill, J. M. 2001, *AJ*, 122, 2858
- Omma, H., Binney, J., Bryan, G., & Slyz, A. 2004, *MNRAS*, 348, 1105
- Owen, F. N., Eilek, J. A., & Kassim, N. E. 2000, *ApJ*, 543, 611

- Peletier, R. F., Davies, R. L., Illingworth, G. D., Davis, L. E., & Cawson, M. 1990, *AJ*, 100, 1091
- Peterson, C. J. 1986, *PASP*, 98, 486
- Peterson, J. R. & Fabian, A. C. 2006, *Phys. Rep.*, 427, 1
- Peterson, J. R., Kahn, S. M., Paerels, F. B. S., et al. 2003, *ApJ*, 590, 207
- Peterson, J. R., Paerels, F. B. S., Kaastra, J. S., et al. 2001, *A&A*, 365, L104
- Pratt, G. W. & Arnaud, M. 2002, *A&A*, 394, 375
- Rafferty, D. A., McNamara, B. R., Nulsen, P. E. J., & Wise, M. W. 2006, *ApJ*, 652, 216
- Rasia, E., Etti, S., Moscardini, L., et al. 2006, *MNRAS*, 369, 2013
- Rasia, E., Mazzotta, P., Bourdin, H., et al. 2008, *ApJ*, 674, 728
- Read, A. M. & Ponman, T. J. 2003, *A&A*, 409, 395
- Rebusco, P., Churazov, E., Böhringer, H., & Forman, W. 2006, *MNRAS*, 372, 1840
- Reiprich, T. H. & Böhringer, H. 2002, *ApJ*, 567, 716
- Renzini, A., Ciotti, L., D'Ercole, A., & Pellegrini, S. 1993, *ApJ*, 419, 52
- Reynolds, C. S., Heinz, S., & Begelman, M. C. 2001, *ApJ*, 549, L179
- Roediger, E., Brüggén, M., Rebusco, P., Böhringer, H., & Churazov, E. 2007, *MNRAS*, 375, 15
- Salomé, P., Revaz, Y., Combes, F., et al. 2008, *A&A*, 483, 793
- Salpeter, E. E. 1955, *ApJ*, 121, 161
- Sanders, J. S. & Fabian, A. C. 2007, *MNRAS*, 381, 1381
- Sanders, J. S., Fabian, A. C., Allen, S. W., et al. 2008, *MNRAS*, 385, 1186
- Sanders, J. S., Fabian, A. C., Allen, S. W., & Schmidt, R. W. 2004, *MNRAS*, 349, 952
- Sanders, J. S., Fabian, A. C., & Dunn, R. J. H. 2005, *MNRAS*, 360, 133
- Santos, J. S., Rosati, P., Tozzi, P., et al. 2008, *A&A*, 483, 35
- Sarazin, C. L. 1986, *Reviews of Modern Physics*, 58, 1
- Sato, K., Yamasaki, N. Y., Ishida, M., et al. 2007, *PASJ*, 59, 299
- Scannapieco, E. & Brüggén, M. 2008, *ApJ*, 686, 927
- Sijacki, D., Springel, V., di Matteo, T., & Hernquist, L. 2007, *MNRAS*, 380, 877

- Simionescu, A., Böhringer, H., Brüggén, M., & Finoguenov, A. 2007, *A&A*, 465, 749
- Simionescu, A., Roediger, E., Nulsen, P. E. J., et al. 2009a, *A&A*, 495, 721
- Simionescu, A., Werner, N., Böhringer, H., et al. 2009b, *A&A*, 493, 409
- Simionescu, A., Werner, N., Finoguenov, A., Böhringer, H., & Brüggén, M. 2008, *A&A*, 482, 97
- Smith, R. K., Brickhouse, N. S., Liedahl, D. A., & Raymond, J. C. 2001, *ApJ*, 556, L91
- Snowden, S. L., Mushotzky, R. F., Kuntz, K. D., & Davis, D. S. 2008, *A&A*, 478, 615
- Sparks, W. B., Donahue, M., Jordán, A., Ferrarese, L., & Côté, P. 2004, *ApJ*, 607, 294
- Spitzer, L. 1962, *Physics of Fully Ionized Gases* (Physics of Fully Ionized Gases, New York: Interscience (2nd edition), 1962)
- Stewart, G. C., Fabian, A. C., Jones, C., & Forman, W. 1984, *ApJ*, 285, 1
- Sutherland, R. S. & Dopita, M. A. 1993, *ApJS*, 88, 253
- Swartz, D. A., Clocchiatti, A., Benjamin, R., Lester, D. F., & Wheeler, J. C. 1993, *Nature*, 365, 232
- Tamura, T., Bleeker, J. A. M., Kaastra, J. S., Ferrigno, C., & Molendi, S. 2001, *A&A*, 379, 107
- Tamura, T., Kaastra, J. S., den Herder, J. W. A., Bleeker, J. A. M., & Peterson, J. R. 2004, *A&A*, 420, 135
- Tittley, E. R. & Henriksen, M. 2005, *ApJ*, 618, 227
- Tonry, J. L., Dressler, A., Blakeslee, J. P., et al. 2001, *ApJ*, 546, 681
- Tsujimoto, T., Nomoto, K., Yoshii, Y., et al. 1995, *MNRAS*, 277, 945
- Vikhlinin, A., Burenin, R., Forman, W. R., et al. 2007, in *Heating versus Cooling in Galaxies and Clusters of Galaxies*, ed. H. Böhringer, G. W. Pratt, A. Finoguenov, & P. Schuecker, 48–53
- Vikhlinin, A., Kravtsov, A., Forman, W., et al. 2006, *ApJ*, 640, 691
- Watson, M. G., Auguères, J.-L., Ballet, J., et al. 2001, *A&A*, 365, L51
- Werner, N., Böhringer, H., Kaastra, J. S., et al. 2006a, *A&A*, 459, 353
- Werner, N., de Plaa, J., Kaastra, J. S., et al. 2006b, *A&A*, 449, 475
- Werner, N., Durret, F., Ohashi, T., Schindler, S., & Wiersma, R. P. C. 2008, *Space Science Reviews*, 134, 337

Wheeler, J. C. & Levreault, R. 1985, *ApJ*, 294, L17

Wise, M. W., McNamara, B. R., Nulsen, P. E. J., Houck, J. C., & David, L. P. 2007, *ApJ*, 659, 1153

Wolf, M. 1906, *Astronomische Nachrichten*, 170, 211

Woosley, S. E., Langer, N., & Weaver, T. A. 1993, *ApJ*, 411, 823

Woosley, S. E., Langer, N., & Weaver, T. A. 1995, *ApJ*, 448, 315

Young, A. J., Wilson, A. S., & Mundell, C. G. 2002, *ApJ*, 579, 560

Zwicky, F. 1937, *ApJ*, 86, 217

# Acknowledgements

A PhD is not just about getting some original research done; it's also a test of... endurance, for you as a person, to see if you can stand up to the challenge. Someone I won't name yet told me this in the first year - and though I didn't appreciate it then, among all the frustration of not being able to wrap my brain and keyboard around a whole number of issues, it's for the better that it is so. I have grown during this graduate program immensely, and not just from a scientific perspective. And for this I thank everyone who was part of my academic and private life, during and before my PhD years - and especially those of you who brought me inspiration, ambition, pride, happiness, sadness, melancholy, fear, passion, guidance, doubt, advice, more inspiration, tears, smiles and the power to enjoy life with its ups and downs all the same. There are enough people without whom I would be a different person now (and this would be a different thesis, if at all) to fill an entire book all by itself, and seeing as you probably already skipped the larger part of this book to get to the Acknowledgements, I'll have to keep things short in hope you go back and read a few chapters once you finish these couple of pages of personal remarks.

I would like to thank...

- ... my PhD supervisor, Hans Böhringer, for asking many of the questions I tried to answer in this thesis, discussing these answers with me, and tolerating my frequent traveling sprees.
- ... my first Astrophysics professor, Marcus Brüggen, for being a constant source of inspiration, enthusiasm, and just about the right touch of exuberance.
- ... my Physics teacher from high-school, Nicoleta Becheanu, for opening my eyes to the beauty of Physics and for the passion and joy with which she cherishes my accomplishments.
- ... my collaborator Norbert Werner for his help with data reduction, encouragement against the frustration related to data reduction, and for enlightening debates about the science arising upon completion of the data reduction; my fiancé Norbert Werner, the only person who could ever walk with me on fresh hot lava, climb out the toilet window of a mountain hut to see the moon rise, drive a Passat into the Grand Canyon, and still make me feel at home anywhere with him.
  - ... Bill Forman, for giving me the opportunity to visit the Harvard-Smithsonian Center for Astrophysics for several months and for fruitful discussions during that time and thereafter.
  - ... Alexis Finoguenov, for explaining to me some secrets of XMM-SAS, for sharing his expertise about producing entropy and pressure maps, and most certainly not least for the salsa dancing.
- ... Elke Roediger, for performing the 3D hydrodynamic simulations presented in Chapter 5 and for taking care of part of the logistics during my visits to Bremen.

- ... Paul Nulsen, for the code for the 1D shock simulations presented in Chapter 5, and for inspiring discussions about Physics.
- ... Alessandro Baldi for throwing me a great 25th birthday party, hosting me in Cambridge, introducing me to baseball and putting up with my complaints about the referee report of the second M87 paper.
- ... Jelle Kaastra, for his advice on the spectral fitting performed in Chapter 4.
- ... Eugene Churazov, based on whose suggestions I developed some of the discussion points presented in Chapter 3.
- ... Steven Diehl, for making available the Voronoi binning algorithm in IDL and taking into account my suggestions to include new features to this code which have been used in this work.
- ... Eric Miller, for his patience with my nagging questions about Suzaku data reduction.
- ... Steve Allen and Greg Madejski for their hospitality at Stanford University despite occasional complications.
- ... my students Adina Moiş, Alexandra Weissmann and Georgiana Ogreaan - keep up the good work, girls! And publish those papers, would you? ;) Also a big thanks to Nina Hatch for helping with Georgiana's project - we \*will\* get those observations of M87 in  $H\alpha$ !
- ... all of my teachers at the now Jacobs University Bremen, the Gh. M. Murgoci National College in Brăila, Deerfield Academy in Massachusetts, the Nicolae Iorga highschool in Brăila, and my elementary school which was back then simply called No. 7, for reasons too obvious to state.
- ... William J. Kaufmann, III, for writing the textbook which inspired me to study Astrophysics.
- ... René Fassbender and Martin Muehlegger for making the 6 (very) cloudy nights of observing time at Calar Alto a good memory and for providing encouragement and good spirits in general.  
Good spirits in the spiritual, not the alcoholic sense.
- ... Robert Suhada for the wrong coffee at the right times.
- ... the rest of the galaxy cluster group at MPE for sometimes funny, relaxing (I won't mention bordering on ridiculous), and sometimes instructive and informative discussions over lunch and coffee breaks: Gabriel Pratt, Daniele Pierini, Stefania Giodini, Filiberto Braglia, Yu-Ying Zhang, Naomi Ota, Joana Santos.
- ... all current and previous IMPRS students with whom I shared for over 3 years lectures, seminars, excursions, workshops and not least of all a great time socializing. Especially to Miro Mocak, Payel Das, Marco Baldi, Umberto Maio, Margarita Petkova, Martin Henze, Tom Mädler, Paula Jofre Pfeil, Marco Ajello, Rasmus Voss, Paulo Afonso. Many thanks to Julius Donnert for his patience in helping me translate the summary into German.
- ... Harald Baumgartner and Kyle Welch for prompt and sometimes (a.k.a. usually) vital IT support.
- ... Peter Buschkamp for the occasional cup of cocoa plus a bit of philosophizing and/or venting, as well as for his help with anything related to design, RGB to CMYK and anything to EPS figure conversions.
- ... the CfA postdocs for sharing with me some late nights in the office, the election of Barack Obama as US President, and some of the fellowship application stress: Anca Constantin, Vallia Antoniou, Francesca Civano, Francesco Massaro, Maria Laura Conciatore.
- ... Martin Pančičin for the way you make me completely incapable of not smiling.

- ... the former dean of the former International University Bremen, Gerhard Haerendel, without whose advice I would not have applied to MPE in the first place.
- ... Klaus Dolag for not letting me forget my inclination towards numerical simulations.
- ... the IAYC team for being great friends, fun people, and because now I can recognize about four more constellations in the night sky, which is at least a 200% improvement.
- ... dem Debattierclub München, wo gewährleistet wurde, dass mein Gehirn mindestens ein Paar Stunden pro Woche nicht an Astrophysik denkt, und wo ich endlich mal Deutsch habe lernen müssen! A big thank you to all my debating team partners and all the German and international debating scene for amazing tournaments, legendary parties, fiery debates and uplifting friendships. Among many many others, this goes out to Wladi Jachtchenko, Markus Dankerl, Florian Steininger, Dennis Gotta, Stefan Brainbauer, Marco Witzmann, Patrick Ehmann, Daniel Hinkeldein, Alyona Asyamova, Anna and Oliver Hörtensteiner.
- ... especially my best debating team partner ever, Daniel Grotzky, for goo-goo-bashing at the highest european levels and for introducing me to Harry Potter.
- ... my former flatmate from Belgradstraße, Bruno Rino, for keeping me company and occasionally listening to my ranting.
- ... the Romanian media for the big hype around one of our press releases last May. Fie ca pe viitor să prețuim, să recompensăm și să sprijinim din ce în ce mai mult cercetarea și cercetătorii români.
- ... vecinilor mei, pe care de fiecare data când mă întorc acasă îi regăsesc la fel de joviali.
- ... all my great friends who have always been there for me across time, country borders, and sometimes oceans: Dana Iordache, Raluca Pancratov, Dominik Bedorf, Roxana Voitcu, Alex Trifan, Bartek Grychtol, Mark Kim, Cassie Baron and many more... It's amazing how you can meet after years upon years and pick up right where you left off as if it were only yesterday.
- ... my whole family and soon to be family, simply for being there for me.
- ... mamei tatălui meu, care m-a crescut cu toată dragostea, a mers cu mine până la școală și m-a învățat poezii și valsul vienez, și tatălui mamei mele, care a fost întotdeauna convins că de la el am moștenit gena inteligenței.
- ... părinților mei, care mi-au inspirat curajul de a încerca și ambiția de a reuși, și au fost și sunt mereu alături de mine.

Danke. Thank you. Mulțumesc. Gracias. Köszönöm. Grazie. Ďakujem. Спасибо.



Aurora Simionescu,  
born on September 21, 1983  
in Braila, Romania;

Current address:  
Max Planck Institute for Extraterrestrial Physics  
Giessenbachstr., D-85748 Garching  
aurora@mpe.mpg.de

### Education:

- PhD project at the Max Planck Institute for Extraterrestrial Physics on the topic  
*"The Interaction between Active Galactic Nuclei and the Intracluster Medium"*  
under supervision of Dr. Hans Böhringer **Aug '05 - Jun '09**
- Undergraduate student of Physics and Geosciences and Astrophysics at the International University Bremen, Germany; Preparation of BSc Thesis  
*"Magnetic Fields in Galaxy Clusters"*  
under the supervision of Prof. Marcus Brügger **Aug '02 - Jun '05**
- Bachelor of Science title awarded by the International University Bremen, Germany **Jun '05**
- Bacalaureate at the "Gh.M.Murgoci" National College in Braila, Romania. Final grade: 9.80 (1.00-10.00 scale) **Jun '02**
- Nine months as Soros Foundation scholar at Deerfield Academy, Deerfield, Massachusetts, USA. **Aug '00 - Jun '01**

### Work Experience:

- Supervised internships of two students and two Bachelor Theses research projects on the X-ray (XMM-Newton and Chandra) and optical line emission (VIMOS/IFU) in RXCJ1504-0248.1 and on characterizing substructure in X-ray images using power ratios. **Jun '07 to date**
- Teaching Assistant at the International University Bremen for various courses including Engineering and Science Mathematics I and II, Advanced Physics BI (Electromagnetism), Physics Laboratory I and II, Geosciences and Astrophysics I, II and III **Nov '02 - Jun '05**
- Intern, Siltronic A.G., modeling flatness data of silicon wafers **Jun '04 - Aug '04**
- Intern, marine geology and physical oceanography onboard the research vessel "Pelagia" of the Royal Netherlands Institute for Sea Research (NIOZ) **Jul '03 - Aug '03**

**Scholarships and Awards:**

- awarded "Person of the Year" by Romanian national daily newspaper Cotidianul **Dec '08**
- 80ks Suzaku observation of the outskirts of M87 as PI **Apr '08**
- Visiting scholar at Harvard-Smithsonian Center for Astrophysics (NASA grant) **Oct - Nov '07**
- DFG (German Research Foundation) grant BR 2026/3 within the Priority Programme Witnesses of Cosmic History **and Oct - Nov '08**
- grant of the DAAD (German academic exchange service) for academic and cultural involvement **Oct '06**
- Full Merit-Based Scholarship, International University Bremen **Sep '04**
- Full Merit-Based Scholarship, International University Bremen **Aug '02 - Jun '05**

**Other Activities:**

- Working visits at Jacobs University Bremen, Harvard-Smithsonian CfA, SRON (Netherlands Institute for Space Research) and Stanford University **Oct '06 to date**
- Popular science talk on The Drake Equation at the International Astronomical Youth Camp, Tremešek, Czech Republic **Aug '07**
- President of the Munich Debating Club. Successful participation in several debating tournaments including ESL finalist European Championships 2006, semifinalist German Championships 2007, finalist Riga IV 2006, best speaker of the final Bremen Open 2007, Deputy Chief Adjudicator at the German Championships 2008. **Aug '06 - Aug '07**

**Publications:**

- (1) **A. Simionescu**, E. Roediger, P. E. J. Nulsen, M. Brüggen, W. R. Forman, H. Böhringer, N. Werner, A. Finoguenov, “The large-scale shock in the cluster of galaxies Hydra A”, 2009, *A&A*, 495, 721
- (2) **A. Simionescu**, N. Werner, H. Böhringer, J. S. Kaastra, A. Finoguenov, M. Brüggen & P. E. J. Nulsen, “Chemical enrichment in the cluster of galaxies Hydra A”, 2009, *A&A*, 493, 409
- (3) A. Baldi, W. R. Forman, C. Jones, P. E. J. Nulsen, L. P. David, R. P. Kraft & **A. Simionescu**, “Chandra observations of the fossil galaxy group AWM 5: cool core re-heating and thermal conduction suppression”, 2008, *ApJ*, 694, 479
- (4) N. Werner, A. Finoguenov, J. S. Kaastra, **A. Simionescu**, J. P. Dietrich, J. Vink & H. Böhringer, “Detection of hot gas in the filament connecting the clusters of galaxies Abell 222 and Abell 223”, 2008, *A&A*, 482, L29
- (5) **A. Simionescu**, N. Werner, A. Finoguenov, H. Böhringer & M. Brüggen, “Metal-rich multi-phase gas in M 87. AGN-driven metal transport, magnetic-field supported multi-temperature gas, and constraints on non-thermal emission observed with XMM-Newton”, 2008, *A&A*, 482, 97
- (6) M. Brüggen, S. Heinz, E. Roediger, M. Ruszkowski & **A. Simionescu**, “Shock heating by Fanaroff-Riley type I radio sources in galaxy clusters”, *MNRAS*, 380, L67
- (7) **A. Simionescu**, H. Böhringer, M. Brüggen & A. Finoguenov, “The gaseous atmosphere of M 87 seen with XMM-Newton”, 2007, *A&A*, 465, 749
- (8) N. Werner, H. Böhringer, J. S. Kaastra, J. De Plaa, **A. Simionescu**, J. Vink, “Carbon and Nitrogen in the X-ray Emitting Hot Gas of M 87”, 2007, *Heating versus Cooling in Galaxies and Clusters of Galaxies*, ESO Astrophysics Symposia, Springer-Verlag Berlin Heidelberg, p. 309
- (9) **A. Simionescu**, H. Böhringer, M. Brüggen & A. Finoguenov, “The gaseous atmosphere of M 87 seen with XMM-Newton”, 2007, *Heating versus Cooling in Galaxies and Clusters of Galaxies*, ESO Astrophysics Symposia, Springer-Verlag Berlin Heidelberg, p. 87
- (10) N. Werner, H. Böhringer, J. S. Kaastra, J. de Plaa, **A. Simionescu** & J. Vink, “XMM-Newton high-resolution spectroscopy reveals the chemical evolution of M 87”, 2006, *A&A*, 459, 353
- (11) M. Brüggen, M. Ruszkowski, **A. Simionescu**, M. Hoeft, C. Dalla Vecchia, “Simulations of Magnetic Fields in Filaments”, 2005, *ApJ*, 631, L21

**Presentations:**

- *Using the multitemperature structure to characterize AGN-ICM interaction in cool core clusters*, Cosmology Seminar at KIPAC (Stanford University), USA, **Dec '08**
- *Effects of AGN-ICM interaction vs. gas sloshing on metal transport in M87*, lunch talk at Columbia University, USA, **Oct '08**
- *Multitemperature structure and metallicity distribution in cool core clusters*, CXC/HETG Group Meeting at MIT, USA, **Oct '08**
- *Sources of metals and AGN-induced metal transport in cool-core clusters*, HEAD lunch talk, Harvard Smithsonian CfA, USA, **Sep '08**
- *Multi-temperature structure and the dynamical state of clusters*, short oral contribution for The Cool, the Cooler and the Cold: clusters of galaxies in a new light workshop in Leiden, the Netherlands, **Sep '08**
- *The AGN-driven large-scale shock in Hydra A*, poster at the Putting Gravity to Work invitational conference in honor of A. C. Fabians 60th birthday, Cambridge, UK, **Jul '08**
- *AGN-driven shocks and metal transport*, talk at The X-ray Universe conference in Granada, Spain, **May '08**
- *AGN-driven shocks and metal transport*, talk at the MPE X-ray/Gamma-ray group meeting in Ringberg, Germany, **Feb '08**
- *AGN-driven phenomena in cluster cooling cores*, 5 minute talk and poster presented at the conference The Suzaku X-ray Universe, San Diego, USA, **Dec '07**
- *Metal-rich multi-temperature gas in M87 seen with XMM-Newton*, talk at the EPIC Consortium Meeting in Leicester, UK, **Sep '07**
- *Complex multi-temperature structure in M87*, poster for the conference Tracing Cosmic Evolution with Clusters of Galaxies in Sesto, Italy, **Jun '07**
- *Substructure in the gas halo of M87*, oral presentation at the Frauenwoerth Cluster Workshop in Frauenwoerth, Germany, **May '07**
- *The gaseous atmosphere of M87 seen with XMM-Newton*, talk and poster for the MPE Science Days and MPE advisory board meeting, Garching, Germany, **March & May '07**
- *The gaseous atmosphere of M87 seen with XMM-Newton*, poster for the Heating and Cooling in Galaxies and Clusters of Galaxies conference in Garching, Germany, **Aug '06**
- *The X-ray halo of M87*, poster for the Observing the X- and Gamma-ray sky Spring school in Cargese, Corsica, **Apr '06**